Author:
Brown, Julian Tom

Title:
The computer simulation of Liquid Crystals

The Computer Simulation of Liquid Crystals

Julian Tom Brown

H. H. Wills Physics Laboratory,
University of Bristol

A thesis submitted to the University of Bristol
in accordance with the requirements of the degree of
Doctor of Philosophy
in the Faculty of Science

October 1996

Abstract

In this thesis we describe investigations of the properties of several idealized model liquid crystal systems, focusing primarily on the Gay-Berne potential.

Results are reported from extensive simulations of the Gay-Berne family of molecular models, examining phase behaviour as systematic variations are made to the shape anisotropy κ, at fixed well-depth anisotropy κ', and vice-versa. Major changes occur in the range $3 \leq \kappa \leq 4$, with the growth of a stable smectic-A phase and the disappearance of the liquid-vapour critical point. With κ fixed, the nematic phase of low-κ' fluids, $\kappa' \leq 1.25$, is seen to be stable at temperatures low enough to intersect the liquid-vapour region.

The liquid-vapour properties of the Kihara/spherocylinder fluid are reported for elongations $L/D \leq 6$; in all cases the liquid phase remains isotropic. Similar studies of a variant of the Gay-Berne fluid in which the strength parameter is fixed, ϵ = constant, indicate an interesting low-temperature glass-like phase at elongations $\kappa > 5$.

Finally, we report two investigations of the nematic-phase elastic properties of the Gay-Berne fluid. Comparison is made between use of a perturbing field and previous measurements of director fluctuations, as routes to the Frank elastic constants. Measurements of the twist elastic constant using twisted periodic boundary conditions are also reported. The systems studied here prove less satisfactory than director fluctuation measurements, but show broad agreement in both cases.

Acknowledgements

I would like thank my advisor, Dr. M. P. Allen, for his instruction, creativity and patience throughout this project. I have also benefited from useful discussions with Drs. E. de Miguel, E. Martín del Río and S. Hanna and Prof. R. Evans. Thanks are due to M. A. Warren for making available visualization software and Dr. J. A. Odell for providing Figure 5.21. I wish to acknowledge financial support from the University of Bristol through a Postgraduate Scholarship, and the Engineering and Physical Sciences Research Council through research grants for computer hardware. I would also like to acknowledge the staff of the Maria Mercer Physics Library for all their help, and J.-P. Melot for his considerable assistance with computer hardware and networking.

For their technical assistance and friendship, thanks to other members of the research group, particularly Carl, Mark, Héctor, Philip and Jeroen. Thanks also to the other friends on whom I have relied, whether in or out of the department, especially Tim and Jane. I would like to acknowledge my family, (all of them), for their on-going love and support.

Final thanks go to those who have taken most of the strain over the last three years and continued to believe in me: to Rachel, (words are not enough), and God.

The horse is made ready for the day of battle,
but victory rests with the Lord.

Proverbs 21 v. 31

Author's Declaration

I declare that no part of this thesis has been submitted for a higher degree in this, or any other, university. The research reported herein is the result of my own investigation except where reference is made to the work of others. All research was carried out under the supervision of Dr. M. P. Allen at the University of Bristol, between October 1993 and October 1996.

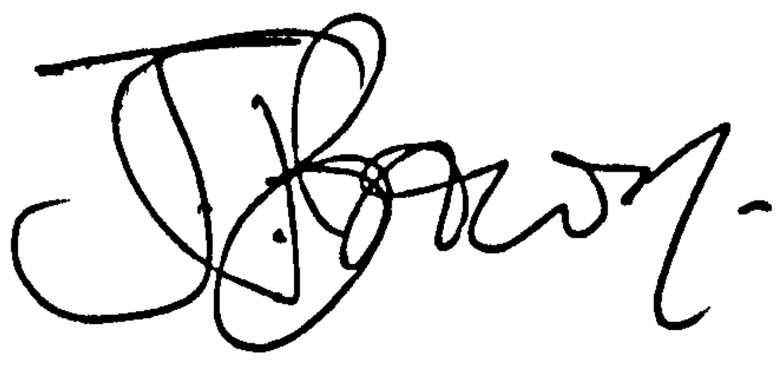

Julian T. Brown

October 1996

The views expressed in this thesis are those of the author and not necessarily those of the University of Bristol.

Contents

List of Figures

List of Tables

Chapter 1

Introduction

1.1 Liquid Crystal Mesogens and Phases

Liquid crystal phases appear between the liquid and solid states of matter. They are absent from the phase behaviour of most materials, but when they do arise they show properties intermediate between those of the amorphous liquid and the crystalline solid. In a liquid crystal a limited degree of ordering is present in the orientations and sometimes positions of the constituent molecules, but these materials will have, for example, diffusion and flow properties in common with isotropic liquids. The class of molecules which do form liquid crystalline phases exhibit a high degree of geometrical anisotropy. They can be elongated organic molecules such as PAA, (*p*-azoxyanisole), and MBBA, (*N*-(*p*-methoxybenzylidene)-*p*-butylaniline), shown schematically in Fig. 1.1, small discoid organic molecules, polymers or long helical rods such as tobacco mosaic virus (TMV) which is 3000 Å in length and 200 Å in width. These different types of unit tend to display different sets of mesophases.

There is a rich variety of liquid crystalline phases. Transitions to these states may be induced by thermal processes, (thermotropic behaviour), or interactions with a solvent, (lyotropic behaviour). Rod-like molecules, which are the subject of this work, form liquid crystalline phases that may be classified broadly into three types known as nematic, smectic and cholesteric. The arrangement of molecules within these phases is illustrated in Fig. 1.2. The nematic is the simplest of the liquid crystalline mesophases, its name coming from the thread-like defects which it commonly displays. The transition from an isotropic

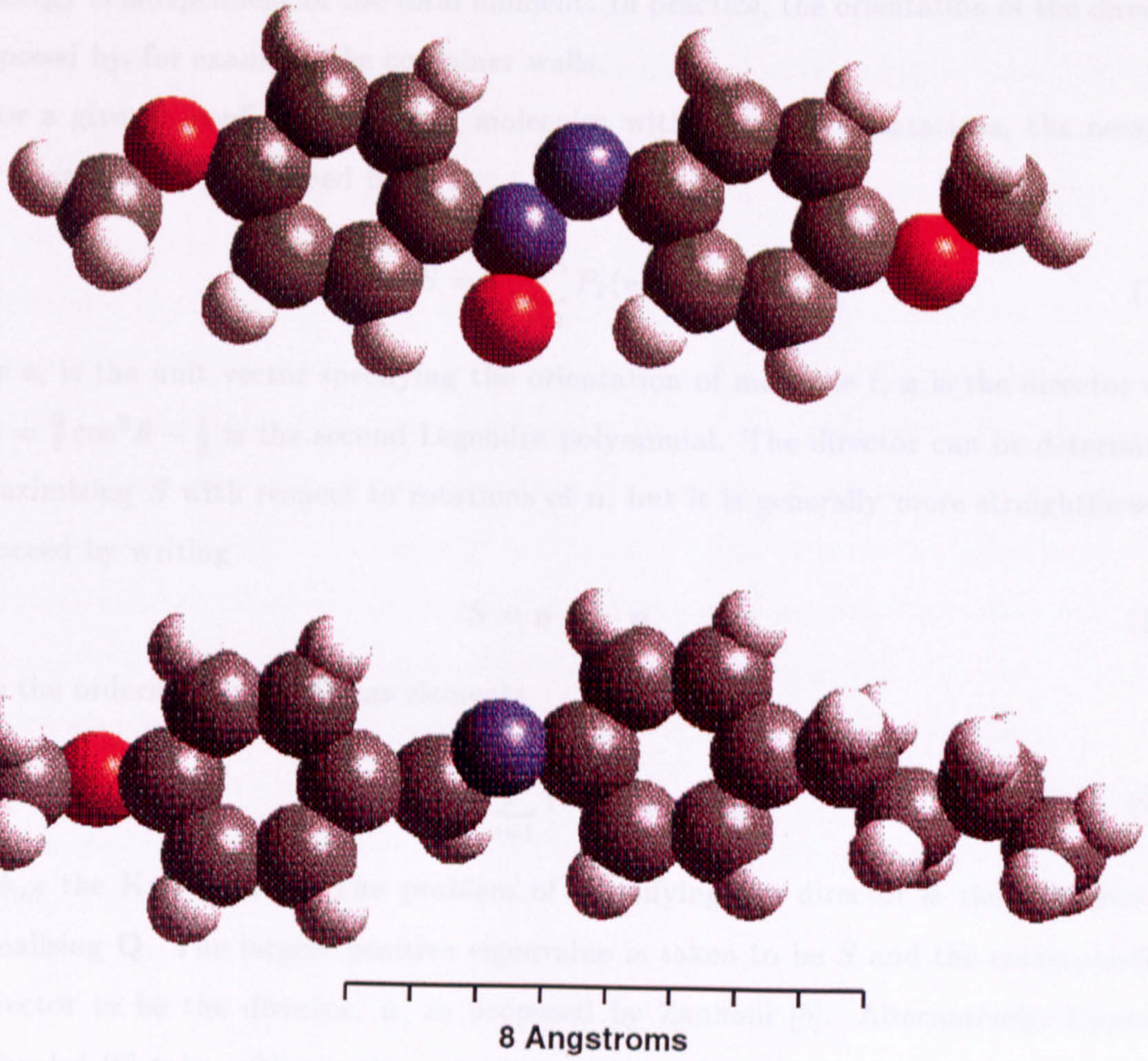

Figure 1.1: The mesogens PAA (top) and MBBA

fluid phase to the nematic phase occurs when the molecules align preferentially along one direction, known as the director, but nematics do not have long-range translational order and flow like conventional liquids. Particle orientations are a distinct degree of freedom and since the alignment in a nematic corresponds to a spontaneously broken rotational symmetry, the orientation of the director is arbitrary in space. This is analogous to the situation in a Heisenberg ferromagnet, where all the spins tend to be parallel, but where the energy is independent of the total moment. In practice, the orientation of the director is imposed by, for example, the container walls.

For a given a configuration of N molecules with specified orientations, the nematic order parameter, S, is defined by

$$S = \frac{1}{N}\sum_{i=1}^{N} P_2(\mathbf{e}_i \cdot \mathbf{n}) \tag{1.1}$$

where $\mathbf{e}_i$ is the unit vector specifying the orientation of molecule i, $\mathbf{n}$ is the director and $P_2(\theta) = \frac{3}{2}\cos^2\theta - \frac{1}{2}$ is the second Legendre polynomial. The director can be determined by maximizing S with respect to rotations of $\mathbf{n}$, but it is generally more straightforward to proceed by writing

$$S = \mathbf{n} \cdot \mathbf{Q} \cdot \mathbf{n} \tag{1.2}$$

where the ordering matrix $\mathbf{Q}$ has elements

$$Q_{\alpha\beta} = \frac{1}{2N}\sum_{i=1}^{N} \{3\, e_{i\alpha} e_{i\beta} - \delta_{\alpha\beta}\}\,. \tag{1.3}$$

with $\delta_{\alpha\beta}$ the Kronecker δ. The problem of identifying the director is then reduced to diagonalising $\mathbf{Q}$. The largest positive eigenvalue is taken to be S and the corresponding eigenvector to be the director, $\mathbf{n}$, as proposed by Zannoni [5]. Alternatively, Eppenga and Frenkel [6] take $-2\lambda_0$ as the order parameter, where λ_0 is the 'middle' eigenvalue of $\mathbf{Q}$. This often helps to distinguish the nematic from the isotropic in the vicinity of the phase transition, since the former definition leads to small positive values of S in the isotropic phase of order $N^{-1/2}$, whereas the latter is of order N^{-1}, fluctuating about zero [6, 7]. Clearly this becomes more significant as the isotropic-nematic phase transition weakens. Both choices give $S = 1$ for perfectly parallel alignment, and will agree closely in the nematic phase, where S has a value between 0 and 1, generally showing strong

temperature dependence. Since the director is a 'headless' vector the states $\mathbf{n}$ and $-\mathbf{n}$ are indistinguishable.

The second type of mesophase commonly exhibited by liquid crystals displays positional order in one or two dimensions, rather than three as in a crystal. Molecules in these so-called smectics, named after soap in which they were first observed, form layered structures. There is a well-defined interlayer spacing which can be measured by X-ray diffraction. Smectic phases are further classified according to the molecular arrangement within the layers. In a smectic A, (S_A), the molecules are upright within each layer, with no long-range in-plane positional ordering of their centres. The smectic C is a tilted form of S_A. The hexatic smectic B shows a high degree of bond orientational order within each layer but remains a liquid crystal. The layers are a two-dimensional liquids but locally the molecules occupy a triangular lattice. The liquid nature is retained because of the high number of defects, ensuring that the positional order does not extend for more than a few 100 Å, whilst the bond order propagates over macroscopic distances. When the positional order is also able to propagate over macroscopic distances the system becomes crystalline. Such crystals can form with only weak binding between the layers and resulting observations of plastic deformations under very weak imposed forces have led to the mistaken conclusion that these are liquid crystals. The pure smectic B is one example of such a phase, now designated the crystal B. Other, 'exotic' smectic phases have also been identified - at least 14 others have been named [4]. Identification of a smectic phase in simulation is aided by a positional order parameter. A suitable, origin-independent order parameter is given by

$$s_k(\mathbf{k}) = \left\langle \frac{1}{N} \left\{ \left(\sum_{i=1}^{N} \cos(\mathbf{k}.\mathbf{r}_i) \right)^2 + \left(\sum_{i=1}^{N} \sin(\mathbf{k}.\mathbf{r}_i) \right)^2 \right\}^{1/2} \right\rangle \tag{1.4}$$

where $\mathbf{k}$ is a reciprocal lattice vector commensurate with the box dimensions [5]. For appropriate $\mathbf{k}$, s_k becomes unity in a perfectly ordered lattice, and in a translationally disordered system fluctuates about a value $\mathcal{O}(N^{-1/2})$. For a box of given shape and dimensions there is a discrete set of appropriate reciprocal lattice vectors and in identifying the onset of order rather than its disappearance, as when an initial lattice system melts, it can be instructive to calculate $s_k(\mathbf{k})$ for a fixed set of $\mathbf{k}$ and monitor both the peak value and the corresponding vector, $\mathbf{k} = \mathbf{k}_{max}$, from which additional information about

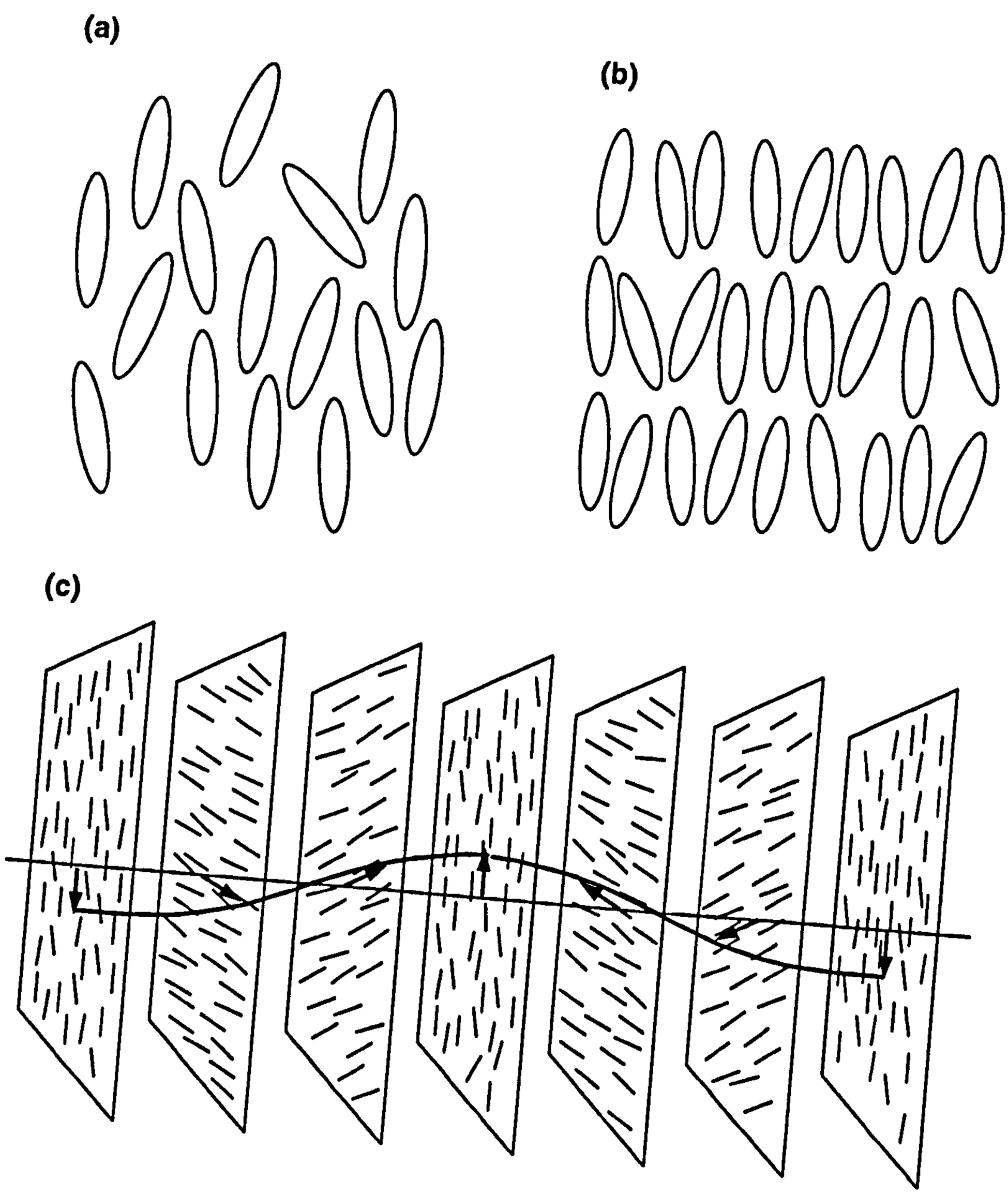

Figure 1.2: Liquid crystalline mesophases : (a) nematic, (b) smectic and (c) cholesteric

the structure and periodicity of the system can be inferred. The required sorting for the s_k(k) values is a fast procedure.

The third type of mesophase in this broad classification is related to the nematic: the cholesteric phase, originally seen in pure cholesterol esters. appears when optically active molecules form a nematic liquid crystal. As a consequence of the chirality of the molecules, a spontaneous twist forms in the nematic about an axis perpendicular to the director. The twist may be right- or left-handed, depending on the conformation of the molecules, but the preferred variation of **n** in space is helical, as shown in Fig. 1.2. Optically inactive molecules or a racemic mixture of chiral molecules give a helix of infinite pitch - a true nematic. The energy of the twist is only a tiny part of the total energy associated with the parallel alignment of the molecules, (about 10^{-5}), so just a small quantity of a chiral substance can induce a helical distortion in the director field of a nematic normally without twist [4].

Twisted nematics have particularly interesting optical properties - the pitch of the helix can be comparable with optical wavelengths and generally shows a marked temperature dependence allowing the material to change colour dramatically in a small temperature interval. This has been exploited in a range of applications, from identification of points of overheating in electronic circuits to location of fractures and tumors in humans and so it is useful to study the relationship between concentration of the chiral dopant molecules and the pitch of the induced helix. Both nematics and cholesterics are highly sensitive to external fields and this is exploited in display technology, perhaps the best known application of liquid crystals. By modulating the reflected light, including sunlight, liquid crystal displays can maintain a good contrast under a wide range of operating conditions. Smectic phases are of interest in a number of areas including the development of new generations of displays with high speeds and intrinsic memory. With such possibilities, industrial interest in liquid crystals is well-established. These systems also still hold a good deal of scientific interest in the fields of statistical mechanics and hydrodynamics, offering highly original experimental systems.

The phase behaviour of liquid crystal systems may be investigated experimentally using, for example, differential scanning calorimeter measurements to locate transition temperatures. The nature and degree of ordering in the system may be investigated in a

number of ways. It is possible to relate S to experimentally determinable quantities, e.g. diamagnetic anisotropy, when it is necessary to measure the susceptibility either parallel or perpendicular to the director, and also to know the principal diamagnetic susceptibilities of the relevant crystal. Another route to S requires the optical anisotropy of the molecule and the effective polarizabilities of the nematic phase. It is also possible to extract S from NMR measurements, where the splitting of the resonance line on moving from an isotropic fluid to a nematic is the necessary measurement. Liquid crystal systems can be probed by X-ray diffraction, of particular relevance when studying smectic phases. Optical techniques offer significant opportunities to examine and characterize liquid crystal phases, and the patterns displayed by polarization experiments demonstrate why this field has attracted such interest.

1.2 Historical development and rôle of simulation

The remarkable appearance and properties of liquid crystals have caught the interest of both experimentalists and theoreticians. Studies of these materials have made a significant contribution to the wider field of phase transitions and critical phenomena. Computer modelling and simulation have played a valuable part in the process, growing as a bridge between experiment and theory, with the essential techniques now well established [9]. By necessity, theoretical studies tend to be based on simple models, reducing the number of physical features but aiming to retain those essential to the behaviour of interest. Often, even highly idealized models cannot be solved exactly and approximations must be introduced, making it difficult to judge the validity of a model by direct comparison with experimental data. Discrepancies could indicate that the theoretical treatment is inadequate or that the model itself misses some essential feature. It is here that computer experiments can be of great value. Essentially exact results can be obtained for a given model, so exposing inappropriate approximations in an analytic approach. Furthermore, the model itself can be tested by comparison with experiment. Once a model has been established as a good description of a physical system, parts of parameter space not readily accessible to experimentalists can be easily probed by numerical studies. Length and time scales too small for laboratory examination become open to scrutiny, with obser-

vation possible at a molecular level, albeit for microscopic system-sizes, offering a fuller understanding of the processes at work.

The first computer simulation studies were able to test only highly idealized models. The pioneering studies of two-dimensional hard spheres reported in 1953 [10] made use of one of the most powerful computers then available, but the system size was limited to a few hundred particles. These experiments could now be repeated on home computers. Both the size and the complexity of systems open to simulation study have grown greatly in the last 40 years. The latest generations of supercomputers allow the simulation of tens of thousands of particles interacting via continuous potentials, and the largest Ising lattice systems currently simulated contain over 10^{10} spins [11]. These massively parallel machines, like the Cray T3D, can achieve tens of gigaflops, (1 gigaflop = 10^9 floating point operations per second) and have dozens of gigabytes of memory, vastly outperforming the state-of-the-art machines of just a few years ago. Most of the studies reported here have been performed on individual workstations, (Silicon Graphics or DEC Alpha machines), allowing the study of 10^4 particles with reasonable comfort. With increasing computer power, the variety of model systems studied and the range of techniques available to the simulator has grown, allowing computer experiments to enhance understanding in many theoretical and experimental contexts. The discovery of the algebraic decay of the velocity autocorrelation function at long times in the hard sphere fluid [12] is one of the best known success of simulation since these observations were ahead of theory, discovering new results rather than testing predictions. Recently, first calculations by simulation of the direct correlation function, $c(1,2)$, have appeared for the hard ellipsoid [13] and Gay-Berne [14] fluids. This is a fundamental quantity in the theory of liquid structure and these measurements allow testing of basic assumptions of many density functional approaches and a new route to calculations of derived quantities such as Frank elastic constants. In addition to probing fluids at this fundamental level, increasingly realistic systems are being studied by simulation, either by extension of simple model systems or using quantum-mechanical first-principles techniques, (see, for example, K. Kremer and R. Car in [15]).

1.3 Model Potentials

1.3.1 Rigid Bodies

Simulation studies of liquid crystals began in the early 1970s [16, 17] with subsequent growth in two main directions, looking at systems of 'soft' particles interacting via simple 'ellipsoidal' generalizations of the Lennard-Jones potential, or at systems of rigid bodies, ('hard' particles), with an infinitely repulsive core and no attractive interactions, largely motivated by Onsager's predictions that excluded volume effects can be sufficient to induce liquid crystalline ordering. Rigid particles have been used in computer simulations of liquid crystals with much success [7], with hard spheres being frequently called upon as a reference system for atomic fluids.

Hard body simulations can use highly efficient algorithms, and they have done much to increase the understanding of, for example, the rôle of molecular shape in the formation of liquid crystal phases. Studies of spheroidal particles have indicated a phase diagram with approximate prolate/oblate symmetry about the hard sphere system [18]. This shows two phases, an isotropic fluid and a crystal, but where the axial ratio of the particles exceeds about 3, (or $\frac{1}{3}$), a nematic phase is also observed. Since they can be mapped onto the hard sphere case by an affine transformation, hard spheroids do not show smectic phase behaviour. Hard spherocylinders, however, do show a S_A phase at length/width ~ 4 and above [19]. The full range of phases shown by these and other hard convex particles make them intrinsically interesting, and in addition to their application as reference systems for more realistic fluids, they provide useful building blocks for simulation of larger molecules.

1.3.2 Atomic Soft-Body Potentials

The study of systems with purely repulsive interactions is of great importance, and, as indicated above, studies of hard particle fluids have shown that pure steric repulsion is sufficient to produce a number of liquid-crystalline phases. It is, however, generally recognized that for real mesogens both repulsive and attractive interactions make significant contributions to phase behaviour, and in terms of simulation studies it can be more straightforward to employ a continuous form of potential. The repulsive core of the potential can be thought of as modelling the overlap of electronic wavefunctions of atoms

in molecules, the shape being elucidated from molecular structure or from a knowledge of the charge density determined by diffraction measurements or quantum calculations. In a real system, van der Waals attraction will also play a rôle, varying as r^{-6} at short range. These two effects are the basis of the standard Lennard-Jones (LJ) potential, where the repulsive core is conventionally represented by a term in r^{-12}. The LJ potential is often written as

$$U_{LJ}(r) = 4\varepsilon\left[\left(\frac{\sigma_0}{r}\right)^{12} - \left(\frac{\sigma_0}{r}\right)^{6}\right], \tag{1.5}$$

with σ_0 the separation of centres at zero potential and ε the minimum pair energy. This potential can provide a reasonable fit to the measured potentials for simple atomic systems, such as inert gases. Alternatively, the LJ potential can be used in computer simulation to reproduce the properties of such systems with reasonable results. In this case, the values taken by ε and σ_0 will differ from those giving the best fit to the potential between two isolated atoms. This potential is pair-wise additive, so that the effective values of these parameters must incorporate any significant higher-order effects. There have been some investigations into the importance of three-body interactions in simulations of argon [20], where the pair potential generally performs well but three-body repulsion is claimed to become a significant effect at higher densities. The simple LJ form can be applied beyond atomic systems in a phenomenological description of molecular interactions, where the interaction between molecules is given by the sum of LJ interactions between designated sites, which may or may not coincide with the nuclei, giving the site-site Lennard-Jones potential (SSLJ),

$$U_{SS} = \sum_{\alpha\beta} U_{LJ}(\varepsilon_{\alpha\beta}, r_{\alpha\beta}/\sigma_{\alpha\beta}). \tag{1.6}$$

The labels α and β run over interaction sites in molecules i and j respectively. The SSLJ has been proved widely useful in the modelling of real fluids of slightly non-spherical molecules like nitrogen and carbon dioxide, and short chain fluids [21], although clearly other choices of site potential can be made, (e.g. r^{-n}, fused hard sphere or Kihara forms).

1.3.3 The Kihara Potential

The SSLJ model becomes less useful in the simulation of liquid crystal phases, since the many sites required to model each realistic mesogenic molecule makes the process pro-

hibitively expensive. In the Kihara potential [22], the separation variable is made to model the molecular shape, becoming a function of particle orientations. The molecular cores are modelled by convex bodies and longer-ranged force fields may be superimposed, with a common choice being a LJ form, (1.5), with the range parameter r replaced by $\rho = \rho(\mathbf{r}, \omega_1, \omega_2)$, the shortest distance between a pair of molecular cores with orientations ω_1 and ω_2 and separation $\mathbf{r}$. The strength and range parameters, ε_0 and σ_0, are constants. The core of linear molecules, or nearly-linear molecules is naturally represented by rods or spherocylinders, and calculation of $\rho(\mathbf{r}, \omega_1, \omega_2)$ is reduced to finding the minimum separation of two finite line-segments. This is a standard procedure [7] and can be readily programmed. With its simple form, and since it can describe physical and thermodynamic properties reasonably well the Kihara potential has proved to be a useful tool in, for example, perturbation theory [23, 24].

1.3.4 The Gaussian Overlap Potential

Another early proposal for a computationally feasible potential for the relatively complex molecules that form liquid crystals was due to Berne and Pechukas [25] in 1972, who suggested representing each molecule by a three-dimensional Gaussian distribution of forces, defined in terms of the axial vector $\mathbf{e}$ and the parallel and perpendicular dispersions of the distribution, $\sigma_{\parallel}$ and $\sigma_{\perp}$. The interaction between two such molecules is governed by the extent to which their Gaussian distributions overlap. This overlap integral can be written in the form

$$I_{OV} = \varepsilon_{GO}(\mathbf{e}_1, \mathbf{e}_2) \exp\left(\frac{-r^2}{\sigma^2_{GO}(\hat{\mathbf{r}}, \mathbf{e}_1, \mathbf{e}_2)}\right) \tag{1.7}$$

where $\mathbf{r}$ is the centre-centre vector, and ε_{GO} and σ_{GO} are the Gaussian overlap (GO) strength and range parameters, given by

$$\varepsilon_{GO}(\mathbf{e}_1, \mathbf{e}_2) = \varepsilon_0 \left[1 - \chi^2 (\mathbf{e}_1 \cdot \mathbf{e}_2)^2\right]^{-\frac{1}{2}}, \tag{1.8}$$

$$\sigma_{GO}(\hat{\mathbf{r}}, \mathbf{e}_1, \mathbf{e}_2) = \sigma_0 \left[1 - \frac{\chi}{2}\left(\frac{(\hat{\mathbf{r}} \cdot \mathbf{e}_1 + \hat{\mathbf{r}} \cdot \mathbf{e}_2)^2}{1 + \chi(\mathbf{e}_1 \cdot \mathbf{e}_2)} + \frac{(\hat{\mathbf{r}} \cdot \mathbf{e}_1 - \hat{\mathbf{r}} \cdot \mathbf{e}_2)^2}{1 - \chi(\mathbf{e}_1 \cdot \mathbf{e}_2)}\right)\right]^{-\frac{1}{2}}, \tag{1.9}$$

where $\chi = \{(\kappa^2 - 1)/(\kappa^2 + 1)\}$ and $\kappa = \sigma_{\parallel}/\sigma_{\perp}$ is the geometrical anisotropy parameter. The resulting potential is then

$$U(r, \hat{\mathbf{r}}, \mathbf{e}_1, \mathbf{e}_2) = \varepsilon_{GO}(\mathbf{e}_1, \mathbf{e}_2) \exp\left[-r^2/\sigma^2_{GO}(\hat{\mathbf{r}}, \mathbf{e}_1, \mathbf{e}_2)\right]. \tag{1.10}$$

The orientation dependence is now built in using a simple functional form, but no account is taken of the distance dependence of realistic potentials. This can be achieved by importing the same strength and range parameters into a potential with a more appropriate distance dependence. The Lennard-Jones potential is a suitable candidate, giving

$$U_{GO}(r, \hat{\mathbf{r}}, \mathbf{e}_1, \mathbf{e}_2) = 4\varepsilon_{GO}(\mathbf{e}_1, \mathbf{e}_2)\left\{\left(\frac{\sigma_{GO}(\hat{\mathbf{r}}, \mathbf{e}_1, \mathbf{e}_2)}{r}\right)^{12} - \left(\frac{\sigma_{GO}(\hat{\mathbf{r}}, \mathbf{e}_1, \mathbf{e}_2)}{r}\right)^{6}\right\} \quad (1.11)$$

For convenience this will be labelled the GO potential. Approximately ellipsoidal particles of any elongation may be represented in this way, which can be more convenient in simulation than rigid body or Kihara potentials, for example, since it is differentiable. It has been applied in a number of contexts, including liquid crystals [26].

A modification of this, in which the orientational dependence of ε is neglected, has been suggested [27, 28]; this will be referred to as the Gaussian Overlap Constant ε (GOCE) potential. Leaving the anisotropy of well-depth out may seem a retrograde step, but the simplified system is still a useful reference for perturbation theory, being not so distant from the hard ellipsoid fluid and since surfaces of constant r/σ are also equipotential surfaces, allowing mathematical treatments equivalent to those used for spherical systems [29, 30].

Both the GO and the GOCE models suffer from certain unphysical features. In general, one would expect two molecules to favour a side-by-side over an end-to-end arrangement. However, since the strength parameter has no dependence on the intermolecular vector $\hat{\mathbf{r}}$, equal strength interactions arise for these two configurations. Further, it would seem reasonable that the width of the potential well be independent of orientation. Since the GO models have a well-width proportional to σ, the end-to-end well is wider than the side-by-side by a factor equal to the axial ratio as indicated in Fig. 1.3.

1.3.5 The Gay-Berne Potential

The modified potential proposed by Gay and Berne [31] was constructed to address the deficiencies of the GO model outlined above by making two modifications. Firstly, they introduced a dependence on $\hat{\mathbf{r}}$ into the strength parameter:

$$\varepsilon_{GB}(\hat{\mathbf{r}}, \mathbf{e}_1, \mathbf{e}_2) = \varepsilon_{GO}^{\nu}(\mathbf{e}_1, \mathbf{e}_2)\varepsilon'^{\mu}(\hat{\mathbf{r}}, \mathbf{e}_1, \mathbf{e}_2) \quad (1.12)$$

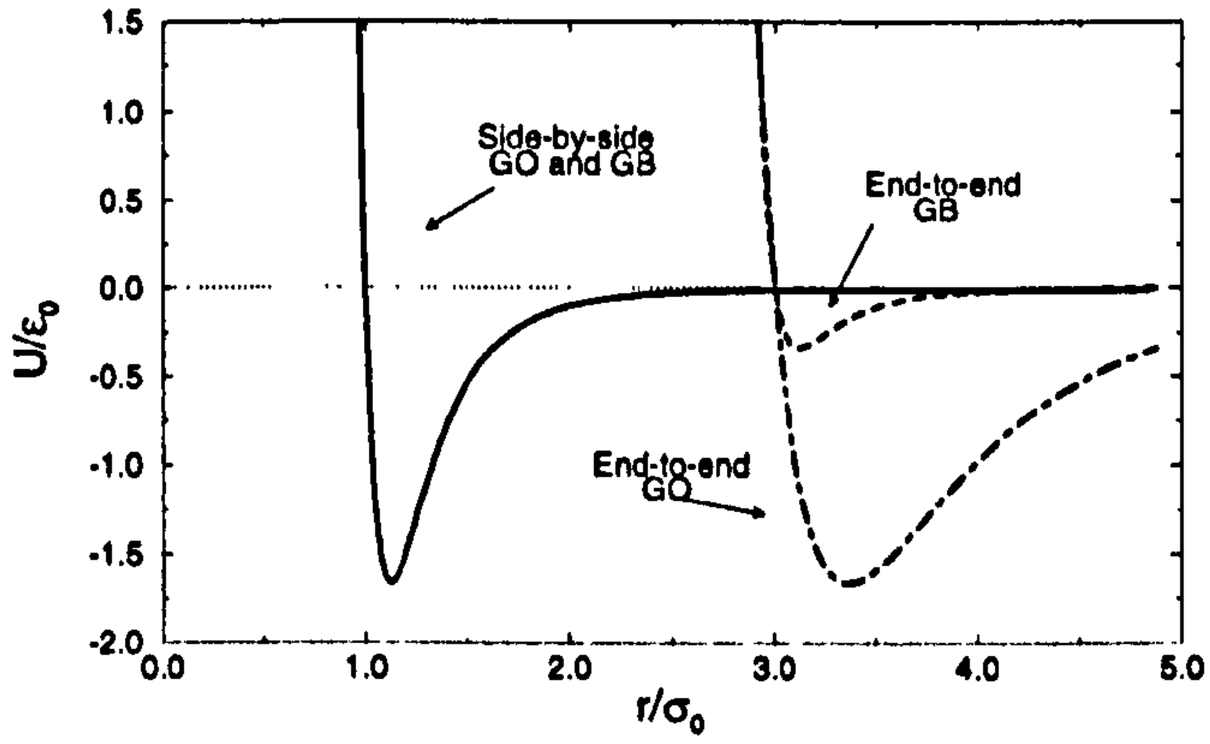

Figure 1.3: The GO and GB potentials for side-by-side and end-to-end pair configurations of parallel molecules with elongation $\kappa = 3$.

where ε_{GO} is as above, and ε' is basically $(1/\sigma^2)$, but with χ replaced by a new parameter χ', allowing the ratio of side-by-side and end-to-end well depths, (ε_{ss} and ε_{ee} respectively), to be adjusted :

$$\chi' = \frac{\kappa'^{\frac{1}{\mu}} - 1}{\kappa'^{\frac{1}{\mu}} + 1} \tag{1.13}$$

with $\kappa' = (\varepsilon_{ss}/\varepsilon_{ee})$. The exponents ν and μ were fixed by requiring a good fit to a site-site Lennard-Jones potential in which equally spaced sites are arranged linearly such that the overall length-to-breadth ratio is equal to κ. Gay and Berne took a four-site Lennard-Jones molecules with $\kappa = 3$ and obtained good agreement using the values $\nu = 1$ and $\mu = 2$.

Secondly, the rôle of σ was changed, so that it displaces the potential, rather than dilating it. The final form of the Gay-Berne (GB) potential is then

$$U_{GB}(r, \hat{\mathbf{r}}, \mathbf{e}_1, \mathbf{e}_2) = 4\varepsilon_{GB}(\hat{\mathbf{r}}, \mathbf{e}_1, \mathbf{e}_2) \left\{ \left(\frac{\sigma_0}{r - \sigma_{GB} + \sigma_0} \right)^{12} - \left(\frac{\sigma_0}{r - \sigma_{GB} + \sigma_0} \right)^{6} \right\} \tag{1.14}$$

with $\sigma_{GB}(\hat{\mathbf{r}}, \mathbf{e}_1, \mathbf{e}_2) = \sigma_{GO}$.

It can be seen that the GB potential reduces to the GO form for $\kappa' = 1$, and for $\kappa = \kappa' = 1$ the GB potential is equivalent to the spherical Lennard-Jones potential. In this sense, the GB potential can be regarded as a generalization of the Lennard-Jones potential to non-spherical systems. It is certainly more than just a fit to the SSLJ, since

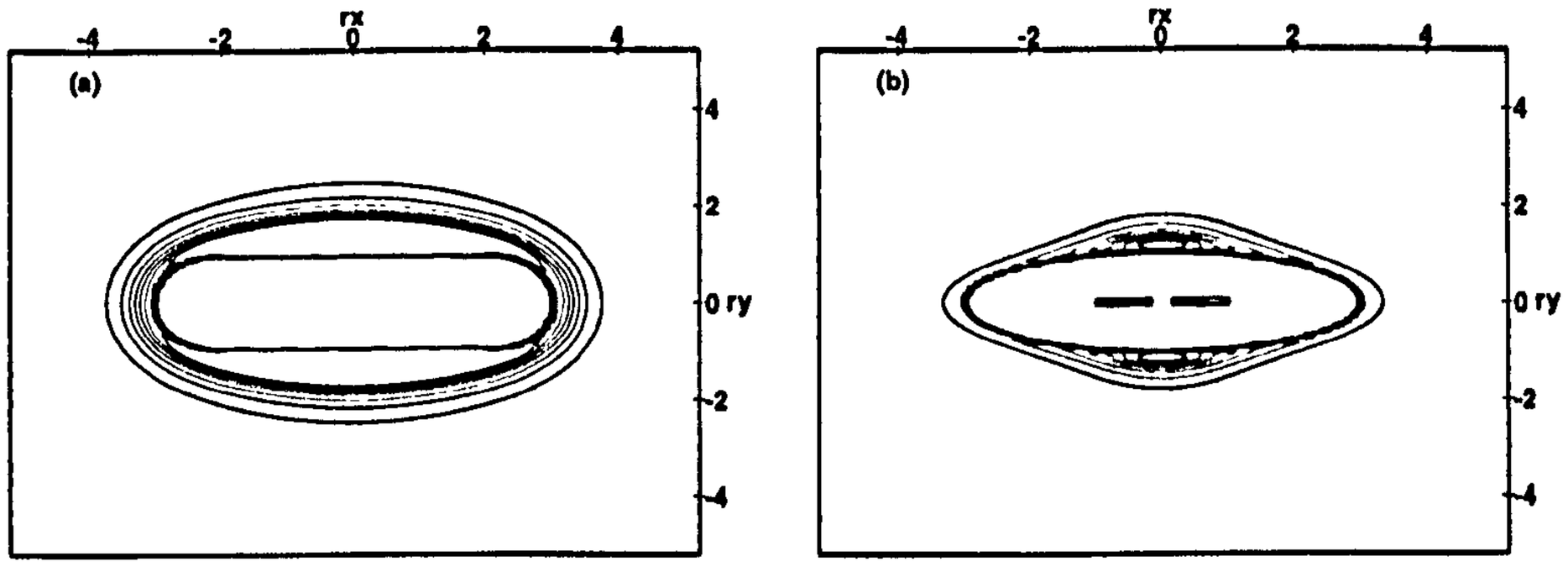

Figure 1.4: Potential energy contours for parallel molecules : (a) Linear 4SSLJ with overall length 3 and (b) GB with $\kappa = 3$, $\kappa' = 5$, $\nu = 1$, $\mu = 2$. Contours are shown at intervals of $0.2\varepsilon_0$ in the range U/ε_0=(-1.4,1.0); r_x and r_y are in units of σ_0.

there are clear geometrical differences between the models. As the number of sites in the linear LJ molecule increases, the shape of the $U = 0$ equipotential surface, which may be taken as the shape of the molecule, comes to resemble a spherocylinder, whereas the molecular core of the GB molecule is ellipsoidal as shown in Fig. 1.4. The attractive part of the potential is also different, since the potential contours of the GB potential lose the ellipsoidal symmetry that the GO system retains. At low pressures the attractive parts of the potentials will dominate, so the two systems can and do exhibit entirely different phase behaviour.

In a wide range of reported simulation studies, the GB model has been shown to exhibit stable nematic and smectic mesophases. The work of de Miguel et al. [1] has provided an approximate phase diagram for a GB system with parameters $\kappa = 3$, $\kappa' = 5$, $\nu = 1$, $\mu = 2$, which indicates stable nematic and smectic B phases. Other sets of parameters have also been studied. Luckhurst et al. [32] found that a system simulated with the values $\kappa = 3$, $\kappa' = 5$, $\nu = 2$, $\mu = 1$ displayed a smectic A phase in addition to N and S_B phases. Berardi et al. [33] worked with $\kappa = 3$, $\kappa' = 5$, $\nu = 3$, $\mu = 1$ and found N and S_B phases. Many aspects of the Gay-Berne model have been studied in addition to its phase behaviour, including single-particle translational and rotational dynamics [34],

behaviour of a solute particle in a liquid crystal solvent [35, 36], interfacial properties [37], elastic constants [14, 3], thermal conductivity [38, 39], viscosity coefficients [40, 41, 42] and behaviour in confining geometries [43]. Different perturbation theories have also been developed to study the phase diagram of GB fluids [28, 44, 45, 46]. A recent generalization of the GB potential has considered non-equivalent Gay-Berne particles in both uniaxial and biaxial cases [47]. This work also confirms that the range function, $\sigma_{GB} = \sigma_{GO}$, can be obtained from an approximation to the Perram-Wertheim contact function for hard ellipsoids, in fact over-estimating the distance of closest approach for true ellipsoids.

1.4 Scope of the thesis

The values chosen for the parameters of a model potential will generally have a significant effect on the resulting behaviour. In the course of this thesis the consequences of systematically varying these parameters for several systems will be considered, with particular emphasis on the GB fluid, for which independent variations of κ, the shape anisotropy, (Chapter 3), and κ', the well-depth anisotropy, (Chapter 4) are investigated. In both cases dramatic changes in phase behaviour are seen. Small increases in elongation are found to stabilize a 'bubble' of S_A in the phase diagram, and destroy the isotropic liquid phase. The low-κ' fluid is also particularly interesting since it displays isotropic-nematic coexistence. This is well-established for experimental systems but has proved elusive in model fluids.

In Chapter 5 the effects of elongation on Kihara and Gay-Berne Constant ε, (GBCE), fluids are explored, with particular reference to the liquid-vapour regions. Under certain conditions a glass-like phase was observed for the GBCE system in which particles are arranged in 'rosettes'. Characterization of this state is described.

Finally, we return to the GB fluid and investigate the elastic properties of the nematic phase via the Frank elastic constants. In recent years a range of simulation routes to these constants have appeared. Two investigations are described, and the suitability of the techniques used is discussed.

In the course of these investigations a variety of simulation techniques have been used. Before moving to the results, these techniques are outlined, along with some technical aspects of computer simulation, in the next chapter.

Chapter 2

Simulation Methods

In the simulation of condensed matter, the computer is used to generate many microscopic configurations, Γ, of the system under study in terms of positions, orientations and velocities of the individual particles, and measurements are made by building up averages over these configurations. In order to relate such averages to macroscopic quantities with any confidence, the sequences of configurations must sample the possibilities in a reasonable way. There are two well established approaches. In a molecular dynamics, (MD), simulation a sequence of configurations is generated according to the classical equations of motion for the system, allowing measurement of time averages. In Monte Carlo, (MC), averages are taken over configurations generated according to an appropriate probability density. Ensembles commonly employed in simulation include the microcanonical, (constant number of particles N, volume V and energy E), canonical, (constant N, V and temperature T), grand canonical, (constant V, T and chemical potential μ), and isothermal-isobaric, (constant N, T and pressure P). The choice between MD and MC may be dictated by the phenomena under investigation. Studies of dynamical properties will, in general, require the use of MD. Major strengths of MC are the ease with which less-common ensembles can be sampled and the ability to bias the sampling to probe the less favoured regions of phase space, exploring rare events. Provided the system visits a representative sample of configurations, the two will give consistent results.

2.1 Monte Carlo Techniques

Configurations in a MC simulation are usually generated using importance sampling, weighting the choice of states according to the ensemble probability density, ρ_{ens}. The canonical ensemble, for example, has

$$\rho_{NVT}(\Gamma) = \frac{\exp\left(-\mathcal{H}(\Gamma)/k_B T\right)}{Q_{NVT}} \tag{2.1}$$

where $\mathcal{H}(\Gamma)$ is the Hamiltonian and Q_{NVT} the canonical partition function. The appropriate weighting of states is thus the Boltzmann factor, $\exp\left(-\mathcal{H}(\Gamma)/k_B T\right)$. In practice the simulation must have a procedure for moving between configurations; commonly the transition probabilities are chosen according to the Metropolis MC scheme [10] although other schemes have been proposed [9]. In essence, given some state m, a modified state, n, is proposed and transfer is accepted or rejected according to a rule embodying the required weighting. For an NVT simulation, state n can be generated by selecting a particle i, either at random or in sequence, currently at position $\mathbf{r}_i$ in the system, and choosing a random displacement $\delta\mathbf{r}_i$ within a small cube of fixed size, centred on $\mathbf{r}_i$. Due to the finite precision available for the coordinates on the computer, the trial position is one of a large but finite number of possibilities. The same number applies to the selection of moves irrespective of the starting point, so that microscopic reversibility, which requires the probability of moving between states m and n to be independent of the direction of motion, is built into the procedure. From the ratio of probabilities of the two states,

$$\frac{\rho_n}{\rho_m} = \frac{\exp(-\beta\mathcal{V}_n)/Q_{NVT}}{\exp(-\beta\mathcal{V}_m)/Q_{NVT}} = \frac{\exp(-\beta\mathcal{V}_n)\exp(-\beta\mathcal{V}_{nm})}{\exp(-\beta\mathcal{V}_n)} = \exp(-\beta\mathcal{V}_{nm}) \tag{2.2}$$

where $\beta = 1/k_B T$, the move is accepted with probability $\mathcal{P} = \min(1, \exp(-\beta\mathcal{V}_{nm}))$. If the move is rejected, state m must be counted again in the measured averages.

The displacement $\delta\mathbf{r}_i$ is generated by picking a change in the three Cartesian coordinates in turn uniformly on the range $(-\delta r_{max}, \delta r_{max})$. Adjusting the size of the maximum move changes the acceptance rate of MC moves. Typically, an acceptance rate of 50% is used, but one measure of movement through phase space may lead to a significantly different target acceptance rate than another. The aim is to get value for money in terms of representative sampling per computer time, but the expense of systematic optimization studies make them rare.

If the system is molecular, the trial move must also incorporate orientation moves. Several approaches have been suggested. That used here selects an axis at random and rotates the molecule about this by an angle also chosen at random, uniformly on some range $(-\delta\Phi_{max}, \delta\Phi_{max})$. If the orientation vector of a molecule is denoted by the unit vector $\mathbf{e}$, the new orientation is given by [48]

$$\mathbf{e}_n = \mathbf{e}_m \cos\Phi + \mathbf{n}_r(\mathbf{n}_r \cdot \mathbf{e}_m)\,[1 - \cos\Phi] + (\mathbf{e}_m \times \mathbf{n}_r)\sin\Phi \qquad (2.3)$$

where $\mathbf{n}_r$ is the unit vector along the axis of rotation. The rotation move is usually combined with the translation move, and the joint displacement accepted or rejected. Many combinations of δr_{max} and $\delta\Phi_{max}$ would give a desired acceptance rate, but in general if the size of the maximum allowed displacement and rotation moves are adjusted within the code, the two are adjusted together. Rotation of non-rigid molecules requires rather more individual attention [9].

Extension to other ensembles is relatively straightforward. Simulations in the isothermal-isobaric, (NPT), ensemble need to incorporate moves taking the system from one volume to another at the chosen pressure. The appropriate transfer probability is now

$$\mathcal{P}_{nm} = \min\left(1, \exp\left(-\beta\left[\delta\mathcal{V}_{nm} + P(V_n - V_m) - N\beta^{-1}\ln(V_n/V_m)\right]\right)\right) \qquad (2.4)$$

for volume moves taken uniformly on an interval $(-\delta V_{max}, \delta V_{max})$ about V. A trial configuration could now involve a displaced particle or a new volume or both, and the maximum move in the volume can be adjusted in the same way as the maximum position and orientation moves. In general an attempt to change the volume will involve recalculating the potential energy for all pairs of particles and so will be significantly more expensive than a single particle displacement, with $\frac{1}{2}N(N-1)$ pair calculations rather than a maximum of $2(N-1)$. Certain potentials, like LJ, scale with the box dimension, allowing very rapid re-calculation. The Gay-Berne potential does not, however, since the orientations appear in combination with the intermolecular vector.

This prescription for choosing new volume states is not unique. Some workers sample uniformly in $\ln(V)$ rather than V, for reasons of convenience and efficiency [6]. This means modifying the acceptance procedure - the factor of N in (2.4) is replaced by $(N+1)$. For uniform sampling of the box side L where $V = L^3$ it becomes $(N + \frac{2}{3})$. If the system

incorporates some degree of positional order, as in a smectic phase, it may be desirable to allow the aspect ratio of the box to alter. This can be implemented by attempting to change one box dimension, chosen randomly, at a time. Sampling $\ln L_i$, the appropriate factor is again $(N+1)$ [49].

In grand canonical ensemble simulations, moves must be included to allow for changes in number of particles at fixed chemical potential. Single-particle moves proceed as above. For particle creation moves, the usual approach is to select a random position in the simulation box and attempt to insert a new particle, whilst for destruction moves, an existing particle is chosen at random and an attempt is made to remove it completely. The two moves have different acceptance criteria. For creation, the probability ratio for states m with N particles, and n with $N+1$ particles, is

$$\begin{aligned} \frac{\rho_{N+1}}{\rho_N} &= \frac{[(N+1)!]^{-1} V^{N+1} z^{N+1} \exp(-\beta \mathcal{V}_n)}{[N!]^{-1} V^N z^N \exp(-\beta \mathcal{V}_m)} \\ &= \exp(-\beta \delta \mathcal{V}_{nm} + \ln(zV/(N+1))) \end{aligned} \tag{2.5}$$

whereas for a destruction move, it is

$$\begin{aligned} \frac{\rho_{N-1}}{\rho_N} &= \frac{[(N-1)!]^{-1} V^{N-1} z^{N-1} \exp(-\beta \mathcal{V}_n)}{[N!]^{-1} V^N z^N \exp(-\beta \mathcal{V}_m)} \\ &= \exp(-\beta \delta \mathcal{V}_{nm} + \ln(N/zV)) \end{aligned} \tag{2.6}$$

where $z = \exp(\beta\mu)/\Lambda^3$ is the activity, and $\Lambda = h/\sqrt{2\pi m k_B T}$ is the thermal de Broglie wavelength. To satisfy microscopic reversibility, the probabilities of attempting creation and destruction moves should be kept equal. The need to cope with a variable number of particles also appears in the Gibbs ensemble method, discussed in §2.5 below.

The use of random numbers is clearly central to the MC technique, even suggesting its name. Repeatability requires use of a deterministic process in the random number generator, implying that the process is only 'pseudo–random'. Many portable generators exist with varying quality, [50, 51]. Here we use 'RANMAR' of [51], which is initialized with two integer seeds. Permutations of these give about 9×10^8 independent sequences of pseudo-random numbers, each of length $\sim 10^{30}$. The generator itself is relatively cheap, and passes all the common tests that indicate statistical correlations in the number sequences [52].

2.2 Molecular Dynamics Techniques

In MD a set of ordinary differential equations, (the equations of motion), is solved, generally using finite-difference techniques with a small timestep δt between configurations. Certain quantities will be conserved, according to the Hamiltonian. Centre-of-mass linear and angular momenta may or may not be conserved in a simulation employing periodic boundary conditions, (§2.3), depending on the cell geometry. For a cuboidal box, the total linear momentum is conserved, (and for convenience is usually set to zero), but the total angular momentum is not. If $\mathcal{V}$ and $\mathcal{K}$ have no explicit time-dependence and $\mathcal{V}$ is independent of the momenta, the energy must be conserved. The conserved quantities provide useful checks for a MD simulation.

For a smoothly varying potential, finite-difference methods of solving ordinary differential equations can be applied; (the collisional dynamics of hard particles require a different treatment [3, 51, 52]). A rigid, linear molecule is naturally described by its centre of mass, $\mathbf{r}$, and orientation, $\mathbf{e}$. For soft potentials, the main task of the MD simulation is evaluation of potential derivatives with respect to these coordinates, i.e. the forces and torques.

The higher order derivatives of the potential generally required for standard predictor-corrector algorithms are expensive to compute. This expense, along with a lack of time-reversibility and a marked degradation of stability (energy conservation) as the size of time step increases, often makes them unsuitable. An alternative which is exactly time reversible and more stable is the widely-used Verlet algorithm. Starting from forward and reverse Taylor expansions, and making use of the fact that the accelerations, $\mathbf{a}$, depend on the positions, (through the potential), but not on the velocities of the particles, this gives positions at time $t + \delta t$ as

$$\mathbf{r}(t + \delta t) = 2\mathbf{r}(t) - \mathbf{r}(t - \delta t) + \delta t^2 \mathbf{a}(t) + \mathcal{O}(\delta t^4) \,. \tag{2.7}$$

If the velocities are required, (for calculation of $\mathcal{K}$, for example), they can be calculated from

$$\mathbf{v}(t) = \frac{\mathbf{r}(t + \delta t) - \mathbf{r}(t - \delta t)}{2\delta t} \tag{2.8}$$

but are subject to errors of order δt^2 and are always lagging behind the calculated positions. Apart from this, the algorithm is stable, compact and requires significantly less memory

than predictor-corrector algorithms.

Other forms of the Verlet algorithm have been proposed that give identical solutions to the equations of motion but handle the velocities differently. The leapfrog approach [55] may be applied to the Verlet scheme, requiring mid-step velocities:

$$\mathbf{r}\left(t+\delta t\right) = \mathbf{r}(t) + \delta t \mathbf{v}\left(t+\tfrac{1}{2}\delta t\right) \tag{2.9a}$$

$$\mathbf{v}\left(t+\tfrac{1}{2}\delta t\right) = \mathbf{v}\left(t-\tfrac{1}{2}\delta t\right) + \delta t \mathbf{a}(t) \tag{2.9b}$$

This algorithm is numerically more precise, since there is now no need to obtain a small quantity as the difference of two large quantities. A further calculation is still required to find velocities contemporaneous with the positions, $\mathbf{v}(t) = \left(\mathbf{v}(t+\frac{1}{2}\delta t) + \mathbf{v}(t-\frac{1}{2}\delta t)\right)/2$, or the velocities can be updated in two half-steps, the first of which brings them to time t for a calculation of $\mathcal{K}$. Finally, the 'velocity Verlet' algorithm [56] stores velocities and accelerations at the same t:

$$\mathbf{r}\left(t+\delta t\right) = \mathbf{r}(t) + \delta t \mathbf{v}(t) + \tfrac{1}{2}\delta t^2 \mathbf{a}(t) \tag{2.10a}$$

$$\mathbf{v}\left(t+\delta t\right) = \mathbf{v}(t) + \tfrac{1}{2}\delta t \left[\mathbf{a}(t) + \mathbf{a}(t+\delta t)\right] . \tag{2.10b}$$

Either the velocities are updated in two steps, before and after the positions are moved and the forces recalculated, or the accelerations at both t and $t+\delta t$ are stored temporarily. This has the same storage requirements as the original Verlet method, and all three produce identical particle trajectories, as can be seen algebraically if the velocities are eliminated from (2.9a) or (2.10a).

The rotational dynamics can also be integrated in a number of ways. Fincham [57] has studied various leapfrog solutions. The equations of motion for $\mathbf{e}$ and $\mathbf{u} = \dot{\mathbf{e}}$ can be solved using the steps

$$\mathbf{u}(t+\tfrac{1}{2}\delta t) = \mathbf{u}(t-\tfrac{1}{2}\delta t) + \delta t \left[\mathbf{g}^{\perp}(t)/I + \lambda(t)\mathbf{e}(t)\right] \tag{2.11a}$$

$$\mathbf{e}(t+\delta t) = \mathbf{e}(t) + \delta t \mathbf{u}(t+\tfrac{1}{2}\delta t) \tag{2.11b}$$

where I is the moment of inertia, $\mathbf{g}_i^{\perp}$ is the 'perpendicular turning force' defined by $\mathbf{g}_i^{\perp} = \mathbf{g}_i - (\mathbf{g}_i \cdot \mathbf{e}_i)\,\mathbf{e}_i$ with $\mathbf{e}_i \times \mathbf{g}_i = \tau_i$, the torque, and the multiplier $\lambda(t)$ is introduced to maintain a constant bond length. This may be determined by initially ignoring the term in λ and using the resulting new vector to calculate the constraint force required at t. This

gives high stability but is expensive. An alternative method of finding λ uses directly the condition that **u** should remain perpendicular to **e**, giving

$$\lambda(t)\delta t = -2\mathbf{u}(t - \tfrac{1}{2}\delta t) \cdot \mathbf{e}(t) \tag{2.12}$$

This can be programmed with more ease than the former solution, and although it does not perform as well, it still produces stable and accurate trajectories. The difference in performance may be even less significant in a full simulation since the translation and orientation moves are performed with the same time step, so that the less stable of the two moves will determine the maximum feasible time step.

2.3 General Practicalities

2.3.1 Periodic Boundary Conditions

The use of periodic boundary conditions has for many years been the standard way of measuring bulk properties whilst simulating a microscopic system, since it avoids the complication of surface effects. The usual cuboidal periodic boundaries have been applied in most of this work, supplemented by hexagonal prism cells. The required modifications for these boundary conditions are described elsewhere [58]. In general, the stored particle coordinates in a simulation remain in the central simulation box, i.e. when a particle crosses a face of the box, attention is switched to the corresponding image particle entering the box through the opposite face. The use of periodic images has associated caveats. The longest wavelength fluctuations that can occur in the simulation are restricted to the size of the box, which becomes particularly significant when approaching a critical point. A further finite-size effect is the 'rounding' of phase transitions: a transition that is first-order in the thermodynamic limit may appear continuous due to the limited box size, and in addition to its strength, the measured location of the transition will be subject to system-size effects. In a nematic fluid, the director will move in the course of a simulation in accordance with thermal fluctuations. The use of periodic boundaries will distort this distribution of director orientations due to the loss of spherical symmetry, leading to preferred director orientations with respect to the box axes in ordered phases. However, first studies [59] have shown that even for small systems, ($N \sim 120$) in a cubic box the

effect is on the limit of statistical significance.

2.3.2 Basic Thermodynamic Quantities

At equilibrium the time derivative of the average of some variable $\mathcal{A}$ must, by definition, vanish. For classical systems, taking $\mathcal{A} = qp$, where p is the momentum conjugate to the generalized coordinate q, and using Hamilton's equations, this condition implies that

$$\langle q\partial\mathcal{H}/\partial q\rangle = \langle p\partial\mathcal{H}/\partial p\rangle = k_B T \tag{2.13}$$

where equipartition of energy leads to the second equality. In particular, if the momenta are quadratic degrees of freedom, they can be used to define an instantaneous temperature function, τ, whose average is the 'true' temperature, T. For molecular systems with orientational degrees of freedom, the definition of τ may include these and the translational contributions or separate 'translational' and 'orientational' temperatures may be defined, which assists in monitoring thermalization:

$$\begin{aligned} \tau_t &= 2\mathcal{K}_t/3Nk_B = \frac{1}{3Nk_B}\sum_{i=1}^{N}|\mathbf{p}_i|^2/m \\ \tau_r &= \mathcal{K}_r/Nk_B = \frac{1}{2Nk_B}\sum_{i=1}^{N}|\mathbf{J}_i|^2/I \end{aligned} \tag{2.14}$$

where $\mathbf{J}_i$ is the angular momentum of particle i.

Applying (2.13) to translational coordinates leads to a definition of instantaneous pressure,

$$\mathcal{P} = \rho k_B \mathcal{T} + \mathcal{W}/V \tag{2.15}$$

where the internal virial is defined by

$$\mathcal{W} = \tfrac{1}{3}\left\langle\sum_{i=1}^{N}\mathbf{r}_i.\mathbf{f}_i\right\rangle = -\tfrac{1}{3}\left\langle\sum_{i=1}^{N}\mathbf{r}_i.\nabla_{\mathbf{r}_i}\mathcal{V}\right\rangle . \tag{2.16}$$

For a pairwise additive potential it is more convenient to explicitly remove the dependence of $\mathcal{W}$ on the coordinate origin by expressing it in terms of a sum of contributions from pair forces, $\mathbf{f}_{ij}$:

$$\mathcal{W} = \frac{1}{3}\sum_i\sum_{j>i}\mathbf{r}_{ij}.\mathbf{f}_{ij} = -\frac{1}{3}\sum_i\sum_{j>i}w(r_{ij}) \tag{2.17}$$

where $\mathbf{r}_{ij} = \mathbf{r}_i - \mathbf{r}_j$ and $w(r) = rdv(r)/dr$ is the pair virial function. The average of $\mathcal{P}$ is P; other, similar definitions are possible.

Quantities related directly to the partition function, rather than its derivatives are inherently difficult to estimate in simulation since the probability distribution of states will be sharply peaked about those with large Boltzmann factors. The chemical potential, μ, can, however, often be measured in simulation since it can be related to a ratio of partition functions, (at large N), by

$$\exp(-\mu/k_BT) = \mathcal{Q}_{N+1}/\mathcal{Q}_N = \mathcal{Q}_N/\mathcal{Q}_{N-1}\,. \tag{2.18}$$

This is the basis of the Widom test-particle insertion method. The probability of successfully inserting an extra particle into the system with random coordinates is related to the excess chemical potential by

$$\mu^{ex} = -k_BT \ln\langle \exp(-\mathcal{V}_{N+1}/k_BT)\rangle\,. \tag{2.19}$$

where $\mu^{ex} = \mu - \mu^{id}$, with μ^{id} the ideal gas contribution. When measuring this quantity the particle is never actually added to the configuration. With slight modifications, this scheme can be applied to NVT, NVE, NPT and μVT ensembles [9], and can be used as the basis of more sophisticated techniques when, at high density for example, the probability of inserting a test particle becomes rather small. This often occurs for fluids at temperatures still significantly above the triple point. The range of applicability of this technique could be extended if it were possible to simply try more insertions as the statistics worsen. This requires the moves to be performed more quickly, and one method allowing this is use of an excluded volume map to rapidly reject any insertion attempt that will result in a significant overlap with existing particles [60]. After coarse-graining the simulation box, some volume around each particle is marked off, providing a quick first check for a test particle. Other improvements to the test-particle method use the gradual insertion of particles, growing from some vanishing size to the full dimensions of the true particles [61, 62], or the force-balance method, in which a biasing potential is used to counteract the poor sampling, as proposed by Attard [63] and subsequently refined [64].

2.3.3 Potential evaluation

The use of periodic boundaries implies that an infinite number of interactions must be considered when evaluating the potential energy of any particle in the simulation box. Unless the potential is long-ranged, e.g. having an electrostatic component, a standard step is restricting interactions of a given particle to include only one image of each of the other $(N-1)$ particles. The stored position of particle j (in the central box) may give an intermolecular distance with particle i greater than that between i and an image of j. The minimum image convention builds in the required correction. The scheme can be coded in FORTRAN in a number of ways, the most efficient of which will in general be processor-dependent. For the SGI and Alpha workstations, a combination of the IF and SIGN functions currently gives the best results[1], i.e.

```
if ( abs(rx) .gt. box/2 ) rx = rx - sign(box,rx)
```

As is stands, this assumes that an uncorrected pair separation will not exceed the box dimension. This is a reasonable assumption for practical purposes, since it is limited by the distance a particle can travel in a single MD timestep or MC attempted displacement. If, for some reason, this cannot be assumed, the extra checks required makes an alternative, using the NINT function, a more efficient option, i.e.

```
rx = rx - box*nint(rx/box)
```

In considering only minimum image pairs, the potential is assumed to be short-ranged on the scale of the simulation box. This can be made explicit by simply ignoring any contributions from particles beyond a certain cut-off distance, r_c. For $r_{ij} > r_c$, u_{ij} is set to zero and a significant number of pairs can be dealt with very quickly in a potential evaluation. Practical bounds are placed on r_c: the smallest box dimension must be at least twice r_c to avoid particles interacting with their own images, and although the potential may fall off quickly with pair separation, the number of particles increases, and the perturbation associated with a cut-off should be kept small. Thus, r_c should be chosen to balance the gain in efficiency against the deviations in thermodynamic quantities from the 'true' values. It is possible to approximately compensate for the neglected particles

[1] Our attention was drawn to the efficiency of this method by D. Kofke.

by applying long-range corrections. The average of a pair property $\mathcal{A}$ may be written in terms of the pair distribution function, $g(r)$, as

$$\langle \mathcal{A} \rangle = \left\langle \sum_i \sum_{j>i} a(r_{ij}) \right\rangle = \tfrac{1}{2} N \rho \int_0^\infty dr 4\pi r^2 a(r) g(r) \tag{2.20}$$

where

$$g(\mathbf{r}_{12}) = \frac{N(N-1)}{\rho^2 Z_{NVT}} \int d\mathbf{r}_3 \, d\mathbf{r}_4 \cdots d\mathbf{r}_N \exp\left(-\beta U(\mathbf{r}_1, \mathbf{r}_2, \cdots, \mathbf{r}_N)\right) \tag{2.21}$$

or equivalently, and more amenable to measurement in simulation,

$$g(r) = \rho^{-2} \left\langle \sum_i \sum_{j \neq i} \delta(\mathbf{r}_i) \delta(\mathbf{r}_j - \mathbf{r}) \right\rangle = \frac{V}{N^2} \left\langle \sum_i \sum_{j \neq i} \delta(\mathbf{r} - \mathbf{r}_{ij}) \right\rangle . \tag{2.22}$$

These expressions are valid for an atomic fluid; in a molecular system, integrals over position are replaced by integrals over position and orientation. The radial distribution function is now given by

$$g(r) = \langle g(\mathbf{r}_{12}, \mathbf{e}_1, \mathbf{e}_2) \rangle_{\mathbf{e}_1, \mathbf{e}_2} \tag{2.23}$$

where $\langle \cdots \rangle_{\mathbf{e}_1, \mathbf{e}_2}$ indicates an unweighted average over orientations $\mathbf{e}_1$ and $\mathbf{e}_2$ [65]. Contributions to the system energy and pressure from beyond the cut-off can be calculated from (2.20) by assuming a form for $g(r)$ at $r > r_c$, (usually taken as uniform), allowing results for a system with the full potential to be (approximately) obtained from a simulation with a cut-off. It is possible to avoid LRCs, considering explicitly a system subject to a truncated potential, although the discontinuity introduced in the potential at r_c gives an additional term in the pressure calculation, arising from the impulse associated with crossing the cut-off, and renders the system less suitable for MD.

In a further modification a constant term is added to $u(r)$ for $r < r_c$ given by $u(r_c)$, generating a cut-and-shifted form guaranteed to go smoothly to zero at the cut-off. The forces remain finite, allowing the usual numerical solution of the equations of motion. Again it is possible to recover approximate values for the system with the full potential. This modification does not remove the discontinuity in the forces at r_c, which will be small for a reasonable cut-off, but the system is not strictly energy conserving and in some cases the effect leads to instability in the solution of the equations of motion. It is possible to take the forces smoothly to zero also by adding a further term to the potential, usually linear or quadratic. Perturbation theory may be employed to recover the full potential properties.

For a purely distance-dependent potential, a cut-and-shift does not affect the forces, but for an anisotropic potential, the cut-and-shift must either be applied at a point where the pair potential has a fixed value, so that it can be taken to zero by a constant term, or account must be taken of the additional impulsive forces introduced by the orientation-dependent shift. If these extra force terms were neglected energy conservation would be further violated.

All of the cut-off methods described require calculation of the separation of every distinct pair in the box. This in itself can be significantly time-consuming and further savings can be made if pairs violating the cut-off condition can be ignored completely. In practice this can be achieved in some measure by constructing for each particle a list of its neighbours, (i.e. other particles within r_c), and considering no other pairs. This is possible using a Verlet neighbour list, or for larger systems, a linked-cell list [9]. The optimum choice is dependent on the system under study, and it is possible on the basis of test simulations to estimate the relative efficiencies of the techniques [66].

2.3.4 Reduced units

All quantities are assumed to be expressed in conventional reduced units, with m, σ_0 and ε_0 as units of mass, distance and energy, respectively. The reduced thermodynamic variables most often quoted are then as follows: density, $\rho^* = \rho\sigma_0^3$; temperature, $T^* = k_BT/\varepsilon_0$; pressure, $P^* = P\sigma_0^3/\varepsilon_0$; energy, $E^* = E/\varepsilon_0$; time, $t^* = (\varepsilon_0/m\sigma_0^2)^{1/2}\,t$. In the rest of this thesis, it will be standard to write these and other reduced quantities without the superscript * except where this may cause ambiguity. The use of reduced units avoids computationally awkward absolute values of the quantities of interest (i.e. far from unity) and makes explicit the law of corresponding states. This second point is more significant when attempting to directly simulate realistic systems, rather than investigating the behaviour of a model system.

2.3.5 Visualization

In general, the phases exhibited by a model system during simulation are identified by measuring signature properties such as the nematic and smectic order parameters de-

scribed above, and distribution functions. It also makes sense to look at the molecular configurations. This is especially important when developing code, to spot and gain insight into 'bugs' and any pathological behaviour. If, for example, the smectic order parameter is measured on a coarse grid of reciprocal lattice vectors, it is possible that it remains low when the system can be clearly seen to have a layered structure. These investigations have drawn on visualization software developed within this department by Mr. Mark Warren. Snapshot configurations shown in this thesis have been produced using this software.

2.4 A Direct Method of Simulating Phase Coexistence

The most conceptually straightforward approach to simulating two coexisting phases is to put both phases in the same box. Where one coexisting phase is a vapour, one can obtain free droplets of the other phase. This is an interesting system in its own right and has been studied by simulation [67, 68], but there are drawbacks in inferring bulk properties and in simulating anisotropic phases. It is often more convenient to place a dense slab in the centre of a cuboidal box extended in one direction, (conventionally z), and surround it with vapour such that the two interfaces have the area of the smallest box cross-section. Usual periodic boundary conditions are then applied. Provided the dense region is sufficiently populated and the system is at stable coexistence, bulk properties may be inferred from behaviour away from the interfaces. This geometry has been used to study liquid-vapour properties of a variety of systems, including the Stockmayer fluid [69], water [36], the Lennard-Jones fluid [70] and the Gay-Berne fluid [37].

Profiles, most significantly of the pressure and particle density, are measured along the long axis of the box, (z). The density profile is split midway between the interfaces and each half fitted to a standard functional form giving the bulk phase densities, ρ_l and ρ_v:

$$\rho(z) = \tfrac{1}{2}(\rho_l + \rho_v) + \tfrac{1}{2}(\rho_l - \rho_v) \tanh\left[\frac{2(z - z_0)}{D}\right] \tag{2.24}$$

where z_0 is the position of the Gibbs dividing surface, ('surface of tension'), and D is a characteristic width of the interface. Any information about the fluid structure in the vicinity of the interfaces will be washed out by this fitting procedure. Equilibration in these large, inhomogeneous systems may be slow, and should be monitored carefully. In

their study of the liquid-vapour interface of the LJ fluid, Holcomb *et al.* [70] proposed three criteria for establishing equilibrium:

- Running averages for the surface tension and density profile should not be changing significantly.
- Block averages, (3×10^4 MD steps), should be equal to the running average.
- The integral of $\Delta P = P_N(z) - P_T(z)$ through the bulk phases should not contribute significantly to the calculation of the surface tension.

The pressure profile, then, is an indicator of equilibration in addition to facilitating calculation of the surface tension at the interfaces. At equilibrium, the component of pressure normal to the interface, P_N will be constant throughout the system, equal to the vapour pressure whilst the tangential component, P_T, will be equal to P_N in the bulk regions and discontinuous at the interfaces. Since there is more than one way of specifying which forces contribute to the stress across a microscopic element of area, there is more than one self-consistent definition for the pressure of an inhomogeneous system [71]. The most common choices are those associated with Harasima [72] and Irving and Kirkwood [73]. In both cases, the pressure components can be written in the form

$$P_T(z) = \rho(z)k_BT - \frac{1}{2A}\left\langle \sum_{i<j} \frac{x_{ij}^2 + y_{ij}^2}{2r_{ij}} \frac{\partial u_{ij}}{\partial r_{ij}} f(z, z_i, z_j) \right\rangle \tag{2.25a}$$

$$P_N(z) = \rho(z)k_BT - \frac{1}{2A}\left\langle \sum_{i<j} \frac{z_{ij}^2}{r_{ij}} \frac{\partial u_{ij}}{\partial r_{ij}} f(z, z_i, z_j) \right\rangle \tag{2.25b}$$

where $\rho(z)$ is the number density at z, A is the area of the interface and $f(z, z_i, z_j)$ depends on the chosen integration contour for the pressure tensor and the discretization used in the simulation. The Irving-Kirkwood (IK) scheme takes the integration path to be a straight line between the molecules, i.e. the line of action of the intermolecular force, giving

$$f^{\mathrm{IK}}(z, z_i, z_j) = \frac{1}{|z_{ij}|}\Theta\left(\frac{z - z_i}{z_{ij}}\right)\Theta\left(\frac{z_j - z}{z_{ij}}\right)\omega\left(z, z_i, z_j\right) \tag{2.26}$$

where z_i, z_j are particle coordinates, z is the mid-point of profile bin $\{z\}$ and

$$\omega(z, z_i, z_j) = \begin{cases} 1, & z_i, z_j \notin \{z\} \\ z_{ij}/\Delta z, & z_i, z_j \in \{z\} \\ (z - z_i + \Delta z/2)/\Delta z, & z_i \in \{z\}, z_j \notin \{z\} \\ (z_j - z + \Delta z/2)/\Delta z, & z_i \notin \{z\}, z_j \in \{z\} \end{cases} \tag{2.27}$$

with Δz the bin width [36, 69, 74]. The contribution due to the i,j interaction is thus divided amongst the bins traversed by $\mathbf{r}_{ij}$ according to the z-distance travelled in each. In the Harasima (II) scheme an asymmetric contour is chosen which moves first parallel to the interface, from (x_i, y_i, z_i) to (x_j, y_j, z_i), and then perpendicular to the interface. The normal pressure component is identical to the IK case, but for the tangential component this gives [74]

$$f_T^{\mathrm{II}}(z, z_i) = \begin{cases} 1/\Delta z, & z_i \in \{z\} \\ 0, & \text{otherwise} \end{cases} \tag{2.28}$$

so that the entire contribution is accumulated in the bin containing i. Some workers have modified the integration contour so that P_T is accumulated in bins containing either particle; the summation in (2.25a) is restricted to pairs of particles for which at least one of i and j is in the bin at z [37, 69]; these applications also apply the restricted summation to P_N, although this does not in general correspond to a physical integration path.

The differences in the IK and II equations is most significant when considering the difference in the components, $\Delta P(z)$. The zeroth moment of ΔP gives the surface tension. This is the same for the two methods. The choice of integration path will, however, allow the dividing surface as defined by the first moment of ΔP, to take different positions in the fluid. For the purposes of measuring only the pressure profile in an inhomogeneous fluid, however, previous studies have indicated the differences between the two schemes to be measurable but rather small [69, 74].

Setting up an initial inhomogeneous configuration generally means generating the vapour phase at random around a previously-equilibrated bulk configuration for the dense phase. Care is required: if the densities are far from coexistence it is possible that the dense slab will evaporate too much to obtain bulk information. Where the dense phase is not an isotropic fluid, but contains positional order, simulating at fixed aspect ratio over a

range of temperatures will not be appropriate, since structural equilibration in the plane parallel to the interface will be inhibited by the periodicity of the image cells. To overcome this, it is possible to incorporate a MC sampling of the box aspect ratio. If there is strong periodic ordering, as in a crystal or smectic phase, the x and y box sides can be scaled by the same factor, so that the structure remains commensurate with the periodic images whilst the intermolecular spacing can relax. Holding the total volume fixed, the overall density of each phase will be unaffected by such a move, the vapour will relax quickly from the perturbation and any imposed strain on the dense phase should be rapidly removed. Since the interfacial area changes, the free energy change of such a move is not strictly zero, but this is expected to be a small effect since the desire to obtain bulk information already requires that the system be large.

The existence of positional ordering along z has implications for profile measurement. The width of the profile bins must not obscure the density modulation and since the equilibrium spacing will not be known *a priori*, it is safest to make the bins small on this scale. The density profile for each layer may then be individually fitted to a Gaussian distribution covering several bins and thus the centre of the layer may be specified. This in turn provides an average layer spacing and density. The small bin width, however, makes the pressure profile discontinuous in the bulk since on this scale the system remains inhomogeneous. Whilst the approach to equilibrium can still be monitored through other thermodynamic quantities and comparison of block and run averages, the integral of ΔP will no longer be appropriate.

2.5 The Gibbs Ensemble Technique

The simulation of coexisting phases is made much more economic if the interface can be avoided. One approach which allows this is the so-called 'Gibbs ensemble' method, first introduced by Panagiotopoulos [75] in 1987. It uses two distinct simulation boxes, each surrounded by periodic images of itself, giving two bulk samples. The boxes are then coupled by Monte Carlo rules. The simulation involves displacing particles in each of the two boxes as in a conventional Monte Carlo simulation, but also changing the volume of the subsystems, and exchanging particles between the boxes. As usual, the acceptance rules

for these moves satisfy and can be derived from the condition of microscopic reversibility [5]. These rules are outlined in §2.5.1 for the typical case where the total volume of the two boxes is maintained at a constant value. For multi-component systems it is possible to simulate at constant pressure rather than constant volume. Practical details of the MC moves depend on the conditions of the system under consideration. As mentioned earlier, the magnitude of the attempted displacement moves is in general adjusted so that the acceptance rate in each box is roughly 50%. The maximum change in volume is also selected so that about 50% of the attempted moves are accepted. This seems reasonable, since the amount of work involved is very similar, whether the move is accepted or rejected. When attempting to exchange particles, one of the boxes is selected at random, and a particle in that box is chosen, again at random. The rest of the move involves the deletion of this particle with the simultaneous creation of another particle at random in the other box. The appropriate number of attempts to exchange a particle will depend on the condition of the system. One can expect the percentage of accepted exchanges to be higher near the critical point than near the triple point, for example. It is useful to note that the attempted particle creations, (or deletions), can give the chemical potential of the system, since this is equivalent to Widom's test particle insertion method. Equality of chemical potentials is equivalent to equality of particle transfer rates in the two directons. It has been noted that an acceptance rate for exchanges of greater than about 3% can lead to biasing and incorrect results [73]. It is possible that a simulation can become trapped in phase space if such biasing goes uncorrected, but once a suitable attempt rate has been established, such problems can be avoided.

2.5.1 Acceptance Criteria

The GEMC technique was originally introduced by considering constant-NVT, constant-NPT and constant-μVT ensembles, with appropriate Monte Carlo acceptance rules derived using fluctuation theory [73]. This derivation uses Stirling's approximation when calculating the ideal gas entropy. Comparison with the exact expressions, derived using only statistical mechanical arguments [74], shows that the original expression for the acceptance probability for particle transfers deviates by terms of order $1/N$, although this did not significantly alter the results of the initial study on the pure Lennard-Jones fluid.

The same acceptance criteria can be derived from the partition function. In a typical GEMC simulation the combined system has a constant temperature, (total) volume and (total) number of particles. The volume and particles are divided between two non-interacting subsystems, I and II. In writing the partition function, the number of possible distributions of particles and volume between I and II must be included, along with the number of possible configurations in each subsystem. Thus the partition function, $\mathcal{Q}_G$, is written

$$\begin{aligned} \mathcal{Q}_G(N,V,T) \quad &\equiv \frac{1}{V\Lambda^{3N}N!}\sum_{N_I=1}^{N}\frac{N!}{N_I!\,(N-N_I)!}\int_0^V dV_I \\ &\int_{V_I} d\mathbf{r}_I^{N_I}\exp\left[-\beta\mathcal{V}_I(N_I)\right]\int_{V-V_I} d\mathbf{r}_{II}^{N-N_I}\exp\left[-\beta\mathcal{V}_{II}(N-N_I)\right] \quad (2.29) \end{aligned}$$

This partition function can, in turn, be used to express the free energy density in the Gibbs ensemble. Using this, Smit [76] has shown rigorously that in the thermodynamic limit the ensemble sampled in these simulations is equivalent to the usual canonical ensemble.

The acceptance criteria for a constant-volume Gibbs ensemble simulation can also be obtained by combining the MC rules already described. The displacement moves proceed as usual in the two boxes independently. When attempting a volume change, ΔV, say, in an isolated NPT simulation, the energy change to test is indicated by (2.4). Combining the terms resulting from the two volume changes in a GEMC volume exchange move, i.e. $V_I \rightarrow V_I + \Delta V$ and $V_{II} \rightarrow V_{II} - \Delta V$, gives an acceptance probability of $\min(1, \exp(-\beta\Delta\mathcal{H}_V))$ where

$$\begin{aligned} \Delta\mathcal{H}_V &= \left\{\Delta\mathcal{V}_I - N_I\beta^{-1}\ln\left[(V_I+\Delta V)/V_I\right] + P\Delta V\right\} \\ &\quad + \left\{\Delta\mathcal{V}_{II} - N_{II}\beta^{-1}\ln\left[(V_{II}-\Delta V)/V_{II}\right] - P\Delta V\right\} \\ &= \Delta\mathcal{V}_I + \Delta\mathcal{V}_{II} - N_I\beta^{-1}\ln\left[\frac{V_I+\Delta V}{V_I}\right] - N_{II}\beta^{-1}\ln\left[\frac{V_{II}-\Delta V}{V_{II}}\right]. \quad (2.30) \end{aligned}$$

The terms in P cancel, since the pressures are required to be equal.

A similar procedure can be applied to the exchange of particles. Suppose a particle is to be deleted in box II and another simultaneously created in box I so that $N_{II} \rightarrow N_{II}-1$ and $N_I \rightarrow N_I + 1$. Combining the acceptance criteria from two grand canonical simulations at activity z gives the acceptance probability for the GEMC particle exchange move,

$\min(1, \exp(-\beta\Delta\mathcal{H}_N))$, with

$$\begin{aligned}\Delta\mathcal{H}_N &= \left\{\Delta\mathcal{V}_I - \beta^{-1}\ln\left[zV_I/\left(N_I+1\right)\right]\right\} \\ &\quad + \left\{\Delta\mathcal{V}_{II} - \beta^{-1}\ln\left[N_{II}/zV_{II}\right]\right\} \\ &= \Delta\mathcal{V}_I + \Delta\mathcal{V}_{II} - \beta^{-1}\ln\left[\frac{V_I N_{II}}{V_{II}\left(N_I+1\right)}\right]. \end{aligned} \tag{2.31}$$

Since equality of chemical potentials is required, the terms in z drop out. Together, these conditions ensure mechanical and chemical equilibrium of the subsystems.

2.5.2 Checking the pressure calculation

It is possible to calculate the pressure in a number of ways. The primary method employed has been the virial approach, as outlined in §2.2. Although the system is driven to a pressure corresponding to coexistence, the internal pressure of each box will fluctuate over the course of the simulation. Other approaches may be used to check that the internal pressures in the boxes are actually equal, if the size of fluctuations is of concern. One way is to calculate the excess pressure in each box by measuring numerically the derivative of potential energy with volume, $\partial U/\partial V$. The relevant quantities for this measurement are already calculated in the course of Gibbs ensemble simulation trial volume moves. Eppenga and Frenkel [6] reported a trick for calculating the pressure in constant-NVT simulations of hard molecules by attempting 'fake' box contractions and calculating the acceptance probability. In the simulation of soft-bodies, both contractions and expansions must be considered. Again, the relevant quantities are calculated in the course of a normal Gibbs ensemble simulation. The pressure is finally expressed in terms of the probability of successful volume moves:

$$P = k_B T \lim_{\delta V\to 0} \frac{\ln\left\langle\left(\frac{V_0+\delta V}{V_0}\right)^N \exp(-\beta\Delta\mathcal{V})\right\rangle}{\delta V} = k_B T \lim_{\delta V\to 0} \frac{\ln\langle\mathcal{P}_{\mathrm{ACC}}\rangle}{\delta V}. \tag{2.32}$$

Since these approaches to obtaining the pressure are only strictly valid in the canonical ensemble, each is subject to the same order of correction when applied to only one of the boxes in a Gibbs ensemble simulation.

2.6 Gibbs-Duhem Integration

2.6.1 Governing equations

In the Gibbs ensemble method, the equality of chemical potential required to bring the two subsystems into equilibrium is achieved by attempting to exchange particles between the boxes. This feature is very significant in practice, since it may be necessary to attempt many exchanges in order to maintain an appropriate rate of particle transfer. Recently, an alternative approach has been put forward by Kofke [77, 78] which allows the direct evaluation of phase coexistence avoiding interfaces and without relying on the particle insertion mechanism. It is a thermodynamic integration technique which draws heavily on aspects of the Gibbs ensemble approach. Here, as in a Gibbs ensemble simulation, the two coexisting phases are simulated separately and simultaneously. The path for the thermodynamic integration is chosen to lie along the coexistence line, so that a single simulation is required for each coexistence point.

If phases α and β are to remain in equilibrium when the temperature is changed, for example, the pressure must also change so that the two chemical potentials remain equal. The required pressure change is given by the Clapeyron equation,

$$\frac{dP}{dT} = \frac{\Delta\left(S/N\right)}{\Delta\left(V/N\right)} = \frac{\Delta s}{\Delta v} \tag{2.33}$$

where $s = S/N$, the entropy per particle, $v = V/N$ and $\Delta X = X_\alpha - X_\beta$. These equations can be re-cast in forms more obviously tractable to simulation using $S = (H - G)/T$, with H the enthalpy and $G = N\mu$, giving

$$N\, d(\beta\mu) = H\, d\beta + \beta V\, dP \tag{2.34}$$

and

$$\frac{dP}{d\beta} = -\frac{\Delta h}{\beta \Delta v} \quad . \tag{2.35}$$

where $\beta = 1/k_B T$ and $h = H/N$. The derivatives here are taken along the coexistence line. This defines a first-order nonlinear differential equation which can be integrated numerically, given an initial condition, to determine the entire coexistence curve.

2.6.2 Integrating the equation

When considering molecular models, accurate evaluation of the right-hand side of (2.35) means using simulation. The integration procedure will always be improved if the integrand is only slowly-varying. When (2.35) is written as

$$\frac{\mathrm{d}\ln P}{\mathrm{d}\beta} = -\frac{\Delta h}{\beta P \Delta v} \tag{2.36}$$

and applied to liquid-vapour equilibrium, the right-hand side varies only very slowly.

A separate simulation is required for each evaluation of the integrand for molecular fluids, a crucial point when choosing the integration scheme. Although schemes requiring multiple evaluations for each step can deliver solutions of high accuracy and stability they are clearly too expensive for for a realistic application of GD. Predictor–corrector techniques, however, store the solution along the way, using previous results to extrapolate the solution to the next step and correcting this estimate using the derivative at the new point. Low order PCs are amenable to simulation, particularly as a feature of the measured averages in a simulation is the possibility of refining the estimated coexistence value as the simulation proceeds. Since the integrand of (2.36) depends on the difference of quantities in the two phases, it is clear that they must be simulated in concert. According to the investigations of Kofke [78] for van der Waals and LJ fluids, the most significant factor governing accuracy is the step size, and a simple scheme such as the trapezoid-rule predictor-corrector method performs reasonably well. Higher-order schemes were seen to give closer agreement with expected results for a given step size, but they require more input data and are more likely to show instabilities.

Given a suitably small step size, the stability of this procedure can be maintained even in the vicinity of the critical point. Other steps may be taken to bolster the stability where necessary, such as coupling the volume moves of the two boxes in order to keep the two phases separated. The scheme may, however, give convergence for a series of integration steps and still deviate from the coexistence line, since numerical errors in the initial condition will propagate throughout the calculations. The hysteresis associated with NPT simulations near a phase transition is a well-known phenomenon, and if one of the phases is lost, deviations from the coexistence curve are likely to have become large. Where possible, integrating between two established data points will provide a check on

the results but in many cases such data are not available. The integration scheme can always be reversed from an end-point, tracing back along the coexistence curve over some interval. This gives a direct indication of the significance of compound errors. Other integration schemes in this vein have been suggested. A very recent proposal of Meijer and El Azhar [79] aims to successively correct the coexistence data by measuring the free energy difference of the two phases at the estimated state points using the overlapping distributions method [66]. Bearing in mind these caveats, though, the basic GD method is a versatile and efficient approach for calculation of phase coexistence boundaries.

2.6.3 Pressure-Elongation integration

The GD approach allows the construction of many other schemes using integration variables other than temperature. Consider mapping out the pressure-elongation coexistence envelope. Now the temperature is held constant and a governing differential equation is required expressing the change in pressure required to maintain equilibrium between the two phases when the particle dimensions are changed. Let a indicate some general particle dimension, the choice of which will depend on the system under study. This approach has been used by Camp and Allen [80] to investigate the coexistence envelope for hard ellipsoids as a function of size, (with the same scaling factor applied to the minor and major axes). Then, writing $\mu = \mu(P, a)$,

$$\mathrm{d}\mu = \left(\frac{\partial \mu}{\partial a}\right)_P \mathrm{d}a + \left(\frac{\partial \mu}{\partial P}\right)_a \mathrm{d}P \tag{2.37a}$$

$$= \Lambda\, \mathrm{d}a + \frac{1}{\rho}\mathrm{d}P. \tag{2.37b}$$

where $\Lambda \equiv \left(\frac{\partial \mu}{\partial a}\right)_P$. The governing equation at coexistence may be written, in a slowly varying form, as

$$\frac{d \ln P}{da} = -\frac{\Delta \Lambda}{P \Delta v} \quad . \tag{2.38}$$

For evaluation of Λ consider a scaling of the particles from a to $a' = a + \delta a$. Then

$$\beta\Lambda = \frac{1}{N}\left(\frac{\partial\left(-\ln Q^{NPT}\right)}{\partial a}\right)_P = \frac{1}{N}\lim_{\delta a \to 0} \frac{\left[\left(-\ln Q^{NPT}_{a'}\right) - \left(-\ln Q^{NPT}_{a}\right)\right]}{\delta a}$$

$$= -\frac{1}{N}\lim_{\delta a \to 0} \frac{\left[\ln\left(Q^{NPT}_{a'}/Q^{NPT}_{a}\right)\right]}{\delta a}$$

$$= -\frac{1}{N}\lim_{\delta a\to 0}\frac{1}{\delta a}\left[\ln\left\{\frac{\int \mathrm{d}V\int \mathrm{d}\Gamma\exp(-\beta(\mathcal{H}_{a'}+PV))}{\int \mathrm{d}V\int \mathrm{d}\Gamma\exp(-\beta(\mathcal{H}_{a}+PV))}\right\}\right] \quad . \tag{2.39}$$

The centre-of-mass coordinates, momenta and moments of inertia are unchanged by this scaling. Thus, $\mathcal{H}_{a'} = \mathcal{H}_a + \Delta\mathcal{V}$, where $\Delta\mathcal{V}$ is the change in potential energy. The result for Λ becomes

$$\begin{aligned}\beta\Lambda &= -\frac{1}{N}\lim_{\delta a\to 0}\frac{1}{\delta a}\left[\ln\left\{\frac{\int \mathrm{d}V\int \mathrm{d}\Gamma\exp(-\beta\Delta\mathcal{V})\exp(-\beta(\mathcal{H}_{a}+PV))}{\int \mathrm{d}V\int \mathrm{d}\Gamma\exp(-\beta(\mathcal{H}_{a}+PV))}\right\}\right] \\ &= \lim_{\delta a\to 0} -\frac{\ln\langle\exp(-\beta\Delta\mathcal{V})\rangle}{N\delta a} \quad . \end{aligned} \tag{2.40}$$

Given a suitably small value of δa, this allows the measurement of Λ.

2.6.4 Simulation procedure

From the initial coexistence condition the integration scheme proceeds in a series of steps in the independent variable, e.g. temperature. At each stage, a prediction is made according to the governing equation and the integration scheme for the required value of the dependent variable, e.g. pressure. Given these new conditions, an equilibration run is conducted. In the absence of additional coupling, this proceeds as two simultaneous but independent NPT simulations using either MC or MD, allowing the systems to respond to the change in the required thermodynamic conditions. Initial equilibration is followed by a run during which the simulation pressure is progressively refined according to the corrector stage of the integration scheme, continuing to convergence within a pre-specified tolerance. Finally, a production stage is used to measure the properties of interest at the new coexistence point, in particular those required to establish the system as the starting point for the next step in the integration series. The length of the stages will be determined by the nature of the phases and proximity to special points, (i.e. critical or triple points).

This chapter by no means exhausts the established tools of the simulator. Rather, it is a description of the techniques that are applied in the following chapters to study a number of model liquid crystal systems. Often, several approaches are applied in succession; rather than repeating them *in situ*, we shall often make reference to the descriptions above.

Chapter 3

Effects of Elongation on the Phase Behaviour of the Gay-Berne Fluid

3.1 Introduction

The choice of parameter values $(\mu, \nu, \kappa, \kappa')$ used in the GB potential specifies the characteristics of the fluid and directly influences the phase behaviour of the system. Since this parameter space is large, an understanding of the systematic effects of varying these values is desirable. Perhaps the most intuitively accessible of these parameters is κ, a measure of the elongation of the molecule. Previous work [81] has used the original [31] values $\mu = 2, \nu = 1$ and $\kappa' = 5$, and investigated liquid-vapour properties for $\kappa \leq 3$. This indicated that increasing molecular elongation is accompanied by a broadening of the liquid-vapour coexistence region, particularly on the liquid side, and a reduction in the critical temperature and density.

The most complete phase diagram available in the literature is that obtained by de Miguel *et al.* [1] for the $\kappa = 3$ fluid, shown schematically in Fig. 3.1. The three phases indicated are isotropic (I), nematic (N) and smectic B (S_B). The work reported here concentrates on $\kappa > 3$. Certain trends in phase behaviour might be expected to accompany increasing elongation. For hard spherocylinders, this enhances the stability of the smectic regions [82], whereas on the basis of Onsager arguments, one might expect the range of the nematic phase to be increased [83]. Nematic-vapour coexistence is possible,

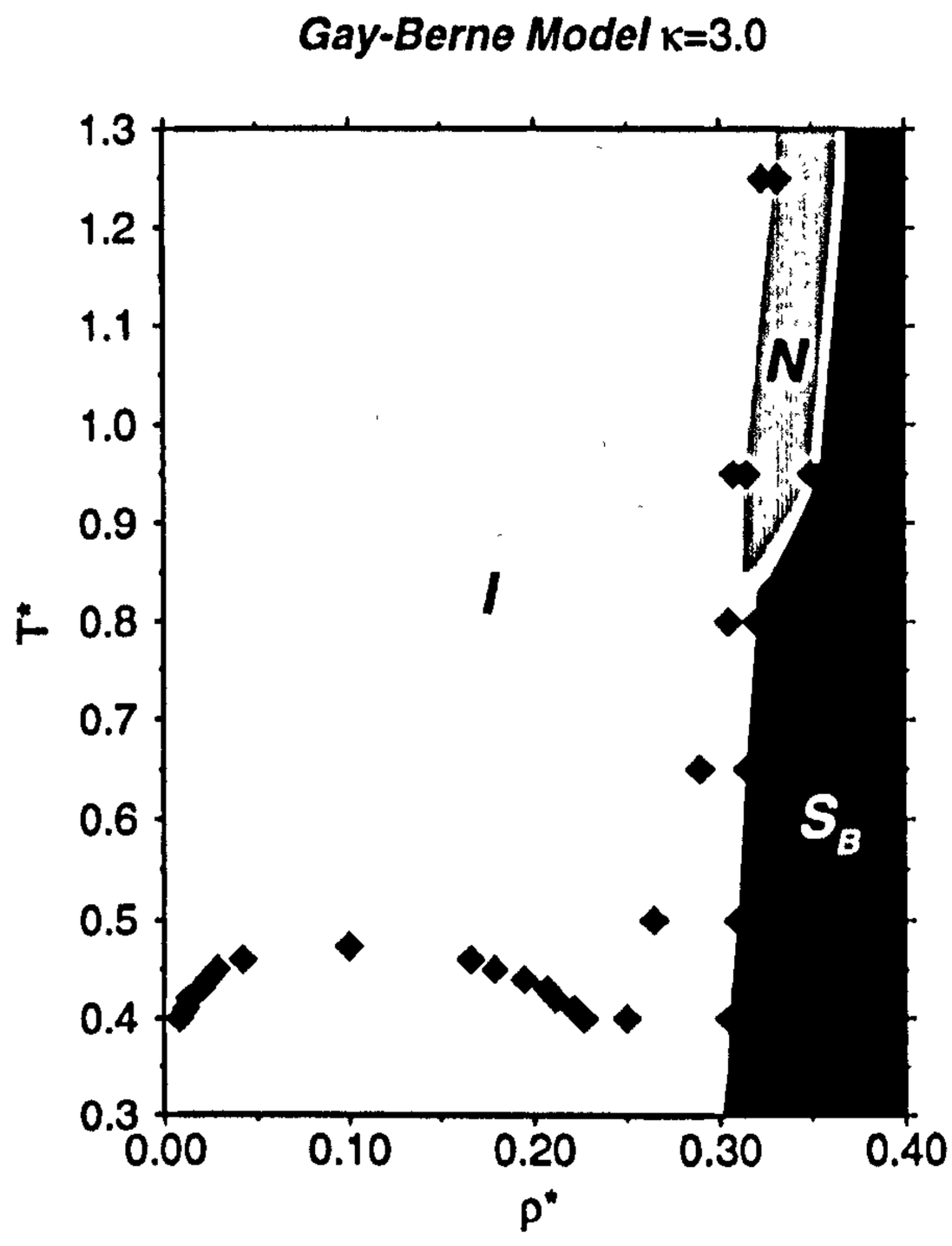

Figure 3.1: Phase diagram for the $\kappa = 3$ Gay-Berne fluid as reported in [1]. White regions correspond to phase coexistence.

and has been predicted for this anisotropic system [45]. The behaviour of the critical temperature T_c should also be borne in mind. From van der Waals theory and as borne out by simulation [84], it is attractive interactions that induce liquid-vapour separation. With the other parameters fixed, increasing κ reduces the effective range of the attractive forces, and will suppress the coexistence envelope. For sufficiently short ranged interactions, (high elongations), the critical point will move below the adjacent coexistence line, (I–S_B in the case of Fig. 3.1).

Initial investigations into the effect of elongation used direct simulation, as described in §2.4, to study liquid-vapour coexistence, with $(\mu, \nu, \kappa, \kappa') = (2,1,3,5)$ as a starting point, followed by higher values of κ. At $\kappa = 4$ the system condensed to give domains of high orientational and positional order, as shown in Fig. 3.2, which were very slow to coalesce.

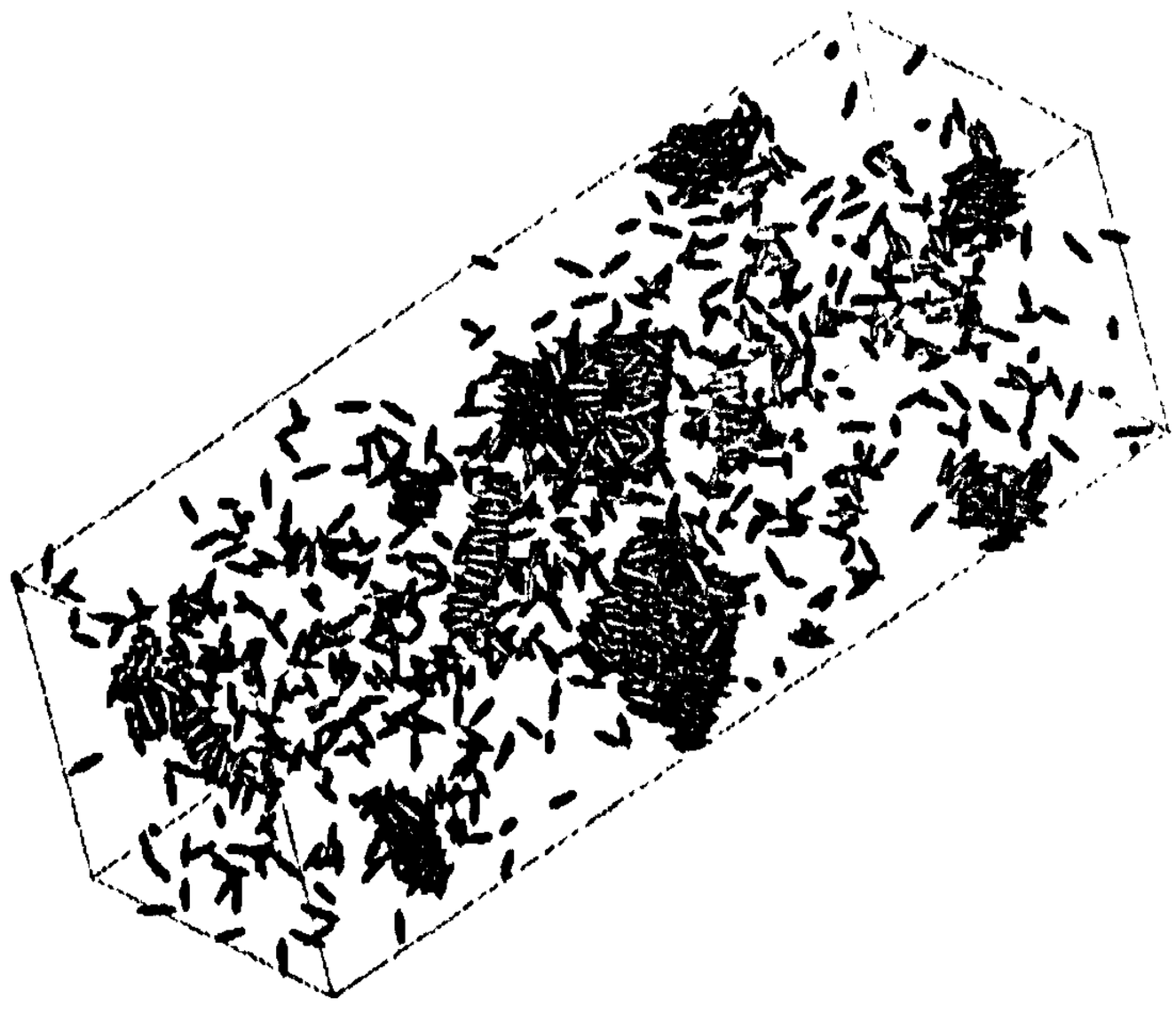

Figure 3.2: Snapshot from direct simulation of $N = 1900$ GB particles with $\kappa = 4$ at $T = 0.40$. Vapour is in coexistence with an ordered phase which has formed domains distributed throughout the box.

This suggests coexistence between a low density vapour and a solid or highly ordered smectic phase. Similar problems were encountered when increasing κ from 3 to 4 in GEMC simulations, where particle exchange becomes problematic with the onset of positional order. These initial results prompted extensive studies for the GB fluid concentrating on $3 \leq \kappa \leq 4$ with the other parameters held fixed. In the following sections, the equation of state is presented for a number of isotherms, obtained by MD and MC techniques. The phase behaviour is further studied using direct simulation of coexisting phases and thermodynamic integration along phase boundaries. Finally, the nature of the highly ordered phase is discussed and the results are summarized in tentative phase diagrams.

3.2 Phase characterization

Along with nematic and smectic order parameters, direct visualization is used to identify the phases of these systems, and positional ordering is examined using a set of 2-body

distribution functions. The first of these is the standard orientationally-averaged radial distribution function, $g(r)$, defined in §2.3.3. In practice, this is measured as a histogram of pair separations with values of r up to some cut-off, r_{gc}. In a fluid with no positional order, $g(r)$ shows a first-neighbour peak, followed by rapidly-decaying oscillations about unity, as shown in Fig. 3.3. When using periodic boundary conditions, $g(r)$ can be measured to a maximum distance of $L_{\mathrm{min}}/2$, where L_{min} is the shortest box side - at larger r, correlations of a particle with its own image are possible.

With the formation of layers in smectic or crystalline phases, a 1-dimensional density wave arises along the layer normal. For the phases encountered here, this direction coincides with the director, (unit vector $\mathbf{n}$), and layering is indicated by the longitudinal component of the pair distribution function, $g_{\|}(r_{\|})$, where $r_{\|} = \mathbf{r} \cdot \mathbf{n}$. Often, the same cut-off is used in the measurement of $g(r)$ and $g_{\|}(r_{\|})$. In a system with well-defined layers, this spherical sampling volume will lead to poor statistics at large $r_{\|}$, as indicated in Fig. 3.4. This effect can be even more significant for $g_{\perp}(r_{\perp})$, which indicates transverse positional correlations. The forms of $g_{\|}$ and $g_{\perp}$ expected in smectic fluids are shown in Fig. 3.3. Due to the small volume of the large-r bins, in-layer correlations are enhanced when the histogram for $g_{\perp}(r_{\perp})$ is normalised, and it is not unusual to discard the outermost bins. The choice of sampling volume is arbitrary provided it avoids self-image correlations. A cylindrical region has been sampled in this work, eliminating the edge effects, but incurring a small penalty in execution speed and a slight reduction in the maximum cut-off allowed by the box.

Even in a layered system with significant interdigitation, practical system sizes usually mean that $g_{\|}$ and $g_{\perp}$ sample few layers, often extending only to the nearest-neighbours, but contributions from the separate layers are still difficult to resolve. Having established 1-d positional ordering, other distribution functions are required to probe the intra- and inter-layer structure. Using the phase and period of the density wave along the director, each particle can be assigned to a specific layer. Positional correlations within single layers are then measured by $g_{11}(r_{\perp})$, a 2-d distribution function averaged over pairs of particles in the same layer. Correlations of particles in separate layers can also be measured. Given the typical system sizes, attention has been restricted to particles in adjacent layers, $g_{12}(r_{\perp})$, and next-nearest layers, $g_{13}(r_{\perp})$. If contributions to $g_{13}(r_{\perp})$ are not to be duplicated,

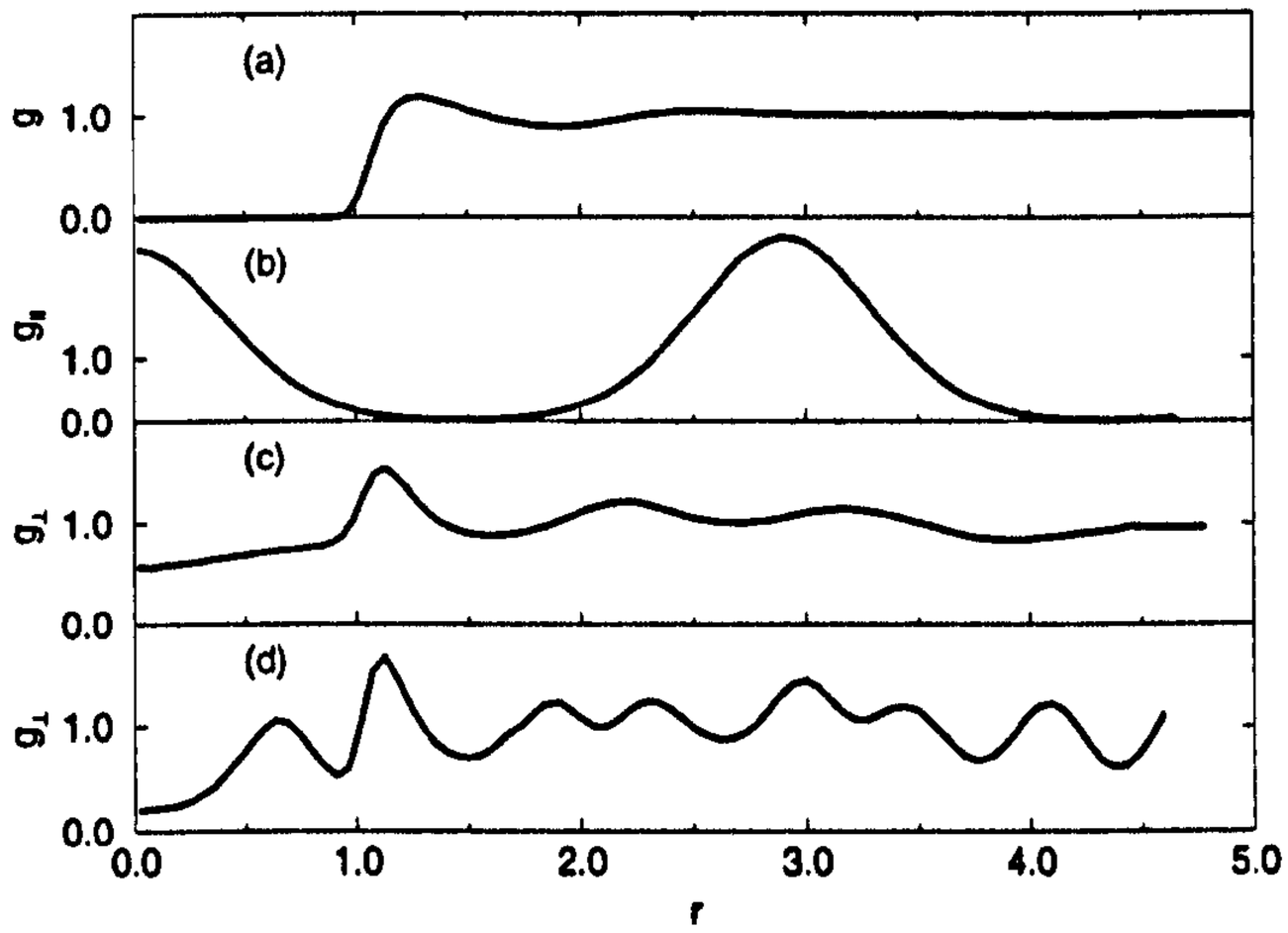

Figure 3.3: Typical forms of pair distribution functions: (a) $g(r)$ in the isotropic phase, (b) $g_{\|}(r_{\|})$ in a smectic phase, (c) $g_{\perp}(r_{\perp})$ in the S_A phase and (d) $g_{\perp}(r_{\perp})$ in the S_B phase.

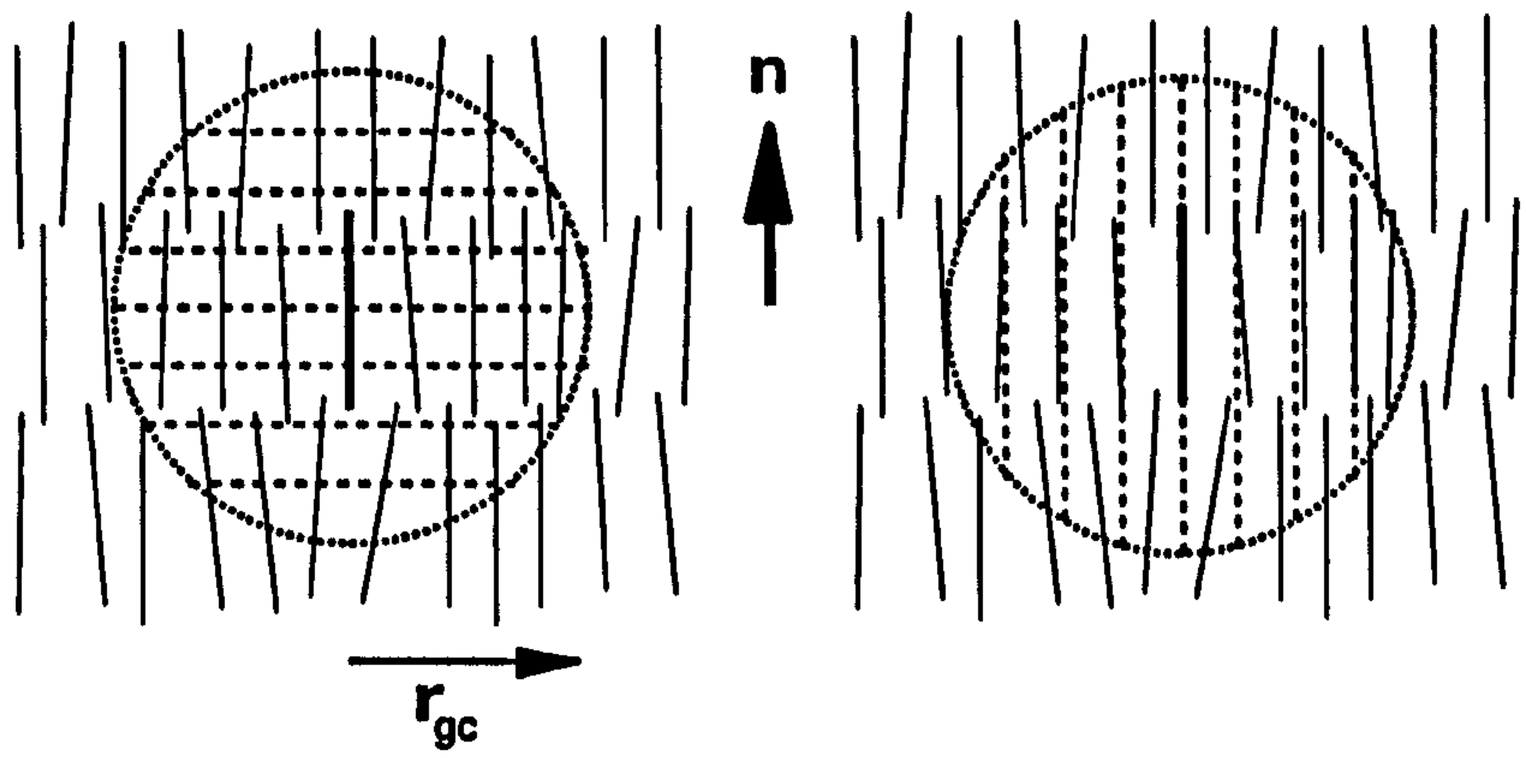

Figure 3.4: Measuring (a) $g_{\|}(r_{\|})$ and (b) $g_{\perp}(r_{\perp})$ with a spherical cut-off, indicated by the dotted circle. Particles are represented by solid lines and successive regions sampled for the histograms by broken lines.

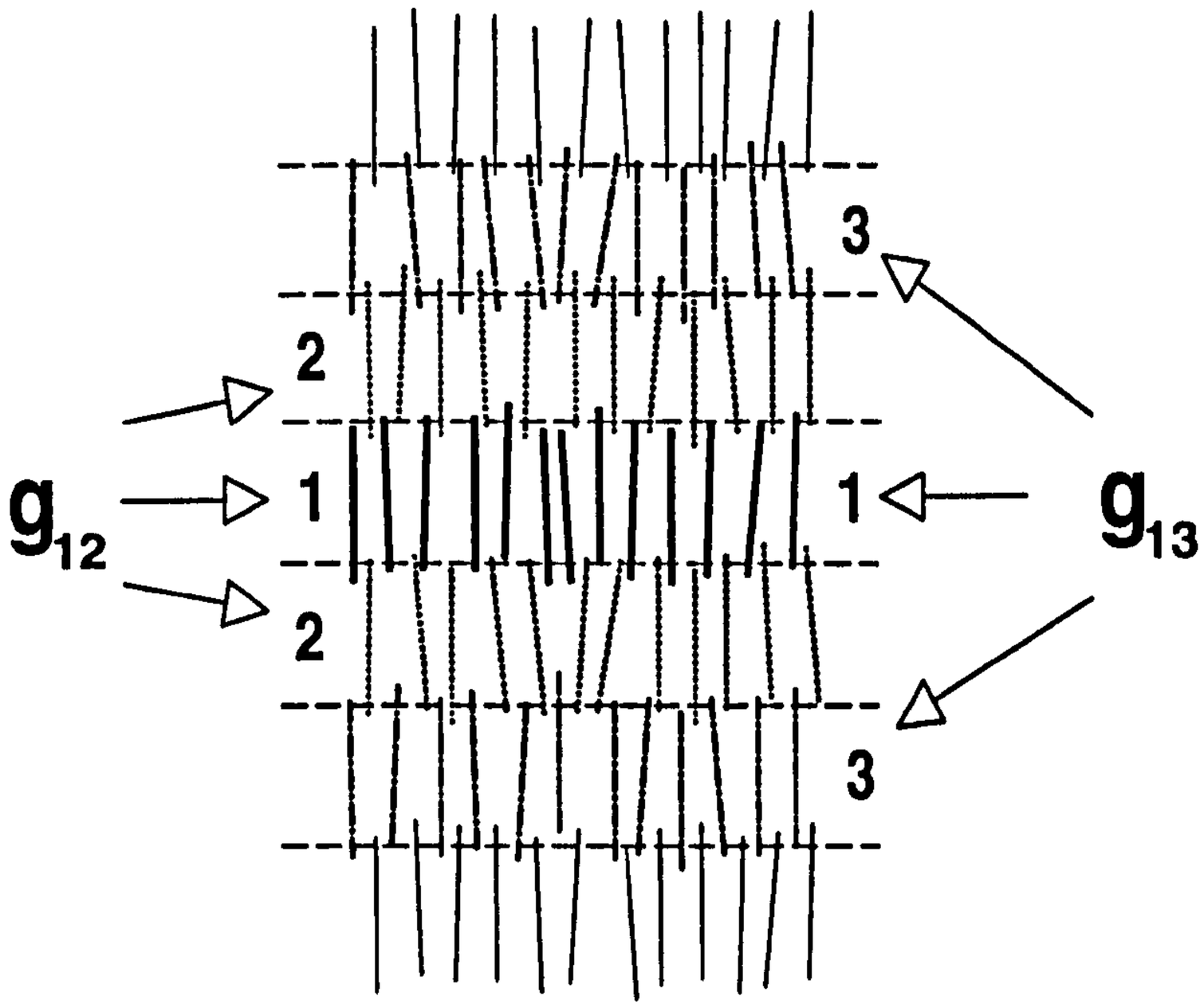

Figure 3.5: The arrangement for measuring between-layer functions $g_{12}(r_\perp)$ and $g_{13}(r_\perp)$. Horizontal lines indicate boundaries used in assigning particles to specific layers.

there must be five or more distinct layers in the simulation box, as can be seen in Fig. 3.5. Layer functions are averaged over all (pairs of) layers in the box in the course of a simulation.

The layer normal, (or director, in these cases), and layer spacing d, must together allow the layered structure to be commensurate with the periodic images. In a box of fixed dimensions, the condition is

$$q_\alpha n_\alpha d = L_\alpha \tag{3.1}$$

for integer q_α, $\alpha = x, y$ and z, and n_α, L_α the corresponding director component and box dimension, respectively. Since they are resisted by an increase in the elastic free energy, transitions between allowed orientations are extremely rare. This allows the layer normal to be taken as fixed in the course of a simulation; if it is known a priori, measurement of these layer-wise functions is greatly simplified, but in general it will be necessary to allow for arbitrary layer orientation.

3.3 MD simulations

3.3.1 Simulation Details

In the first stage of this investigation, MD simulations were performed on a system of $N = 256$ particles in the NVT ensemble, adopting the procedure of previous work [1]. Two isotherms were considered, at reduced temperatures of $T = 1.00$ and $T = 0.45$. It has been shown [1] that for $\kappa = 3$, the $T = 1.00$ isotherm crosses the supercritical isotropic fluid region, shows a stable nematic region, and at high enough densities enters a smectic phase; the $T = 0.45$ isotherm crosses the liquid-vapour coexistence region before also entering a smectic phase at high density, (see Fig. 3.1). A reduction in the critical temperature, T_c, is expected to accompany an increase in elongation. Thus, at some elongation $\kappa > 3$ the $T = 0.45$ isotherm is expected to become super-critical.

The temperature was kept constant throughout these simulations by rescaling the particle velocities [9]. A cubic simulation box was employed with periodic boundary conditions. As in previous work, the molecules were treated as linear rotors, with the moment of inertia about axes perpendicular to the main symmetry axis set to $I = 1$ in reduced units. The intermolecular potential was truncated at a distance $r_c = (\kappa + 1)\sigma_0$ and shifted such that $U_{cs}(r = r_c) = 0$:

$$U_{cs}(r, \hat{\mathbf{r}}, \mathbf{e}_1, \mathbf{e}_2, r_c) = U_{GB}(r, \hat{\mathbf{r}}, \mathbf{e}_1, \mathbf{e}_2) - U_{GB}(r_c, \hat{\mathbf{r}}, \mathbf{e}_1, \mathbf{e}_2) \tag{3.2}$$

Both terms must be included when derivatives of the potential are calculated. The time step used for the numerical solution of the equations of motion was $\delta t = 0.0015$. The initial configurations, (described below), were equilibrated for at least 2.5×10^4 timesteps; runs 3–4 times longer than this were performed when the system was close to a phase transition. After equilibration, quantities of interest were typically calculated and averaged over 2.5×10^4 additional timesteps.

3.3.2 MD results at high temperature, $T = 1.00$

First we consider the simulations at $T = 1.00$, the highest temperature used for these MD simulations. This is well above the critical temperature for liquid-vapour coexistence in the $\kappa = 3$ GB fluid, ($T_c \approx 0.47$), and since $\kappa = 3$ is the lowest elongation considered

here, we do not expect to encounter this coexistence envelope for any of the fluids studied. Particle elongations from $\kappa = 3.0$–3.8 in steps of 0.2 were considered; at each value, simulations were initiated with a f.c.c. lattice generated at a density of $\rho = 0.27$. The director was taken along the main diagonal of the simulation box, but each particle was given a small, random displacement from the ideal position and orientation to assist in disordering. At the lowest elongation this system is unstable, and quickly loses positional order. The orientational order is also lost within 5×10^3 timesteps. As expected from the results of previous work [1], the equilibrium configuration at these thermodynamic conditions is isotropic. The system was then slowly compressed in density steps of 0.01 or less. For higher elongations, the initial density was observed to lie within the ordered region of the phase diagram, and longer equilibration runs were performed, typically of 1×10^5 timesteps. The configuration at $\rho = 0.27$ was used as the starting point for both increasing and decreasing the density. The $\kappa = 4$ fluid was also studied. In this case, the initial configuration was a lattice at $\rho = 0.17$ which equilibrated to an isotropic fluid. The density was both increased and decreased from this point. The pressure values obtained are shown in Figs. 3.6–3.11, along with the behaviour of the orientational order parameter. For each κ, the lowest density shown corresponds to an isotropic fluid, shown by the low values of the orientational order parameter.

The case $\kappa = 4$ is considered below. For all the other elongations, increasing density is accompanied by a phase transition, indicated by a discontinuity in the pressure and a marked increase in orientational order. This phase is nematic, as confirmed by the liquid-like behaviour of the orientationally averaged pair distribution function, shown for $\kappa = 3.2$ in Fig. 3.12. The I–N transition density is seen to fall with increasing elongation. At still higher densities, the systems undergo a weak second transition. This ordered phase was characterized as smectic by studying $g_{\parallel}(r_{\parallel})$, illustrated in Fig. 3.13 for $\kappa = 3.2$: oscillations can be seen at $\rho = 0.300$ as smectic regions develop, but on increasing the density to $\rho = 0.305$ the structure is greatly enhanced.

In the $\kappa = 3$ fluid, the transition to the smectic is accompanied by the development of structure in $g_{\perp}(r_{\perp})$, indicating transverse positional correlations that persist across the box. The behaviour of this function in the region of the transition is indicated in Fig. 3.14, and is as expected from earlier work, [1]. Two features are of particular note. Above

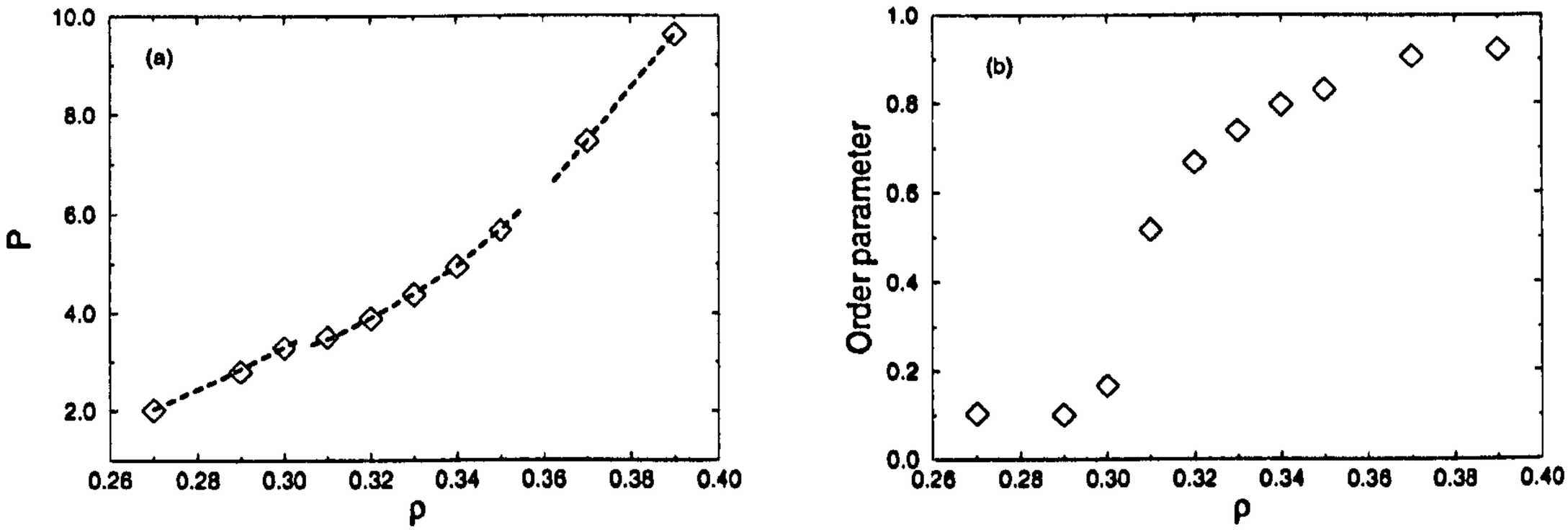

Figure 3.6: (a) Equation of state of the GB fluid with $\kappa' = 5$ and $\kappa = 3.0$ along the isotherm $T = 1.00$ as obtained from MD simulation. (b) Corresponding values of orientational order parameter. Pressure (P) and number density (ρ) are expressed in reduced units. Lines are drawn to guide the eye, indicating the distinct phase regions.

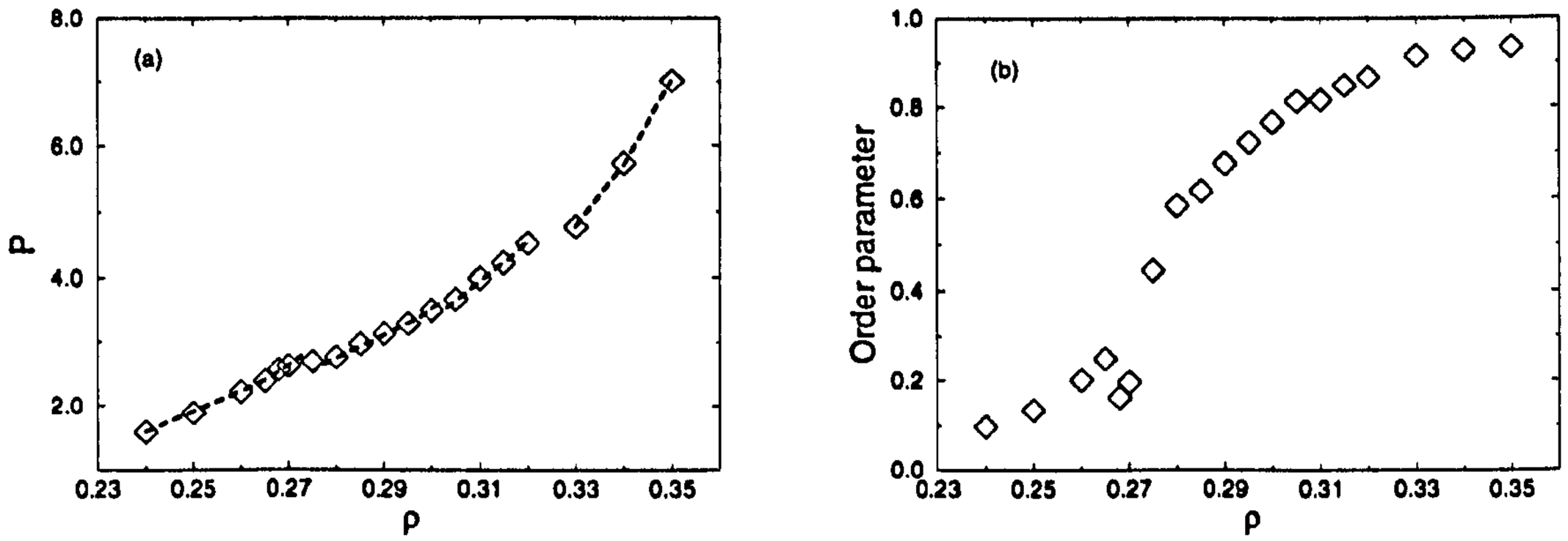

Figure 3.7: As Fig. 3.6 for $\kappa = 3.2$.

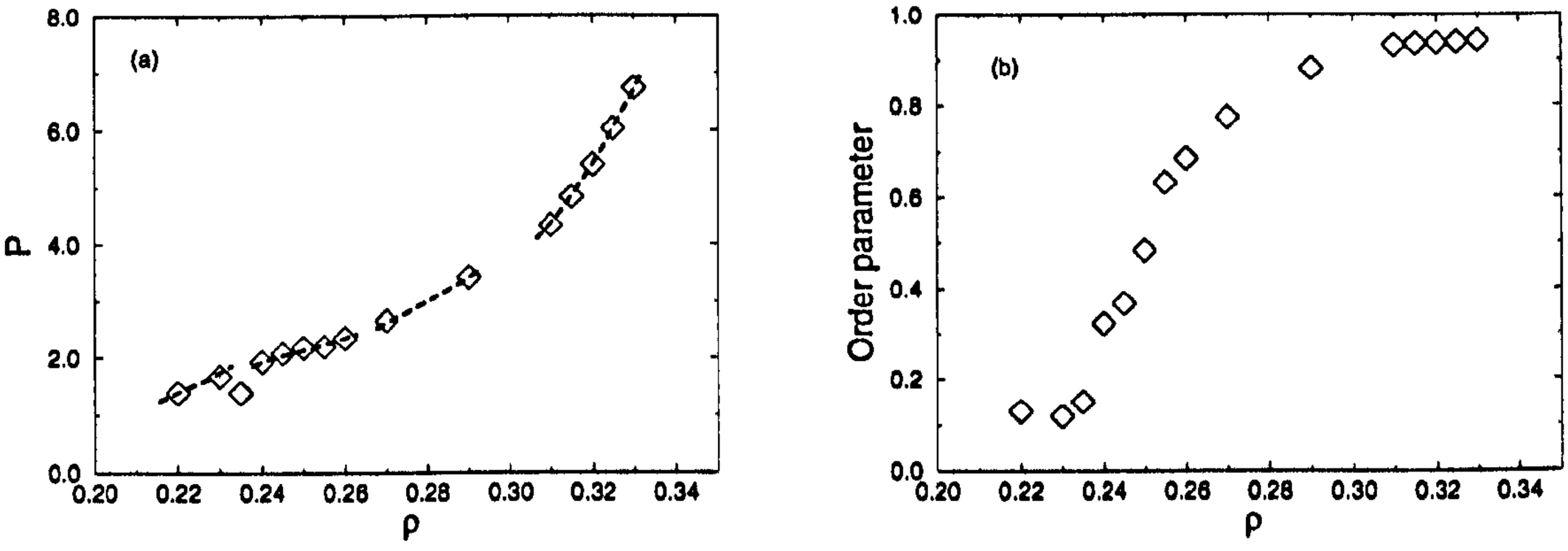

Figure 3.8: As Fig. 3.6 for $\kappa = 3.4$.

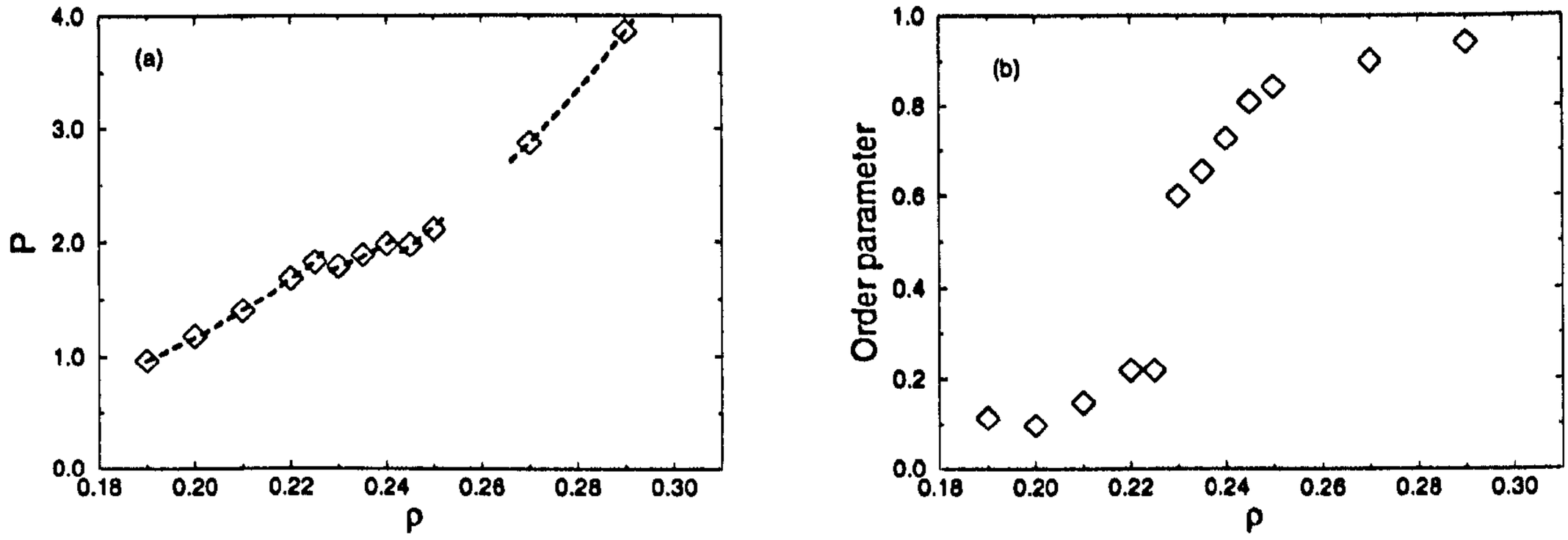

Figure 3.9: As Fig. 3.6 for $\kappa = 3.6$.

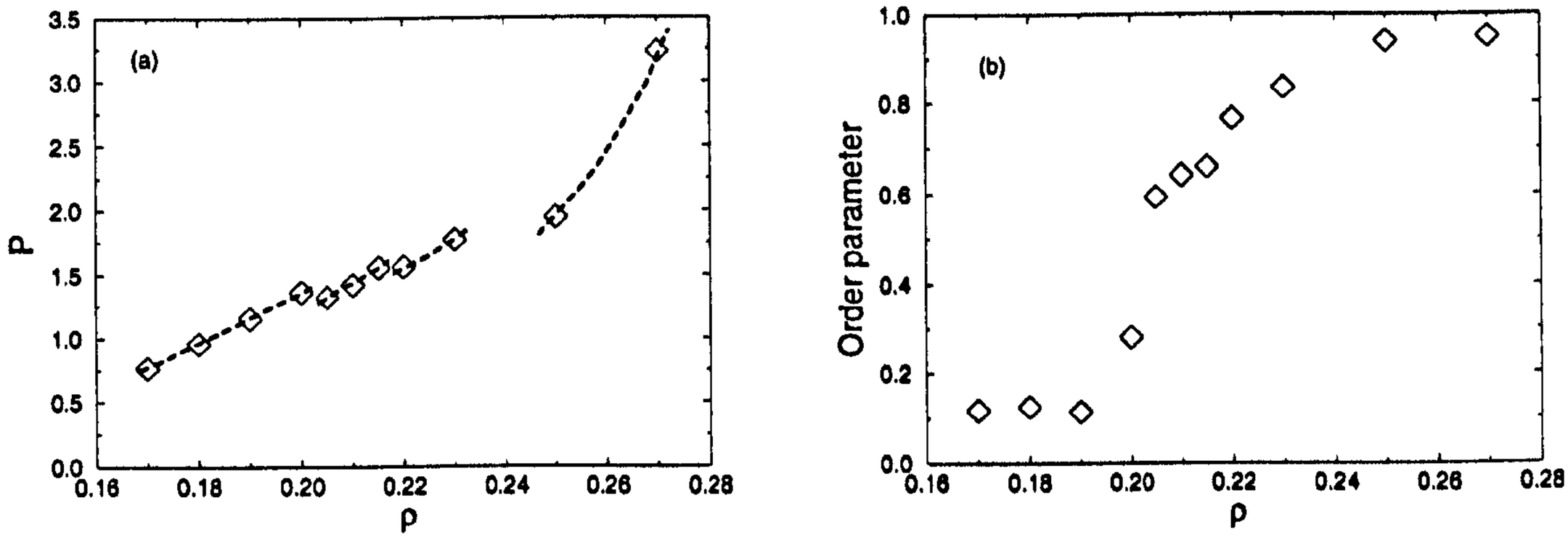

Figure 3.10: As Fig. 3.6 for $\kappa = 3.8$.

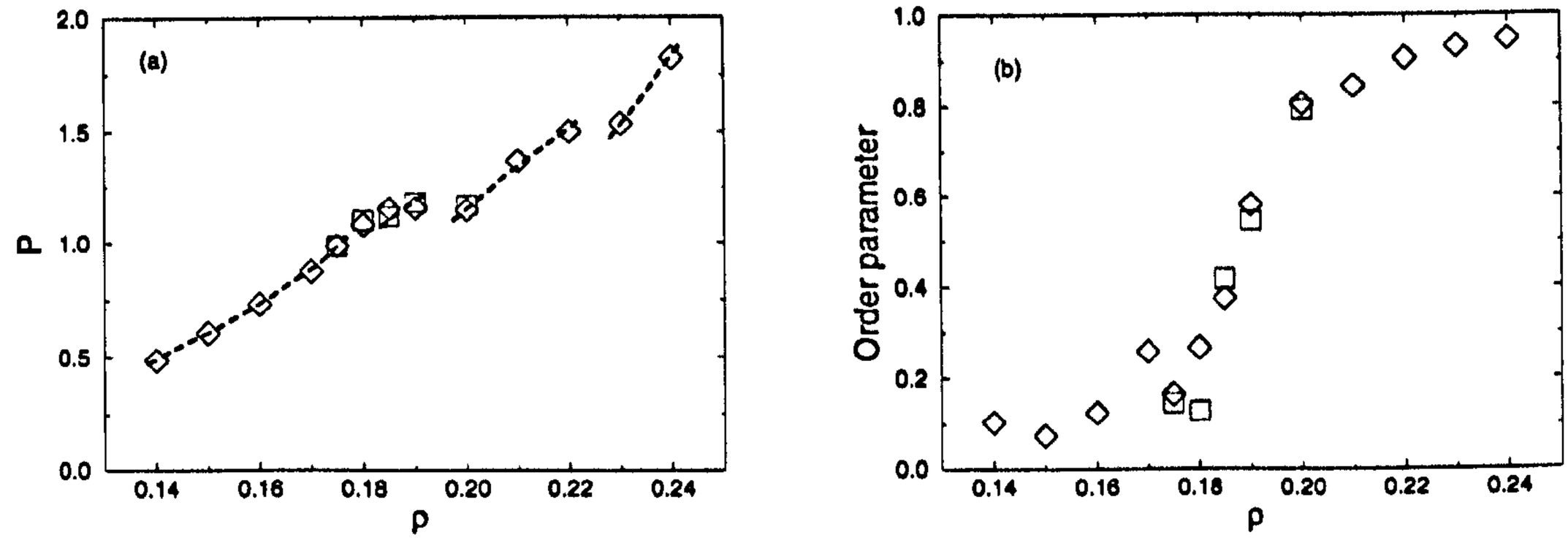

Figure 3.11: As Fig. 3.6 for $\kappa = 4.0$. Squares indicate data obtained with $N = 400$ particles.

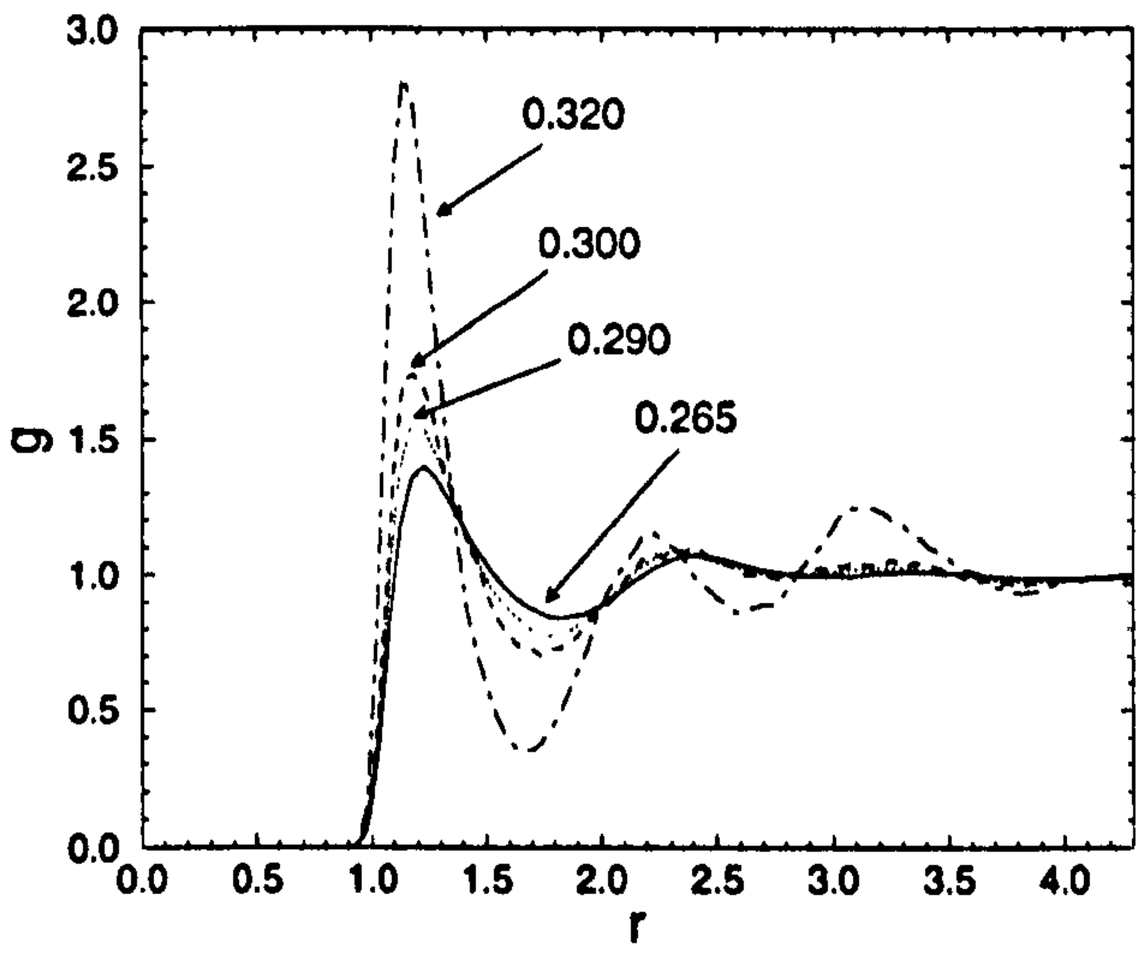

Figure 3.12: Pair distribution function, $g(r)$, for GB fluid with $\kappa' = 5$ and $\kappa = 3.2$ at different number densities, (labelled on the plot), along the isotherm $T = 1.00$, corresponding to isotropic, nematic and smectic A phases.

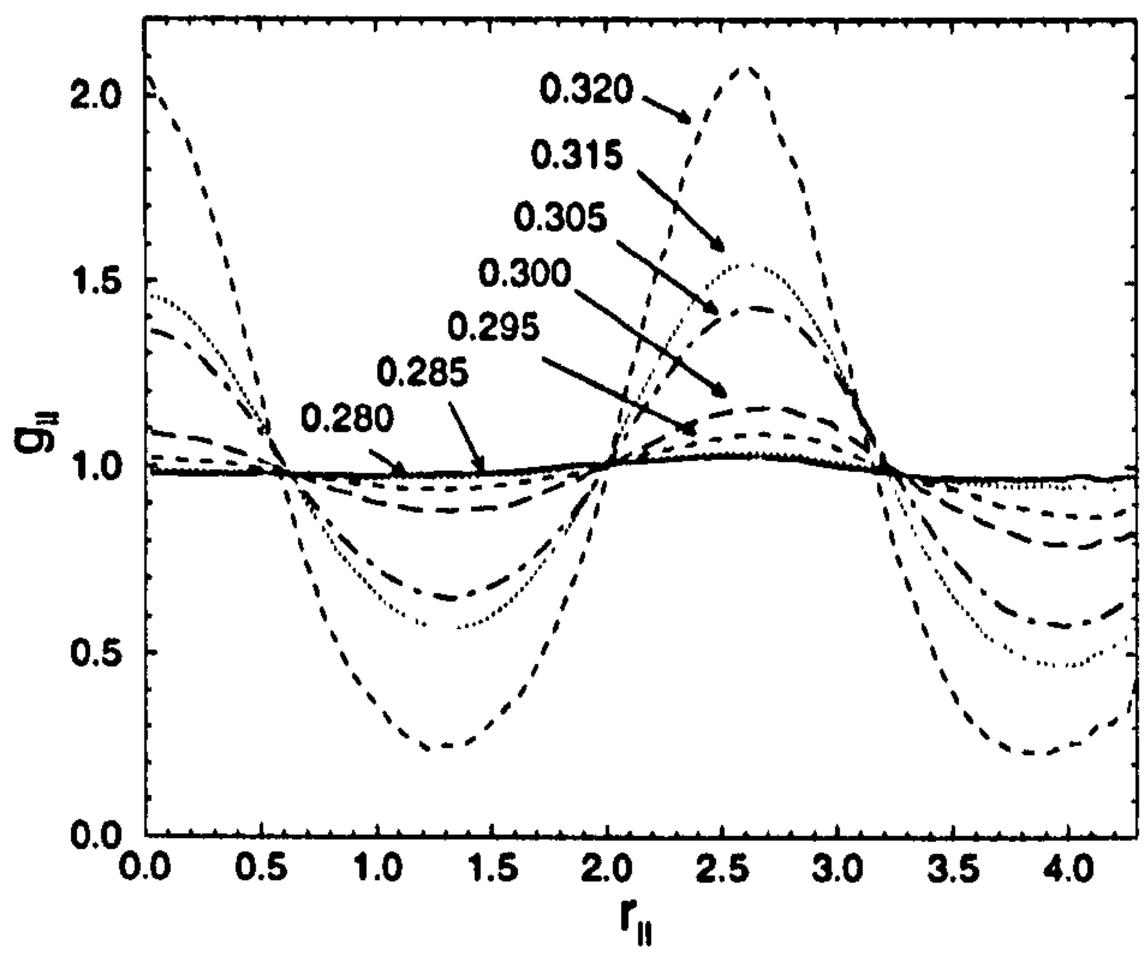

Figure 3.13: Longitudinal pair distribution function, $g_{\parallel}(r_{\parallel})$, for GB fluid with $\kappa' = 5$ and $\kappa = 3.2$ at different number densities, (labelled on the plot), along the isotherm $T = 1.00$.

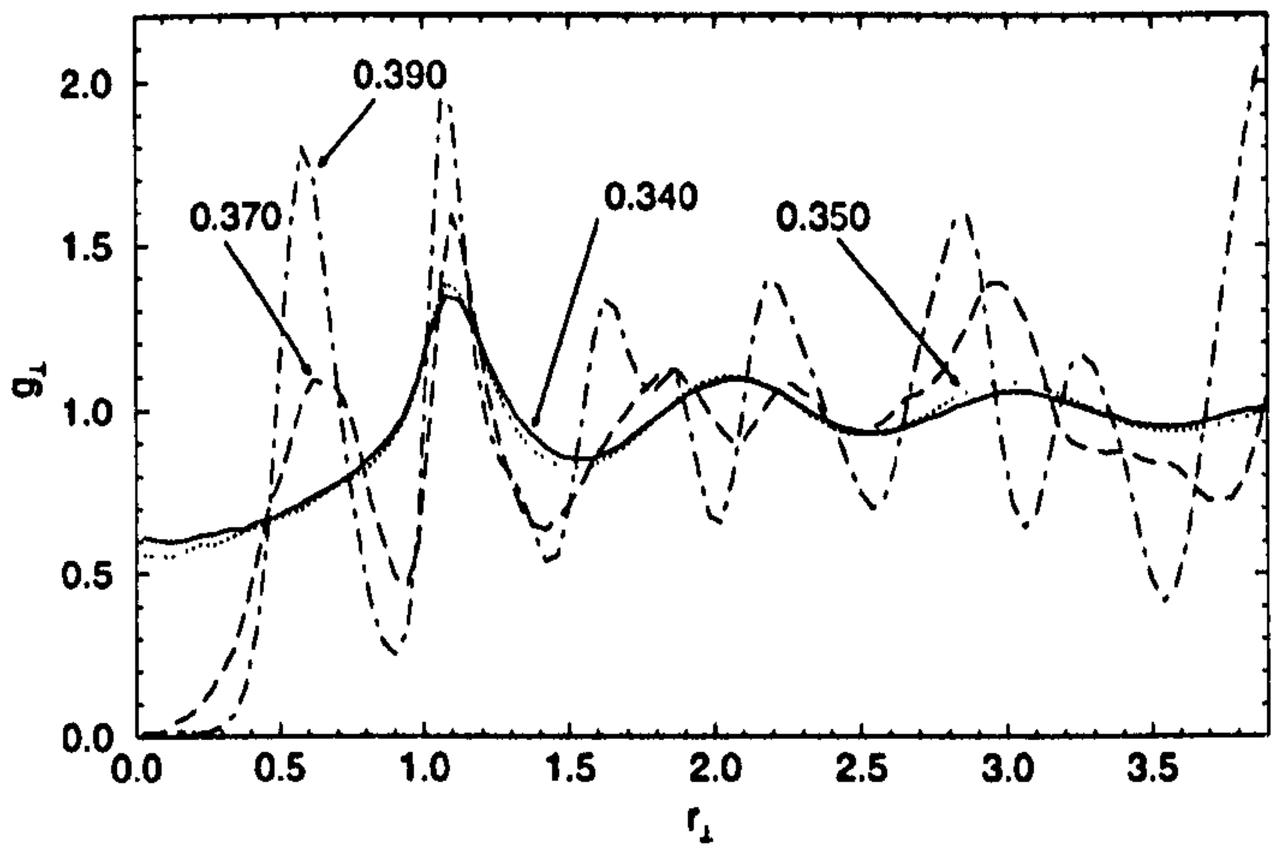

Figure 3.14: Transverse pair distribution function, $g_\perp(r_\perp)$, for GB fluid with $\kappa' = 5$ and $\kappa = 3.0$ at different number densities, (labelled on the plot), along the isotherm $T = 1.00$.

the transition, the distribution function falls to zero at $r_\perp = 0$, indicating that particles in adjacent layers are strongly anti-correlated. Also, the position of the first maximum moves below $r_\perp = 1$, indicating positional correlations between particles of adjacent layers. From $g_{||}$, the layer spacing is around $2.4\sigma_0$; with $r_{gc} \sim 4$, only pairs within a layer or in immediately adjacent layers will contribute. The structure in $g_{11}(r_\perp)$ indicates hexagonal ordering within the smectic layers, consistent with previous identification of a smectic B phase in this region for the $\kappa = 3$ fluid.

For elongations $\kappa = 3.2$–3.8, the behaviour of $g_\perp(r_\perp)$ above the nematic-smectic transition remains liquid-like, without the features described above. This leads us to identify the phase as a smectic A, (S_A), with essentially 2-dimensional liquids within the layers. No stable S_A phase has been identified for the $\kappa = 3$ fluid in this or earlier work [1].

In all cases, the smectic layers form perpendicular to the director, which remains approximately along the main diagonal of the simulation cell. These fluids go on to exhibit a third transition at higher densities. In some cases, the transition can be identified from

[1] Indications of a *metastable* S_A phase for $\kappa = 3$ are reported in [1] at $T = 0.80$ for $0.30 < \rho < 0.34$; only after extensive simulation, ($\sim 6 \times 10^4$ timesteps), did configurations at these state points reach the stable S_B phase.

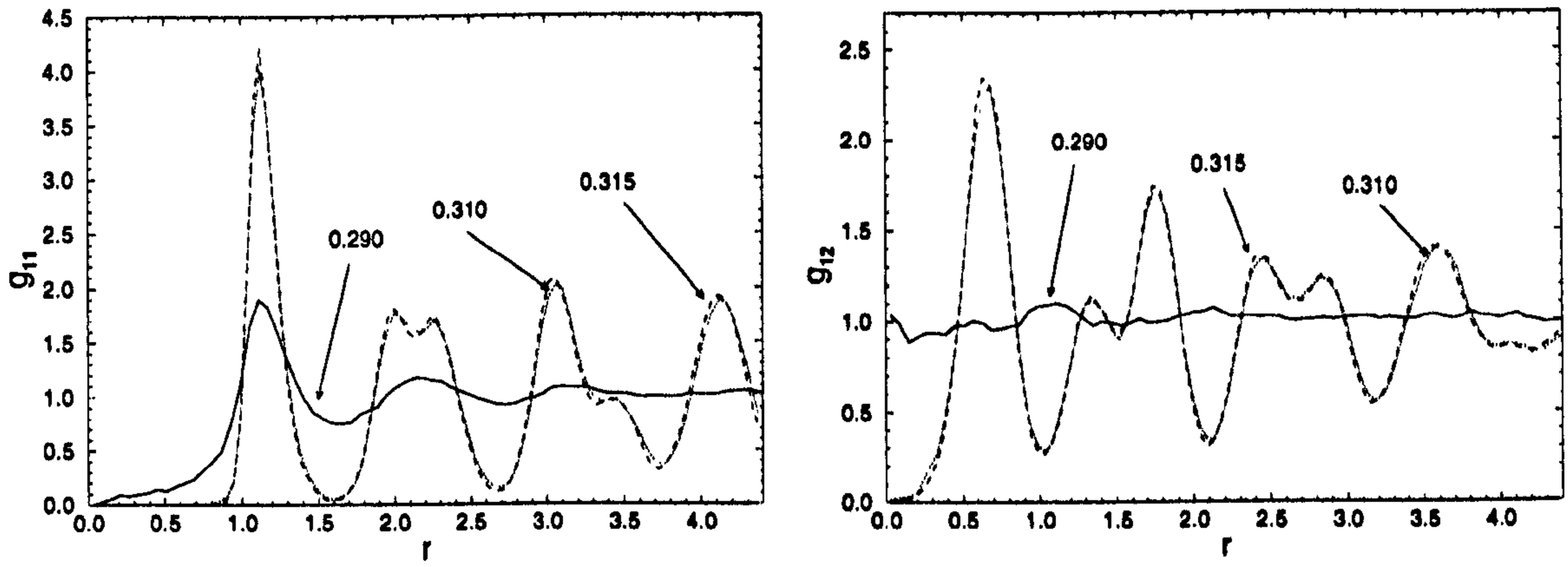

Figure 3.15: (a) In-layer pair distribution function, $g_{11}(r_\perp)$ and (b) between-layer pair distribution function, $g_{12}(r_\perp)$ for GB fluid with $\kappa' = 5$ and $\kappa = 3.4$ at different number densities, (labelled on the plot), along the isotherm $T = 1.00$.

a discontinuity in pressure, but in all cases it is indicated by the behaviour of $g_{11}(r_\perp)$, which clearly shows the onset of additional positional ordering at higher densities, as seen for $\kappa = 3$. This is indicated in Fig. 3.15 for the $\kappa = 3.4$ fluid. The density at this transition is reduced as elongation is increased. The distinction between the hexatic S_B phase and the crystal B is not easy to make in simulation due to the smallness of the systems [1, 32]. For convenience, this will be labelled S_B; the nature of this phase is addressed further in §3.7.

For the case $\kappa = 4$, no clear I–N transition could be identified with $N = 256$, (see Fig. 3.11), despite performing long runs, (of order 2–3 $\times 10^5$ timesteps), in this region. The transition densities quoted below are therefore very tentative. At $\rho = 0.185$, the order parameter takes a value $S = 0.375 \pm 0.006$, which is significantly non-zero even with this system size, but no clear I–N transition is indicated by the equation of state before smectic ordering appears at $\rho \geq 0.190$, when the system exhibits a S_A phase. At still higher densities there is a transition to the S_B. Bearing in mind that the nematic density range displayed by systems of this size is quite narrow for $\kappa \leq 3.8$, this suggests that an I–N–S triple point exists close by, and that the N phase will be absent for elongations

significantly greater than $\kappa = 4$ at this temperature. As a further investigation, we performed simulations on a system of $N = 400$ particles in a cuboidal simulation cell, (non-cubic). The initial configuration was a smectic for which the box aspect ratio was allowed to relax, using MC at a constant pressure (see §3.4.1). The system was then equilibrated at a fixed density of $\rho = 0.200$ using MD, and the density slowly reduced. The S_A phase persisted at $\rho = 0.200$ over 1.5×10^5 timesteps, but at $\rho = 0.190$ the modulation of $g_{||}(r_{||})$ was very weak. Nematic values of order parameter were measured at $\rho = 0.190$ and 0.185, where $S = 0.418 \pm 0.003$. Orientational order was lost at $\rho = 0.180$, where $S = 0.129 \pm 0.003$. These results are indicated in Fig. 3.11. Increasing the system size indicates that a stable nematic phase may indeed exist for this fluid, but that it occupies a very narrow density range.

Combining information from the equations of state, orientational order parameter and the positional distribution functions, approximate transition densities for the system of $N = 256$ particles in a fixed, cubic box are obtained; these are reported in Table 3.1, where they are compared with results obtained using MC simulations. It should be emphasized that in all cases these pairs of values indicate only the approximate coexistence range: the thermodynamic coexistence conditions have not been solved.

3.3.3 MD results at low temperature, $T = 0.45$

Now we turn to the $T = 0.45$ isotherm, recalling that for $\kappa = 3$, this lies well below the stability limit of the N phase, but traverses the liquid-vapour region at sufficiently low densities and shows smectic ordering at high density. The initial configuration for each value of κ was a f.c.c. lattice at $\rho = 0.20$. The $\kappa = 3$ fluid rapidly equilibrated to lose positional and orientational order; at elongations $\kappa \geq 3.4$, this density results in an ordered phase. Other densities were obtained by slow expansion or compression. The system contained $N = 256$ molecules, except in the case $\kappa = 4$, where an $N = 500$ particle lattice was used to allow the simulation of high densities. Elongations $\kappa = 3.0, 3.2, 3.4, 3.6$ and 4.0 were studied giving the equations of state shown in Figs. 3.16–3.20. The corresponding orientational order parameters are also shown. The results of the I–S_B transition densities for the $\kappa = 3$ fluid are consistent with those of [1]. Revised data for the liquid-vapour coexistence curve of this fluid have recently been presented [2]; from these, the expected

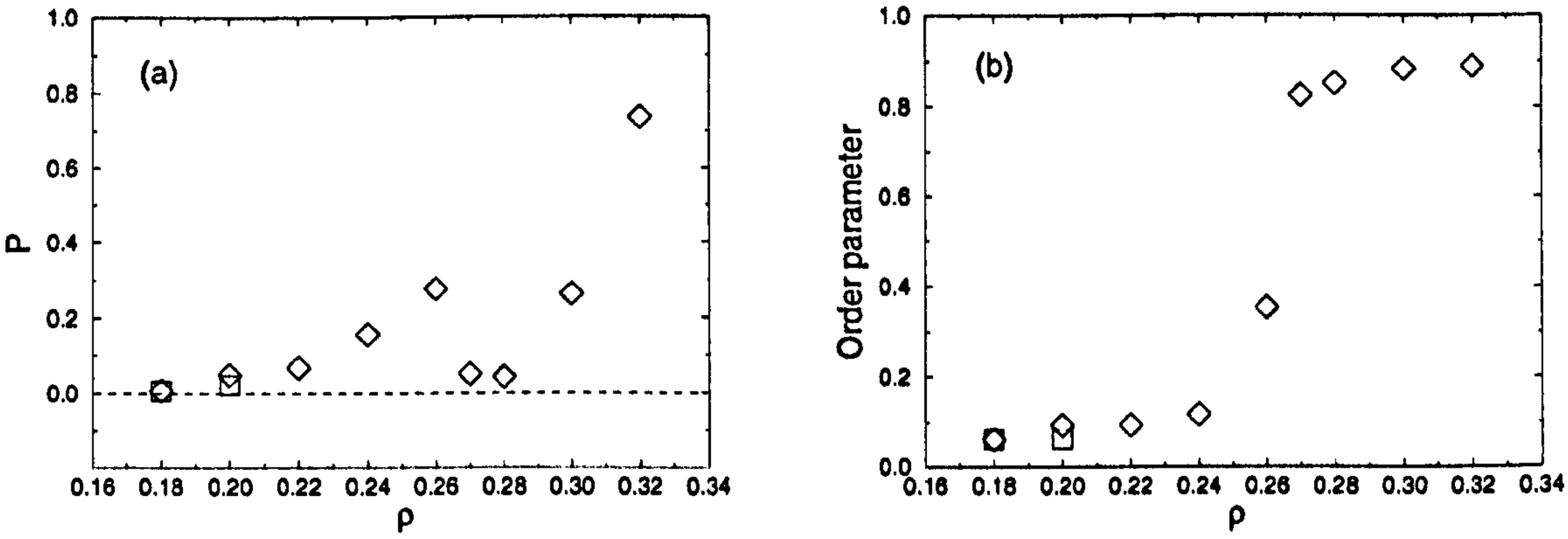

Figure 3.16: (a) Equation of state of the GB fluid with $\kappa' = 5$ and $\kappa = 3.0$ along the isotherm $T = 0.45$ as obtained from MD simulation. (b) Corresponding values of orientational order parameter. Diamonds indicate results obtained with $N = 256$; squares indicate results with $N = 500$.

density for the coexisting liquid at $T = 0.45$ is $\rho = 0.179 \pm 0.006$. As can be seen, we have not simulated below this density.

The equation of state for the $\kappa = 3.2$ fluid at this temperature indicates an I-S_B transition at a significantly lower density than for $\kappa = 3$. The lowest density simulated here, $\rho = 0.20$, seems to lie outside the liquid-vapour coexistence region, i.e. the smectic melts to an isotropic liquid at this temperature. Increasing the system size to $N = 500$ at $\rho = 0.20$ gave no change in the measured pressure. The approximate transition densities for $\kappa = 3.2$ are $(\rho_I, \rho_{S_B}) = (0.220, 0.260)$, with smectic layers clearly developed at $\rho = 0.23$. Between these densities, negative pressures indicate instability; it is likely that these points lie in the two-phase coexistence region. For the $\kappa = 3.4$ fluid, there is a wide range of negative pressures (and some irregular behaviour), but the lowest density studied, $\rho = 0.150$, does yield an isotropic liquid. At the highest density MD simulation, $\rho = 0.240$, the system is apparently still within the coexistence region, and clearly a S_B phase. A similar situation is seen for $\kappa = 3.6$–4.0. The coexistence density of the smectic phase falls consistently with increasing elongation, and by $\kappa = 4$ the suggested coexistence fluid density is quite low, $\rho < 0.08$. This suggests that the smectic sublimes to a vapour at

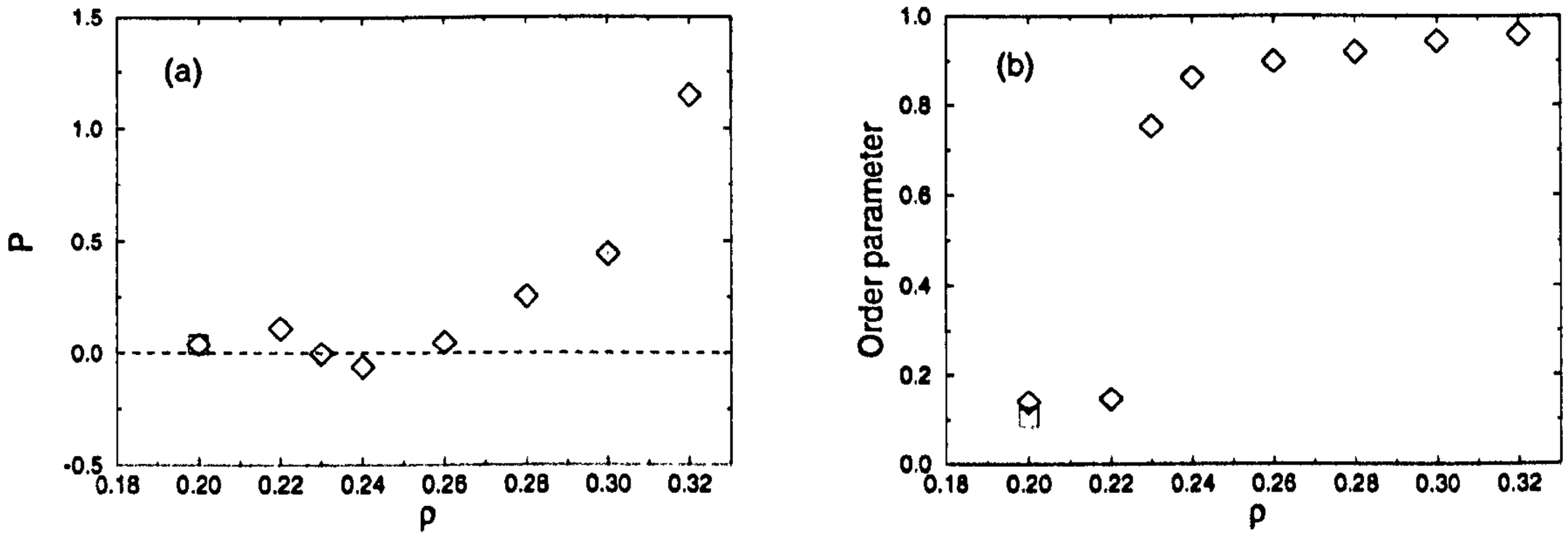

Figure 3.17: As Fig. 3.16 for $\kappa = 3.2$.

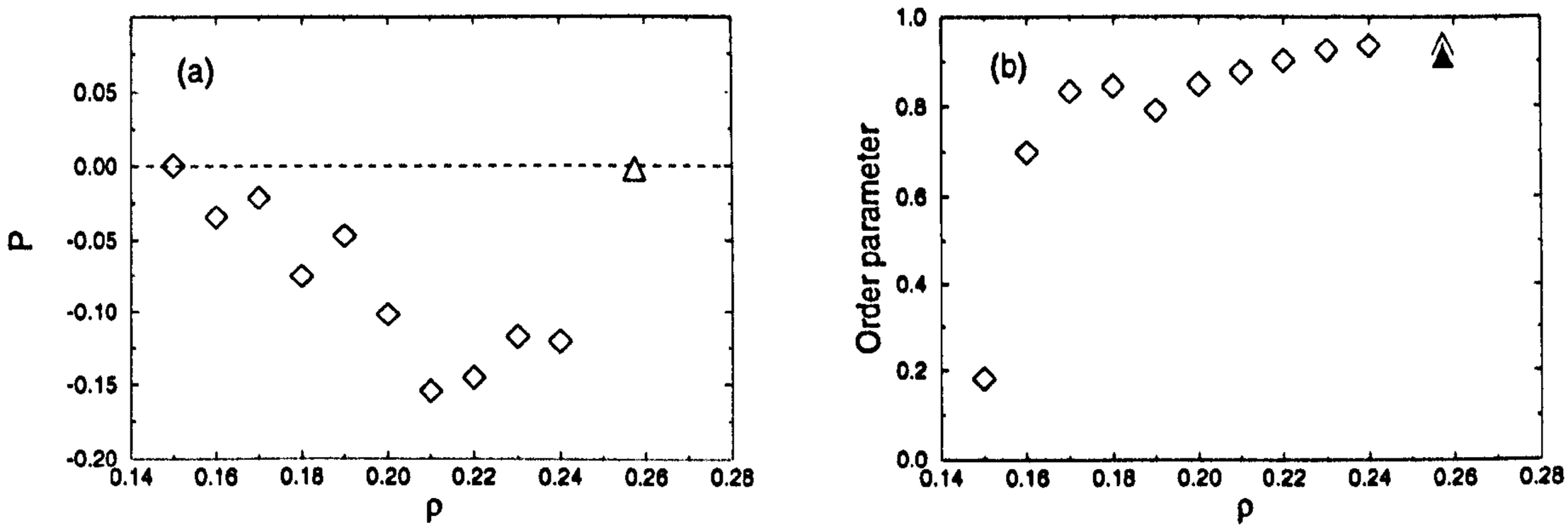

Figure 3.18: (a) Equation of state of the GB fluid with $\kappa' = 5$ and $\kappa = 3.4$ along the isotherm $T = 0.45$ as obtained from MD simulation. (b) Corresponding values of orientational order parameter. Triangles indicate data obtained from MC simulation, and filled symbols indicate values of the smectic order parameter.

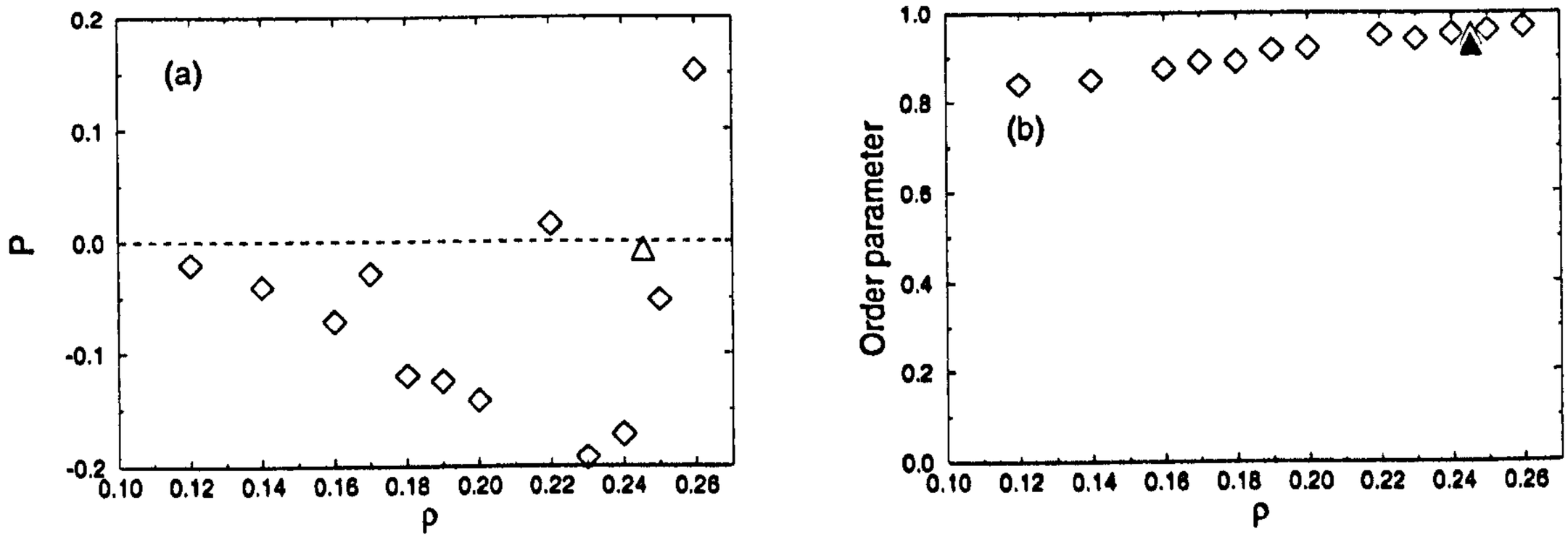

Figure 3.19: As Fig. 3.18 for $\kappa = 3.6$.

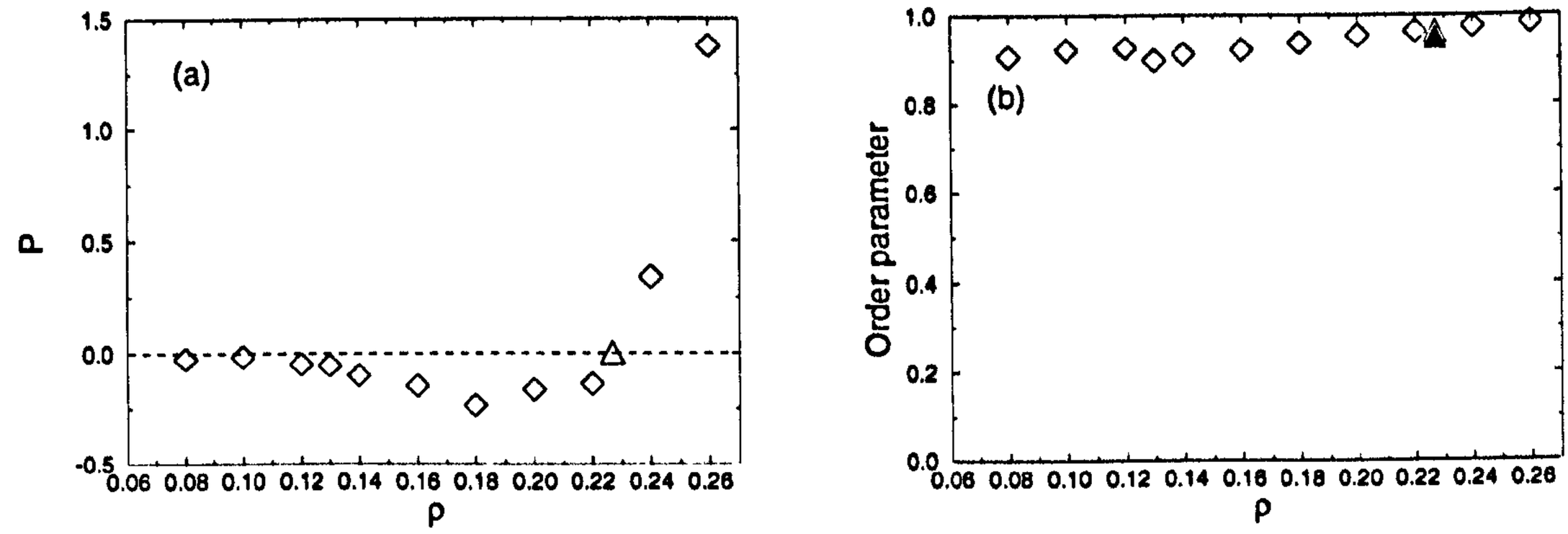

Figure 3.20: As Fig. 3.18 for $\kappa = 4.0$.

this temperature, i.e. the $T = 0.45$ isotherm lies below the vapour-isotropic-smectic triple point, (assuming the existence of a critical point at this elongation).

Bearing in mind the possible effects of finite system size and box shape on the stability of a smectic, we further investigated the cases for which $\kappa \geq 3.4$, using MC NPT simulations with variable box shape, (see §3.4.1). Starting with a smectic configuration of $N = 400$ particles, layers aligned with the box axes, the systems were simulated at $P = 0$ and in all cases the configuration quickly relaxed to a well-ordered smectic phase. Over 5×10^4 MC sweeps, the systems maintained steady orientational order parameter values of $S = 0.939 \pm 0.01$ for $\kappa = 3.4$ at an equilibrium density of $\rho = 0.2569 \pm 0.0002$, $S = 0.951 \pm 0.001$ for $\kappa = 3.6$ at $\rho = 0.2461 \pm 0.0003$, and $S = 0.964 \pm 0.001$ for $\kappa = 4$ at $\rho = 0.2262 \pm 0.0002$. These results are indicated in Figs. 3.18 – 3.20.

Certain isotherms with $0.45 < T < 1.00$ were also studied using NVT MD with $N = 256$, to give an indication of triple-point locations. The results of such runs for the $\kappa = 3.2$ and $\kappa = 3.4$ fluids are included in §3.8.

3.4 MC simulations

3.4.1 Simulation Details

The MD runs described above indicate the presence of positionally ordered phases. It should be borne in mind that periodic boundary effects may have a strong influence on these phases. Since flexibility in the box shape and dimensions can be included more readily in MC than MD, MC simulations were employed in further investigations.

NPT MC simulations were performed in cycles, each consisting of N attempted particle displacement/orientation moves and one attempt to change the box volume. The maximum positional and angular displacements were adjusted to keep the acceptance rate for the combined move close to 50%. Volume moves were attempted by sampling the box sides L_x, L_y, L_z, independently, (§2.1), thus allowing the aspect ratio of the box to vary, (although the box sides were constrained to be mutually orthogonal throughout). Whilst this should have little effect in positionally disordered phases, equilibration of the box shape may have a significant effect on the stability of the smectic phase. In a trial volume move, one of the box axes was chosen at random, and a variation chosen uniformly for the

logarithm of this dimension, $\ln L_i$, since this has been seen to promote efficient equilibration [49]. Again, the maximum variation was adjusted so that about 50% of moves were accepted, typically resulting in a maximum length variation of around 1%.

Where started from scratch, MC simulations were initiated from smectic configurations with layers perpendicular to the z-axis, but with particles positioned at random in the xy-plane, and with the molecular orientations aligned with z. Such configurations contained $N = 600$ particles arranged in 6 layers, and were used to start simulations at various pressures in the nematic and smectic regions for $3 \leq \kappa \leq 4$. Typically, $6 - 10 \times 10^4$ cycles were performed for each state point, increasing to $1 - 3 \times 10^5$ cycles in the vicinity of phase transitions. Some runs, indicated below, were significantly longer than this. Several isotherms were considered for each elongation used in the MD investigations, starting with $T = 1.00$ for comparison with the MD results. The initial layered configuration was allowed to equilibrate at the chosen starting pressure, and from here steps were taken up and/or down in pressure, as appropriate. Where the initial configuration melted to a positionally disordered phase, an initial layered configuration was also used at a higher pressure, in order to study systems with layers perpendicular to z. Starting configurations at other temperatures were taken from the most ordered region of a neighbouring isotherm.

3.4.2 MC results at $T = 1.00$

The results of these runs are indicated in Figs. 3.21–3.26. Considering first the case $\kappa = 3$, the phases seen at the chosen pressures are as expected, although the measured density at given pressure in the S_B phase is somewhat higher than that obtained with MD. Although the system size effect must be borne in mind, addition of the box aspect ratio to the degrees of freedom may be a more significant factor in this density shift, as discussed below.

At the higher elongations, $\kappa \geq 3.6$, the phase behaviour is also in broad agreement with that obtained using MD. Again, the phases can be clearly distinguished by examining order parameter values and distribution functions. In Fig. 3.27, $g_{11}(r_\perp)$ and $g_{12}(r_\perp)$ are shown for the S_A and S_B phases of the $\kappa = 3.6$ fluid, as an example. The correlation between next nearest neighbours can be seen in the S_B phase here, although at this state point it is not as distinct as in Fig. 3.15. There is some hysteresis around the phase transitions for these

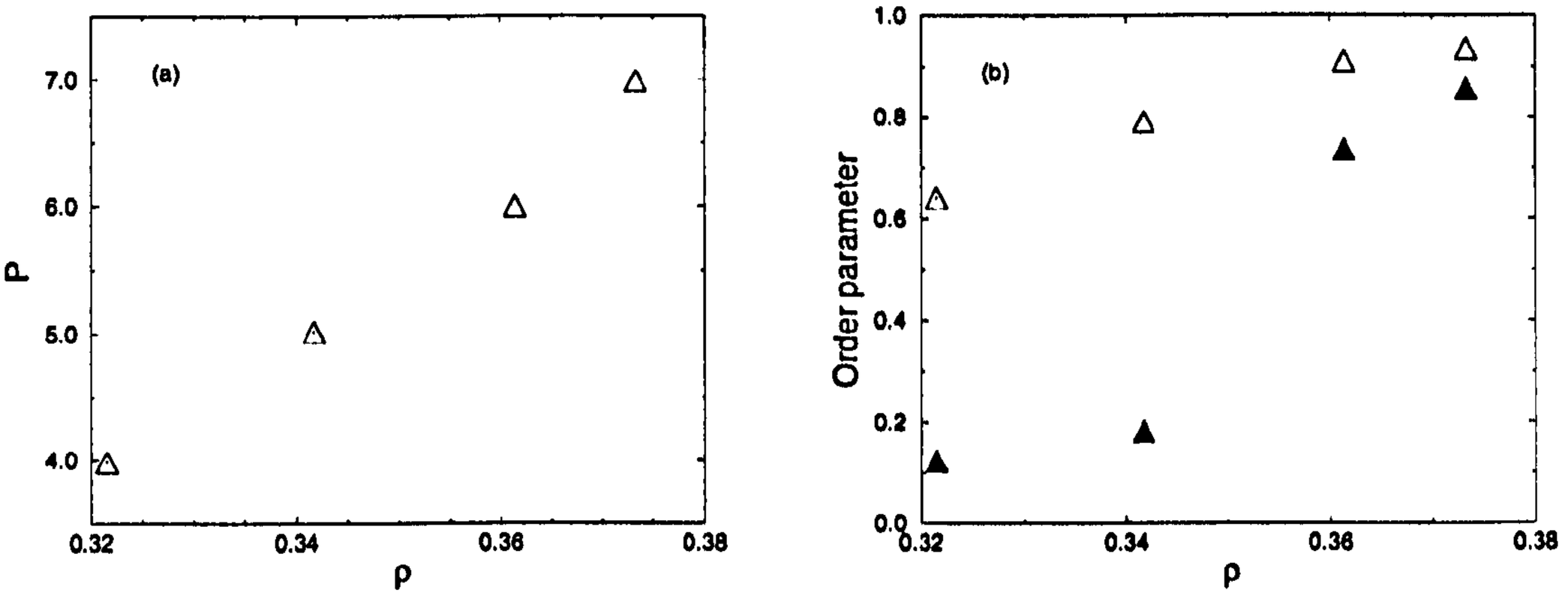

Figure 3.21: (a) Equation of state of the GB fluid with $\kappa' = 5$ and $\kappa = 3.0$ along the isotherm $T = 1.00$ as obtained from MC simulation. (b) Corresponding values of orientational, (open symbols), and smectic (filled symbols), order parameters.

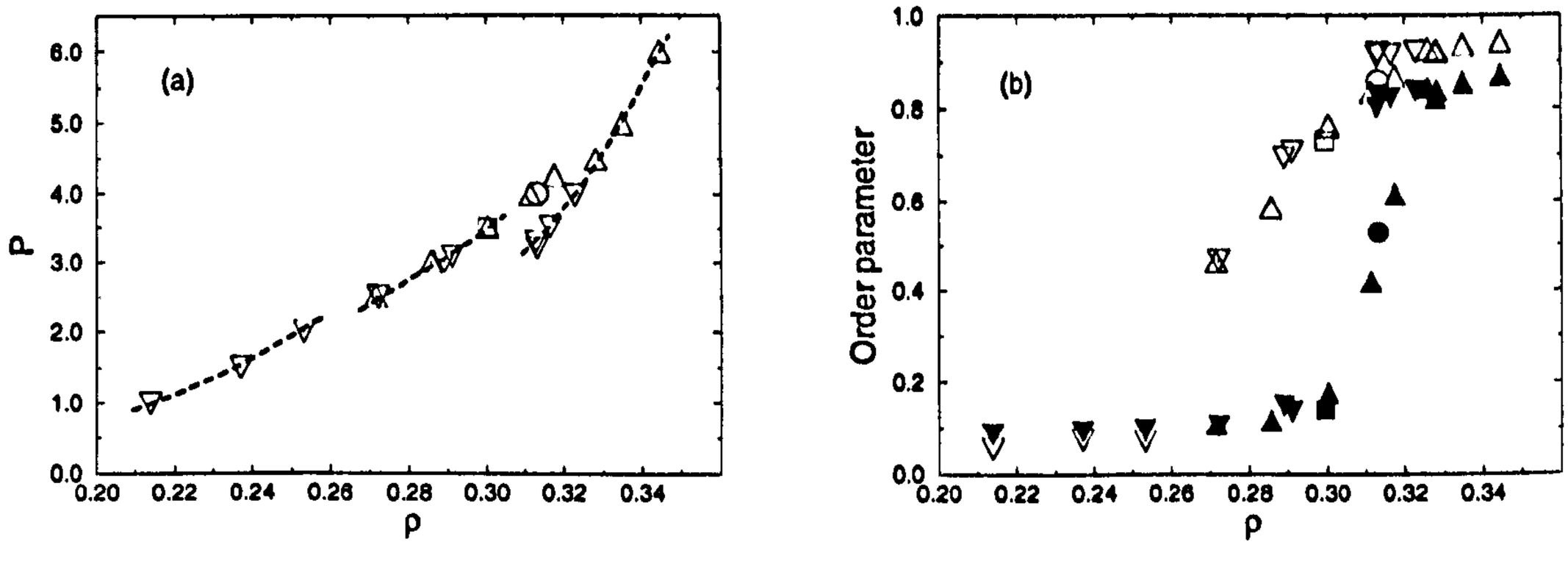

Figure 3.22: As Fig. 3.21 for $\kappa = 3.2$. The increasing pressure series is indicated by up-triangles, and decreasing pressure by down-triangles. Squares and circles indicate isolated simulations using independent starting configurations, (see text for details). Lines are drawn to guide the eye, indicating the distinct phase regions.

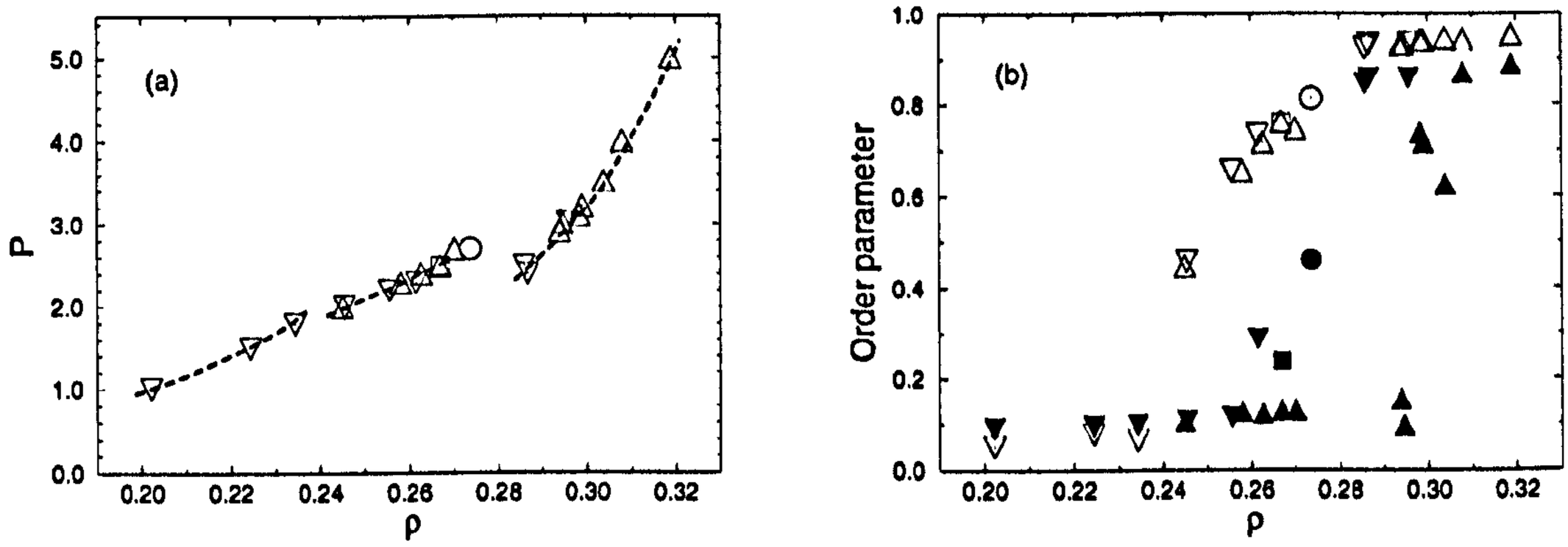

Figure 3.23: As Fig. 3.22 for $\kappa = 3.4$.

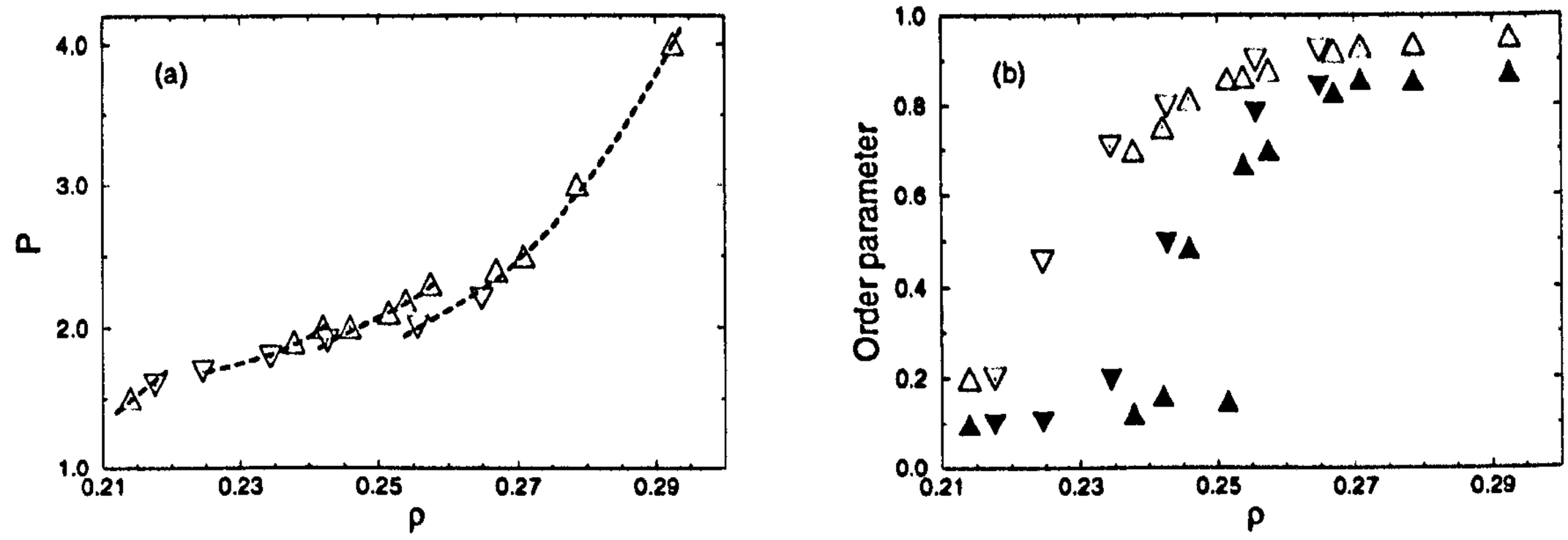

Figure 3.24: As Fig. 3.22 for $\kappa = 3.6$.

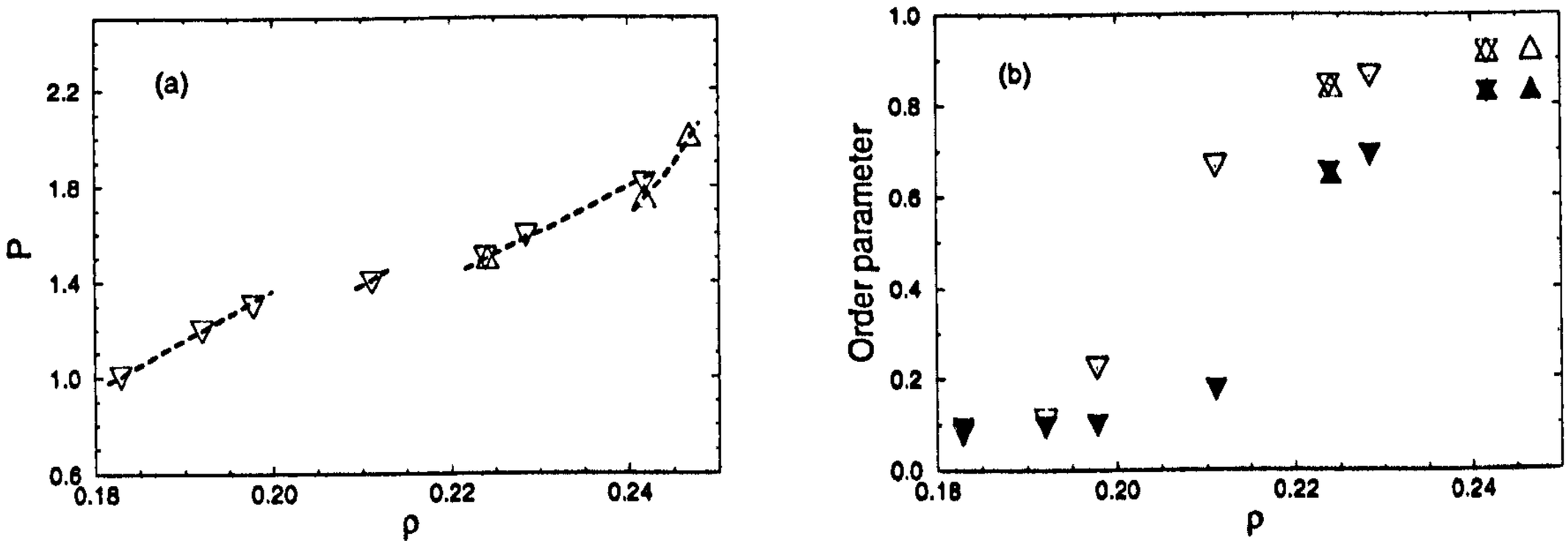

Figure 3.25: As Fig. 3.22 for $\kappa = 3.8$.

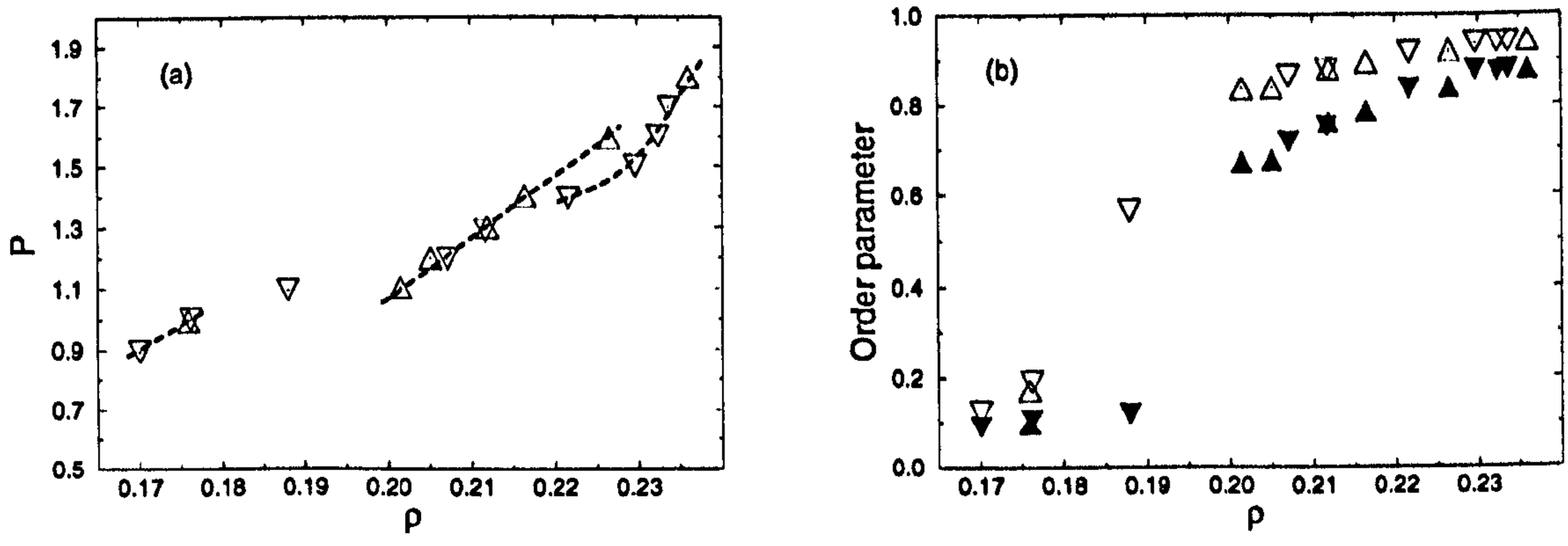

Figure 3.26: As Fig. 3.22 for $\kappa = 4.0$.

systems, but the S_A phase is identified for both increasing and decreasing pressure series. For these elongations, the transition pressures are lower than the corresponding MD values or, where hysteresis effects have been investigated, bracket them. As at $\kappa = 3$, the smectic phases have a slightly higher density for a given pressure in the MC simulations. At $\kappa = 4$ there is difficulty in isolating the nematic phase, as with MD; the phase appears only in the decreasing-pressure branch of the hysteresis loop.

For $\kappa = 3.2$ and 3.4, much weaker indications of the S_A phase are found with MC than MD. On increasing the pressure from the nematic phase, the $\kappa = 3.2$ fluid indicates a rather narrow S_A range, ($0.310 \leq \rho \leq 0.315$), and the $\kappa = 3.4$ fluid gives none. On decreasing the pressure from the S_B region, neither fluid shows a S_A phase, both undergoing a S_B–N transition. At the lowest pressure on this path for which the S_B persisted, the simulation was extended, and for both elongations the structure showed no signs of melting after 9×10^5 sweeps. In both cases, new, layered starting configurations were introduced at pressures in the hysteresis region . After long runs of $5 - 6 \times 10^5$ sweeps, these conformed to the nematic region of the increasing-pressure branch or showed a S_A phase, as indicated in Figs. 3.22 and 3.23.

Approximate transition densities at $T = 1.0$ for $N = 600$ using NPT MC with a cuboidal box of variable aspect ratio, obtained from the equations of state, order parameters and positional distribution functions, are shown in Table 3.1, along with the values obtained from MD simulations, (§3.3.2). Again, the approximate nature of these results is emphasized: the thermodynamic coexistence conditions have not been solved. Furthermore, in some cases the discontinuity in density indicated is as much a reflection of the number of state points it has been possible to study as of the strength of transition.

The results imply that the system used for MD enhances the stability of the S_A phase at lower elongations, or conversely, frustrates S_B formation. Having satisfied the periodic image constraint on the layer spacing, (3.1), there is little freedom to satisfy any similar conditions for the in-plane structure, and the image-interactions, complicated by the orientation of the smectic layers with respect to the box axes, will have a large influence in the smaller systems. Indications of the S_A in the low κ MC results were obscured by hysteresis effects, particularly significant with smectic phases. On balance, the ease of moves allowing equilibration of in-plane order lends more credence to the MC approach.

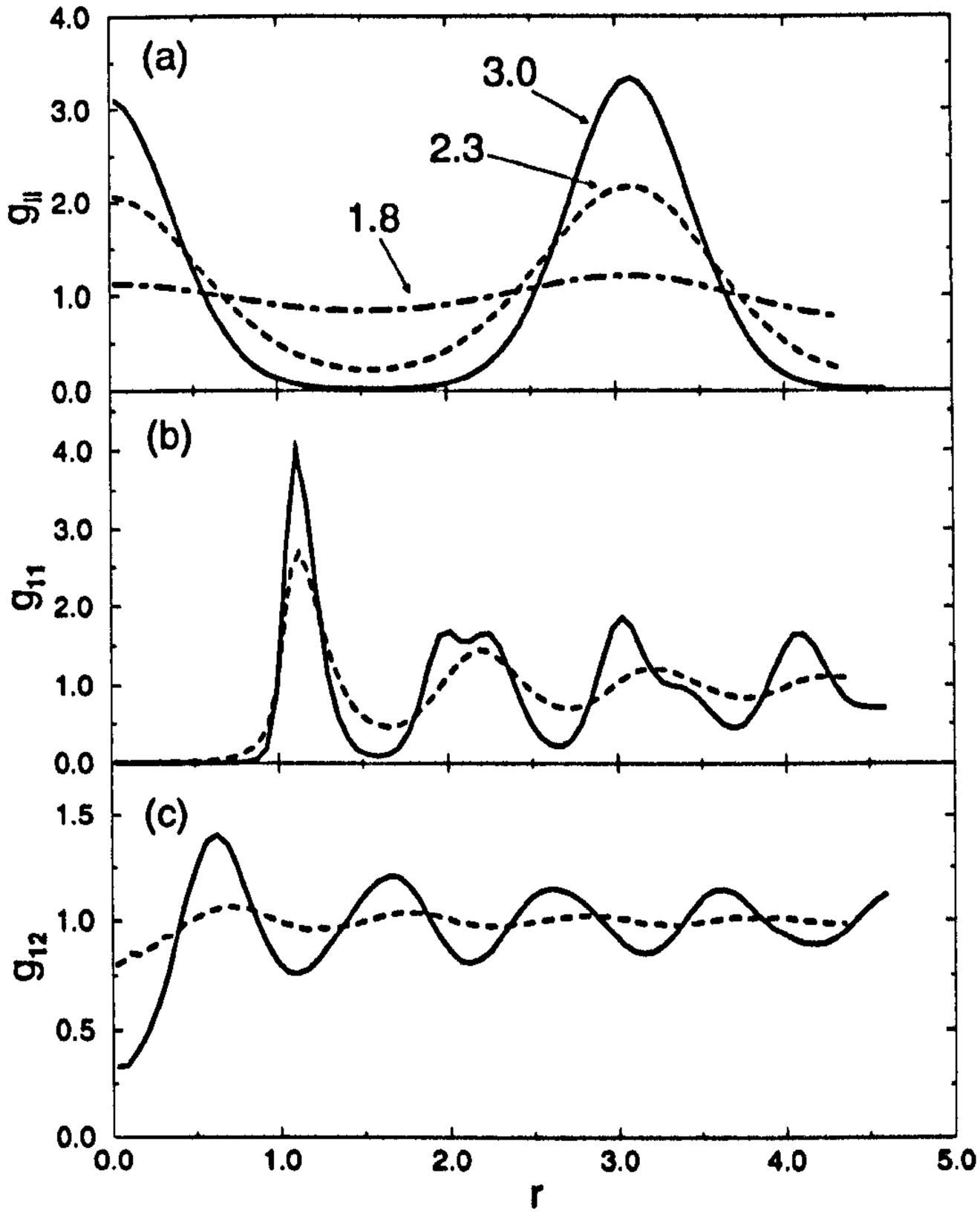

Figure 3.27: Pair distribution functions for the GB fluid with $\kappa' = 5$ and $\kappa = 3.6$ at different pressures, (labelled on the plot), along the isotherm $T = 1.00$: (a) $g_{||}(r_{||})$ in the N (dot-dashed line), S_A (dashed line) and S_B (solid line) phases, (b) $g_{11}(r_\perp)$ and (c) $g_{12}(r_\perp)$ in the S_A and S_B phases.

κ	(ρ_I, ρ_N)	(ρ_I, ρ_{S_A})	(ρ_N, ρ_{S_A})	(ρ_N, ρ_{S_B})	(ρ_{S_A}, ρ_{S_B})
3.0	(0.300, 0.310)			(0.350, 0.370)	
3.2	(0.270, 0.275)		(0.300, 0.305)		(0.320, 0.330)
	(0.253, 0.272)			(0.291, 0.313)	
3.4	(0.230, 0.240)		(0.260, 0.270)		(0.290, 0.310)
	(0.234, 0.245)			(0.266, 0.290)	
3.6	(0.225, 0.230)		(0.240, 0.245)		(0.250, 0.270)
	(0.218, 0.225)		(0.240, 0.243)		(0.256, 0.265)
3.8	(0.200, 0.205)		(0.215, 0.220)		(0.230, 0.250)
	(0.198, 0.211)		(0.211, 0.224)		(0.242, 0.247)
4.0	(0.175, 0.185)		(0.185, 0.200)		(0.220, 0.240)
	(0.176, 0.189)‡	(0.178, 0.202)†	(0.189, 0.207)‡		(0.224, 0.233)

Table 3.1: Approximate transition densities for GB fluids with $3 \leq \kappa \leq 4$ at $T = 1.00$. In each case the upper line gives MD results and the lower line MC results. Results marked † and ‡ are obtained for increasing and decreasing pressure respectively.

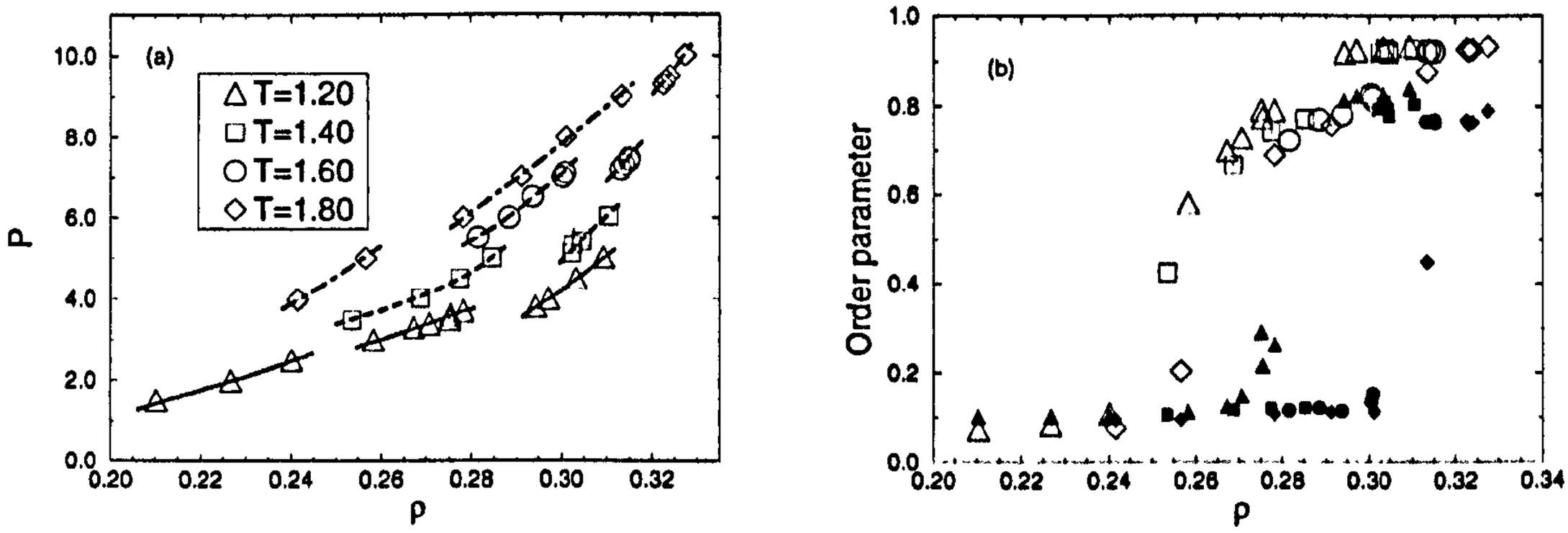

Figure 3.28: (a) Equation of state of the GB fluid with $\kappa' = 5$ and $\kappa = 3.4$ along the isotherms indicated in the figure, as obtained from MC simulation. (b) Corresponding values of orientational, (open symbols), and smectic (filled symbols), order parameters. Lines are drawn to guide the eye, indicating the distinct phase regions.

3.4.3 MC results at $T \neq 1.00$

Isotherms above and below $T = 1.00$ were considered for $N = 600$ systems, with particular interest in the range of the S_A regions at various elongations, beginning at $\kappa = 3.4$. These sets of isotherms are shown in Figs. 3.28–3.31. For the $\kappa = 3.4$ fluid, no S_A phase is observed at these temperatures, and the discontinuity at the N–S_B transition is narrowing as the temperature increases.

At higher elongations it can be seen that the range of the S_A phase is increasing in both directions as the elongation is increased, but that it remains bounded below *and above* in temperature. As the temperature is raised, the significance of the attractive interactions is reduced until, at sufficiently high temperature[2], the particles may be regarded as interacting only through their repulsive cores. These are approximately ellipsoidal, and it is known that in the hard ellipsoid limit, only I, N and crystalline solid phases are displayed. This sheds light on the upper bound on the S_A, but raises questions about the nature of the phase here labelled S_B; these are discussed in §3.7 below.

[2]At $T^* = kT/\epsilon_0 = 2.0$, thermal energies are comparable with the side-by-side well depth for parallel molecules: for $\kappa = 4$, $\epsilon_{ss}/\epsilon_0 = 2.125$.

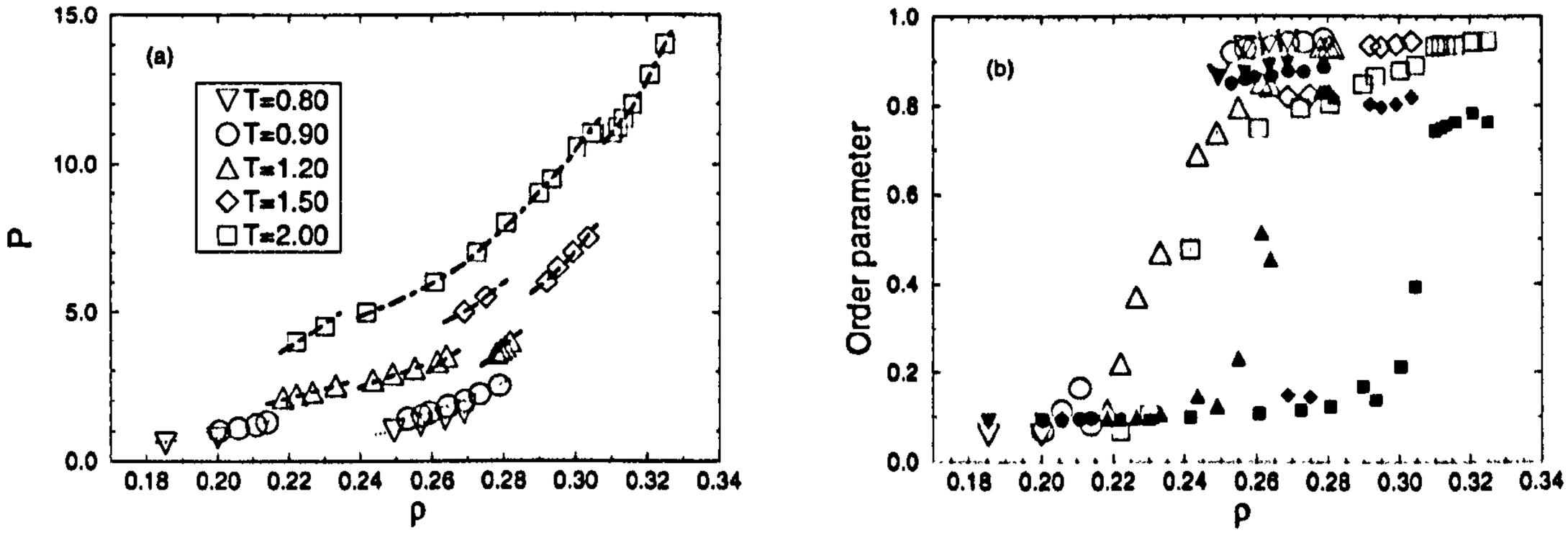

Figure 3.29: As Fig. 3.28 for $\kappa = 3.6$.

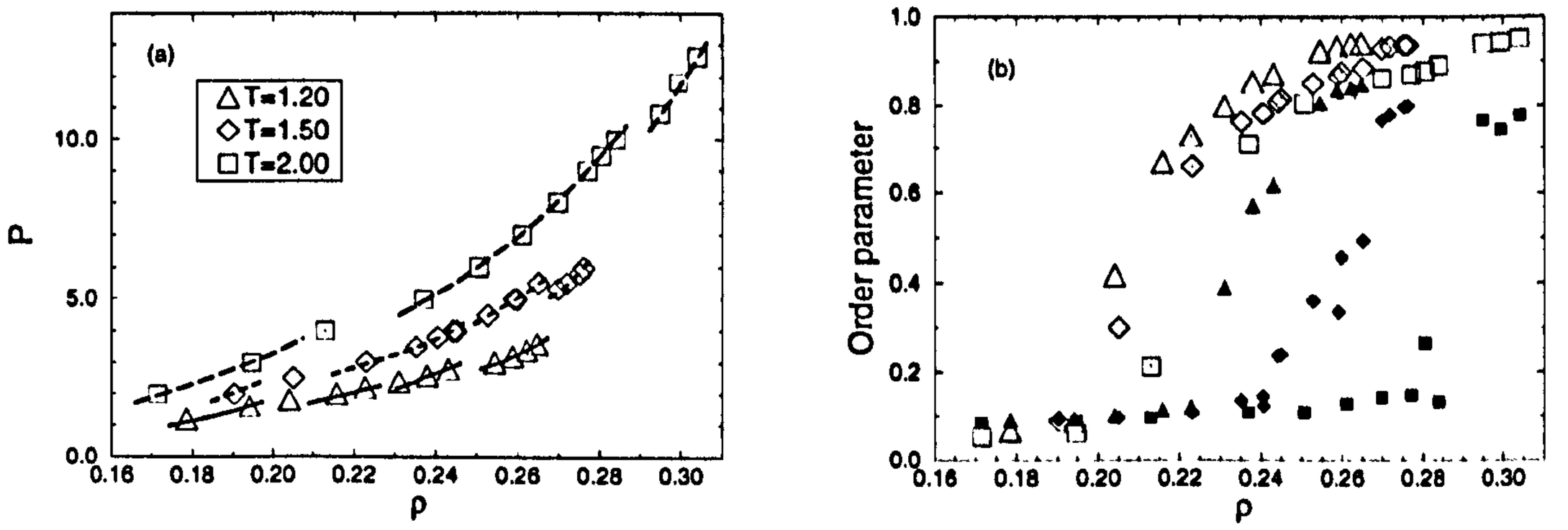

Figure 3.30: As Fig. 3.28 for $\kappa = 3.8$.

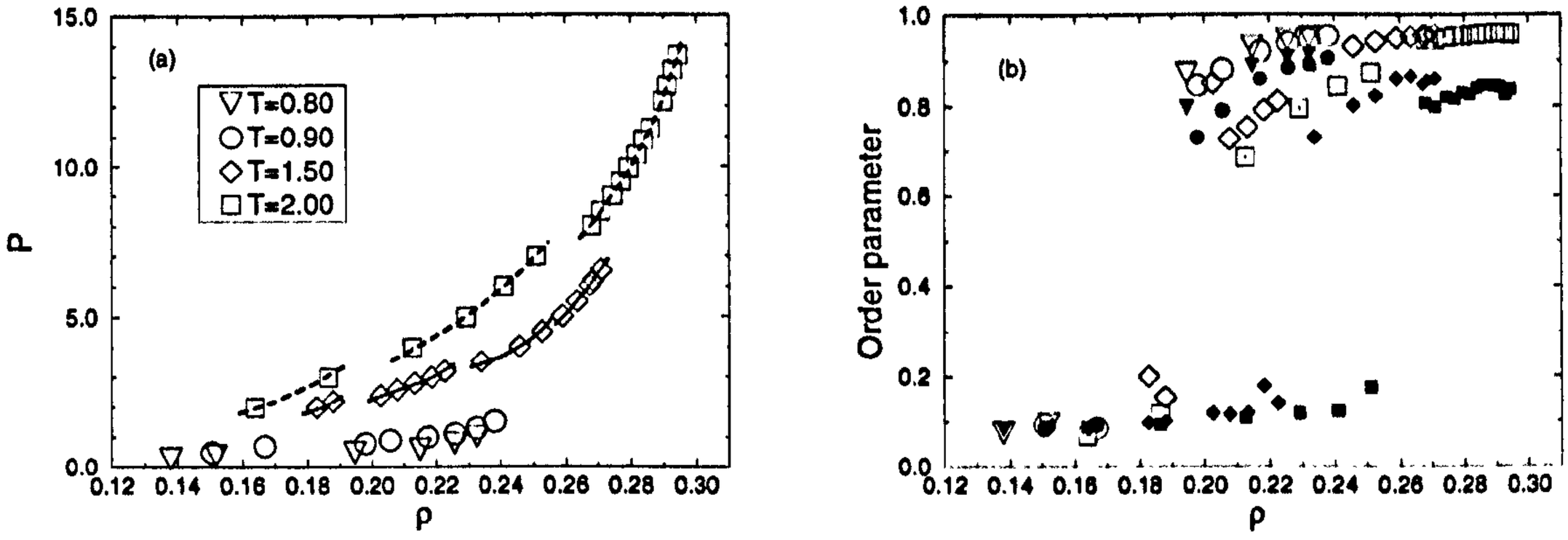

Figure 3.31: As Fig. 3.28 for $\kappa = 4.0$.

For $\kappa = 4$, isotherms at $T < 1.0$ indicate a S_A phase but no N, so that this appears at an I–N–S_A triple point. The competition between the N and S_A phases is harder to resolve at lower elongations, with neither phase observed at $T = 0.90$ for $\kappa = 3.6$.

3.5 Liquid-vapour region

The MD results at $T = 0.45$ indicate coexistence between an isotropic fluid and the S_B phase, with the coexistence density of the isotropic fluid falling as elongation is increased. This is expected, since the temperature is below the nematic (and S_A) triple point. With the fluid tending to vapour densities at the highest elongations, we turn to the behaviour of the critical point. As usual, the GEMC and GD techniques were used to explore the liquid-vapour envelopes, in the first instance.

Using GEMC with a system of $N_1+N_2 = 1000$ particles, liquid-vapour coexistence data for the GB fluid with $\kappa = 3.2$ were obtained. Typically, 1×10^4 MC sweeps were allowed for equilibration, and production averages were measured over a further 1×10^4 sweeps. The initial configurations were taken from $\kappa = 3$ simulations at $T = 0.44$. Moving to this higher elongation, the phases remained separated, and after equilibration, the configurations were used to start heating and cooling sequences of simulations. The vapour branches of the two fluids are almost indistinguishable. Although the liquid density for $\kappa = 3.2$ is $\sim 5\%$

lower than that of the $\kappa = 3$ system at the same temperature, the volume occupied by the particles will be higher by the ratio of the molecular volumes, (i.e. 3.2/3.0). As a result, the rate of successful particle exchanges between phases was lower at $\kappa = 3.2$ for given temperature, making the simulations more expensive. The results are presented in Fig. 3.32; the $\kappa = 3$ curve is shown for comparison. The critical point, as estimated from the law of rectilinear diameters and assuming a critical exponent of 1/3, is indicated on the plot. The estimated values are $T_c = 0.47 \pm 0.04, \rho_c = 0.10 \pm 0.03$. With these uncertainties the values cannot be distinguished from the $\kappa = 3$ results. Coexistence data at temperatures closer to T_c should reduce the uncertainty, but simulations at $T \geq 0.46$ departed from the coexistence envelope, with both boxes displaying the vapour phase. The lowest temperature used was $T = 0.42$, at which positional ordering in the dense phase could be identified visually, making particle exchange an unreliable mechanism for equalizing chemical potential. The situation was confirmed by GD simulations, starting at $T = 0.44$ from equilibrated GEMC configurations, and reducing the temperature in steps of 0.1, to follow previous state points. The resulting data is also shown in Fig. 3.32. Agreement between the two methods is reasonable. At $T = 0.42$, fluctuations in the orientational order parameter of the dense phase could be seen; at $T = 0.41$ the fluid took on a layered structure with positional order consistent with the S_B phase. Since the I–S_B phase transition is usually rather strong, the results at this temperature cannot be relied upon as the correct coexistence point; they are included to indicate the lower limit on I–V coexistence.

The MD simulations for $\kappa = 3.2$ at $T = 0.45$, (Fig. 3.17), did not extend to sufficiently low densities to compare with these results, but the isotropic phase can now be identified as a (sub-critical) liquid. At $\kappa = 3.4$, the results of Fig. 3.18 indicate an isotropic phase at reasonably high density. Given the change of T_c from $\kappa = 3$ to 3.2, one would expect this to be sub-critical, but even at $T = 0.45$, the liquid phase of GEMC simulations with $\kappa = 3.4$ indicated some smectic ordering, suggesting that this is rather close to the V–I–S_B triple point, (if the critical point has survived). GD integration can be used with κ as the independent integration variable. Initial investigations with this scheme were performed by increasing elongation from $\kappa = 3$ at a fixed temperature of $T = 0.44$. Above $\kappa = 3.3$, technical difficulties were encountered, with the system becoming too small for

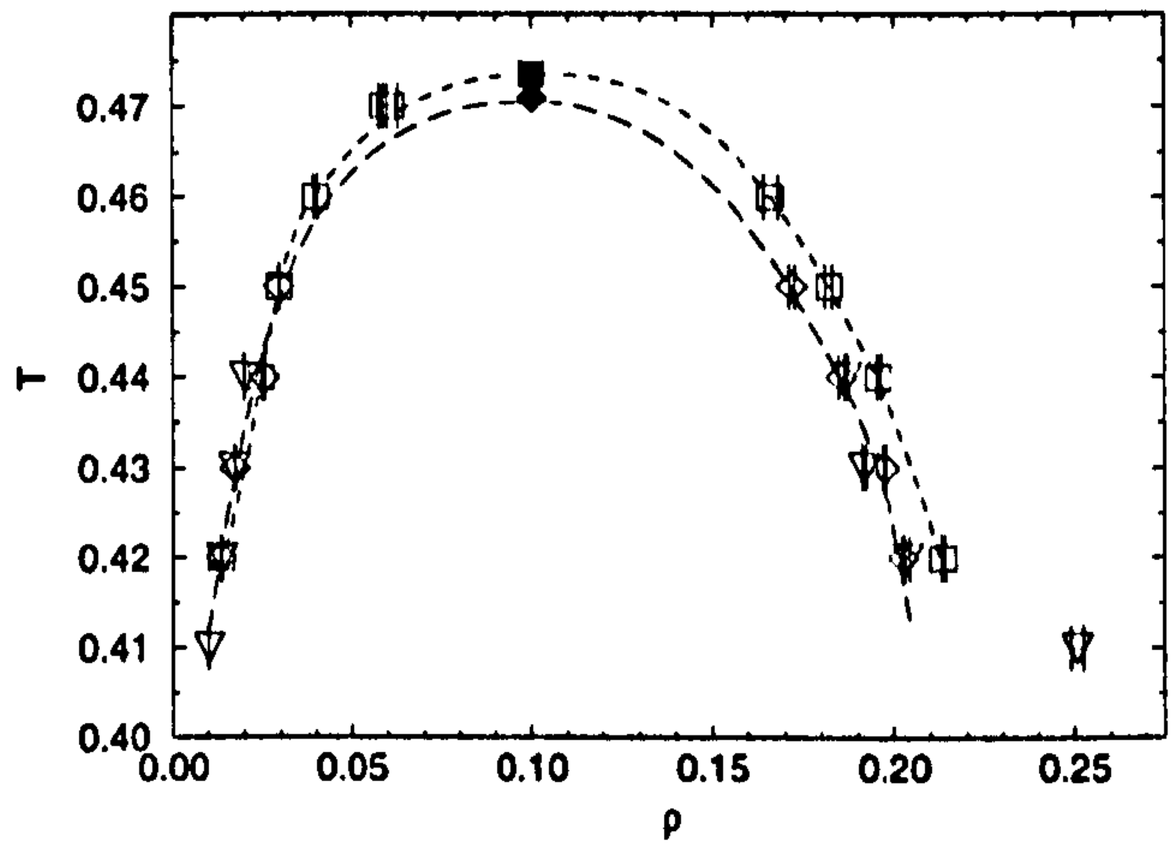

Figure 3.32: The liquid-vapour envelope for the the GB fluid with $\kappa = 3.0$, (squares), and $\kappa = 3.2$, (diamonds), by GEMC. Filled symbols indicate estimates of the critical points. Triangles indicate liquid-vapour coexistence points for the $\kappa = 3.2$ fluid obtained by GD. Lines are to guide the eye.

the potential cut-off. Since long simulations are required in the vicinity of a transition involving positional order, larger systems would make this an expensive proposition, and it was not pursued.

3.6 Phase boundaries

Measuring equations of state indicates the phase behaviour of a system and gives insight into the locations of phase boundaries. Where possible, phase diagram studies are more economical if these boundaries can be traced out directly. Examination of the liquid-vapour envelopes has already been described. GD integration can be applied to any phase boundary, although it can at best be only as reliable as the initial coexistence condition. With this in mind, approximate starting points were taken from equation of state (eos) data for further integration series.

Results above for $\kappa = 3.4$ give no indication of the S_A phase for $T > 1.0$. The N–S_B phase boundary was studied with a starting point inferred from the $T = 1.40$ eos

shown in Fig. 3.28. Systems of $N = 600$ were prepared for both phases at $P = 5.05$ using NPT MC with variable box aspect ratio, from the well-equilibrated systems at neighbouring pressures. Heating and cooling runs followed, using (2.36) and a trapezoid rule predictor-corrector. At each step temperature was changed by $\Delta T = 0.1$, and 5×10^3 equilibration sweeps were allowed at the predicted new pressure. The refinement process typically converged after a further $4\text{–}5\times10^3$ sweeps. The production phase covered 5×10^4 sweeps, completing the procedure. Integration continued to a minimum of $T = 1.0$, at which temperature the coexistence curve was lost, both boxes becoming isotropic fluids. The maximum temperature considered was $T = 2.0$, already above the highest isotherm studied. Results of these simulations are shown in Fig. 3.33, along with approximate N–S_B boundary values from eos runs. Agreement is reasonable, but worsens considerably at the lower temperatures, before final departure from coexistence. The eos bounding values indicate the coexistence curve changes gradient reasonably quickly here. Although the simulations are of reasonable length, it appears that in combination with this step size they are inadequate to accurately trace the N–S_B curve. The slow relaxation of the smectic phase will be an important factor in this. In addition, the approximate nature of the starting point must be remembered, which may be as significant as the integration procedure.

At $\kappa = 3.6$, the S_A region is small, but the S_A–S_B transition is shown clearly at $T = 1.20$, (see Fig. 3.29). Again taking the mid-point of the eos bounding pressure values, the phases were separately equilibrated at $P = 3.55$ for 2×10^4 sweeps before starting separate heating and cooling integration runs. In the light of the N–S_B results, and since now *both* phases have positional order, a smaller temperature step, $\Delta T = 0.05$, and longer runs were used. The initial equilibration covered 1×10^4 sweeps, convergence was achieved in typically $3\text{–}5\times10^3$ sweeps and a further 1×10^5 sweeps were allowed for the production phase. By $T = 1.50$, the curve had passed through the N–S_A–S_B triple point, as expected from eos results, but the S_A–N transition was hard to locate from either the density or order parameters. For decreasing temperatures, the system is expected to encounter the I–S_A–S_B triple point. Recognizing that the S_A–I transition may be sluggish, the production phase for $T \leq 0.90$ was extended to 2×10^5 sweeps. The S_A phase persists to below the expected temperature, indicating hysteresis around the transition or a departure

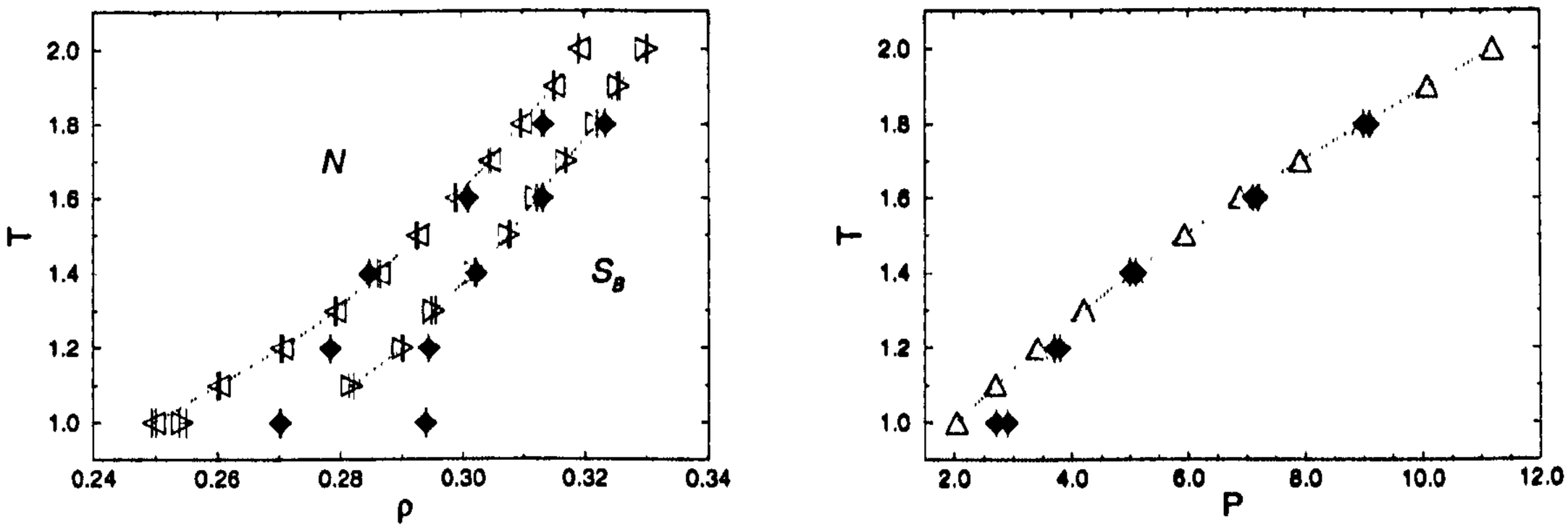

Figure 3.33: N–S_B phase boundary of the GB fluid with $\kappa' = 5$ and $\kappa = 3.4$ as obtained from GD integration, (triangles), with approximate coexistence data from eos simulations, (diamonds). Results are shown in (a) the density-temperature plane (left- and right-pointing triangles indicate N and S_B phases respectively), and (b) the pressure-temperature plane.

from the true coexistence curve. At $T = 0.85$, the smectic order parameter is still high, $s_k = 0.668(4)$ and stable. The full results are indicated in Fig. 3.34.

The difficulties associated with liquid-vapour measurements for the higher elongation fluids suggests that the phase behaviour in the region of the critical point is changing rather rapidly as κ is increased. Results presented thus far indicate that the S_B phase in coexistence with vapour persists to higher temperatures with increasing elongation, but have not been able to show the systematic behaviour of the V–I–S_B triple point. There remains the possiblilty for high κ that this point moves to a temperature $T_{tr} > T_c$, so that there would no longer be a distinct liquid phase and the triple point would collapse to an I–S_B transition. A positionally ordered phase rules out use of the usual GEMC technique. The GD technique remains a possible mechanism for tracing out the coexistence curve, but it is vulnerable to errors in the initial condition. A datum point may be reliably established by free energy calculations or by direct simulation of coexistence.

In the light of the investigations presented in the preceding sections, the uncontrolled behaviour of early inhomogeneous-system investigations, as illustrated in Fig. 3.2, can

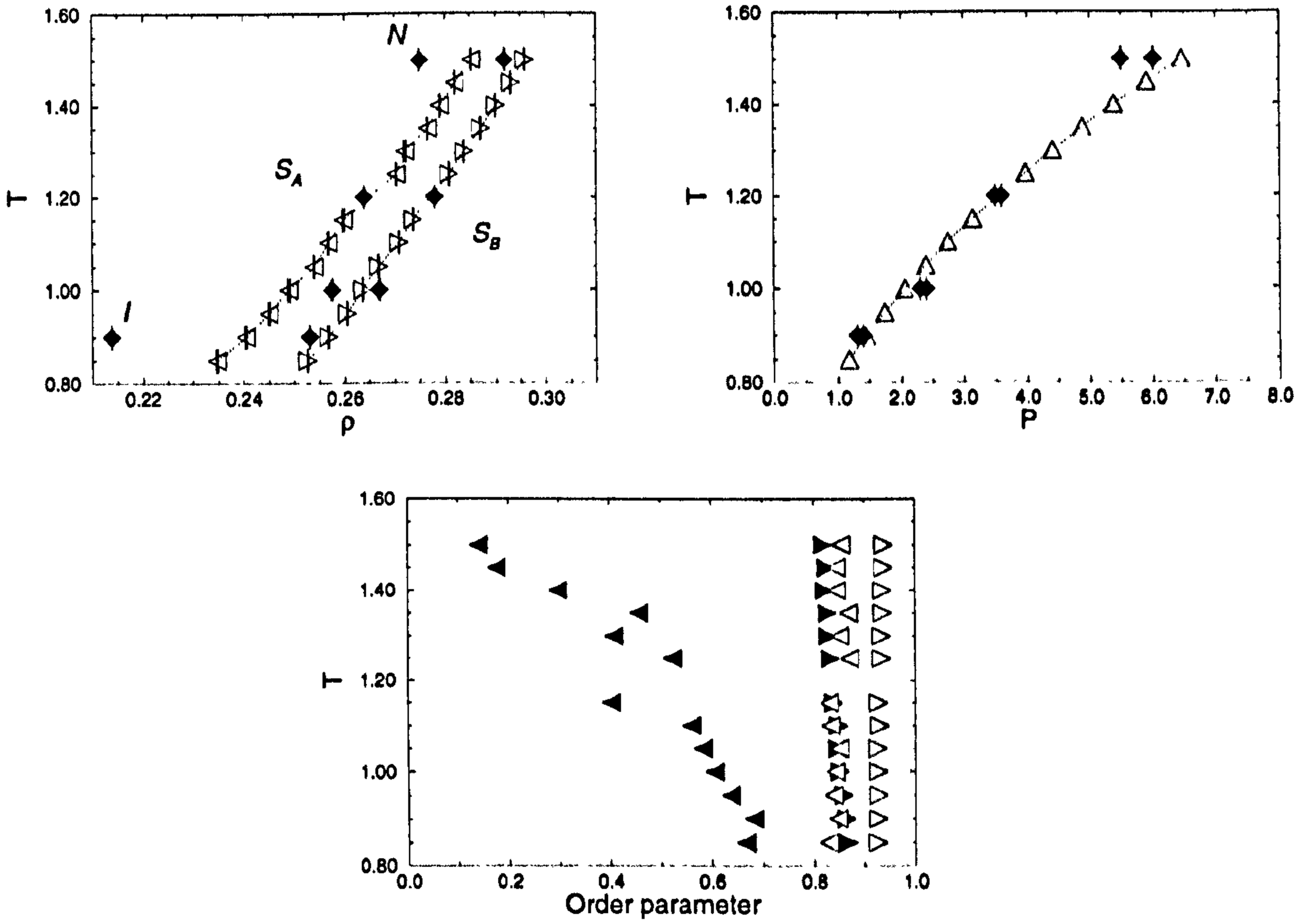

Figure 3.34: S_A–S_B phase boundary of the GB fluid with $\kappa' = 5$ and $\kappa = 3.6$ as obtained from GD integration, (triangles), with approximate coexistence data from eos simulations, (diamonds). Results are shown in (a) the density-temperature and (b) the pressure-temperature planes. (c) Nematic, (open), and smectic, (filled), order parameter values. In (a) and (c), left-pointing triangles indicate the S_A or N phase and right-pointing triangles the S_B.

be understood and avoided. This technique also avoids any complications of free energy calculations for molecular ordered phases. Since the positional order of the dense phase persists across the box, simulating with fixed box dimensions introduces an additional strain which, if ignored, will lead to deviations from the coexistence curve. As discussed in §2.4, this may be addressed by including MC moves that allow the aspect ratio of the box to vary whilst preserving the ratio of the box dimensions pertaining to the in-layer structure, and the total volume. Significant deviation from the equilibrium 'lattice spacing' should be quickly addressed by such a scheme.

Given that the gap between triple and critical points is narrowing with increasing elongation, the most extreme case examined so far, $\kappa = 4$, was chosen for an investigation of vapour-smectic coexistence. Previous results imply that at $T = 0.45$ the ordered phase sublimes directly to vapour, (§3.3.2). The next lowest isotherm presented, $T = 0.80$, showed the phase sequence I–S_A–S_B. Together these observations suggest that the intermediate phase behaviour will exhibit one of the following sequences:

i. $T_{V-I-B} < T_c < T_{I-A-B}$, i.e. liquid-vapour coexistence as established for $\kappa \leq 3.2$ with the S_A becoming stable at higher temperatures,

ii. $T_{V-A-B} < T_{V-I-A} < T_c$, so that a critical point is still exhibited but with the V–I–S_B triple point preempted by the S_A phase, or

iii. no critical point, with the lowest significant temperature being T_{I-A-B}.

By tracking up in temperature from $T = 0.45$, it should be possible to distinguish between case (i) and the others. Furthermore, if V–S_B coexistence persists to temperatures greater than $T \sim 0.47$, case (ii) would be inconsistent with the reduction in T_c with elongation observed at lower κ.

A starting configuration for $\kappa = 4$ was generated by taking a smectic configuration of 648 particles, previously equilibrated at $T = 0.50$ using NPT MC at $P = 0$, doubling-up in the z direction, and adding 204 vapour particles at randomly generated positions and orientations to give $N = 1500$. The layers were arranged perpendicular to the long box axis, (z), to facilitate profile measurement. The new system was equilibrated at $T = 0.50$, and subsequently the temperature was increased in small steps, $\Delta T = 0.05$. The results are

summarized in Table 3.2; the values shown are based on profiles measured typically over the final 2.5×10^4 timesteps. The table indicates the number of smectic layers, n_l, the inferred bulk values of layer spacing, d, and densities in the smectic, ρ_S and isotropic, ρ_I. The coexistence points are also shown in Fig. 3.41. From the isotropic side, interface regions are identified from a systematic increase in the density when averaged over an increasing number of profile bins, with the origin fixed at the mid-point of the isotropic region. Excluding these regions, the averaged isotropic densities are those shown in the table; uncertainties reflect the spread of individual bin values. In the absence of systematic trends in the smectic density calculated layer-by-layer, bulk values are obtained by averaging over the central 6 layers, (or 4 for $T = 0.65$). The measured bulk isotropic density increases only rather slowly until, moving from $T = 0.60$ to $T = 0.65$, it changes markedly. Such a sharp change in the coexistence conditions introduces practical difficulties; care must be taken that the smectic region remains sufficiently populated to infer bulk properties. At each temperature, profiles of orientational order parameter indicate the low density phase to be isotropic; distribution functions measured over the central layers of the dense slab indicate a S_B structure. The inferred smectic bulk values at $T = 0.65$ should be taken with caution, due to the small number of layers in the final equilibrium configuration. There is, however, no doubt that this coexistence is stable and investment of sufficient computing time would allow simulation with a wider smectic region. Given the location of this 'shoulder' in the I–S_B coexistence curve, at $T \sim 0.65$, and the low isotropic densities at temperatures below this, the evidence indicates the critical point has indeed disappeared.

3.7 S_B or solid?

The nature of the dense phase labelled S_B thus far is called into question by the lack of a phase transition to a crystal as it is compressed. Furthermore, the pair distribution functions indicate strong positional correlations in a layer and between layers. Care should be taken when defining the nature of the S_B. As mentioned in Chapter 1, phases historically designated S_B have in some cases been shown to be crystals with rather weak coupling between layers, closer in nature to graphite than to any liquid crystal phase [85], with the unusually small shear elastic moduli leading to confusion. Currently a distinction is drawn

T	Total run length ($10^4\ \delta t$)	n_l	d	ρ_S	ρ_I
0.50	21	12	3.647(4)	0.2368(10)	0.0148(3)
0.55	21	12	3.721(1)	0.2281(8)	0.0147(3)
0.60	24	12	3.819(3)	0.2152(6)	0.0158(3)
0.65	60	6	3.800(7)	0.2139(19)	0.0878(5)

Table 3.2: Results of direct simulation of isotropic-smectic coexistence for $\kappa = 3.4$. See text for details.

Phase	Orientational order within layers	Bond orientational order	Positional order	
			within layers	normal to layers
S_A	LRO	SRO	SRO	SRO
S_B^h	LRO	LRO	SRO	QLRO
C_B	LRO	LRO	LRO	LRO

Table 3.3: Range of structural correlations in phases discussed in the text. SRO, LRO and QLRO refer to short, long and quasi-long ranged order respectively.

between the three-dimensional hexatic phase, (S_B^h), a liquid state, and the solid crystal B (C_B), phase, as indicated in Table 3.3.

In these finite-size simulations it is almost impossible to draw a distinction between quasi-long-ranged and true long-ranged order [32]. The distribution functions indicate that positional correlations in a layer persist across the box, and although decaying in amplitude, layer-layer correlations also persist across the box. One may therefore question the liquid nature of this S_B phase. With no evidence of a further phase transition to a crystal at high density/pressure along the isotherms studied, the $\kappa = 3.4$ system was cooled to very low temperatures. These runs were performed using NPT MC at zero pressure, in practice indistinguishable from the coexistence pressure at these low temperatures. A $N = 648$ system was generated as a defect-free structure with hexagonal in-layer packing.

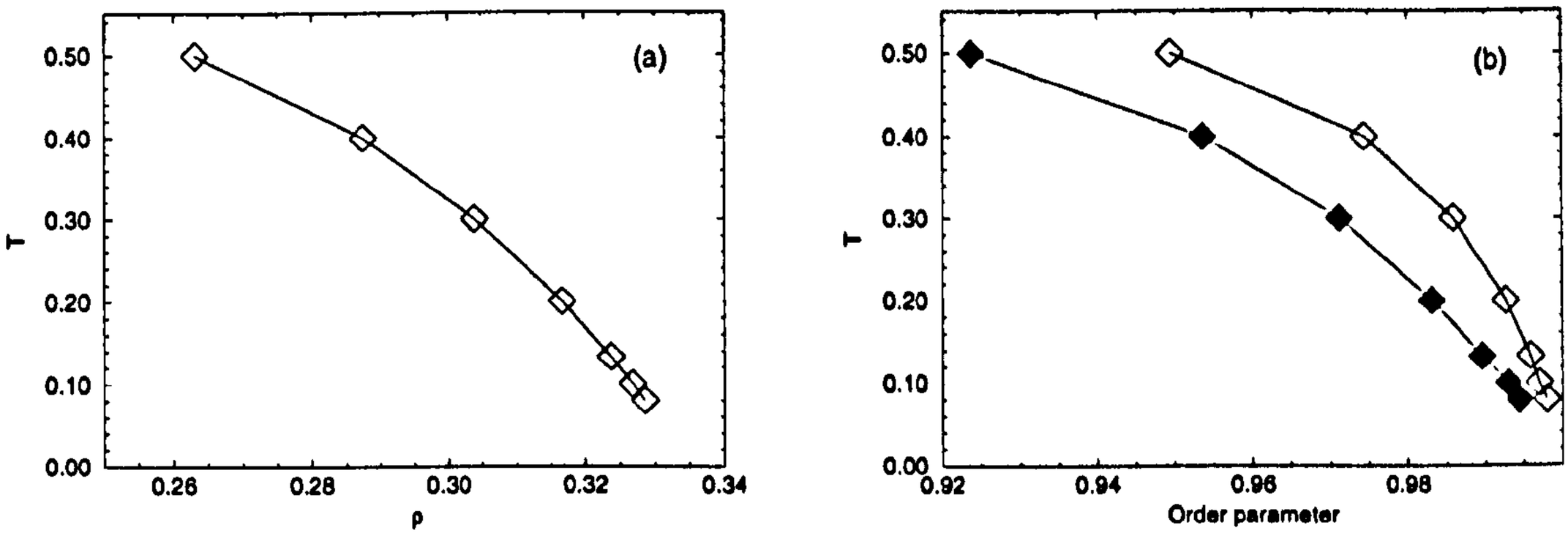

Figure 3.35: (a) Equation of state of the GB fluid with $\kappa' = 5$ and $\kappa = 3.4$ at $P = 0$ and low temperatures as obtained from MC simulation. (b) Corresponding values of orientational, (open symbols), and smectic (filled symbols), order parameters.

This was equilibrated at $T = 0.40$. The final production run configuration was used to start cooling runs to $T = 0.08$ in steps of $\delta(1/T) = 2.5$ or less. It was also used to start heating runs, also performed at zero pressure. The system evaporated at $T = 0.60$, with the vapour heading to zero density. At each temperature at least 6×10^4 sweeps were performed, with final averages being taken over the last 3×10^4. The results of these runs are shown in Fig. 3.35, with no visible discontinuity.

Finally, investigations into the shear modulus were performed. As indicated above, this takes a rather low value in the C_B phase, but following the temperature dependence gives another opportunity to identify a solid-fluid transition. Simulations were performed by applying a shear to the box at $t = 0$, allowing the system to equilibrate and measuring the equilibrium response of the stress tensor during NVT MD. For convenience, 'shifted brick' boundary conditions were used, as in non-equilibrium simulations of homogeneous shear [9]. These allow the simulation to proceed as usual in a cubic cell, but apply an appropriate shift to the periodic images in the shear direction, equivalent to taking periodic images of a sheared central box. Simulations were performed at temperatures from $T = 0.50$ to 0.20 at intervals of 0.05. At each T, a system was prepared with six hexagonally-ordered layers arranged perpendicular to z with ABC packing, i.e. an f.c.c. structure taken along the (111)

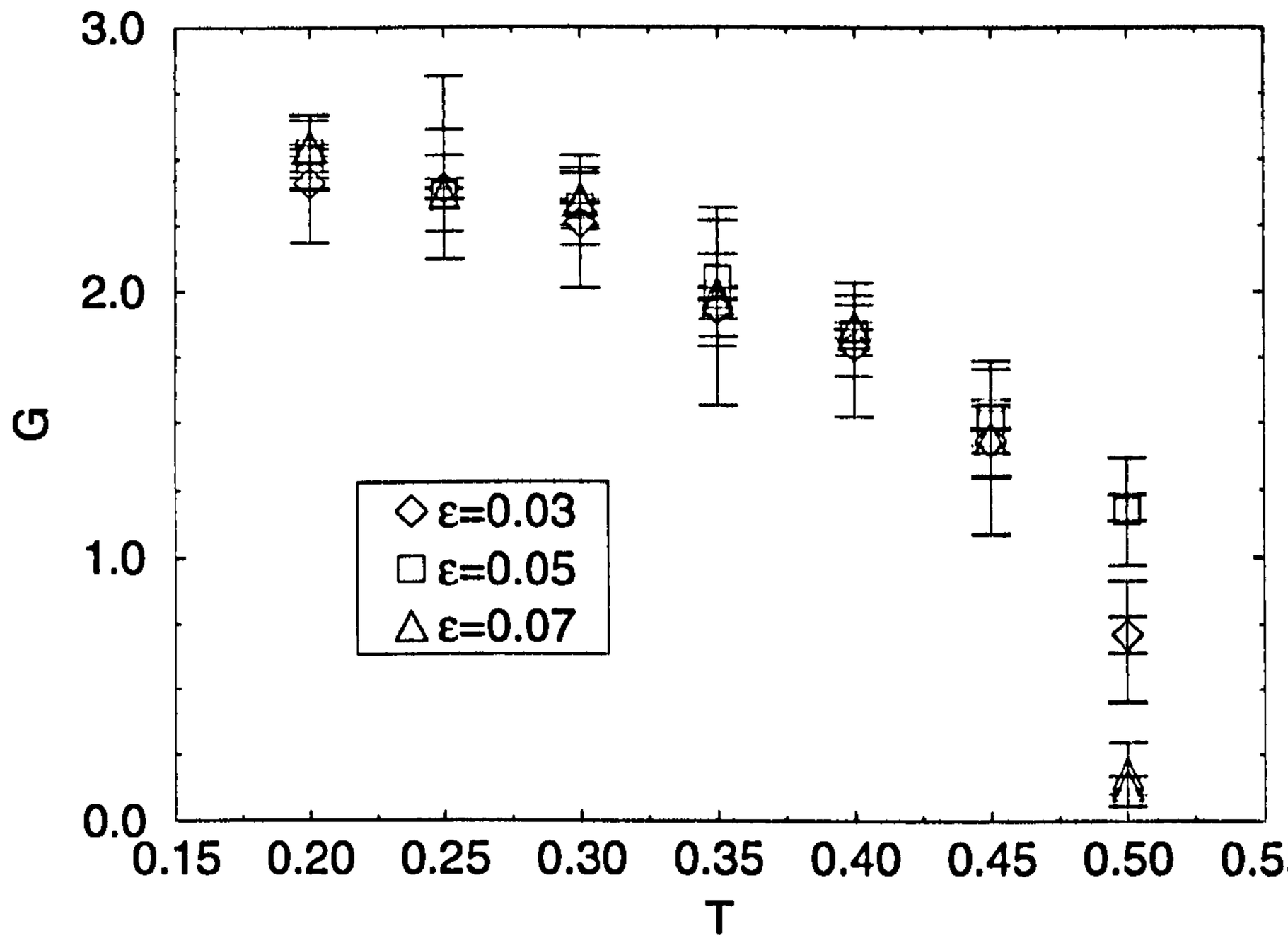

Figure 3.36: Temperature dependence of shear elastic modulus for the GB system with $\kappa = 3.4$. Results are shown for three applied strains, ε, at each temperature.

direction. This was equilibrated with NPT MC, variable aspect ratio, at $P = 0$ with no imposed shear. The final configuration was modified 'by hand' to incorporate the required shear, in the $x - z$ plane, to prevent excessive overlaps on switching to MD with sheared boundary conditions. Three values of strain were applied at each temperature, viz. 3%, 5% and 7%, corresponding to convenient changes in box dimension. After equilibration of 2×10^4 timesteps, stress tensor components were measured over a further 1×10^4 timesteps.

The values of stress/strain obtained are shown in Fig. 3.36. Below $T = 0.50$ they are constant at given temperature indicating linear response. This ratio gives the shear elastic modulus, G, which shows a slow decrease with increasing temperature over the valid response range, but with no discernible discontinuity. The degree of interdigitation

falls steadily as the temperature is raised; at $T = 0.50$ very little remains, and coupling between layers appears to be very weak and correspondingly hard to measure, as indicated by the violation of linear response at these low strains.

According to Quesnel *et al.* [86], the LJ f.c.c. solid has a shear modulus of $G = 57.2\varepsilon_0/\sigma_0^2$ along the (100) crystallographic direction. This is significantly higher than the present values. We note that in our case the f.c.c. structure is taken along the (111) direction to obtain hexagonally-packed layers, and stretched along one axis, as are the particles, so that the LJ value above is far from ideal for direct comparison. This said, a low value of shear modulus is expected in this B phase.

Both the eos and shear modulus indicate continuous behaviour to low temperature. At such low temperatures the phase would naturally be labelled a solid. With no sign of a phase transition, it would seem reasonable to apply the same classification at higher temperatures.

3.8 Phase diagrams

In Fig.s 3.37–3.41 the simulation results reported in this chapter are summarized in approximate phase diagrams. The points shown indicate the approximate locations of phase boundaries; they are not exact. The symbols refer to the following techniques:

- Squares : MD NVT, $N = 256$, cubic box, (§3.3).
- Filled diamonds : MC NPT, $N = 600$, cuboidal box, variable aspect ratio, (§3.4).
- Filled circles : MC NPT at $P = 0$, $N = 648$, cuboidal box, variable aspect ratio, (§3.7).
- Open diamonds : Gibbs Ensemble Monte Carlo (GEMC), $N_1 + N_2 = 1000$, liquid-vapour, (§3.5).
- Open triangles : Gibbs-Duhem (GD) integration, with respect to T, (§3.6).
- Filled triangles : Direct coexistence, ('slab'), MD + MC aspect ratio moves, $N = 1500$, smectic-vapour, (§3.6).

Bulk phase regions are shaded. White regions correspond to phase coexistence.

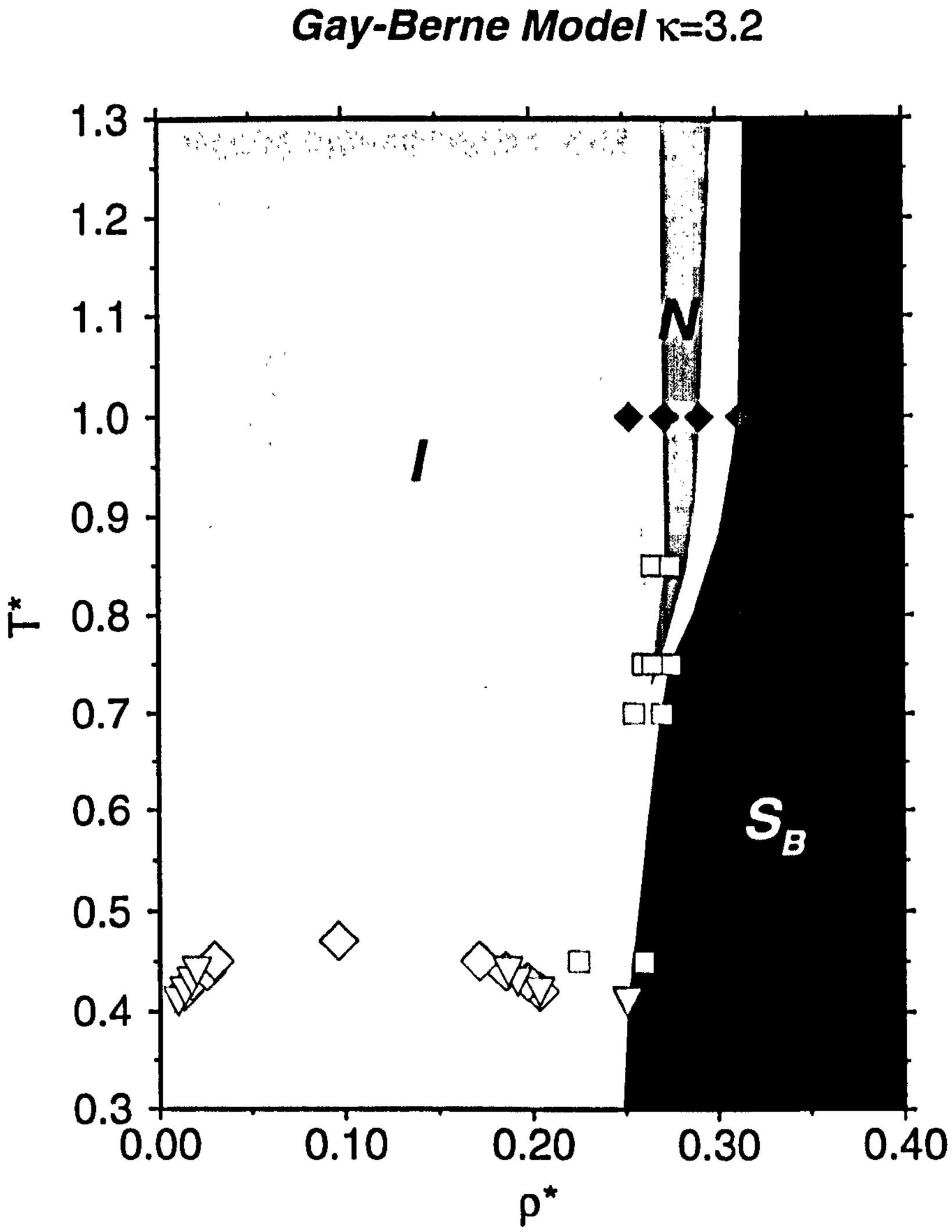

Figure 3.37: Summary of results and approximate phase diagram for the $\kappa = 3.2$ fluid. Symbols are described in the text. A metastable S_A point is indicated at $T = 1.0$.

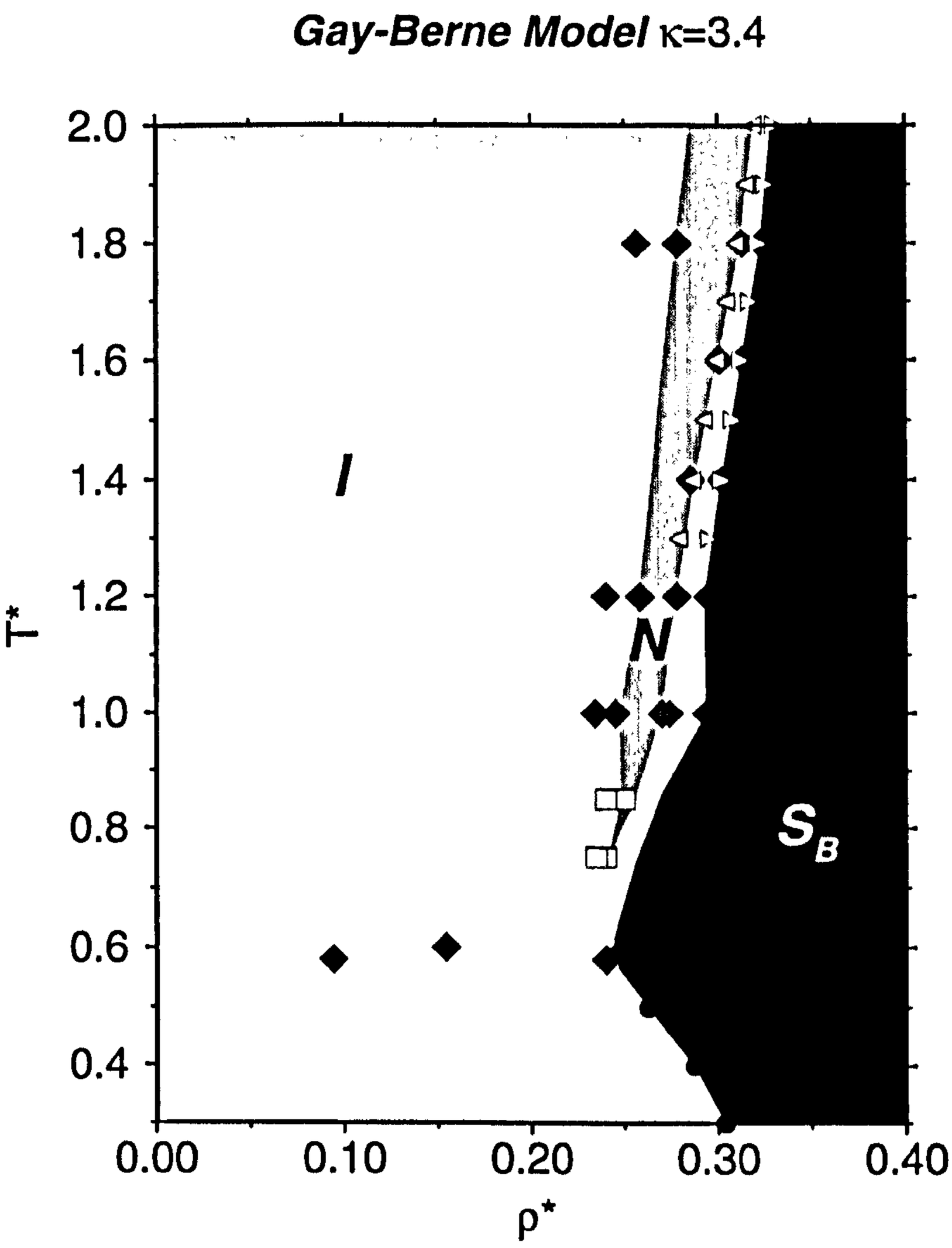

Figure 3.38: Summary of results and approximate phase diagram for the $\kappa = 3.4$ fluid. Symbols are described in the text. A metastable S_A point is indicated at $T = 1.0$.

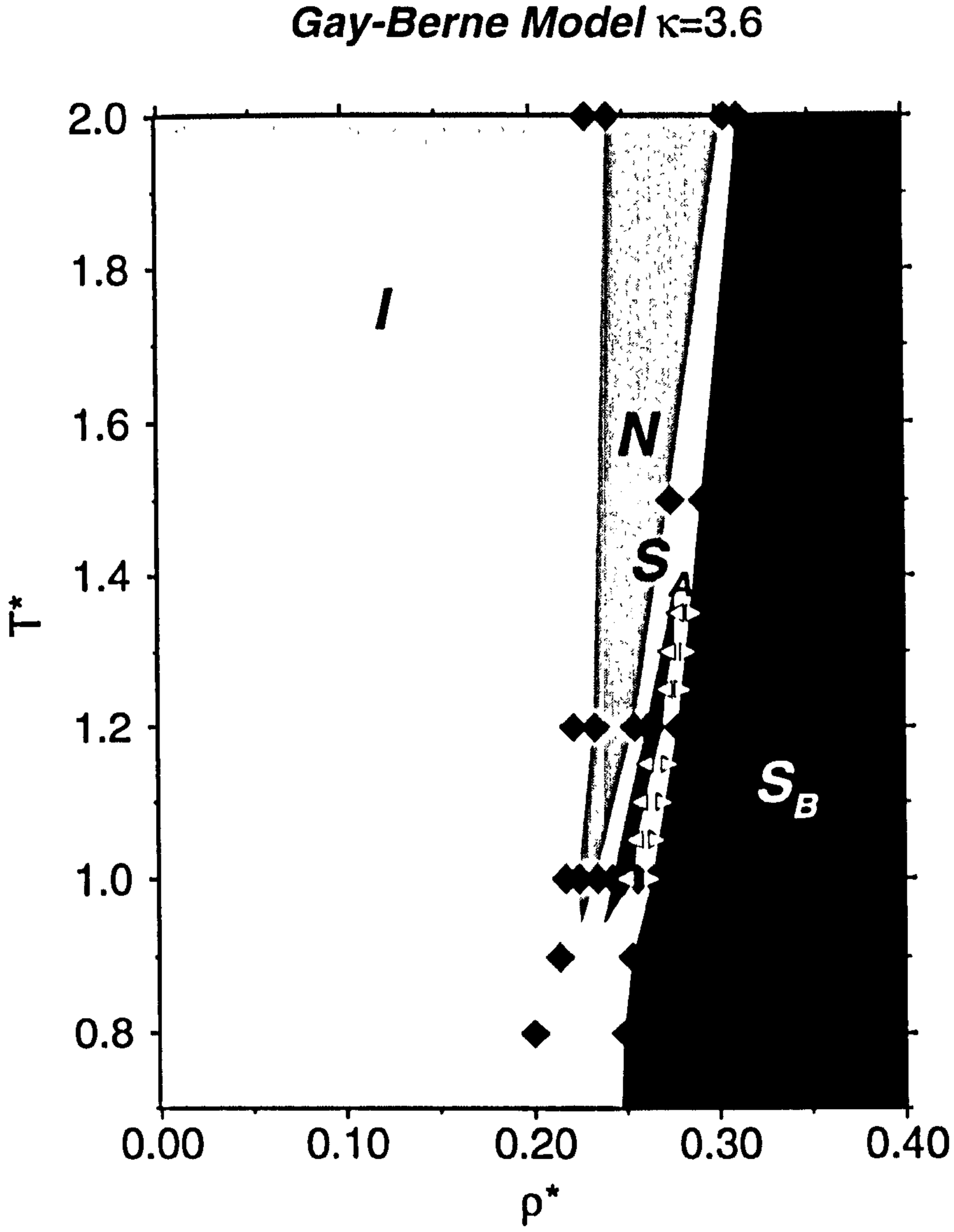

Figure 3.39: Summary of results and approximate phase diagram for the $\kappa = 3.6$ fluid. Symbols are described in the text.

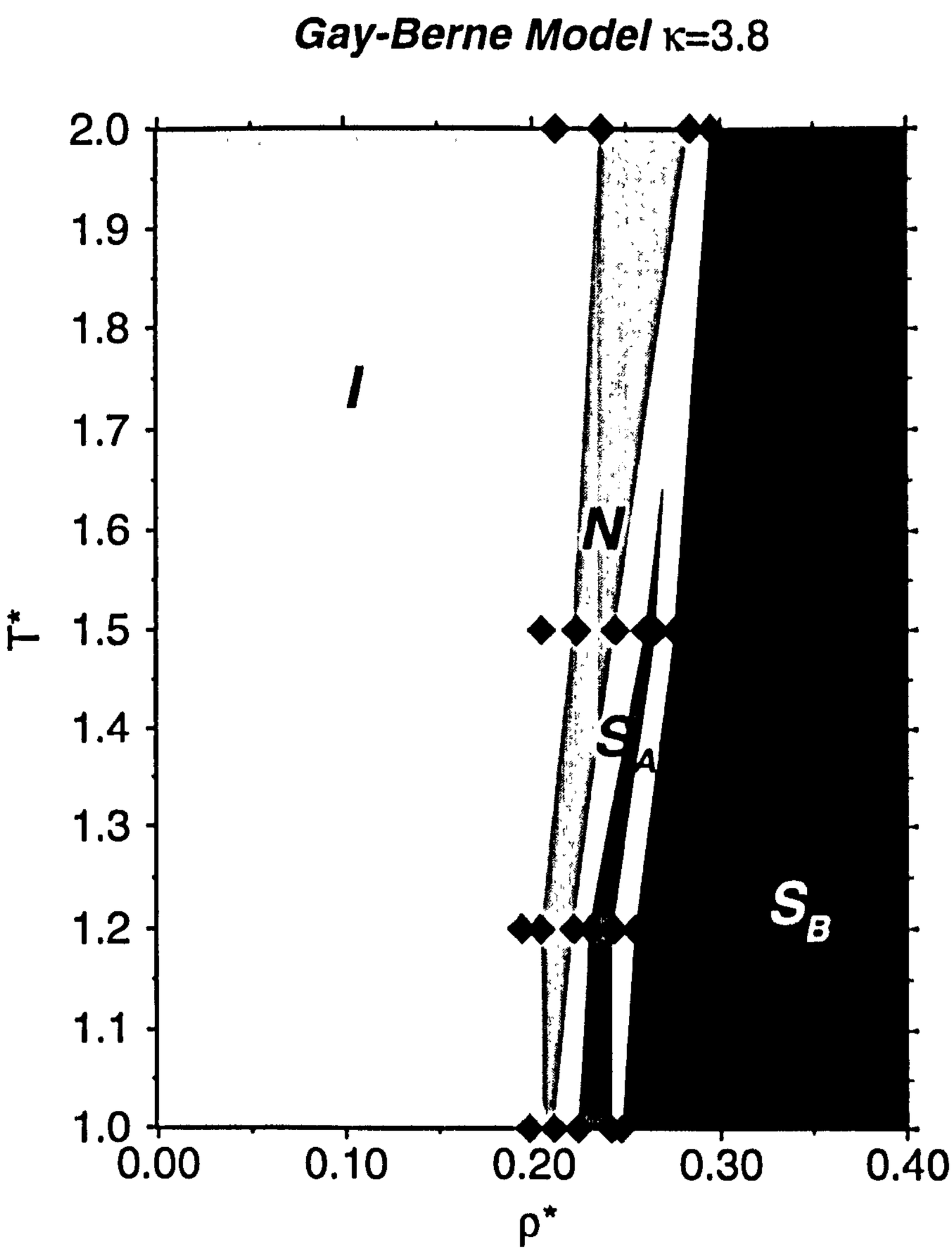

Figure 3.40: Summary of results and approximate phase diagram for the $\kappa = 3.8$ fluid. Symbols are described in the text.

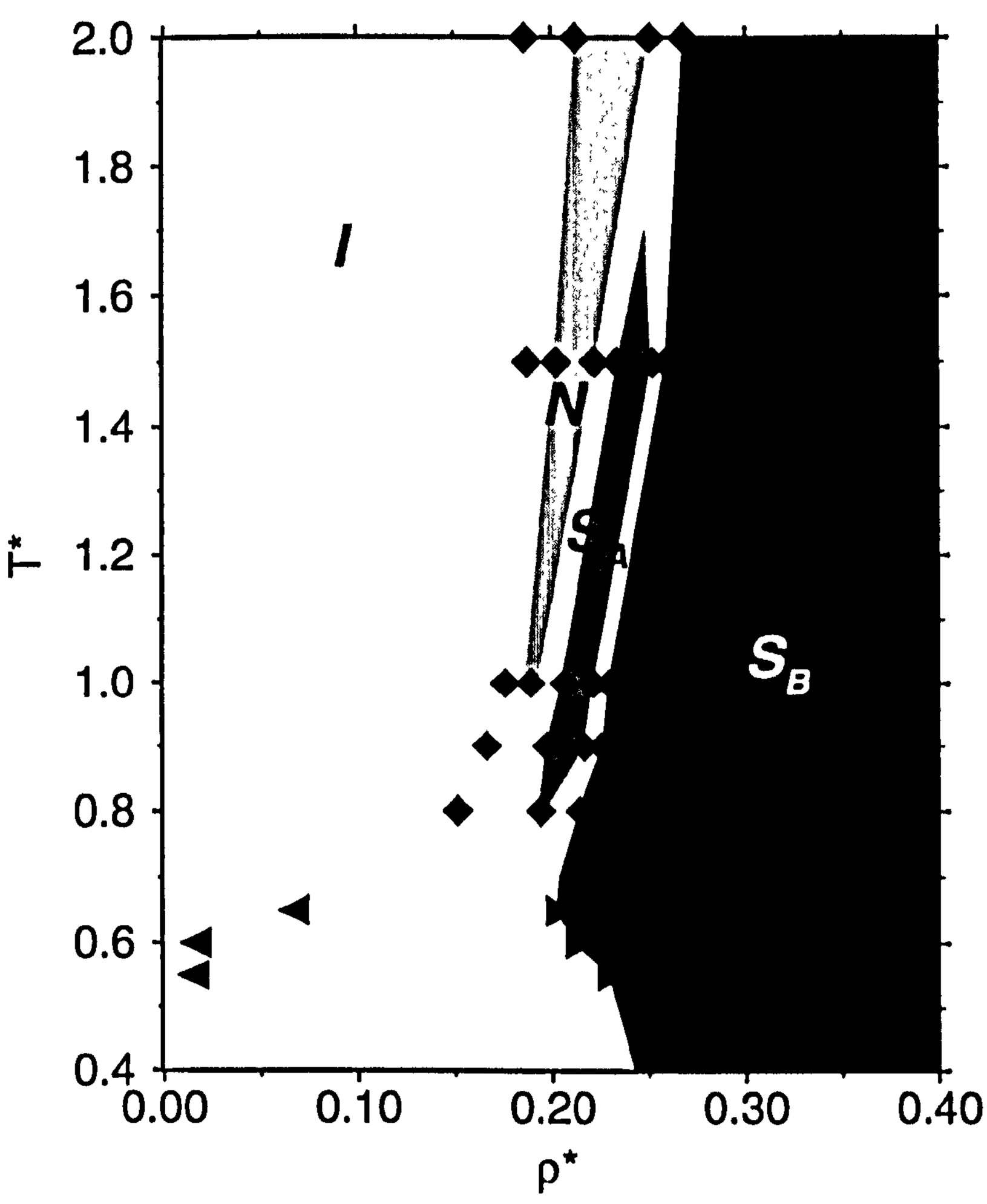

Figure 3.41: Summary of results and approximate phase diagram for the $\kappa = 4.0$ fluid. Symbols are described in the text.

3.9 Discussion

In this chapter we have presented studies of the GB phase diagram at a number of elongations in the range $3 \leq \kappa \leq 4$. A variety of simulation methods have been applied, using both MD and MC. Differences in the phase behaviour indicated by the two techniques at lower elongations result from system size effects and the simulation conditions: using NVT MD in a fixed, cubic cell gives a stable S_A phase at lower elongations than NPT MC in a variable-aspect-ratio cuboidal cell. At higher elongations the two approaches give good agreement. The trends in phase behaviour are indicated in approximate phase diagrams for these systems. We have not reported any free-energy calculations, which must be the subject of further study. It should be possible to find a suitable reference system for the S_B phase, such as the molecular Einstein crystal [87, 88], particularly at low temperatures. The S_A phase may pose more of a problem; a possibility is the route taken for hard spherocylinders by Veerman and Frenkel [19], in which the system is first subjected to an aligning field and then treated as a system of parallel particles.

Within this small range of elongation, the phase diagram shows significant changes. On increasing κ, the critical point moves to lower temperature until it falls below the I–S_B coexistence line; this occurs at around $\kappa = 3.4$, where liquid-vapour proves hard to establish using GEMC or GD. There is some indication of a reasonably high-density isotropic phase at $T = 0.45$ from the NVT MD runs with $N = 256$, but the disappearance of the critical point is clearly demonstrated at $\kappa = 4$. The liquid-vapour coexistence region is essentially determined by attractive interactions. Increasing κ with κ' fixed reduces the effective range of these attractions and makes the coexistence region vulnerable; the liquid side of the coexistence envelope has already been seen to broaden on increasing κ at $\kappa \leq 3$ [81]. Similar effects can be seen in polymer-colloid mixtures, for example, where the depletion mechanism allows the range and strength of attractions to be tuned [89]. In this case, it is possible to see the liquid-vapour coexistence point escaping, and re-emerging in the *solid* region when the width of the attractive well is less than $\sim 7\%$ of the molecular diameter, although we are far from this regime. The van der Waals description indicates that liquid-vapour separation is possible since the increased interactions of repulsive cores in the dense phase is balanced by the greater attractive interactions. The increased volume

of the particles in these GB systems at higher κ appears to prevent the phase separation.

Another dramatic effect is the growth of a stable S_A 'island' in the phase diagram at elongations slightly above $\kappa = 3$. The S_A region moves to both higher and lower temperatures as κ is increased. The anisotropic attractions in the GB model are highly significant in the formation of smectic phases: a purely repulsive WCA form of the $\kappa = 3$ GB potential does not yield a S_B [28]. Decreasing the range of these attractive forces with respect to the particle size appears to be sufficient to split the transitions that give order along and perpendicular to the director. Luckhurst *et al.* [29] stabilized the S_A phase in a GB system by enhancing the side-by-side interactions; in this case a better description might be a weakening of the in-layer interactions in the S_B phase, since side-by-side and end-to-end well depths scale identically with κ.

Increased stability of the smectic phases was one possible result of increased elongation. Another was increased stability of the nematic phase. As κ is increased, the I–N transition is seen to move to lower density and pressure, at given temperature, although the I–N–S triple point does not shift significantly in temperature. The effect on the I–N transition of changes in κ (and κ') has recently been studied theoretically by Ginzburg *et al.* [82] using a second virial approximation for the free energy. This reproduces the trends in the location of the I–N transition presented here, but the transition pressure is seriously underestimated, even at higher elongations, where the transition density is lower and the inadequacies of a second virial treatment are expected to be less significant. As expected at the second-virial level, the width of the coexistence region is overestimated, and the transition density somewhat underestimated. Comparison with these simulation results should allow systematic improvements to the theory.

We have noted that on cooling to low temperatures, no S_B-crystal transition can be identified in the equation of state. Measured values of the shear modulus also indicate continuous behaviour, before, at reasonably high temperature, linear response is violated. The values obtained are low, as expected in a B phase. The continuous behaviour shows that the same designation should be used for this phase at all temperatures, and since it persists at very low temperatures, we suggest that this should be termed a solid phase.

Chapter 4

Effects of Attractive Interactions on the Phase Behaviour of the Gay-Berne Fluid

4.1 Introduction

In the previous chapter the effects of varying the shape anisotropy parameter of the GB fluid were considered and small changes in elongation were shown to produce a significant effect on phase behaviour. Systematic variations of κ', the well-depth anisotropy parameter, have also been studied. Using values in the range $1 \leq \kappa' \leq 25$, extensive simulations at $T = 0.70$, well above the critical temperature of the widely-studied $\kappa = 3, \kappa' = 5$ fluid, have found an I–S_B transition for $\kappa' \geq 5$, moving to lower density with increasing κ', and an I–N transition for $\kappa' \leq 2.5$, moving to higher density with increasing κ'. These studies are described fully in [2]; here we focus on the liquid-vapour regions of the low κ' fluids, where the nematic phase extends to temperatures low enough to intersect the liquid-vapour envelope.

The physical meaning of the parameter κ' is not as clear as that of κ. As defined, κ' represents the ratio of the interaction strength for a pair of parallel molecules when they are side-by-side and end-to-end. It can also be considered as a parameter which controls the relative contribution of the attractive interactions for a range of different

molecular configurations: raising κ' increases of the anisotropy of the interactions. This can be seen in Fig. 4.1 where the well depth of the interaction is represented for a pair of parallel GB molecules (with $\kappa = 3$) as a function of the angle θ between the axial vector and the intermolecular vector. It can be observed that when molecules are parallel to each other, high values of κ' will tend to favour the side-by-side configuration of the molecules ($\theta = 90°$) over the end-to-end configuration ($\theta = 0°$). The relative stability of the side-by-side configuration decreases as κ' is lowered and for $\kappa' = 1$ all configurations (for parallel molecules) are equally stable. This follows from the fact that $\varepsilon(\hat{\mathbf{r}}_{ij}, \mathbf{u}_i, \mathbf{u}_j)$ does not depend on the angle θ when $\kappa' = 1$ but only on the angle γ between the axial vectors $\mathbf{u}_i$ and $\mathbf{u}_j$. The variation of the well depth with γ for $\kappa' = 1$ is illustrated in Fig. 4.2, ($\gamma = 90°$ corresponds to the '$\times$' configuration).

4.2 Liquid-vapour region

The MD results of [2] suggest vapour-nematic coexistence at sufficiently low temperatures for $\kappa = 3$ and low values of the anisotropy parameter κ'. This finding is of relevance as it would provide a relatively simple liquid crystal model to study the wealth of interfacial phenomena occurring at the liquid crystal interfaces, such as induced orientational transitions, layering, wetting and surface tension [90].

In order to investigate this point further, a systematic study of the region where vapour-liquid separation is expected was performed using the Gibbs ensemble Monte Carlo method, (§2.5). The results obtained by de Miguel and del Río and reported in [2] are shown here to illustrate the changes in behaviour as κ' is reduced from 5 to 1, (we note that our results for the $\kappa = 3$, $\kappa' = 5$ fluid are in complete agreement with those presented in [2], which correct those of [91]). It can be seen that the vapour-liquid phase boundaries shift to higher temperatures as the value of κ' decreases. This is the expected tendency, recalling that the attractive interactions in the GB model become stronger as lower values of κ' are considered.

The suggestions of N–V coexistence occur for $\kappa' \leq 1.25$ at relatively low temperatures, $T \leq 0.6$. In this region the increasing liquid density makes particle exchange too expensive for practical use of GEMC. Two approaches were adopted that do not rely on the transfer

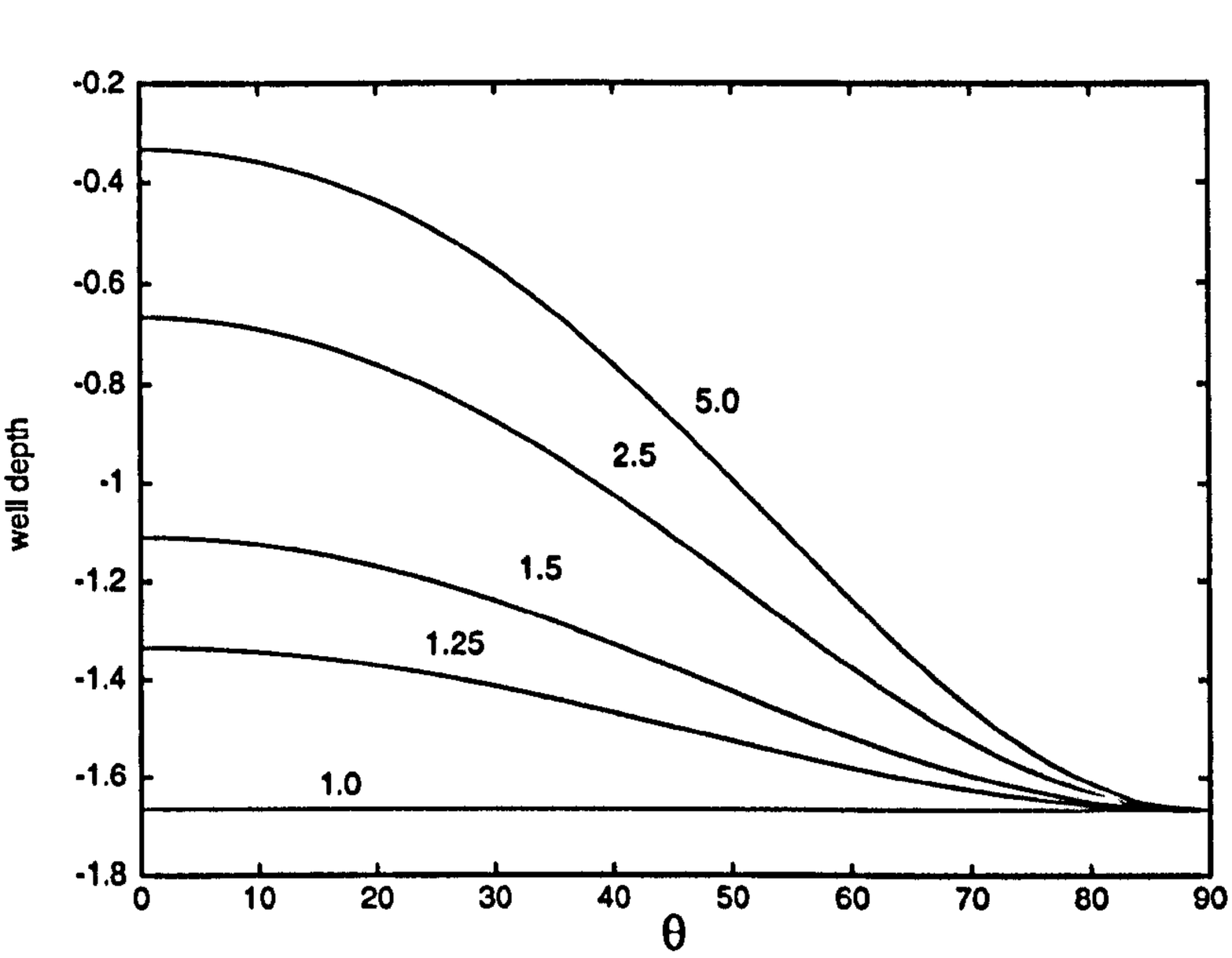

Figure 4.1: Well depth of the interaction between a pair of parallel GB molecules with $\kappa = 3$ and different values of κ' (shown in the plot) as a function of the angle θ (in degrees) between the axial vector and the intermolecular vector. The well depth is expressed in units of ε_0.

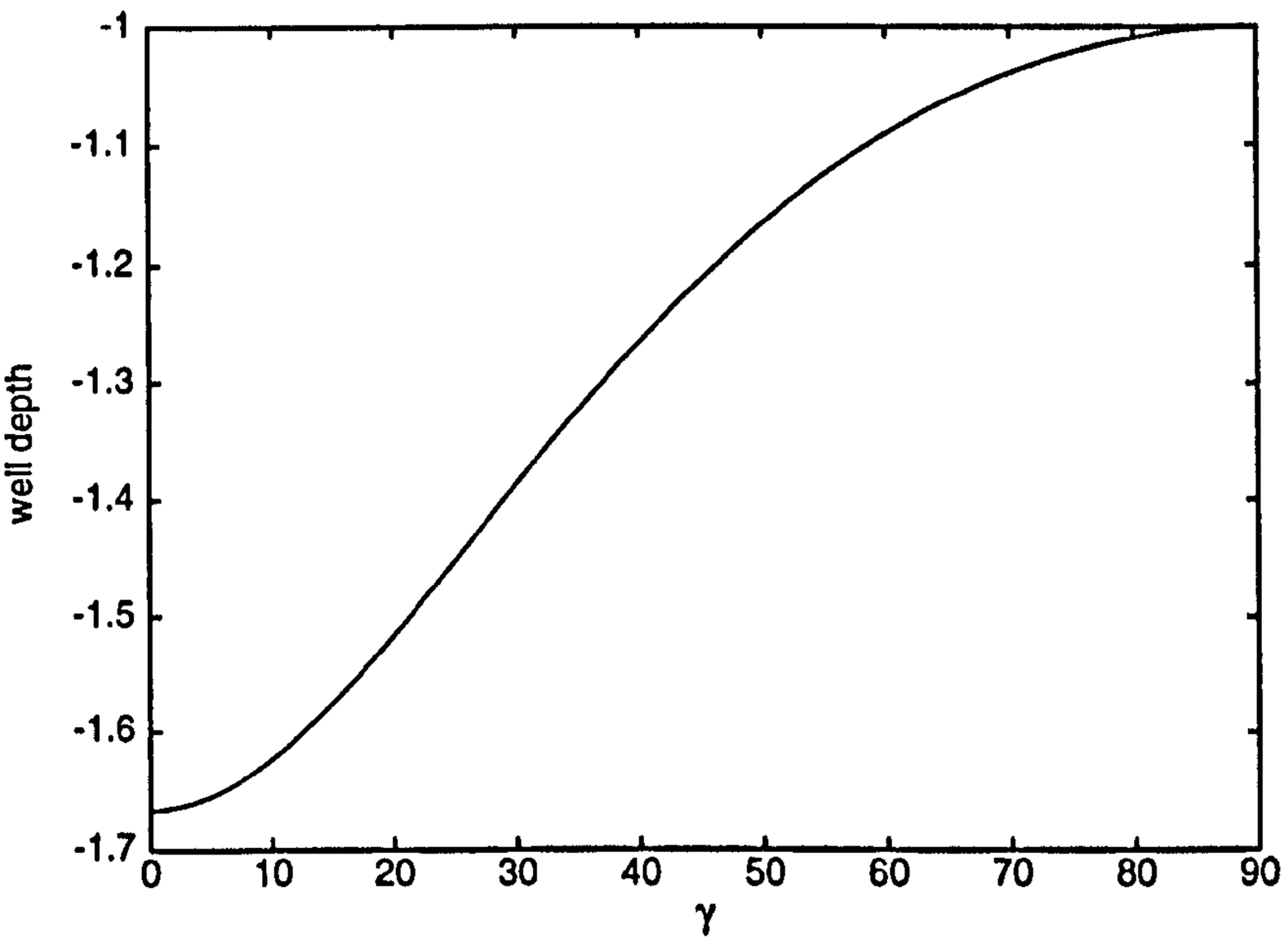

Figure 4.2: Well depth of the interaction between a pair of GB molecules perpendicular to the intermolecular vector with $\kappa = 3$, $\kappa' = 1$ as a function of the angle γ between the axial vectors.

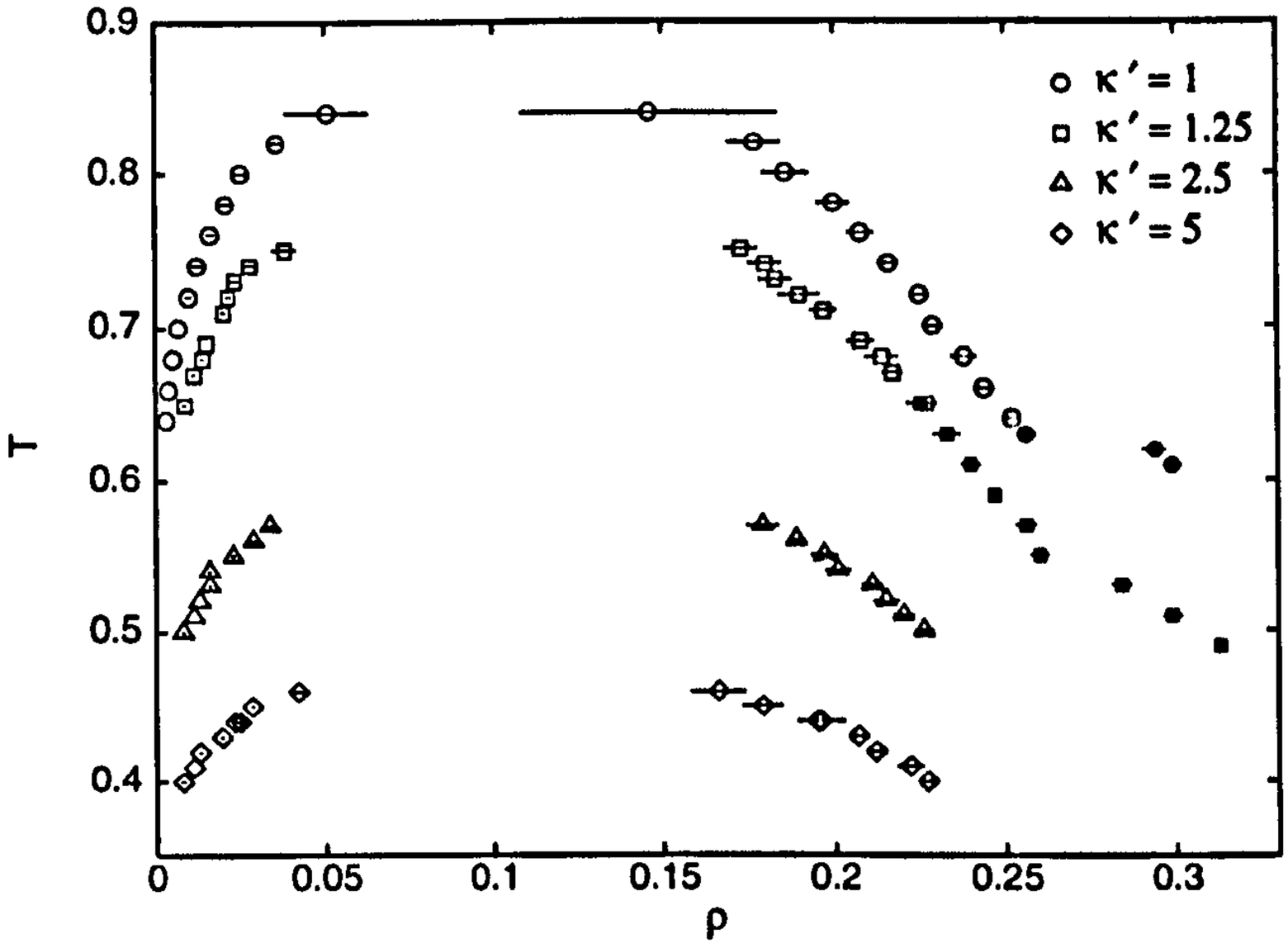

Figure 4.3: Liquid-vapour coexistence curves for GB fluids with $\kappa = 3$ and different values of the anisotropy parameter κ', as reported in [2]. Open symbols represent the vapour and liquid densities as obtained by using the Gibbs ensemble Monte Carlo technique. Filled symbols correspond to the liquid densities obtained from zero-pressure Monte Carlo simulation. The high-density data shown for $\kappa' = 1$, and 1.25 correspond to the nematic phase.

of particles to maintain the equality of chemical potentials. Since the saturation vapour pressure is so low in these systems at such temperatures, simple constant-NPT simulation of the liquid phase at $P = 0$ and the chosen T will be a very close representation of the liquid at the true coexistence pressure. In Fig. 4.3, results obtained by de Miguel and del Río with this method are shown for systems of $N = 326$ particles with $\kappa' = 1.00$, and $N = 256$ particles with $\kappa' = 1.25$. An ordered fluid phase develops in both cases at the lower temperatures. An obvious limitation of this approach is that no information regarding the coexisting vapour density is available.

The second approach adopted, and our major contribution to this work, was the technique of Gibbs-Duhem integration, introduced by Kofke [77, 78], (§2.6). This was applied to systems with $\kappa' = 1$ and $\kappa' = 1.25$, starting from well-equilibrated GEMC runs in the isotropic phase, and proceeding down in temperature intervals (typically ΔT =0.01–0.02) using constant-NPT MC. At each stage a predicted value of the required pressure was made, applying a trapezoid rule scheme to the governing equation

$$\frac{\mathrm{d}\ln P}{\mathrm{d}\ln T} = \frac{\beta\Delta h}{\Delta z} \tag{4.1}$$

where $\Delta h = h_1 - h_2$ is the difference in enthalpy per particle between coexisting phases 1 and 2, and $\Delta z = z_1 - z_2$ with $z = PV/Nk_BT$. This is a more slowly varying form of (2.36), used due to the proximity of the I–N transition. Subsequently an equilibration run was conducted, typically of 1×10^5 MC sweeps, where each sweep consisted of N attempted particle moves and an attempted volume change. This was followed by the refinement stage for the required pressure, continuing to convergence of the pressure to within a specified tolerance ($\frac{\Delta P}{P} < 1 \times 10^{-5}$), which typically took 1-2 $\times 10^3$ MC sweeps. Finally, the production stage was used to measure properties of interest. Since the liquid phase is moving along the liquid-vapour coexistence curve *through* the I–N transition, substantial run lengths were required to reach equilibrium: a total of up to 2.5×10^5 MC sweeps were allowed at each T.

To take advantage of the low vapour density, in many of the runs the MC simulation of the vapour phase was replaced by the use of a virial equation of state (VEOS), truncated

T	$B_2(T)$	$\frac{dB(T)}{dT}$
$\underline{\kappa' = 1.25}$		
0.490	-37.17(3)	185.5(1)
0.500	-35.38(3)	172.1(1)
0.510	-33.72(3)	160.1(1)
0.520	-32.17(3)	149.2(1)
0.530	-30.73(3)	139.41(9)
0.540	-29.38(3)	130.49(9)
0.550	-28.12(2)	122.36(8)
0.560	-26.93(2)	114.95(8)
0.570	-25.82(2)	108.17(7)
0.580	-24.77(2)	101.95(7)
0.590	-23.77(2)	96.23(6)
0.600	-22.84(2)	90.96(6)
0.610	-21.96(2)	86.11(6)
$\underline{\kappa' = 1}$		
0.600	-28.44(3)	113.43(8)
0.605	-27.88(2)	110.20(8)
0.610	-27.33(2)	107.10(7)
0.615	-26.80(2)	104.12(7)
0.620	-26.29(2)	101.27(7)
0.625	-25.79(2)	98.52(7)
0.630	-25.31(2)	95.88(7)
0.635	-24.83(2)	93.34(6)
0.640	-24.37(2)	90.60(6)

Table 4.1: Temperature dependence of the second virial coefficient and its temperature derivative for GB fluids with $\kappa = 3$ and κ' as shown.

at the $B_2(T)$ level, $\beta P = \rho + B_2(T)\rho^2$. Obtaining ρ from P in this approximation is straightforward, and the enthalpy h may be calculated given $\mathrm{d}B_2/\mathrm{d}T$. The values of $B_2(T)$ and its derivative were calculated at the desired temperatures using Monte Carlo integration with 2×10^7 trials. The values obtained are shown in Table 4.1. The VEOS agreed very well with full GEMC simulation data for the vapour phase up to temperatures of at least $T = 0.75$ for both $\kappa' = 1.00$ and $\kappa' = 1.25$.

Results from these Gibbs-Duhem simulations appear in Table 4.2. For the $\kappa' = 1$ case, the starting configuration was taken from the final GEMC configurations at $T = 0.76$. The vapour phase configuration contained 181 particles and the liquid contained 331 particles. The temperature was decreased in steps of 0.02, following the GEMC data points, but the step size was reduced to 0.01 in the neighbourhood of the transition. Initially, the full Gibbs-Duhem scheme was applied, but at $T = 0.64$ the vapour phase simulation was replaced by the VEOS and integration continued to $T = 0.605$. This point was used to initiate a series of simulations in which the temperature was *increased*, again using the VEOS scheme. The results for the liquid branch are shown in Fig. 4.4, where they are compared with the zero-pressure results also appearing in Fig. 4.3. At the higher temperatures the GD results follow the GEMC coexistence curves quite accurately. On cooling to $T = 0.63$ the orientational order parameter reached an equilibrium value of $S = 0.685 \pm 0.004$; this ordering was accompanied by an increase in the density. No positional order was apparent, so the new phase was identified as a nematic. On the return, heating, path some hysteresis was encountered at the phase transition, the liquid remaining nematic until $T = 0.65$, when the orientational order is lost. Notwithstanding this slight hysteresis, the system appears to have returned to the original coexistence curve at $T = 0.66$.

The zero-pressure results for the liquid differ only slightly from those obtained with the GD integration scheme. The small discrepancies are most likely not due to the pressure difference but to the much longer equilibration times employed in the Gibbs-Duhem runs than in the preliminary zero-pressure runs. The GD run at $T = 0.62$ took more than 1.5×10^5 MC sweeps to reach the equilibrium value of the order parameter. The values of vapour pressure obtained from the GD runs are indicated in Fig. 4.5; heating and cooling runs are almost indistinguishable here, and the liquid-phase transition has little effect on

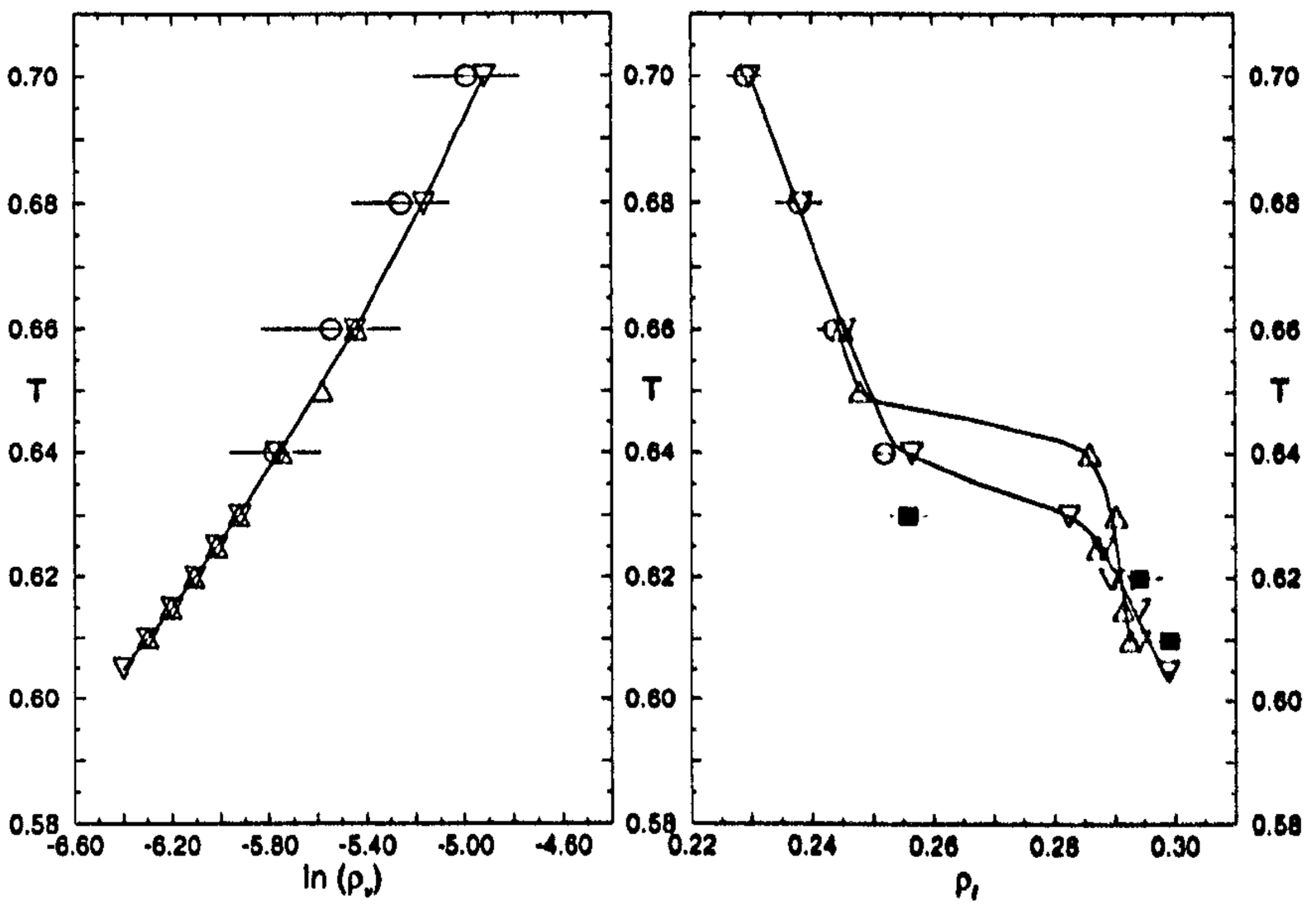

Figure 4.4: Detail of the liquid branch of the coexistence curve shown in Fig. 4.3 for the $\kappa' = 1$ fluid in the neighbourhood of the I–N transition. Circles represent the liquid densities as obtained by the Gibbs ensemble Monte Carlo technique. Down-triangles indicate GD results on reducing the temperature and up-triangles are the corresponding results for increasing temperature. Lines are drawn to guide the eye along these two paths. The squares represent the results obtained with zero-pressure NPT simulations.

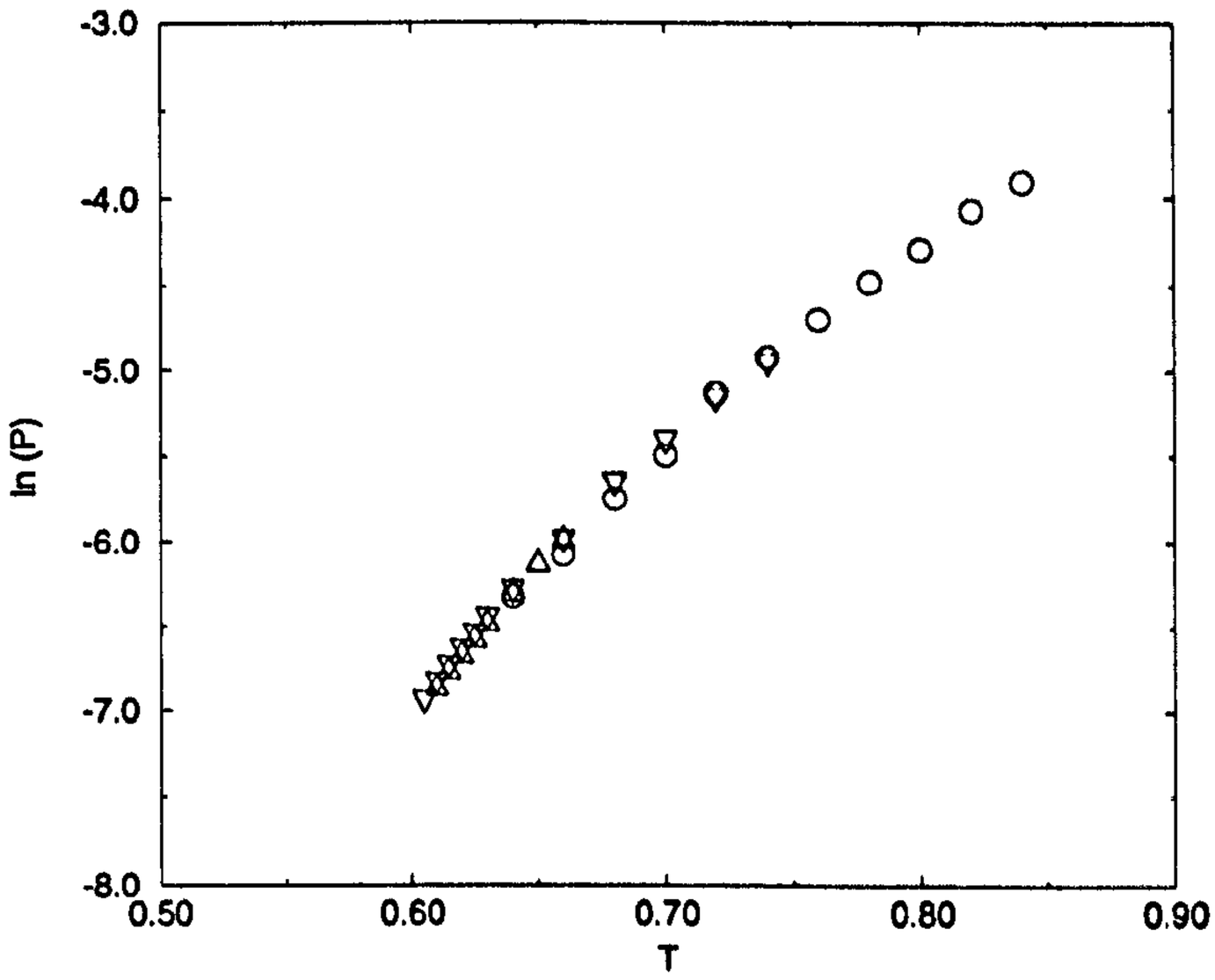

Figure 4.5: Semi-logarithmic plot indicating the coexisting vapour pressure as a function of temperature for the $\kappa' = 1$ fluid. Circles represent values obtained by GEMC, down-triangles indicate GD results on reducing the temperature and up-triangles show GD results on increasing the temperature.

T	P	ρ_v	ρ_l	u_v	u_l	S
$\kappa' = 1.25$ (cooling)						
0.680†	0.006909	0.0128(1)	0.2111(7)	-0.366(4)	-4.09(1)	0.105(3)
0.670†	0.006092	0.0112(1)	0.2168(5)	-0.329(3)	-4.21(1)	0.074(3)
0.650†	0.004670	0.0085(1)	0.2253(6)	-0.258(3)	-4.43(1)	0.142(5)
0.630†	0.003517	0.0064(0)	0.2339(6)	-0.200(2)	-4.64(1)	0.095(6)
0.610	0.002578	0.00471	0.2407(6)	-0.1512	-4.81(1)	0.147(7)
0.600	0.002225	0.00409	0.2446(7)	-0.1340	-4.93(2)	0.131(7)
0.590	0.001902	0.00352	0.2464(7)	-0.1176	-4.98(2)	0.142(5)
0.580	0.001615	0.00301	0.2541(7)	-0.1029	-5.18(2)	0.165(9)
0.570	0.001363	0.00256	0.2546(6)	-0.0890	-5.20(1)	0.104(5)
0.560	0.001140	0.00216	0.2574(6)	-0.0783	-5.29(1)	0.117(6)
0.550	0.000944	0.00181	0.2602(6)	-0.0664	-5.36(1)	0.166(6)
0.540	0.000771	0.00149	0.2797(7)	-0.0580	-5.95(2)	0.589(6)
0.530	0.000613	0.00120	0.2964(5)	-0.0474	-6.46(2)	0.745(3)
0.520	0.000477	0.00095	0.2992(4)	-0.0361	-6.54(1)	0.754(3)
0.510	0.000367	0.00074	0.2976(6)	-0.0294	-6.51(2)	0.736(4)
0.500	0.000281	0.00057	0.3049(5)	-0.0278	-6.72(1)	0.784(3)
0.490	0.000211	0.00044	0.3115(4)	-0.0701	-6.95(1)	0.818(2)
$\kappa' = 1.25$ (heating)						
0.570	0.001348	0.00253	0.2533(6)	-0.0890	-5.17(2)	0.109(4)
0.560	0.001130	0.00214	0.2599(7)	-0.0776	-5.34(2)	0.176(6)
0.550	0.000935	0.00179	0.2652(5)	-0.0663	-5.53(1)	0.318(6)
0.540	0.000762	0.00148	0.2771(6)	-0.0544	-5.87(2)	0.528(7)
0.530	0.000607	0.00119	0.2971(5)	-0.0460	-6.47(1)	0.755(3)
0.520	0.000476	0.00094	0.2973(4)	-0.0403	-6.48(1)	0.729(3)
0.510	0.000368	0.00074	0.3012(4)	-0.0308	-6.62(1)	0.773(2)
$\kappa' = 1$ (cooling)						
0.740†	0.007237	0.0123(1)	0.2145(6)	-0.389(6)	-4.60(2)	0.067(2)
0.720†	0.005733	0.0095(1)	0.2243(5)	-0.315(4)	-4.86(1)	0.067(2)
0.700†	0.004432	0.0073(1)	0.2298(5)	-0.250(4)	-5.00(1)	0.089(3)
0.680†	0.003390	0.0057(1)	0.2384(4)	-0.197(3)	-5.26(1)	0.109(4)
0.660†	0.002526	0.0043(1)	0.2454(8)	-0.157(6)	-5.45(2)	0.111(7)
0.640	0.001847	0.00312	0.2565(4)	-0.1170	-5.82(1)	0.282(4)
0.630	0.001573	0.00268	0.2826(4)	-0.1016	-6.72(1)	0.685(4)
0.625	0.001431	0.00244	0.2880(6)	-0.0949	-6.90(2)	0.721(4)
0.620	0.001302	0.00223	0.2892(5)	-0.0871	-6.93(2)	0.713(4)
0.615	0.001179	0.00203	0.2940(4)	-0.0791	-7.11(1)	0.767(3)
0.610	0.001065	0.00184	0.2941(4)	-0.0727	-7.12(1)	0.768(2)
0.605	0.000959	0.00166	0.2989(4)	-0.0678	-7.28(1)	0.787(2)
$\kappa' = 1$ (heating)						
0.660	0.002566	0.00431	0.2450(6)	-0.1536	-5.44(2)	0.101(3)
0.650	0.002227	0.00376	0.2479(5)	-0.1366	-5.53(1)	0.122(7)
0.640	0.001877	0.00318	0.2859(3)	-0.1334	-6.82(1)	0.727(4)
0.630	0.001569	0.00267	0.2902(5)	-0.1019	-6.97(2)	0.756(2)
0.625	0.001427	0.00244	0.2872(4)	-0.0929	-6.87(1)	0.711(2)
0.620	0.001296	0.00222	0.2914(6)	-0.0864	-7.01(2)	0.747(5)
0.615	0.001177	0.00202	0.2914(4)	-0.0808	-7.02(1)	0.740(3)
0.610	0.001065	0.00184	0.2925(4)	-0.0727	-7.06(1)	0.746(2)

Table 4.2: Simulation details and data obtained for GB fluids with $\kappa = 3$ and values of κ' as shown using the Gibbs-Duhem integration technique. Runs labelled † were implemented with the full GD scheme, the remainder with the VEOS scheme. T is the temperature, P the pressure, ρ_v and ρ_l the vapour and liquid densities, u_v and u_l the corresponding configurational energies per particle, and S the orientational order parameter.

the curve.

A similar procedure was followed for the $\kappa' = 1.25$ case. Here, the starting point was the GEMC run at $T = 0.69$, where the vapour configuration contains 321 particles, and the liquid 191 particles. The VEOS scheme was introduced at $T = 0.61$ and the temperature was reduced to a minimum of $T = 0.49$. In this case, the onset of nematic order was observed at $T = 0.54$, where the order parameter took a value $S = 0.589 \pm 0.006$. A return path was followed from $T = 0.50$ to $T = 0.57$, and a degree of nematic order persisted at $T = 0.55$, with $S = 0.318 \pm 0.006$, but was lost by $T = 0.56$. Again, agreement with the GEMC data is good, as can be seen in Fig. 4.6. Agreement between the cooling and heating integration paths is good, with little hysteresis. The transition is not as sharp as in the $\kappa' = 1$ case. Again, the agreement of $P = 0$ results for $\kappa' = 1.25$ with the GD results is reasonable. The vapour pressure curve is shown in Fig. 4.7: again no dramatic effects of the I–N transition are seen, and the heating and cooling branches agree well.

4.3 Discussion

Thermodynamic integration by the Gibbs-Duhem method has been used to supplement investigations of the liquid-vapour properties of GB fluids with low values of κ' and other parameters fixed to $\kappa = 3, \mu = 2$ and $\nu = 1$ using Gibbs-ensemble Monte Carlo, and zero-pressure Monte Carlo simulations. The liquid-vapour coexistence curves are found to shift up in temperature, and hence for a given temperature the coexistence density range increases, as κ' is reduced. Although direct Gibbs ensemble simulation becomes impractical as the liquid density increases, the use of Gibbs-Duhem integration along the coexistence curve, backed up by zero-pressure Monte Carlo, provides strong evidence for nematic-vapour coexistence at sufficiently low temperatures for $\kappa' = 1$, 1.25. For higher values of κ' the nematic phase does not seem to extend to low enough temperature to intersect the liquid-vapour line; for $\kappa' = 2.5$ results of [2] provide evidence of a very narrow nematic range at $T = 0.7$ (but the critical point is clearly significantly lower than this, $T_c \approx 0.6$) while it is already known for $\kappa' = 5$ that the lower limit for nematic is $T_0 \approx 0.85$ while the critical point is depressed even lower at $T_c \approx 0.47$. As κ' increases, we expect to find the nematic region being pushed up to higher temperatures, while the

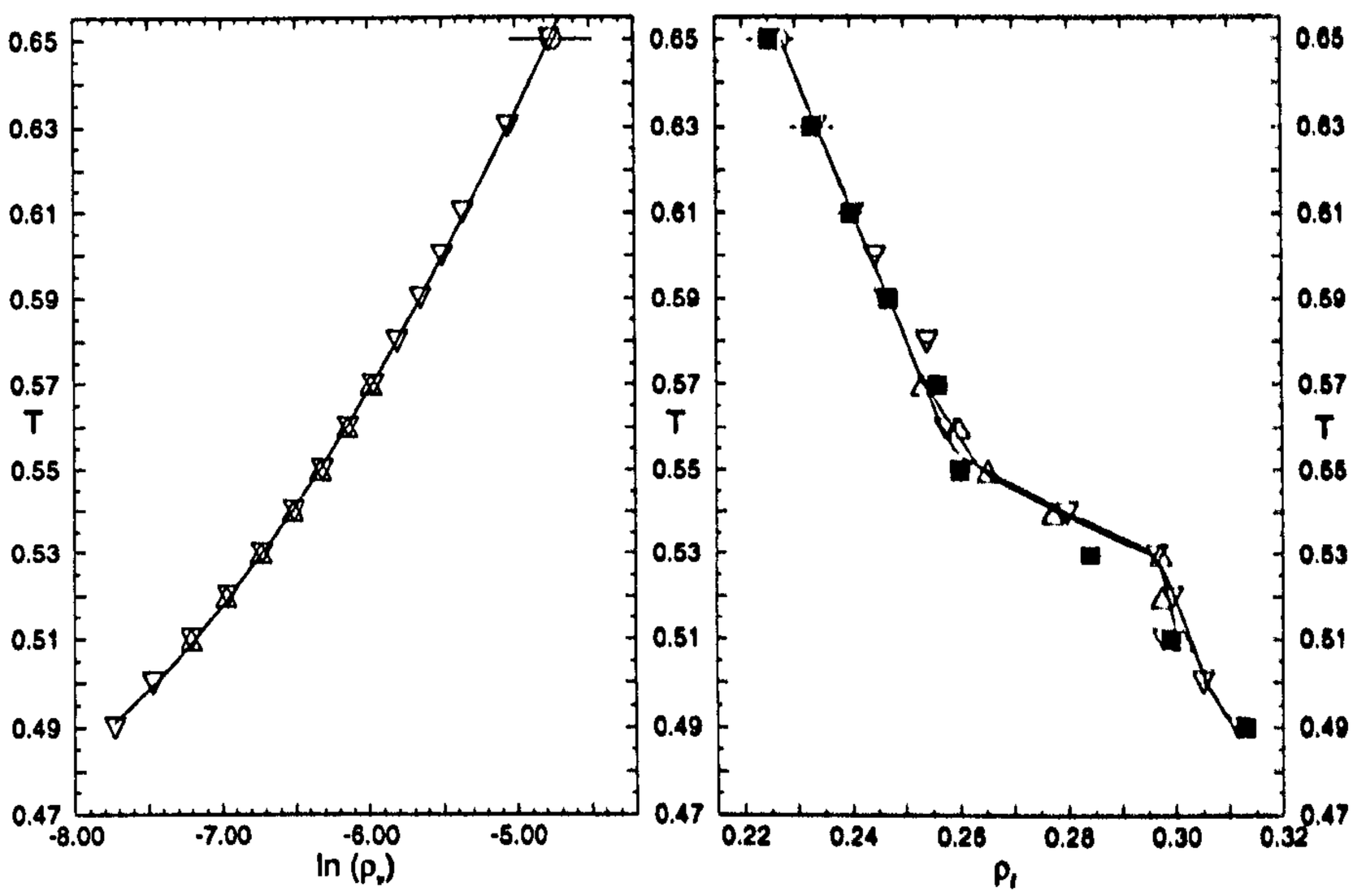

Figure 4.6: Detail of the liquid branch of the coexistence curve shown in Fig. 4.3 for the $\kappa' = 1.25$ fluid in the neighbourhood of the I–N transition. Symbols are as in Fig. 4.4

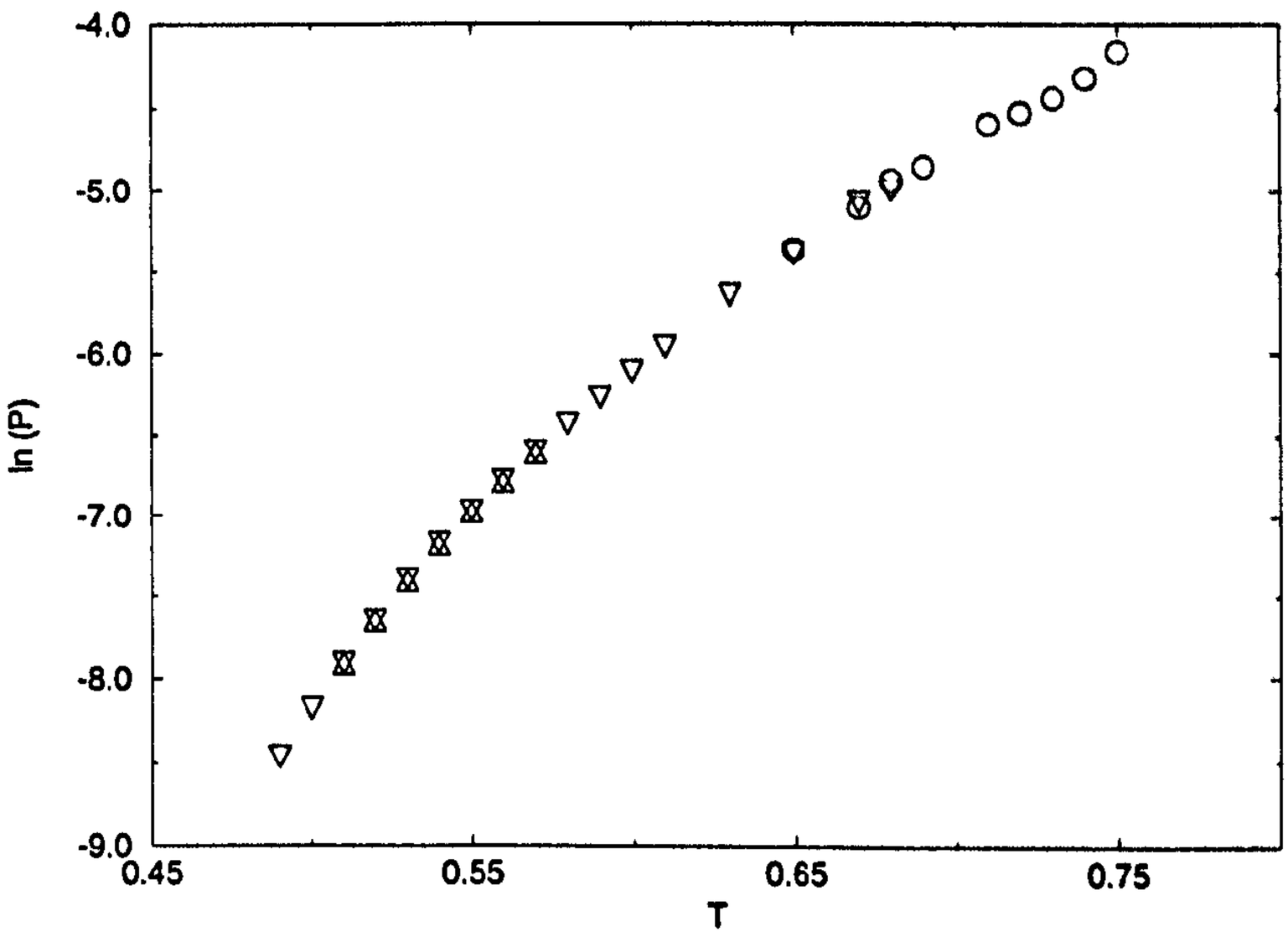

Figure 4.7: Semi-logarithmic plot indicating the coexisting vapour pressure as a function of temperature for the $\kappa' = 1.25$ fluid. Symbols are as in Fig. 4.5

liquid-vapour coexistence curves are further depressed.

The use of Gibbs-Duhem integration through the isotropic-nematic transition on the liquid branch is subject to the caveat that thermodynamic integration paths should be reversible. We have attempted to verify this by integrating up and down the coexistence curve very slowly, allowing ample time for the dense phase to equilibrate. There is some hysteresis, but the transition seems sufficiently weak that this is not a major problem, and it seems to be possible to rejoin the original branch of the coexistence curve having traversed the I–N transition both ways.

Together with other work presented in [2], these results give an outline of the salient points of the phase diagrams for the selected parameter values. In particular, the $\kappa' = 1$ and $\kappa' = 1.25$ systems should be capable of supporting a nematic-vapour interface, which opens up the possibility of studying liquid crystal surface properties.

Chapter 5

Effects of Elongation on the Phase Behaviour of Kihara and GBCE Fluids

As indicated in the previous chapter, despite the wide variety of model systems explored using computer simulation, the nematic phase is generally not stable at sufficiently low densities for nematic-vapour coexistence to be possible. From purely entropic arguments, the stability of the nematic phase is expected to persist to lower densities as the particle elongation moves away from unity. This has been clearly demonstrated for hard convex bodies [7, 82]. Although the Kihara potential and the earlier Gaussian overlap potentials have been widely used as reference systems for thermodynamic perturbation theories, there has little systematic study of the effect of elongation on the phase behaviour of these systems, with no exploration for nematic-vapour coexistence. In this chapter, the results of such studies are presented.

5.1 The Kihara Model

As indicated in §1.3.3, the Kihara potential is of Lennard-Jones form with the range variable replaced by the intermolecular distance of closest approach. This simple form can take reasonable account of the molecular shape; a major simplification is the total lack

of anisotropy in the well depth. Despite this, it is possible, with an appropriate choice of molecular core, to model a range of molecules using this form of interaction. The shape of the core is selected to match the molecular geometry. The second virial coefficient, B, is conveniently given in terms of the three fundamental measures of a hard convex body, (volume V_c, surface area S_c, and R_c, the integral of the mean curvature over the surface of the convex body). Selection of range and well-depth constants to fit experimental data for B of a specific molecule is thus made tractable [92]. For the purposes of this work, the core is taken as a spherocylinder of length L and diameter D, the total axial length being $L + D$. The behaviour of the fluid has been considered primarily for a 12-4 form, for which the range of attractions is greater than the usual 12-6 form.

Using NPT MC simulations, first investigations ware carried out using a 12-4 potential truncated at a cut-off distance, $s_c = 4$, where s is the minimum separation in reduced units with $D = 1$. Simulations were undertaken on $L/D = 5$ systems with $N = 1152$, at a range of pressures. The initial configuration was a randomly generated low density isotropic system, subsequently simulated at $T = 1.0$, $P = 1.0$. This was heated in steps of $\Delta T = 1$ and also used to start simulations at lower pressures.

The resulting equations of state are shown in Fig. 5.1 as functions of packing fraction, f, indicating the fraction of the system volume taken up by the particles:

$$f = \frac{N}{V} V_c \tag{5.1}$$

where V_c denotes the spherocylinder volume,

$$V_c = \frac{\pi}{6} D^2 \left(D + \tfrac{3}{2} L \right) . \tag{5.2}$$

This allows more direct comparison of results at different elongations for this convex-body potential. The equations of state indicate the smooth variation of thermodynamic properties with pressure over the range studied. In particular, the nematic order parameter remains close to zero indicating a lack of preferred orientation. The pressures used are not sufficiently high to observe the isotropic-nematic transition, (although orientational order is growing at the highest densities for $T = 1.0$), but it should be borne in mind that the main objective of these initial investigations was to search for nematic-*vapour* coexistence. At the lowest pressures the results follow a smooth curve, implying that these isotherms are super-critical, showing no liquid-vapour separation.

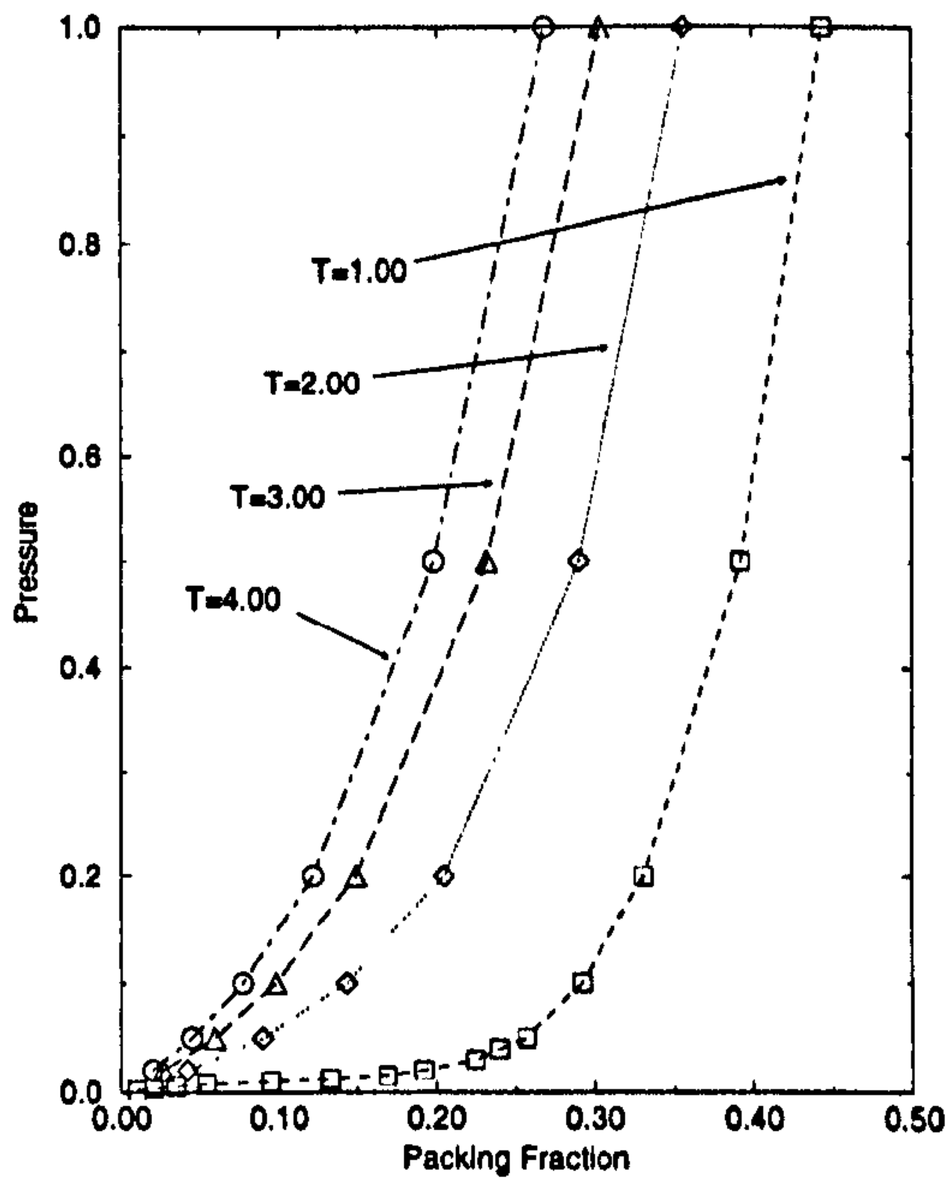

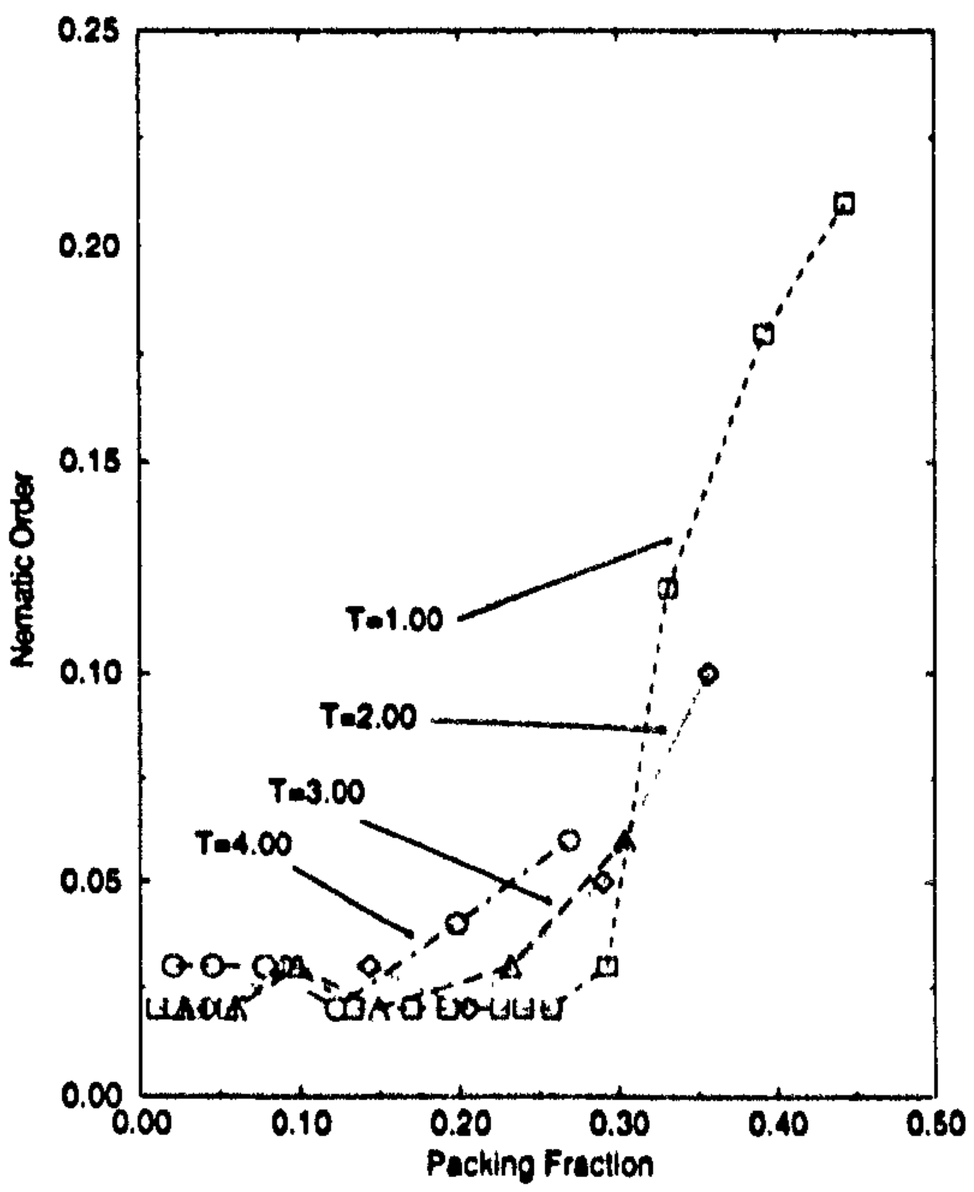

Figure 5.1: (a) Pressure as a function of packing fraction for Spherocylinder/Kihara 12-4 fluid with $L = 5$ for isotherms as labelled. (b) Corresponding values of nematic order parameter.

The liquid-vapour coexistence region of these fluids was investigated using the GEMC method. Runs were initiated from configurations generated at random at two distinct densities with a combined system size of $N_1 + N_2 = 1000$. In order to improve efficiency of particle exchange moves, an excluded-volume mapping scheme was used in which each spherocylinder was represented as a line of spheres and these used for rapid rejection of exchange moves resulting in significant overlap. The saving in CPU time is most significant at high densities, where $\sim 30\%$ reductions were found. For $L \geq 5.0$, temperatures below $T = 0.85$ still showed a low probability of successful particle exchange between boxes, rendering them too expensive to pursue. Having established stable phase separation at $T = 0.85$ the temperature was increased in steps of typically $\Delta T = 0.1$ until the simulations moved outside the coexistence envelope, (which in practice may be at $T < T_c$ if fluctuations become large). Initial configurations at higher elongations were taken from the next lowest elongation, and values of $L = 5.0, 5.5$ and 6.0 were considered. Run lengths of $5 - 10 \times 10^4$ sweeps were typically required to reach equilibrium with final averages taken over a further $5 - 10 \times 10^4$ sweeps. The results are indicated in Fig.s 5.2 - 5.4. For clarity, the estimated critical points are shown without error bars.

When a simple cut-off is employed, both the potential and pair-virial functions are made discontinuous at s_c. This may, depending on the density, make the averaged virial an unreliable route to the pressure since a particle may suddenly cross the cut-off boundaries of neighbouring particles - there is an impulsive contribution to the pressure. The measured pressures indicated above show this as the virial pressure measured without impulsive corrections are systematically higher in the liquid phase than in the vapour whilst the chemical potentials, measured by particle insertion probability, remain in broad agreement. The critical temperatures are falling slowly with increasing elongation: the estimated values are $T_c = 0.935 \pm 0.040$, $T_c = 0.920 \pm 0.032$ and $T_c = 0.905 \pm 0.011$ respectively for $L = 5.0, 5.5$ and 6.0. Corresponding packing fractions are $f_c = 0.12 \pm 0.05$, 0.11 ± 0.07 and 0.13 ± 0.03. The major source of uncertainty for the critical densities lies in the scatter of the rectilinear diameters, $(\rho_l + \rho_v)/2$ and the small number of reliable data points.

It is, of course, possible to avoid the effects of a discontinuous potential. Corrections for the long-range part of the potential, neglected when using a simple cut-off, may be included given the behaviour of the pair distribution function, $g(s)$, at separations $s \geq s_c$.

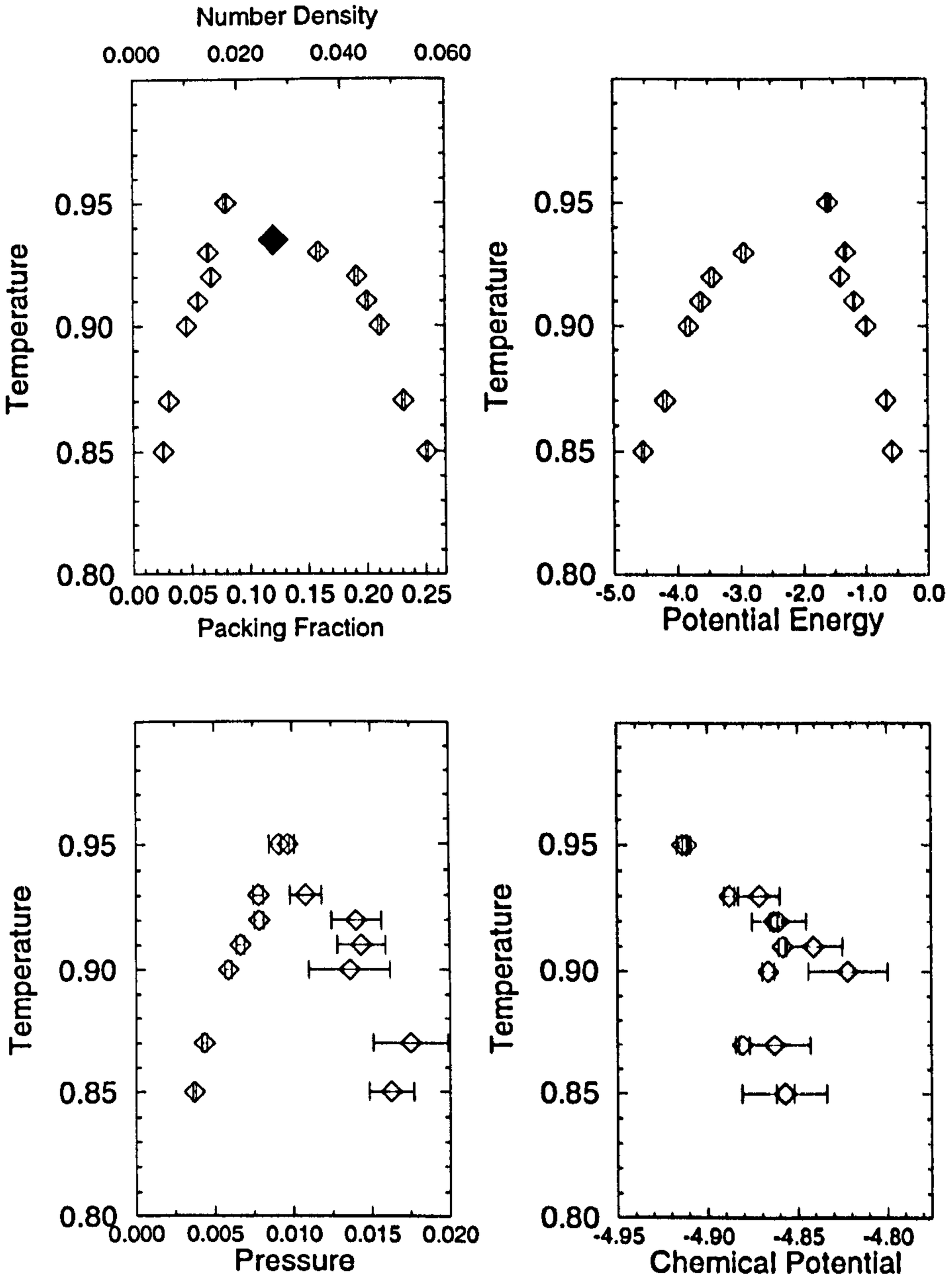

Figure 5.2: Liquid-vapour coexistence properties for Spherocylinder/Kihara 12-4 fluid with $L = 5.0$ from GEMC simulation.

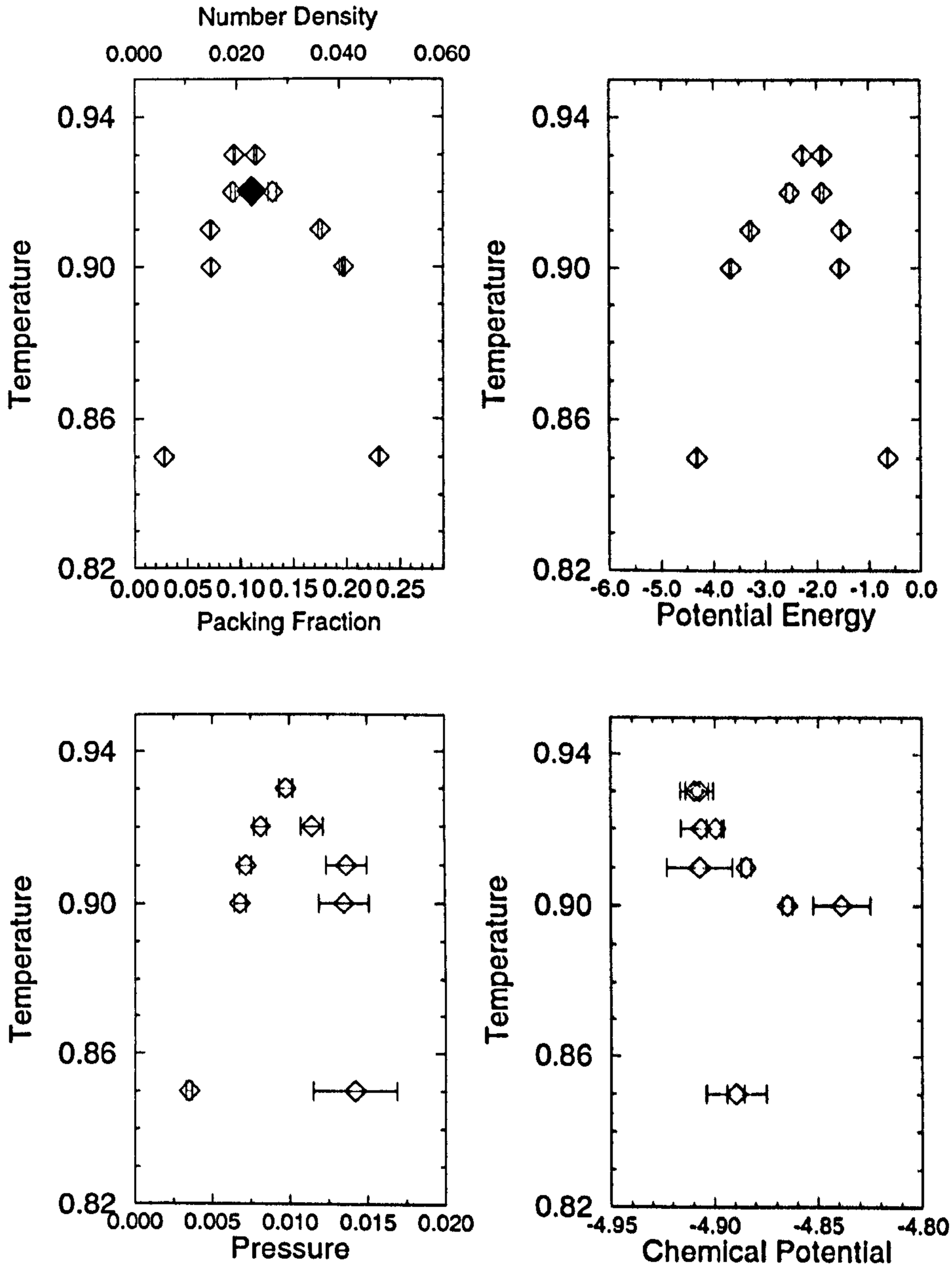

Figure 5.3: Liquid-vapour coexistence properties for Spherocylinder/Kihara 12-4 fluid with $L = 5.5$ from GEMC simulation.

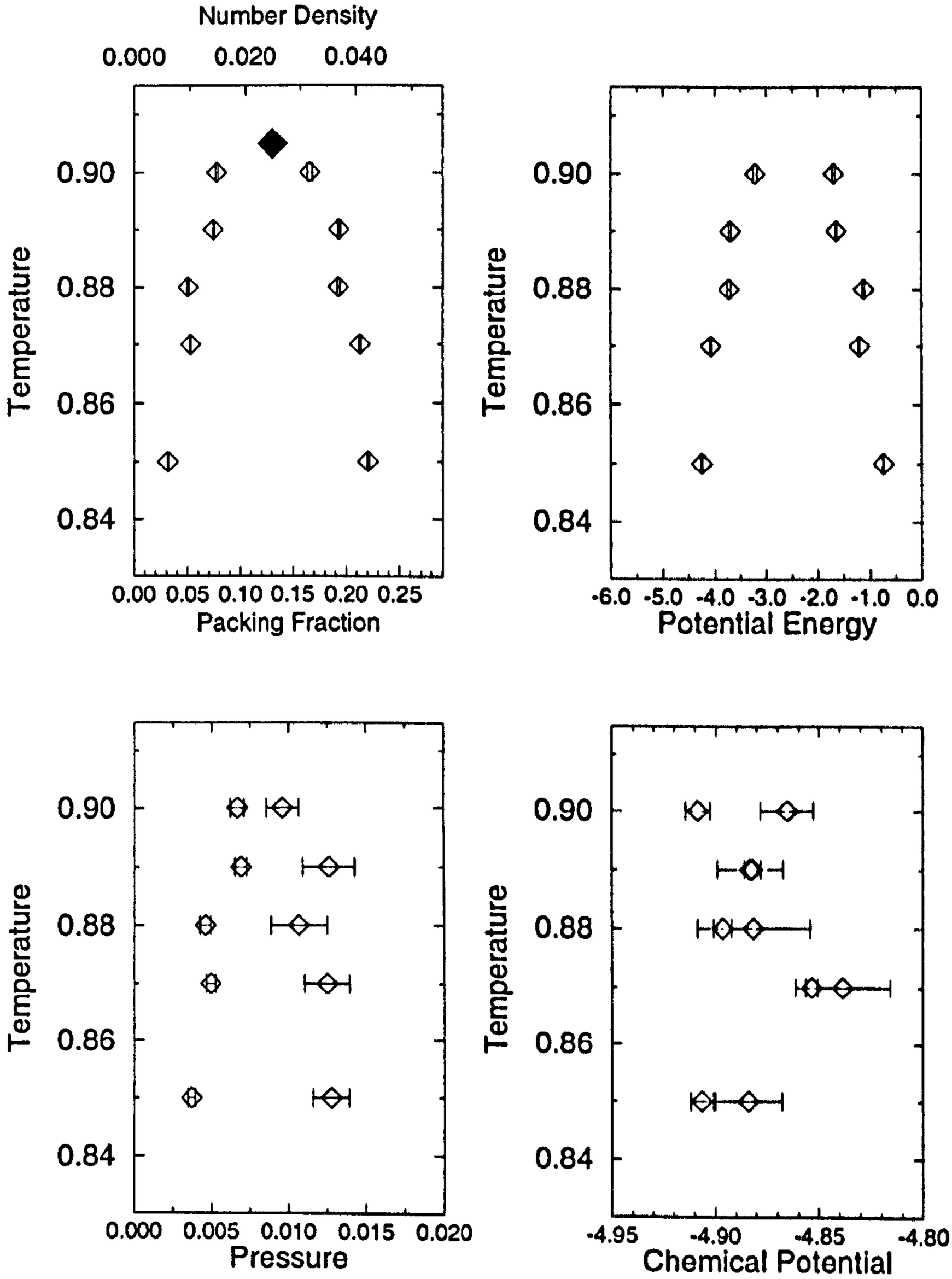

Figure 5.4: Liquid-vapour coexistence properties for Spherocylinder/Kihara 12-4 fluid with $L = 6.0$ from GEMC simulation.

If, as usual, it is taken to be uniform, the long-range corrections (LRCs) to the potential energy and pressure have the form [93]

$$\begin{aligned} U^{\text{tail}}/N &= \frac{1}{2}\frac{N}{V}\int_{\rho_c}^{\infty} d\rho\, U(\rho) S_{c+\rho+c} \\ P^{tail} &= \frac{1}{6}\left(\frac{N}{V}\right)^2 \int_{\rho_c}^{\infty} d\rho\, (dU/d\rho) 3V_{c+\rho+c} \end{aligned} \tag{5.3}$$

where $S_{c+\rho+c}$, the surface averaged over all relative orientations traced by the centre of one particle when it moves around another at constant distance, ρ, and $V_{c+\rho+c}$, the corresponding excluded volume, are

$$\begin{aligned} S_{c+\rho+c} &= 2S_c + 8\pi R_c^2 + 16\pi R_c \rho + 4\pi\rho^2 \\ V_{c+\rho+c} &= 2V_c + 2S_c R_c + \left(2S_c + 8\pi R_c^2\right)\rho + 8\pi R_c \rho^2 + 4\pi/3\rho^3 . \end{aligned} \tag{5.4}$$

For a spherocylinder $V_c = \pi/6D^2(D + 3L/2)$, $S_c = \pi D(D + L)$ and $R_c = \pi(2D + L)$.

Including these contributions, the virial pressure is in full agreement with the pressure measured by box scaling, (see §2.5.2). Again GEMC was used to map out the liquid-vapour coexistence envelope for elongations $L = 5.0, 5.5$ and 6.0 and the results are shown in Fig. 5.5 – 5.7. The critical temperatures measured for these systems are estimated as $T_c = 1.036 \pm 0.084, 0.997 \pm 0.068$ and 0.992 ± 0.143 respectively, with corresponding packing fractions of $f_c = 0.117 \pm 0.080, 0.09 \pm 0.24$ and 0.104 ± 0.102. Difficulties in maintaining phase separation near T_c lead to the large uncertainty in f_c for $L = 5.5$. In general, the effect of including the LRCs is to shift the coexistence curve up in temperature, as has been observed for the LJ fluid [94]. Although the attractive interactions are fully represented in this case, the liquid phase remains isotropic for the elongations studied. GEMC was also used to study the 12-6 Kihara system at $L = 0.8$ for $N_1 + N_2 = 512$. This is the system studied by Vega *et al.* [95], and as can be seen in Table 5.1, the results are in broad agreement.

Also shown in Fig. 5.5 and Table 5.2 are results obtained by Gibbs-Duhem integration for $L = 5.0$, starting from the GEMC data for $T = 0.97$ and cooling. Typically, 3–5×10^3 sweeps were required for the predictor-corrector algorithm to converge at a given temperature and a further $3 - 4 \times 10^4$ sweeps allowed for the production phase. At low temperature the measured chemical potential in the dense phase increases sharply. This

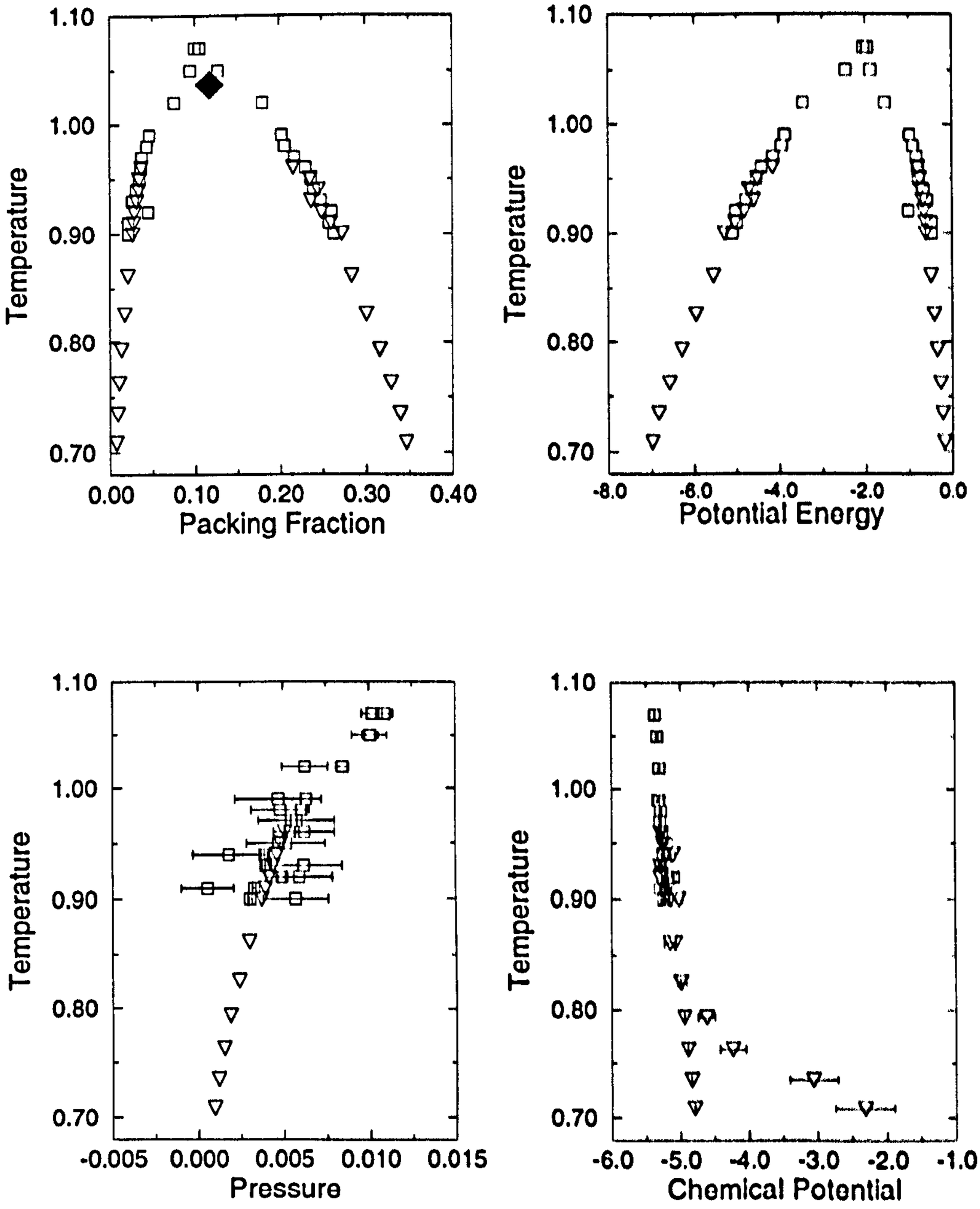

Figure 5.5: Liquid-vapour coexistence properties for Spherocylinder/Kihara 12-4 + LRC fluid with $L = 5.0$. Results of GEMC simulations are indicated by squares and GD integration by triangles. The estimated critical point is shown, without error bars, by the diamond.

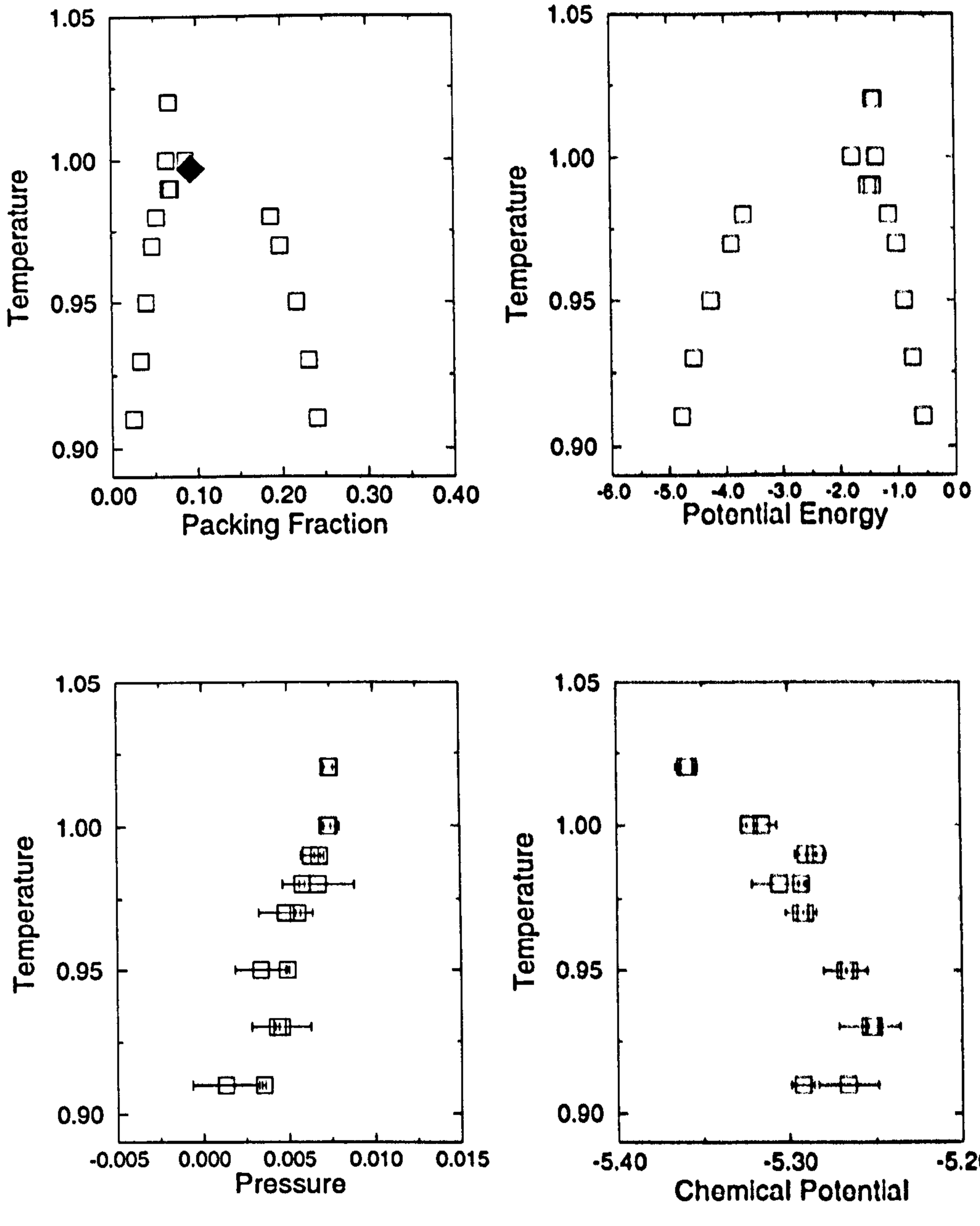

Figure 5.6: Liquid-vapour coexistence properties for Spherocylinder/Kihara 12-4 + LRC fluid with $L = 5.5$ from GEMC simulation.

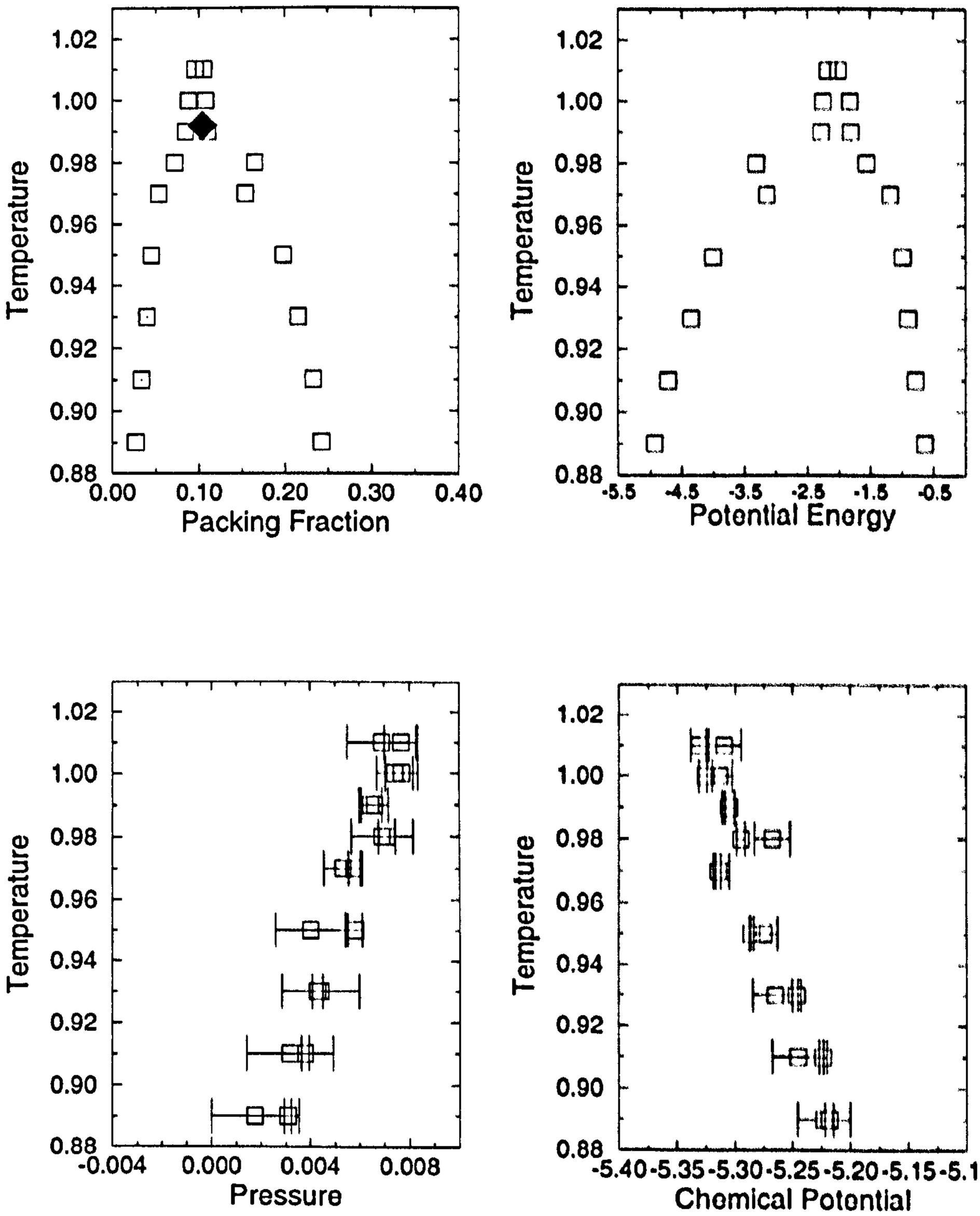

Figure 5.7: Liquid-vapour coexistence properties for Spherocylinder/Kihara 12-4 + LRC fluid with $L = 6.0$ from GEMC simulation.

Temperature	Packing Fraction	Number Density, ρ	ρ from [93]	Pressure, P	P from [93]	Chemical Potential, μ
0.825	0.0288(4)	0.0250(3)	0.025(1)	0.0152(4)	0.015(1)	-3.455(5)
	0.3344(7)	0.2903(6)	0.290(9)	0.013(6)	0.013(23)	-3.43(1)
0.875	0.0468(4)	0.0406(4)	0.035(2)	0.0241(5)	0.022(1)	-3.414(3)
	0.305(1)	0.265(1)	0.256(10)	0.020(7)	0.022(15)	-3.41(1)
0.920	0.0734(7)	0.0637(6)	0.064(3)	0.0346(9)	0.032(2)	-3.396(4)
	0.241(3)	0.209(3)	0.237(14)	0.035(5)	0.033(16)	-3.39(1)

Table 5.1: GEMC results for 12-6 + LRC Kihara system, L=0.8

is at high density, where particle insertion is expected to become a less efficient means of measuring μ. Note also the large fluctuations in measured pressure in the dense phase. Although now the LRCs are included, the effects of the discontinuity at s_c will still be present in measuring the average pair virial.

Even with LRCs, fluctuations in the liquid pressure are large. One further system was investigated to examine the size of these fluctuations. It is straightforward to construct a potential form which matches the original for $s \leq s_c$ but without discontinuities. One simple procedure is to generate a tail function, matching some low order polynomial to the potential and its derivative at some $s \leq s_c$ and going smoothly to zero at some subsequent s. This simplest choice for this tail function is a cubic, matching the usual potential at $s = a$, say, and going to zero at $s = b$. The potential is then given by

$$U_{CT}(s) = \begin{cases} 4\varepsilon\left(s^{-12} - s^{-6}\right), & s \leq a \\ \frac{U_a'}{(a-b)^2}\left(s^3 - (a+2b)\,s^2 + (2ab+b^2)\,s - ab^2\right) & \\ \quad + \frac{U_a}{(a-b)^3}\left(-2s^3 + 3\,(a+b)\,s^2 - 6abs + 3ab^2 - b^3\right), & a < s < b \\ 0, & s \geq b \end{cases} \tag{5.5}$$

where

$$U_a = 4\varepsilon\left(a^{-12} - a^{-6}\right) \tag{5.6}$$

Temperature	Required Pressure	Measured Pressure		Packing Fraction		Chemical Potential	
		Box 1	Box 2	Box 1	Box 2	Box 1	Box 2
0.96	0.005108	0.0052(2)	-0.0005(28)	0.0361(5)	0.216(2)	-5.277(4)	-5.30(2)
		0.0054(2)	0.0062(18)	0.0358(5)	0.230(1)	-5.274(6)	-5.27(3)
0.95	0.004879	0.0049(1)	0.0082(32)	0.0333(3)	0.236(2)	-5.264(3)	-5.25(4)
		0.0047(3)	0.0052(23)	0.0340(6)	0.237(1)	-5.254(5)	-5.20(2)
0.94	0.004643	0.0048(2)	0.0017(30)	0.0328(3)	0.245(1)	-5.232(4)	-5.11(3)
		0.0039(2)	0.0018(21)	0.0304(4)	0.240(1)	-5.256(4)	-5.24(2)
0.93	0.004407	0.0043(1)	0.0052(21)	0.0306(4)	0.2372(9)	-5.216(4)	-5.295(25)
		0.0040(2)	0.0062(22)	0.0257(3)	0.2478(8)	-5.284(6)	-5.29(3)
0.92	0.004188	0.0042(1)	0.0021(24)	0.0283(2)	0.2491(8)	-5.200(3)	-5.30(4)
0.91	0.003968	0.0038(1)	0.0047(26)	0.0271(3)	0.2598(9)	-5.176(4)	-5.176(44)
0.90	0.003760	0.00370(8)	0.0029(28)	0.0261(2)	0.2728(5)	-5.151(3)	-5.02(5)
0.86124	0.002995	0.00293(6)	0.0099(32)	0.0206(1)	0.2837(7)	-5.071(3)	-5.147(81)
0.82569	0.002384	0.00238(4)	0.0002(23)	0.0166(1)	0.3008(6)	-4.996(2)	-4.976(73)
0.79295	0.001883	0.00187(5)	-0.0061(44)	0.0131(1)	0.3164(6)	-4.934(4)	-5.22(13)
0.76271	0.001489	0.00149(2)	0.0062(31)	0.01030(5)	0.3292(5)	-4.883(2)	-4.23(19)
0.73469	0.001177	0.00118(1)	0.0022(36)	0.00840(3)	0.3395(5)	-4.830(2)	-3.06(35)
0.70866	0.000932	0.00094(1)	0.0020(29)	0.00674(3)	0.3465(5)	-4.786(2)	-2.32(43)

Table 5.2: Gibbs-Duhem (T) results for 12-4 + LRC Kihara system, L=5.00

and

$$U_a' = \left.\frac{dU}{ds}\right|_{s=a} = -\frac{24\varepsilon}{a}\left(2a^{-12} - a^{-6}\right) \tag{5.7}$$

Using a cubic tail (CT) is clearly a perturbation of the standard system. Losing the long-range attractions can be expected to bring the liquid-vapour coexistence curve down in temperature, but along with s_c, b must correspond to less than half the minimum box side to avoid self-interactions. Choosing $a = 2.5, b = 3.0$, test runs were performed using GEMC for a range of elongations. It appears, however, that the magnitude of the pressure fluctuations in the dense phase cannot be solely due to the use of a cut-off in the potential function, but is a genuine feature of the simulations. The evolution of the pressure and other quantities for a typical GEMC run with this system are shown in Fig. 5.8.

5.2 The GBCE Model

By fixing the ε parameter to a constant, the GB form reduces to one similar to the Gaussian overlap potential, except that one retains the GB rôle of the range parameter, i.e. shifting rather than dilating the potential well. This Gay-Berne Constant ε (GBCE) model is a computational simplification over pure GB. Figure 5.9 compares potential energy contours for GB and GBCE molecules, also indicating the GO and GOCE behaviour. The GBCE contours retain a non-ellipsoidal nature away from the core but this is less pronounced since the side-by-side well is not so highly favoured. Comparison with the GO potentials makes the shifting rather than dilating effect of σ clear.

The GBCE model was explored with particular attention on the nature of the liquid-vapour coexistence properties. Setting the elongation parameter to $\kappa = 1$ here gives the standard LJ potential, and this was used as the initial reference system. Liquid-vapour coexistence results from GEMC simulations are given in Table 5.3, showing agreement with those in the literature. These simulations include long-range corrections to the potential. To facilitate comparison with the results of Panagiotopoulos *et al.* [4], the cut-off was taken as half the box length, which will vary in the course of a GEMC simulation. The results shown are for a combined system size of $N_1 + N_2 = 300$; Panagiotopoulos *et al.* use $N_1 + N_2 = 500$. Typical run lengths for the present simulations are 1×10^5 equilibration sweeps with a further 5×10^4 production sweeps.

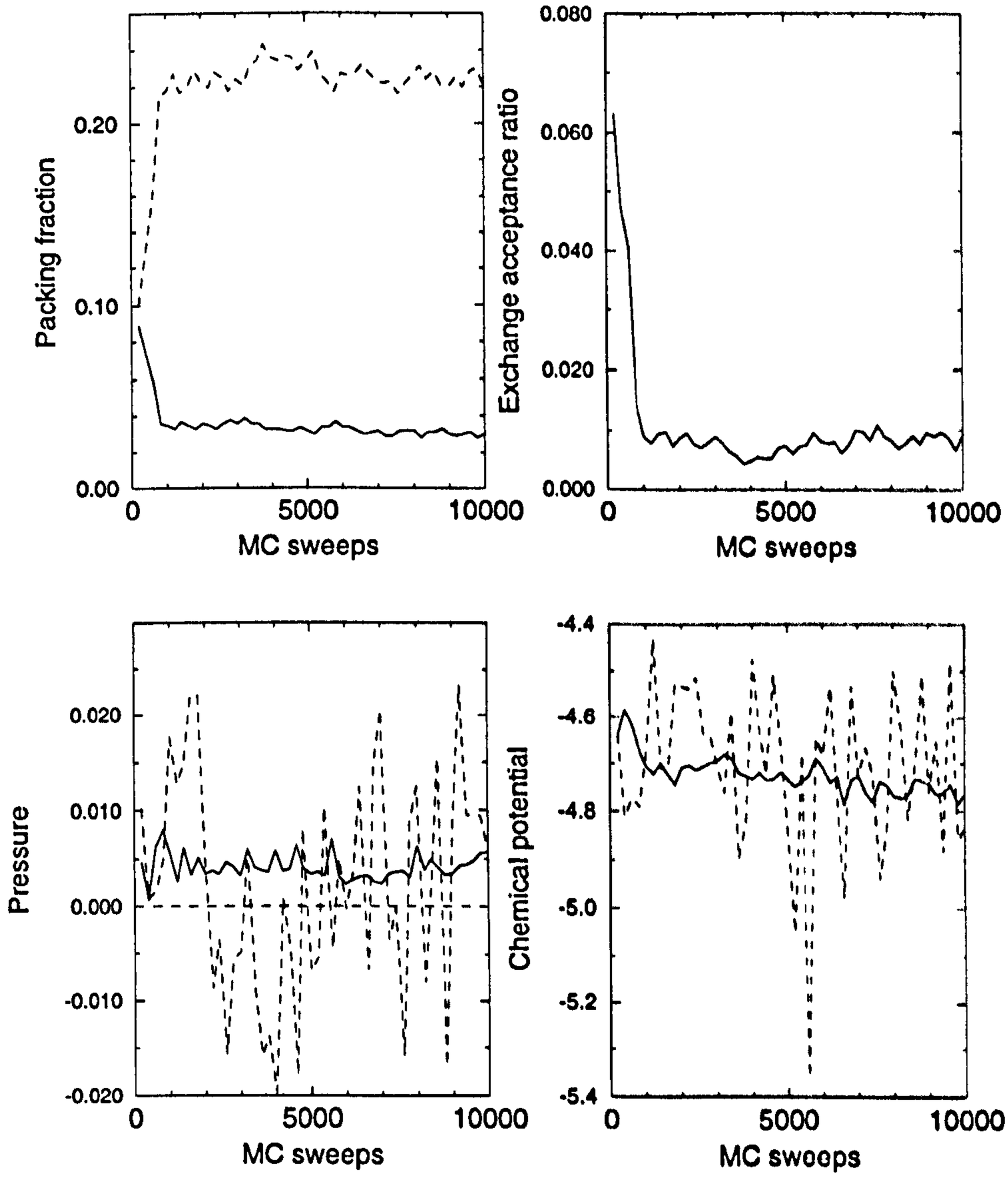

Figure 5.8: Evolution of liquid-vapour properties for Spherocylinder/Kihara 12-6 + CT fluid with $L = 5$, $T = 0.85$ during GEMC simulation.

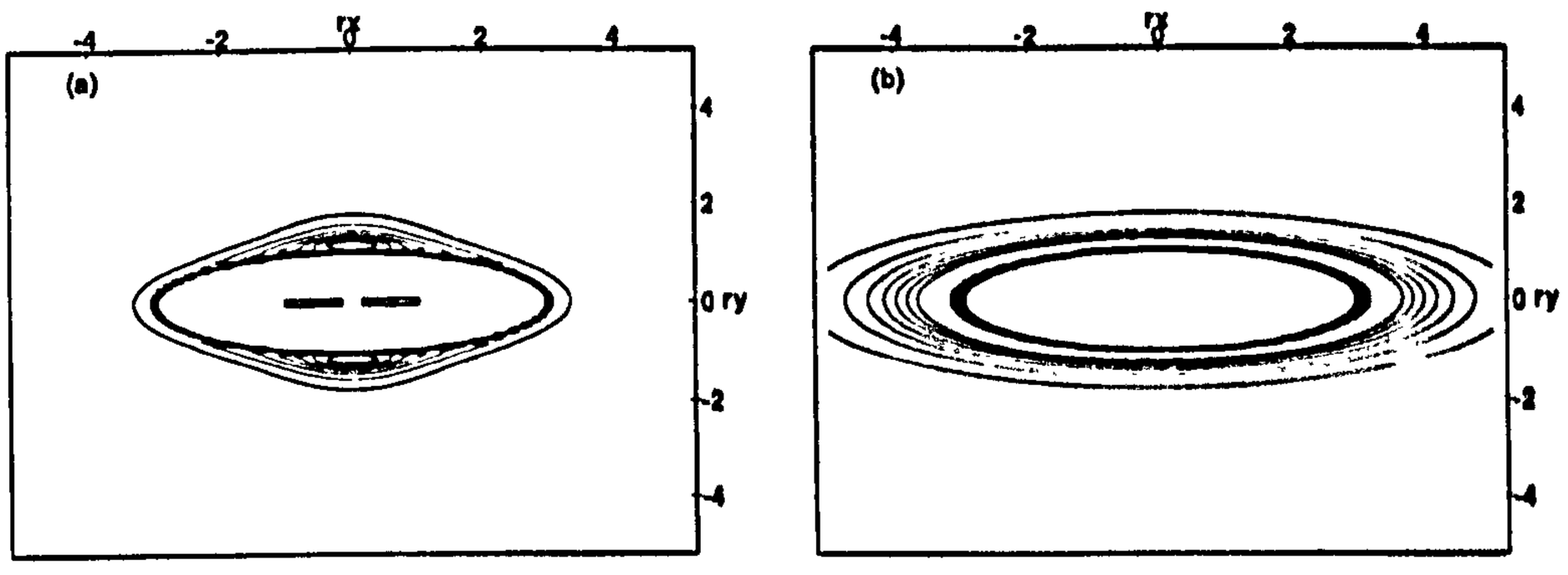

Figure 5.9: Potential energy contours for a pair of parallel molecules of elongation $\kappa = 3$ subject to different potentials : (a) Gay-Berne, (b) Gaussian Overlap, (c) Gay-Berne Constant ϵ and (d) Gaussian Overlap Constant ϵ. Contours are shown in units of ϵ_0 at intervals of 0.2 in the range (-1.4,1.0); potentials (c) and (d) do not extend below $-\epsilon_0$.

Property	Temperature			
	0.90	1.00	1.15	1.25
ρ_v	0.0142(3)	0.0292(4)	0.073(2)	0.149(4)
	0.0151(3)	0.0291(6)	0.072(9)	0.148(3)
P_v	0.0115(3)	0.0247(4)	0.063(2)	0.100(3)
	0.0123(6)	0.0246(12)	0.059(3)	0.101(6)
u_v	-0.142(5)	-0.277(7)	-0.619(16)	-1.19(3)
	-0.145(15)	-0.275(18)	-0.632(9)	-1.18(3)
μ_v	-3.98(1)	-3.839(9)	-3.68(1)	-3.579(8)
	-3.95	-3.90	-3.70	-3.59
ρ_l	0.752(2)	0.703(2)	0.608(3)	0.51(1)
	0.758(9)	0.702(6)	0.605(9)	0.526(15)
P_l	0.012(23)	0.040(25)	0.064(23)	0.098(28)
	0.014(37)	0.024(27)	0.059(17)	0.108(20)
u_l	-5.31(1)	-4.91(1)	-4.18(2)	-3.46(7)
	-5.36(6)	-4.90(3)	-4.16(6)	-3.59(9)
μ_l	-3.96(3)	-3.85(2)	-3.67(1)	-3.57(2)
	-3.86	-3.85	-3.68	-3.56

Table 5.3: Gibbs ensemble simulation results for the spherical L-J system. In each case, the second line indicate the values of [4]

Having established this reference point, the elongation parameter, κ, was increased from unity in steps of 0.5. The potential was used in a cut-and-shifted form, with the cut-off at $\kappa+3/2$. In order to accommodate the larger cut-offs at higher κ, the combined system size was increased to 500 particles. Coexistence densities as a function of elongation are shown in Fig. 5.10 for two temperatures, extending to the greatest elongation for which the rate of particle exchange remains reasonable. Attempts to run at $T < 0.70$ also quickly became expensive and no reliable data were obtained. From the plotted curves, it is apparent that for given temperature there is a 'critical elongation', κ_c, above which there will be no liquid-vapour separation. This is a corollary of the coexistence curve shifting to lower temperatures with increasing elongation. The locations of the 'critical points' shown in the figure have been estimated assuming a critical exponent of 1/3 and the law of rectilinear diameters although few data points are available. This procedure gives large errors: $\sim 50\%$ in κ_c and larger in the corresponding ρ_c. In each case shown the liquid remained isotropic, with nematic order parameter values remaining below 0.1. Measured values of chemical potential and pressure remained in agreement between the coexisting phases, with fluctuations in the measured liquid pressure characteristically larger than in the vapour.

With GEMC effectively ruled out for the exploration of the coexistence regions of higher elongation fluids, two other methods were employed. Using NPT MC simulations, preliminary investigations of phase behaviour were performed for systems with greater elongation, concentrating on $\kappa = 4.5$ and 5.0. Initial configurations taken from systems previously equilibrated at constant density and low temperature, (typically $T = 0.3$), were used to start constant-pressure series of runs at $P = 0$ and $P = 0.2$. These in turn provided starting points for higher pressure runs. At each pressure, temperature was incremented in steps of typically 0.1. These results, using $N = 500$ and $r_c = \kappa + 3/2$, are shown in Fig. 5.11. The low gradient regions of these isobars indicate the liquid-vapour coexistence region. In all of these simulations, however, the nematic order parameter remained below 0.1, indicating that the fluid remains isotropic.

Direct simulation of coexistence was also employed. This was used to investigate the coexistence regions of systems with $\kappa \geq 3$, moving up in elongation with steps of 0.5. Even at quite low temperatures, there was no indication of solid-vapour coexistence as seen in

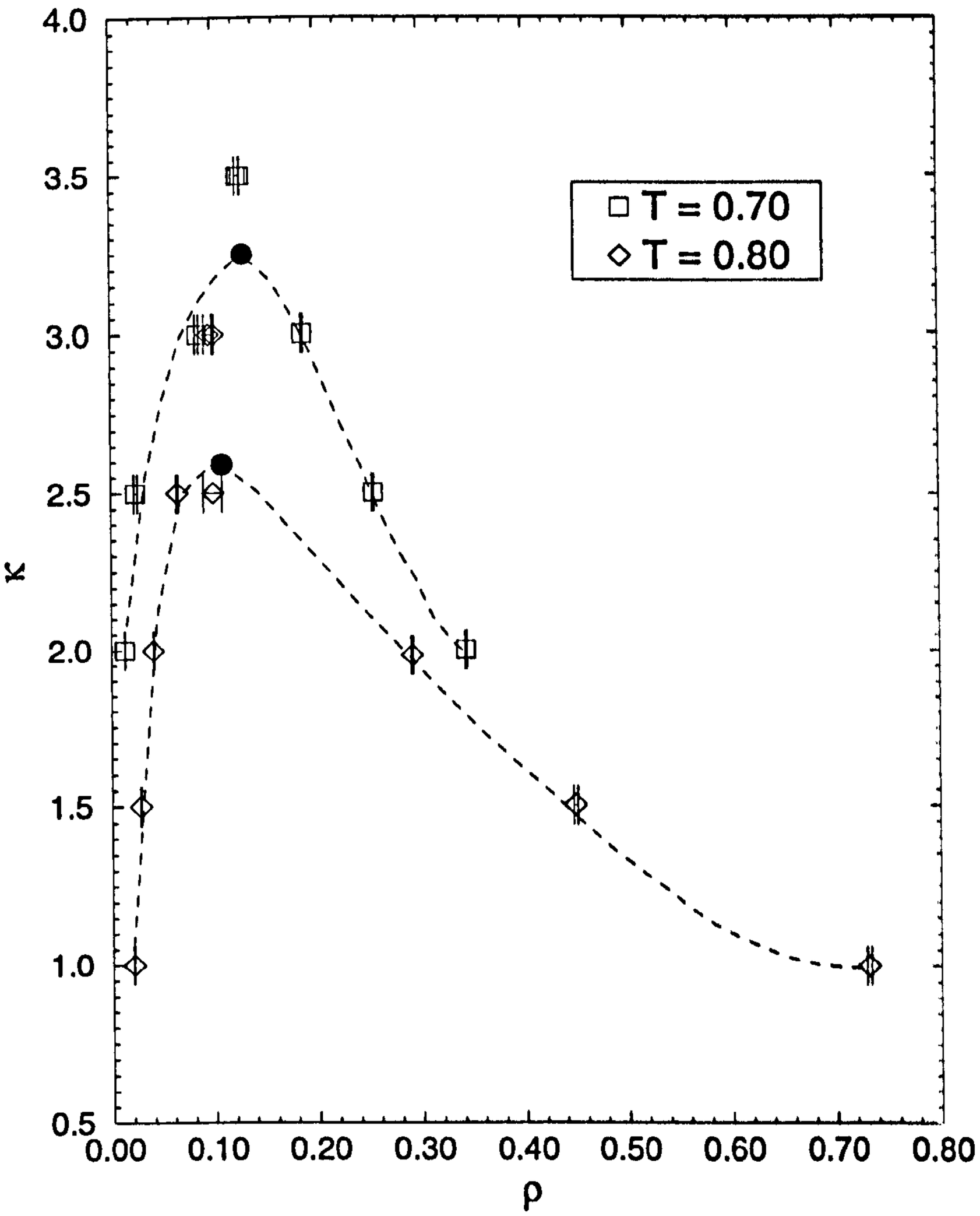

Figure 5.10: Coexistence densities for the GBCE system from GEMC simulation against elongation for temperatures $T = 0.70$ and $T = 0.80$. The filled circles are estimates of the 'critical points'.

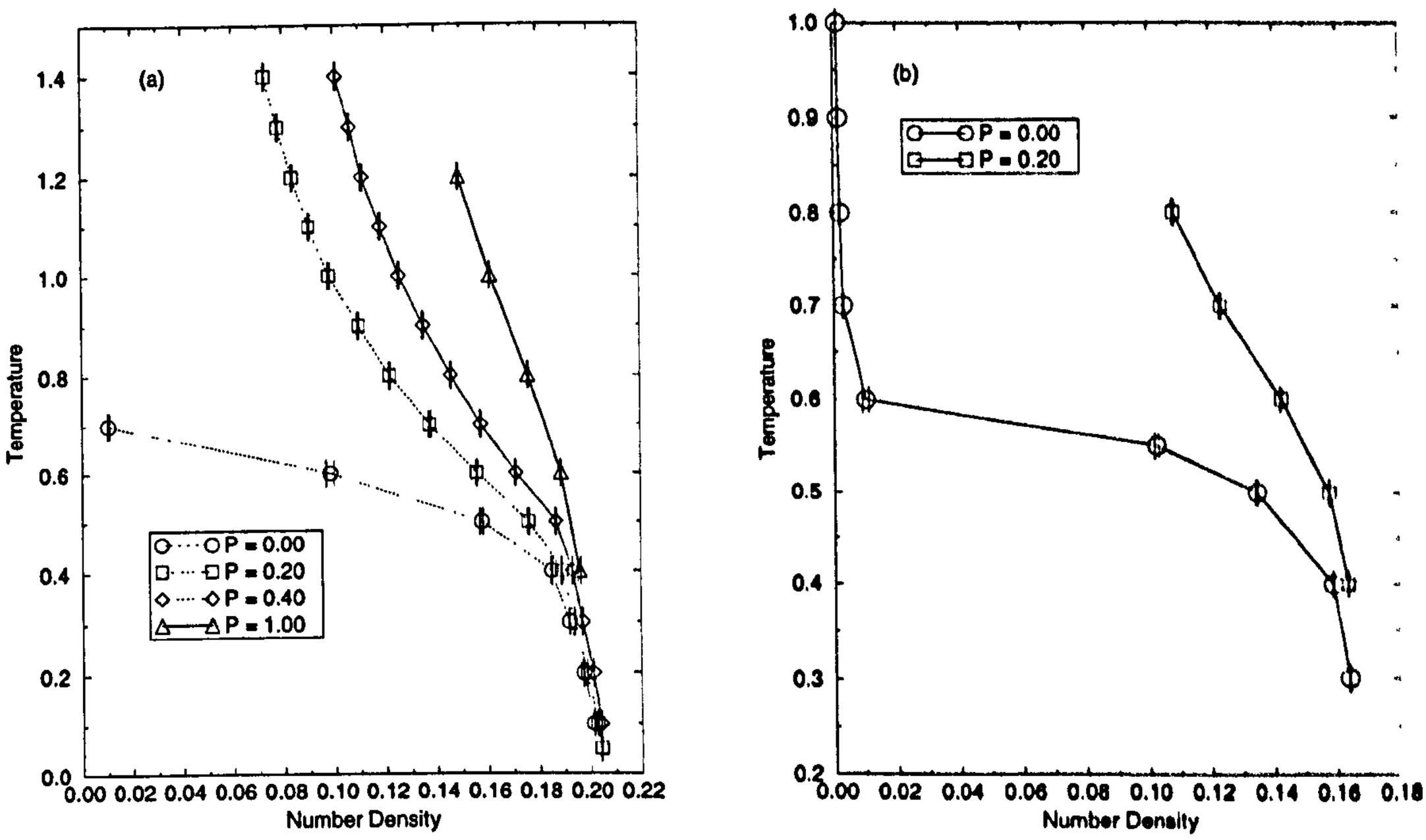

Figure 5.11: Variation of density with temperature along isobars as labelled for the GBCE system with (a) $\kappa = 4.5$ and (b) $\kappa = 5.0$.

the full Gay-Berne systems. In general, an isotropic liquid was in coexistence with a very low density vapour, so low that in many cases the vapour region of the box was almost entirely empty, making the usual fitting procedure using a tanh profile, an unreliable route to the vapour properties. A cautious upper limit on this density can be set by calculating the value that would result from a single particle in each vapour bin. The results of MD runs at constant box volume and constant temperature are indicated in Fig. 5.12 for an elongation of $\kappa = 4$ with the usual spherical cut-off at $r_c = \kappa + 3/2$ and a total of $N = 500$ particles. Equilibration was monitored via the pressure difference $\Delta P(z) = P_N(z) - P_T(z)$, (see §2.4), and evolution of the density profile. From the initial configuration, taken from $\kappa = 3.5$ at $T = 0.60$, the system was separately heated and cooled. The majority of these results were obtained using MC NVT; some MD simulations were performed to compare equilibration times, which were not found to differ significantly. Equilibration required $5 - 20 \times 10^4$ sweeps, (timesteps). Final averages were taken typically over a further 10^5 sweeps. In all cases the liquid remained isotropic, with the nematic order parameter remaining below $s = 0.05$. These long equilibration times make slab runs an expensive way to map out the coexistence curve. One reasonable strategy for reducing execution time is introduction of anisotropy in the cut-off, with a cut-and-shift based on $r - \sigma + 1$, the denominator in the potential, at the value obtained for a pair of parallel, end-to-end molecules separated by $\kappa + 3/2$, i.e. the same distance as the spherical case. In this configuration, $\sigma = \kappa$. For parallel molecules, sweeping out the cut-off boundary gives an ellipsoidal shell, but this will not be the case for a general pair configuration. The perturbation resulting from this change gives a slight downward shift of the coexistence curve in temperature, as can be seen in Fig. 5.13, where results are indicated for elongations of $\kappa = 4.0$ and 4.5. These systems contain a total of $N = 1000$ particles. Again, the liquid remained isotropic. A reduction in execution time accompanies the change in cut-off since the potential is calculated for fewer pairs. Savings of up to 10% were obtained for MD, with a less significant effect for MC.

The value of κ was further increased in steps of 0.5 to $\kappa = 6.5$ at $T = 0.40$. On making a step in κ a short run was performed using MD with a very small timestep, $\delta t = 0.0001$, to allow the system to relax from any overlaps incurred. This was followed, if necessary, by a density-setting stage in which the box dimensions were increased to allow

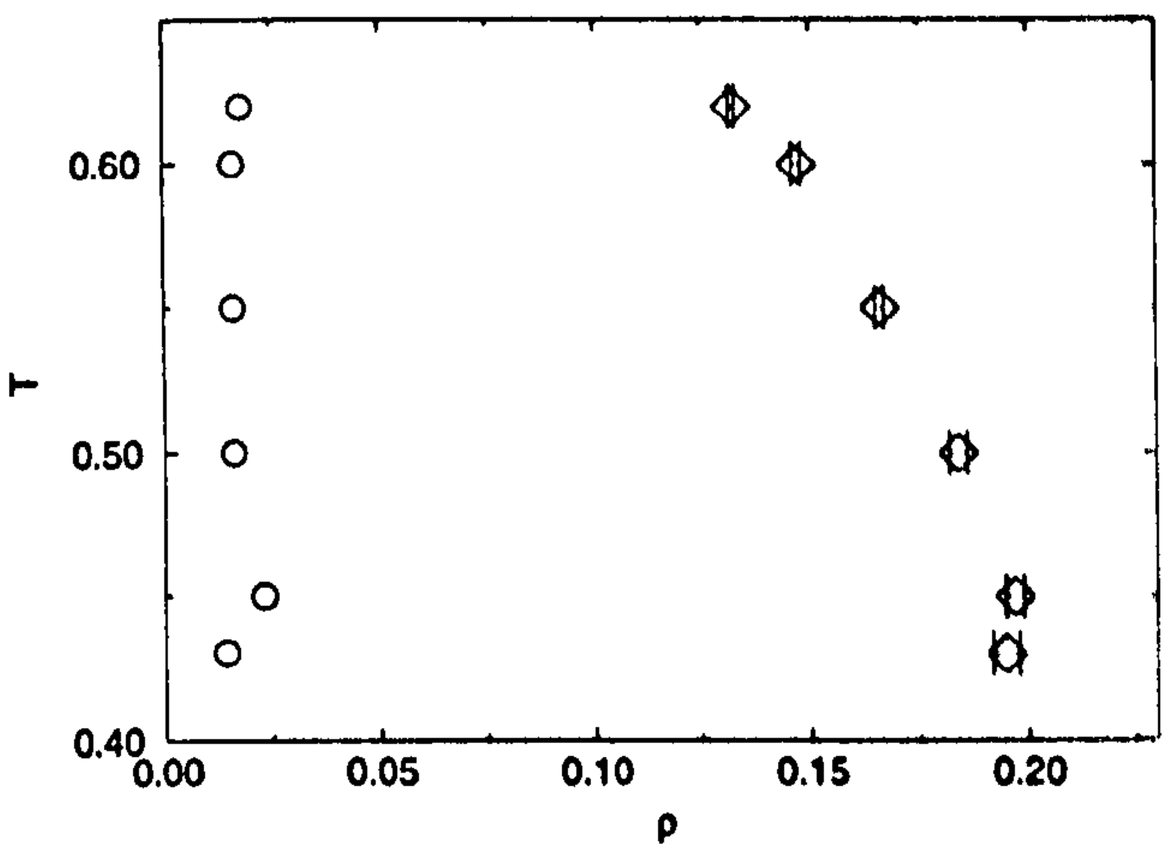

Figure 5.12: Liquid-vapour coexistence envelope for the GBCE system with $\kappa = 4.0$ and a spherical cut-off from slab simulations. Circles indicate upper-bounds on the vapour density, (see text for details).

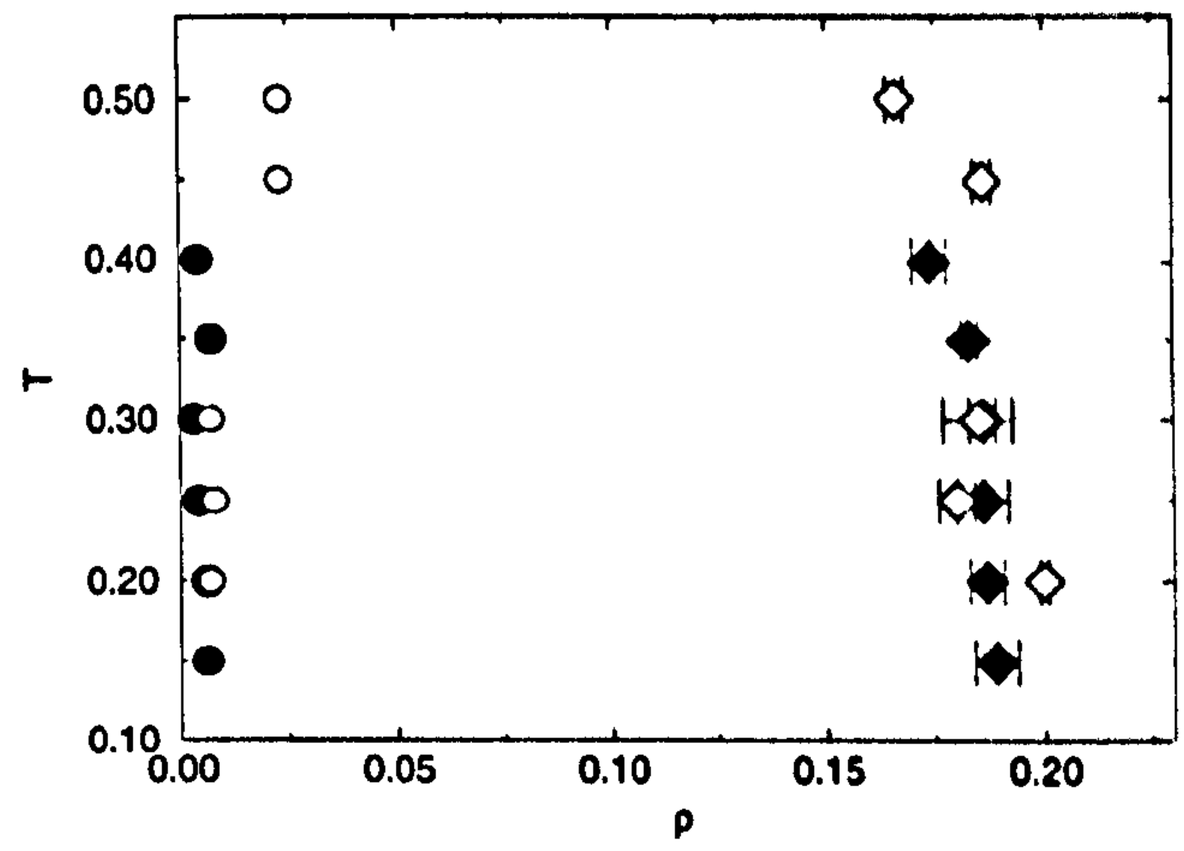

Figure 5.13: Liquid-vapour coexistence envelope for GBCE systems with $\kappa = 4.0$, (open symbols), and $\kappa = 4.5$, (filled symbols), and an $(r - \sigma + 1)$ cut-off from slab simulations. Circles indicate upper-bounds on the vapour density, (see text for details).

for the larger cut-off, maintained at $\kappa + 3/2$. Equilibration and production runs were then performed with $\delta t = 0.0015$. Total run lengths were typically $6 - 8 \times 10^4$ timesteps. After simulation at this temperature the system was heated, but for $\kappa \geq 5.5$, coexistence could not be established for temperatures $T \geq 0.60$, where a single isotropic fluid phase occupied the simulation cell. Visualization of two-phase configurations for $\kappa \geq 6.0$ clearly showed particles in the dense region associating in rosettes or clusters, oriented radially outward in three dimensions from a focal point. A snapshot of the $\kappa = 6.5$ system at $T = 0.50$ is shown in Fig. 5.14 illustrating these clusters, which appear to form a network through the phase. To study the mobility of this phase the average mean-squared displacement was calculated for particles in the slab. In the long-time limit this gives the diffusion coefficient, D_E, using the Einstein relation

$$2tD_E = \tfrac{1}{3} \left\langle |\mathbf{r}_i(t) - \mathbf{r}_i(0)|^2 \right\rangle . \tag{5.8}$$

Since these are inhomogeneous systems, albeit with very low vapour density, rather than attempting to extract a diffusion coefficient, the distribution of squared-displacements, d^2, was monitored over time. As expected, the distribution broadens from $t = 0$, but does not shift significantly from very low values, with $d^2 \leq 1$ for ~50% of particles after 5000 timesteps in both cases.

The number density of the dense phase in these systems is ~ 0.10. The isotropic phase of the $\kappa = 3$ GB fluid has a diffusion constant $\mathcal{O}(0.5)$ at these densities [34], indicating that the particles in this new phase are reasonably fixed in their positions: the isotropic value would lead to mean-squared-displacements of $\mathcal{O}(20)$ over $5000\delta t$. A small number of 'fast' particles were observed, due to the vapour phase.

Subsequently, the diffusive behaviour of the bulk system was examined for the $\kappa = 6.5$ fluid. The initial single phase configuration was generated by increasing the population of the vapour region of the $T = 0.40$ inhomogeneous system by random insertion to give $N = 1500$ and scaling the box to give a cube over 2000 timesteps. The final density was set to $\rho = 0.10$, close to that of the dense slab at this temperature, with the required scaling increasing the box x–y cross section whilst reducing z. This effectively separates

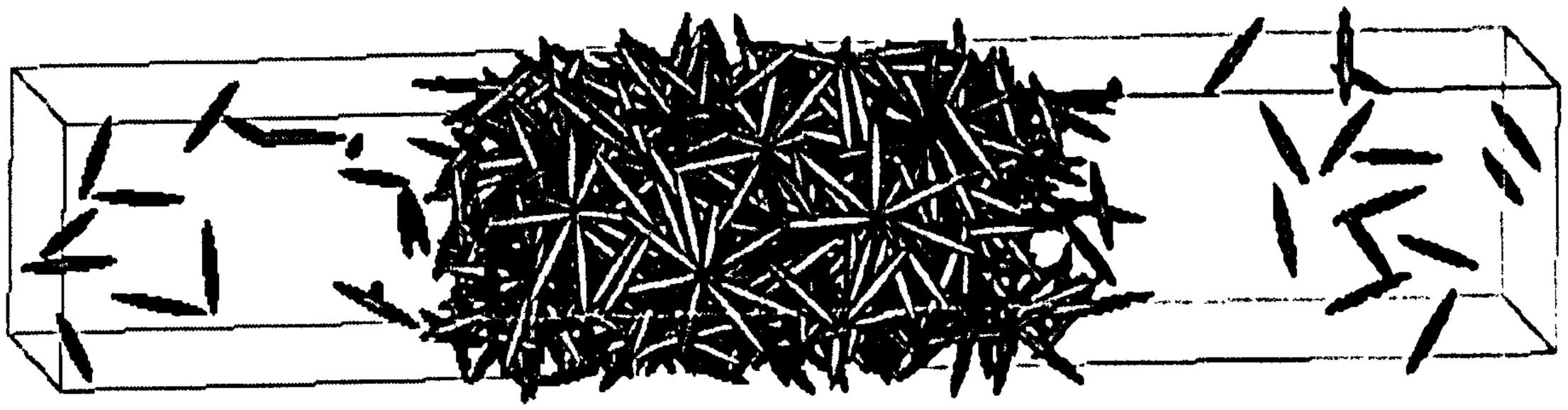

Figure 5.14: Snapshot of the equilibrium configuration of a slab simulation for GBCE with $\kappa = 6.5$ at $T = 0.50$.

the clusters, but after simulating at $T = 0.40$ for 2×10^4 timesteps using NVT MD, the clusters return. On expanding the box isotropically, to $\rho = 0.08$, the clusters persisted and in fact became increasingly established over the first 1×10^5 timesteps, indicating slow equilibration for this phase. The final configuration is illustrated in Fig. 5.15, and histograms of squared-displacement over the final 4×10^4 timesteps are indicated in Fig. 5.16. Examination of this final configuration indicates the presence of a small depleted region in the box, allowing a few particles to move relatively quickly for short periods of the simulation, giving significantly higher values of d^2. The evolution of the distribution is still very slow, as seen from the average values of d^2 plotted against simulation time in Fig. 5.17. The x, y and z components of d^2 are shown separately, indicating that none is preferred. The slope of the fitted line for d^2 yields a diffusion constant of $D_E = 0.0091 \pm 0.0002$. This would suggest the system to be in a solid or glass-like state. It should be possible to examine the shear elastic constant of the system to further characterize the phase, as reported in Chapter 3 for the GB system. Such investigations, however, could not be performed in the course of this project.

A further question is the extent to which the clusters percolate through the system. This was examined by using a sorting algorithm based on that developed to identify a liquid droplet in vapour [9]. Each particle is given a label indicating its group. There are N of these at the start, but this reduces as the particles are sorted by pairs according

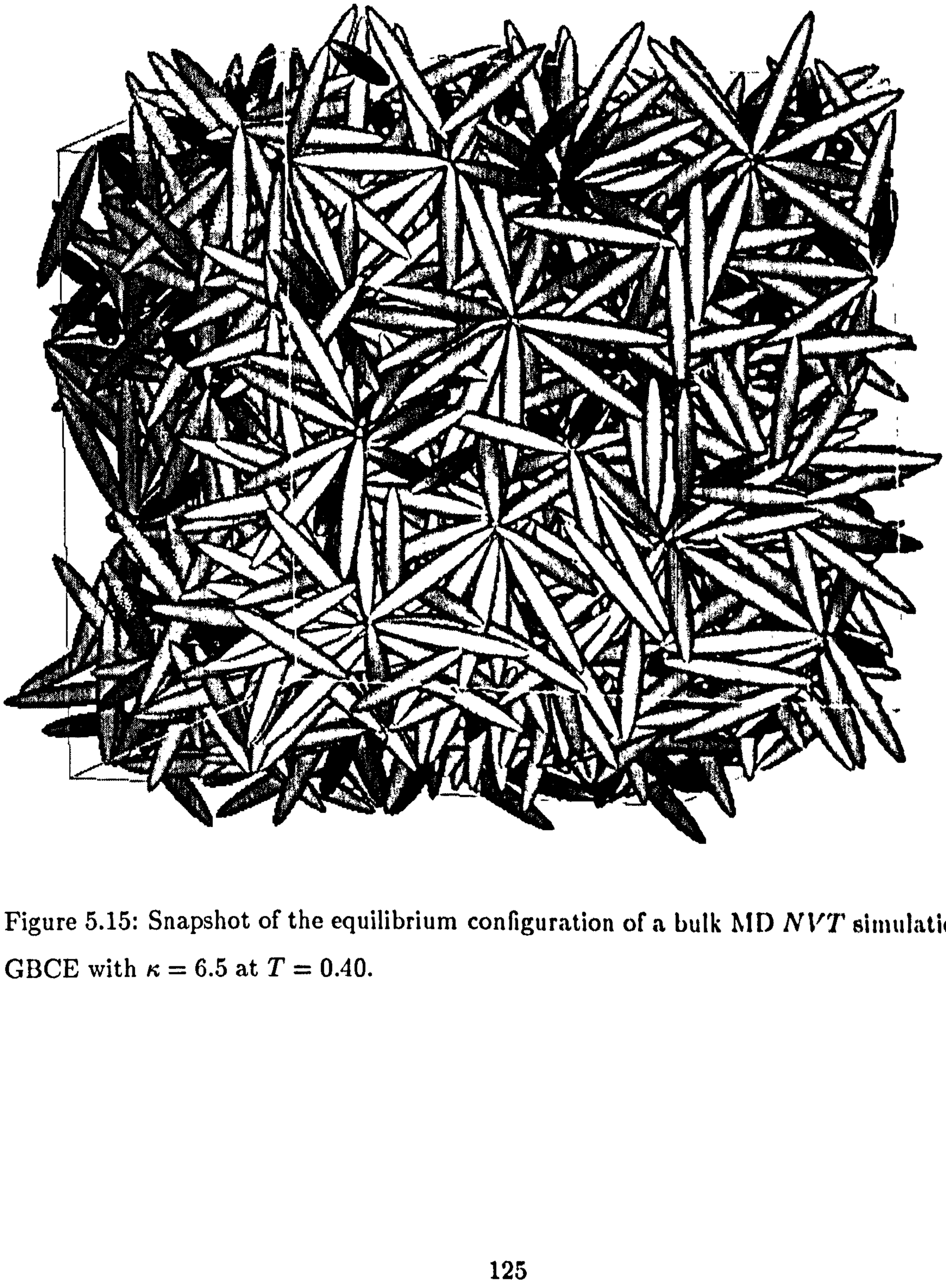

Figure 5.15: Snapshot of the equilibrium configuration of a bulk MD NVT simulation for GBCE with $\kappa = 6.5$ at $T = 0.40$.

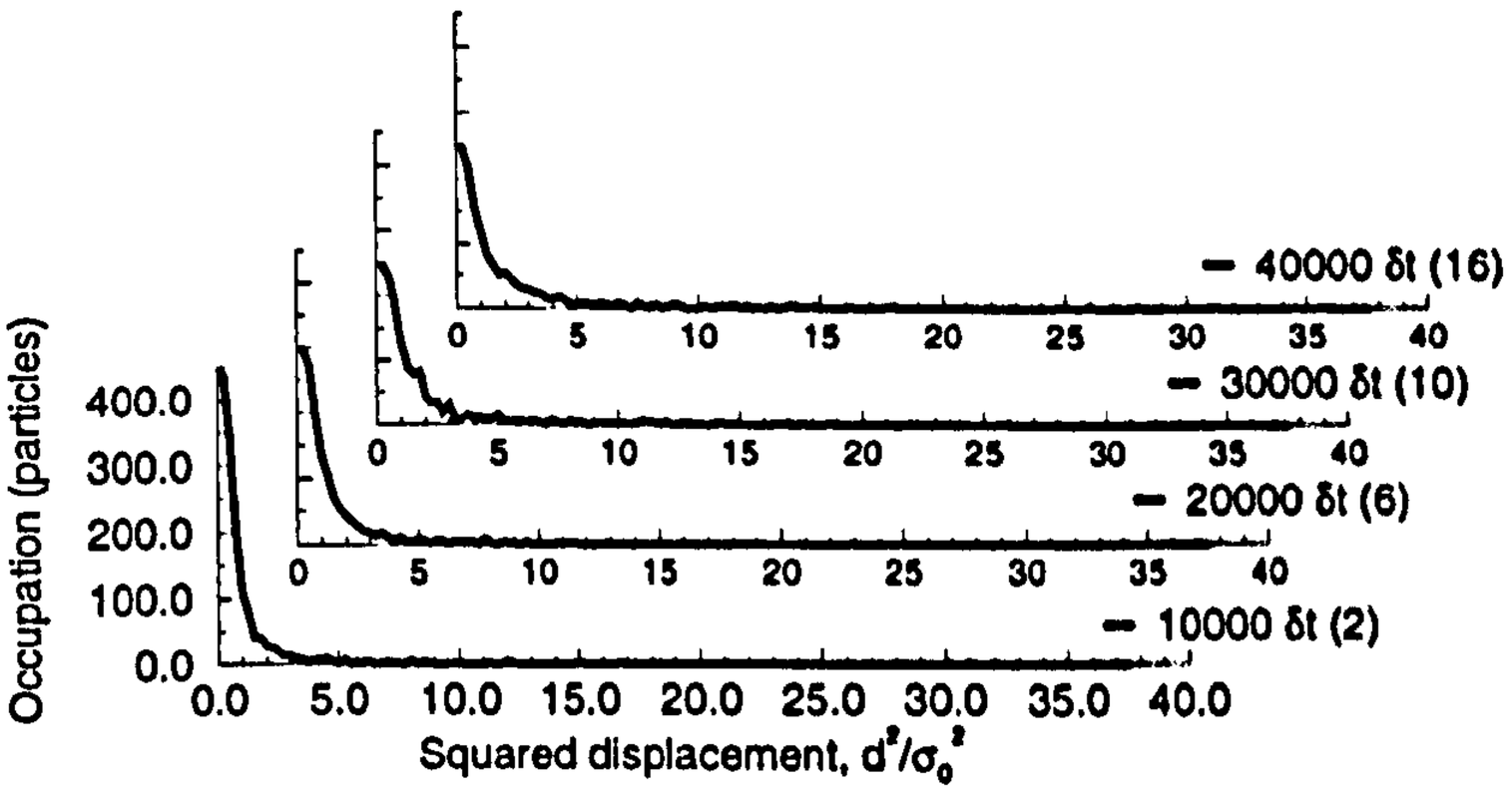

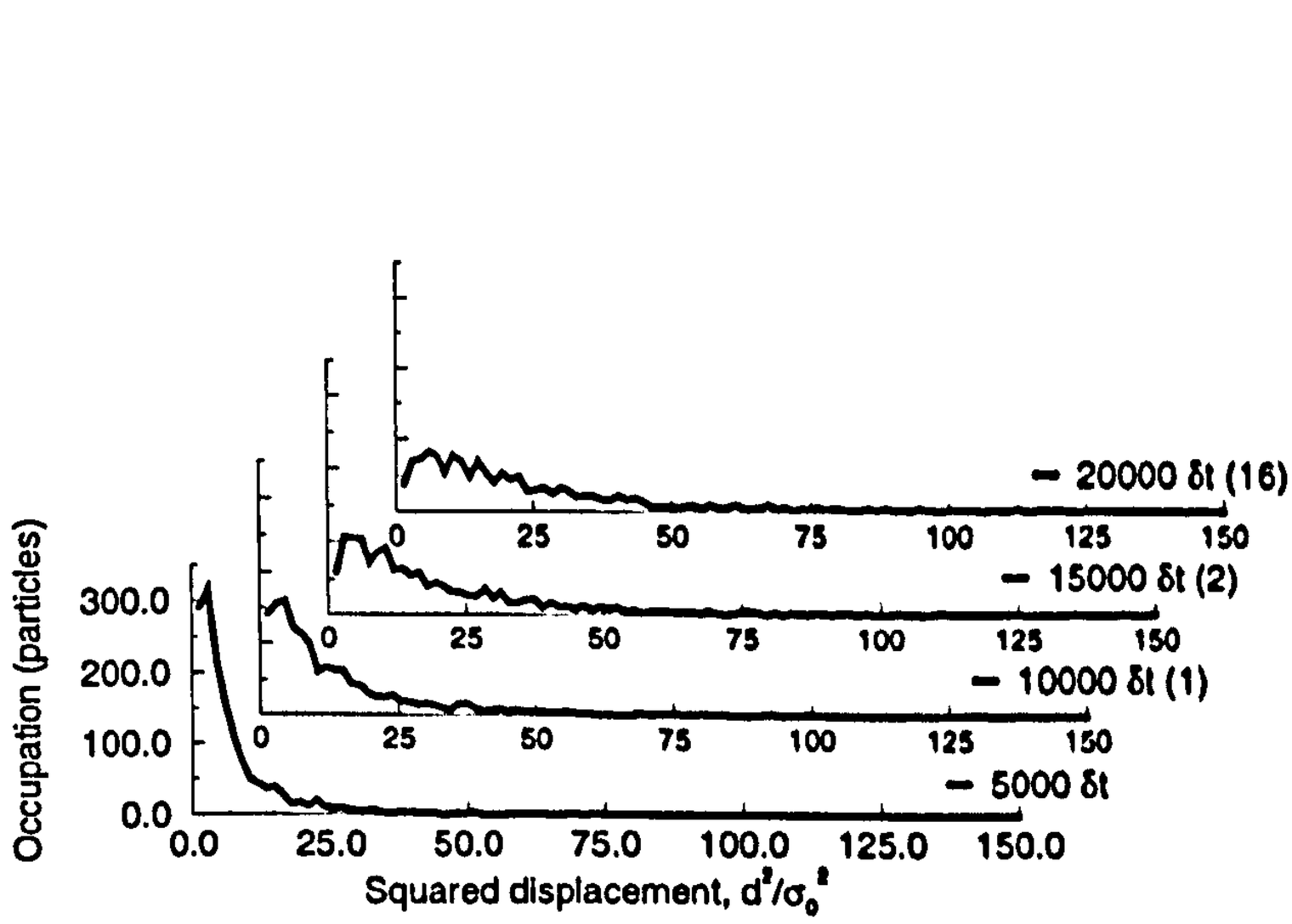

Figure 5.16: Successive histograms of squared-displacement for the $\kappa = 6.5$, $N = 1500$ bulk system at $T = 0.40$, (top), and $T = 0.60$. Note the difference in horizontal scales. Plots are labelled by total elapsed timesteps. Values in parentheses indicate the number of entries off this scale.

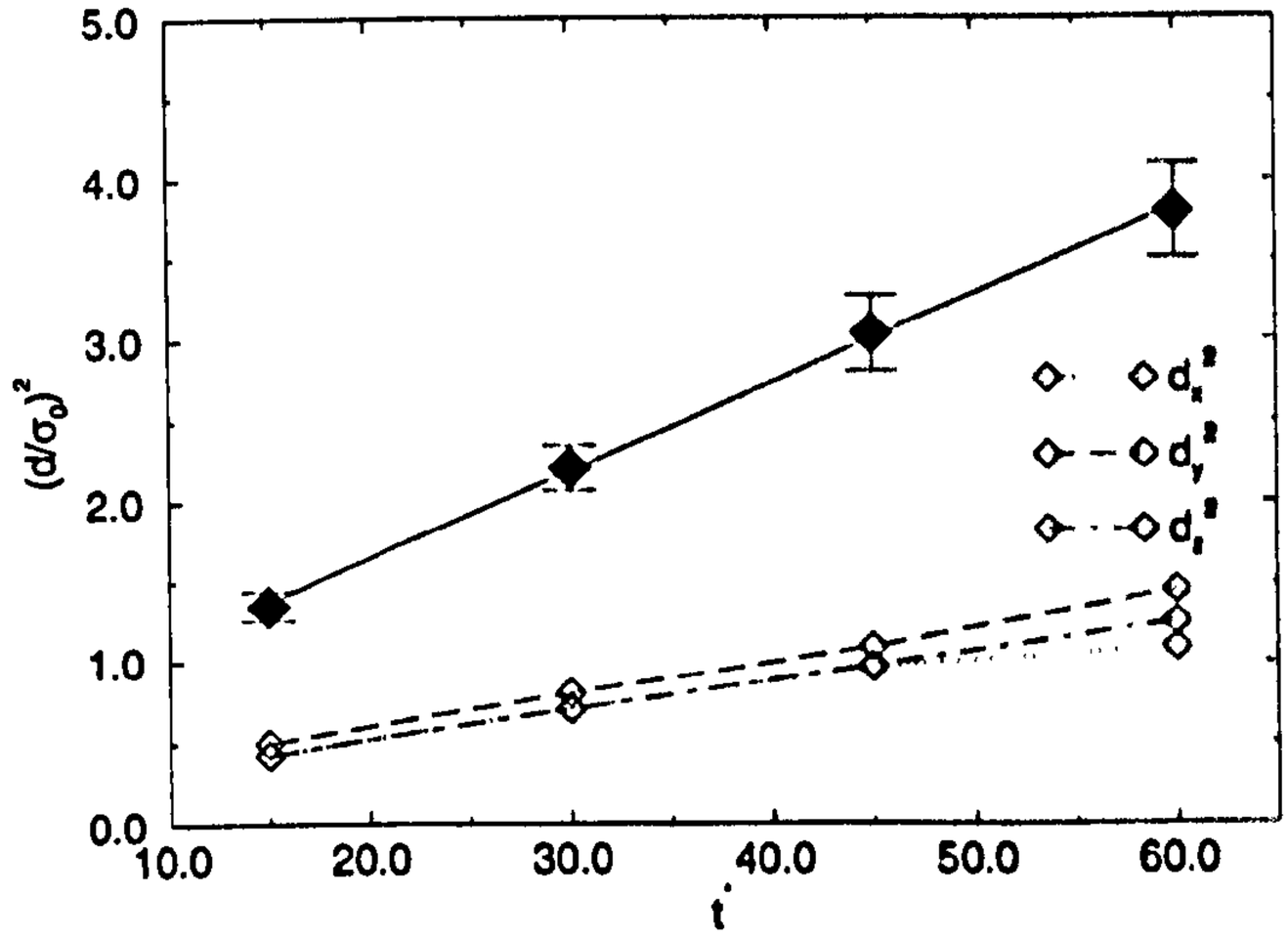

Figure 5.17: Mean-squared displacement with time for the $\kappa = 6.5$, $N = 1500$, $T = 0.10$ bulk system.

to some specified criterion, usually centre–centre separation. At the end of the process, the labels run from 1 to the number of distinct groups in the system. The procedure in this case was two-fold. In the first instance, individual clusters were identified, applying a critical tip-tip separation, r_{nc}. For these purposes the particles were taken as ellipsoids of length κ. The average position of the tips in a cluster with three or more members was taken to define a 'nodal point'. In a second sorting process, nodes with a common member particle were grouped together into 'networks'. The tip-tip criterion is a free parameter that controls the level of structure picked out by the sorting process. Examining the distribution of nearest-neighbour tip separations shows few values below $0.2\sigma_0$, followed by a sharp increase for $0.2\sigma_0 < r_{tip} < 0.3\sigma_0$ and then a slow decay. This distribution is shown in Fig. 5.18 for the bulk system of Fig. 5.15, and, for comparison, an inhomogeneous configuration at $\kappa = 6.5, T = 0.5$.

Searches were performed on inhomogeneous systems with $\kappa \geq 5$ using critical separations of $r_{nc} = 0.25$, 0.30 and 0.35. Bulk configurations at $\kappa = 6.5$ were examined, although the $\rho = 0.10$ system was subjected to rapid heating without full equilibration at each temperature, typically performing only 2×10^4 timesteps at each point. Results of

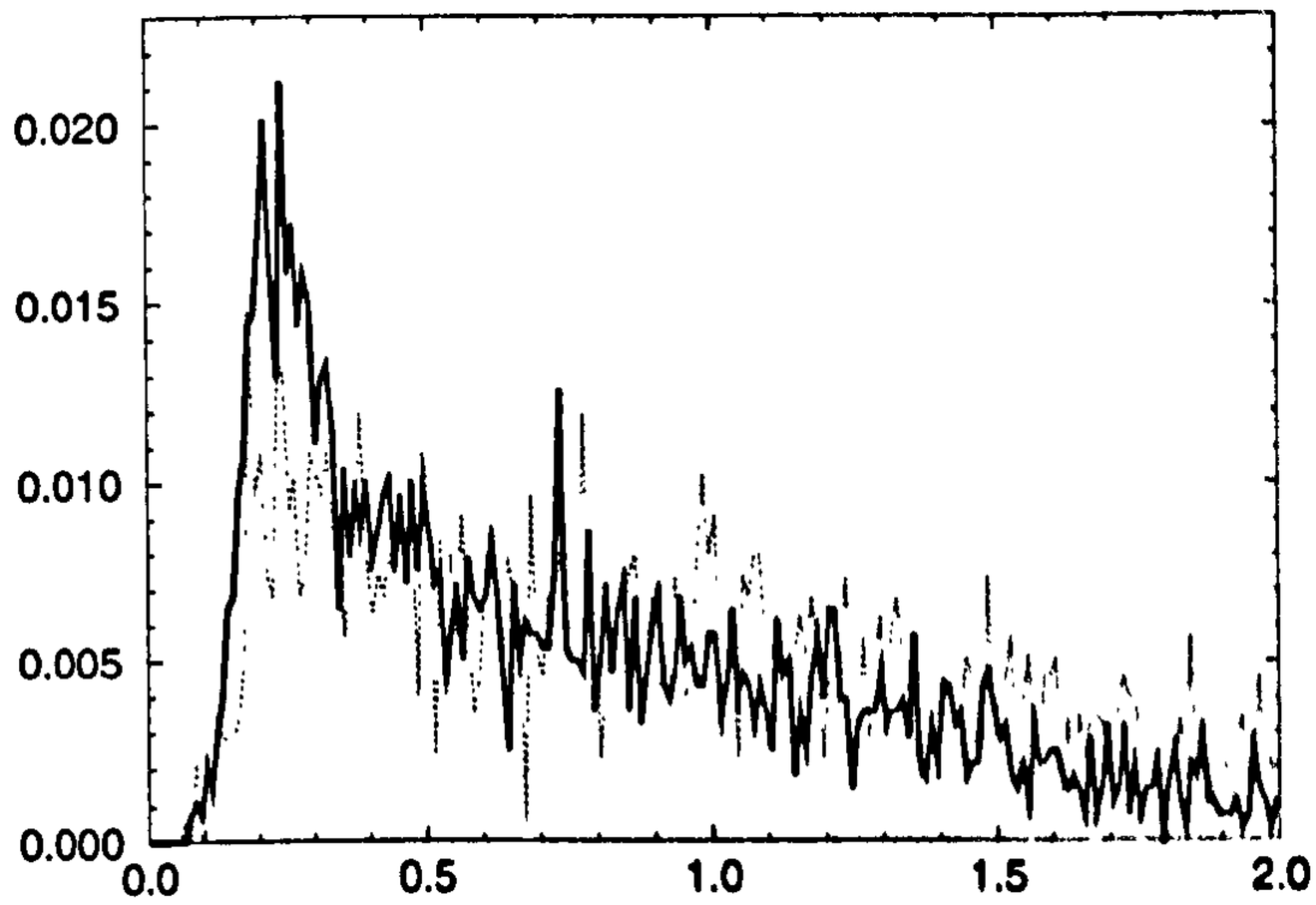

Figure 5.18: Distribution of nearest-neighbour tip separations for $\kappa = 6.5$ systems in the bulk at $T = 0.40$, (solid line) and an inhomogeneous configuration at $T = 0.50$, (dotted line).

these searches are indicated in Table 5.4. Note that the network containing the greatest number of particles is not necessarily that composed of the greatest number of nodes. With the number of nodes for each search, figures in parentheses indicate the number containing only three members, since these account for a significant proportion of the total. At a given temperature the number of nodes generally increases with r_{nc} as more groups are picked out. For the $\kappa = 6.5$ slab the numbers remain steady or fall suggesting that the lowest criterion picks out almost all of the nodes which may 'coalesce' as r_{nc} is increased. The greatest network size increases with r_{nc} at a given temperature, although in most cases taking in a reasonably small fraction of the total system, (recall that $N = 1000$ for the slab simulations and 1500 for the bulk). Increasing the temperature has a marked effect on the number of nodes identified, with very few persisting for $T \geq 0.60$ in the slab systems, where the dense phase has the possibility of expansion along z. In the bulk simulation at fixed volume the numbers fall more slowly with temperature, although the shorter run lengths must be remembered. Even so, very few nodes were identified at $T = 1.00$.

Shown separately, in Table 5.5, are the search results for the $\kappa = 6.5, T = 0.40, \rho = 0.08$

System	r_{nc}	Number of nodes	Order of largest node	Number of networks	Number of nodes in largest network	Maximum number of particles in a network
$\kappa = 5.0$ slab	0.25	17 (12)	7	0	-	-
$T = 0.40$	0.30	31 (21)	10	2	2	13
	0.35	44 (22)	16	4	4	25
$\kappa = 5.5$ slab	0.25	29 (20)	9	2	2	8
$T = 0.40$	0.30	48 (22)	12	7	5	24
	0.35	69 (34)	15	12	15	94
$T = 0.60$	0.25	1 (1)	3	0	.	.
	0.30	2 (2)	3	0	.	.
	0.35	3 (2)	4	1	2	6
$\kappa = 6.0$ slab	0.25	45 (20)	11	4	2	15
$T = 0.40$	0.30	51 (27)	20	7	6	63
	0.35	62 (32)	20	8	13	109
$T = 0.50$	0.25	25 (15)	8	1	2	8
	0 30	33 (12)	13	3	4	24
	0.35	35 (16)	20	3	7	66
$T = 0.60$	0.25	0	-	-	-	-
	0.30	2 (2)	3	-	-	-
	0.35	2 (2)	3	-	-	-
$\kappa = 6.5$ slab	0.25	55 (20)	13	9	5	31
$T = 0.40$	0.30	53 (12)	19	7	14	135
	0.35	54 (14)	23	2	24	299
$T = 0.50$	0.25	55 (20)	13	9	5	31
	0.30	32 (7)	21	5	9	72
	0.35	34 (10)	22	3	17	213
$T = 0.60$	0.25	3 (2)	4	0	.	.
	0.30	3 (1)	8	0	.	.
	0.35	3 (1)	10	0	.	.
$T = 0.80$	0.25	0	-	-	-	-
	0.30	0	-	-	-	-
	0.35	0	-	-	-	-
$\kappa = 6.5$ bulk	0.25	52 (21)	12	4	3	14
$\rho = 0.10, T = 0.40$	0.30	83 (37)	15	11	5	27
	0.35	97 (38)	21	13	17	97
$T = 0.50$	0.25	35 (21)	12	2	3	19
	0.30	58 (28)	14	4	3	26
	0.35	67 (31)	18	6	6	33
$T = 0.60$	0.25	5 (4)	9	0	.	.
	0.30	22 (15)	13	2	2	6
	0.35	40 (27)	16	4	3	15
$T = 1.00$	0.25	2 (2)	3	0	.	.
	0.30	4 (4)	3	0	.	.
	0.35	5 (4)	5	0	.	.

Table 5.4: Results of cluster searches

r_{nc}	Number of nodes	Order of largest node	Number of networks	Number of nodes in largest network	Maximum number of particles in a network
0.25	95 (27)	17	8	30	21·4
0.30	72 (10)	24	1	61	69·5
0.35	83 (12)	24	1	72	85·4
0.50	91 (19)	28	1	82	106·5
1.00	172 (55)	45	1	172	136·5

Table 5.5: Results of cluster searches for $\kappa = 6.5$, $\rho = 0.08$, $T = 0.40$ system

system pictured above. In this case r_{nc} was extended to a maximum of 1.0, where all the nodes are connected in a single network taking in over 90% of the particles. Histograms of the node–node separations, r_{ij}^n, as in Fig. 5.19, indicate a small peak at values below 1, where low r_{nc} forces the subdivision of a single cluster of particles. The distribution increases significantly at $r_{ij}^n \sim 7$, roughly corresponding to a particle length, followed by a plateau region to $r_{ij}^n \sim 14$ after which it decays, (the maximum separation allowed, half the body diagonal of the box, is ~ 23). These features are distinct at $r_{nc} = 0.5$ but considerably blurred at $r_{nc} = 1.0$ suggesting this criterion to be too coarse.

In those systems with a reasonable number of nodes, the size distribution does not indicate any strongly favoured coordination number. Examining the distribution of angles between particles in the same node ($\cos^{-1}(\mathbf{e}_i.\mathbf{e}_j)$), averaged over nodes, does not indicate any preferred pair angle, although given the lack of strong preference for node order and the number of networks in these systems any preference is likely to be obscured. These results support a description of structured networks jammed together in a glassy state. The $\rho = 0.1$ data indicate this to melt to an isotropic fluid on heating. On heating the fully equilibrated system at $\rho = 0.08$ to $T = 0.60$ also shows the clusters disappear. The particles become mobile, with histograms of squared-displacement shown in Fig. 5.16 for comparison with the $T = 0.40$ case, measured over $2 \times 10^4 \delta t$ after a $4 \times 10^4 \delta t$ equilibration phase. The evolution of mean-squared displacement for the same simulation is shown in

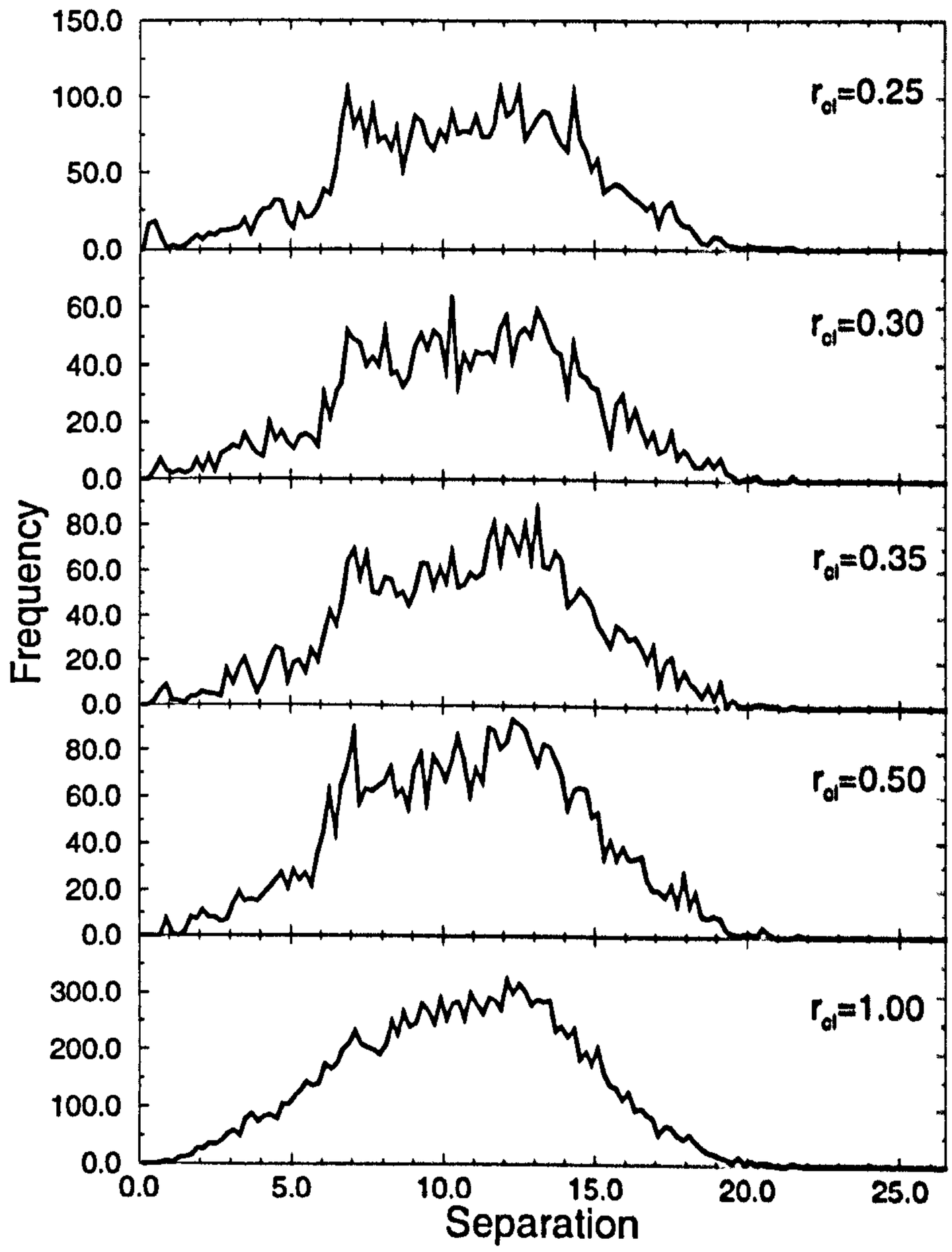

Figure 5.19: Distribution of node–node separations for $\kappa = 6.5$ bulk system at $T = 0.40$, $\rho = 0.08$.

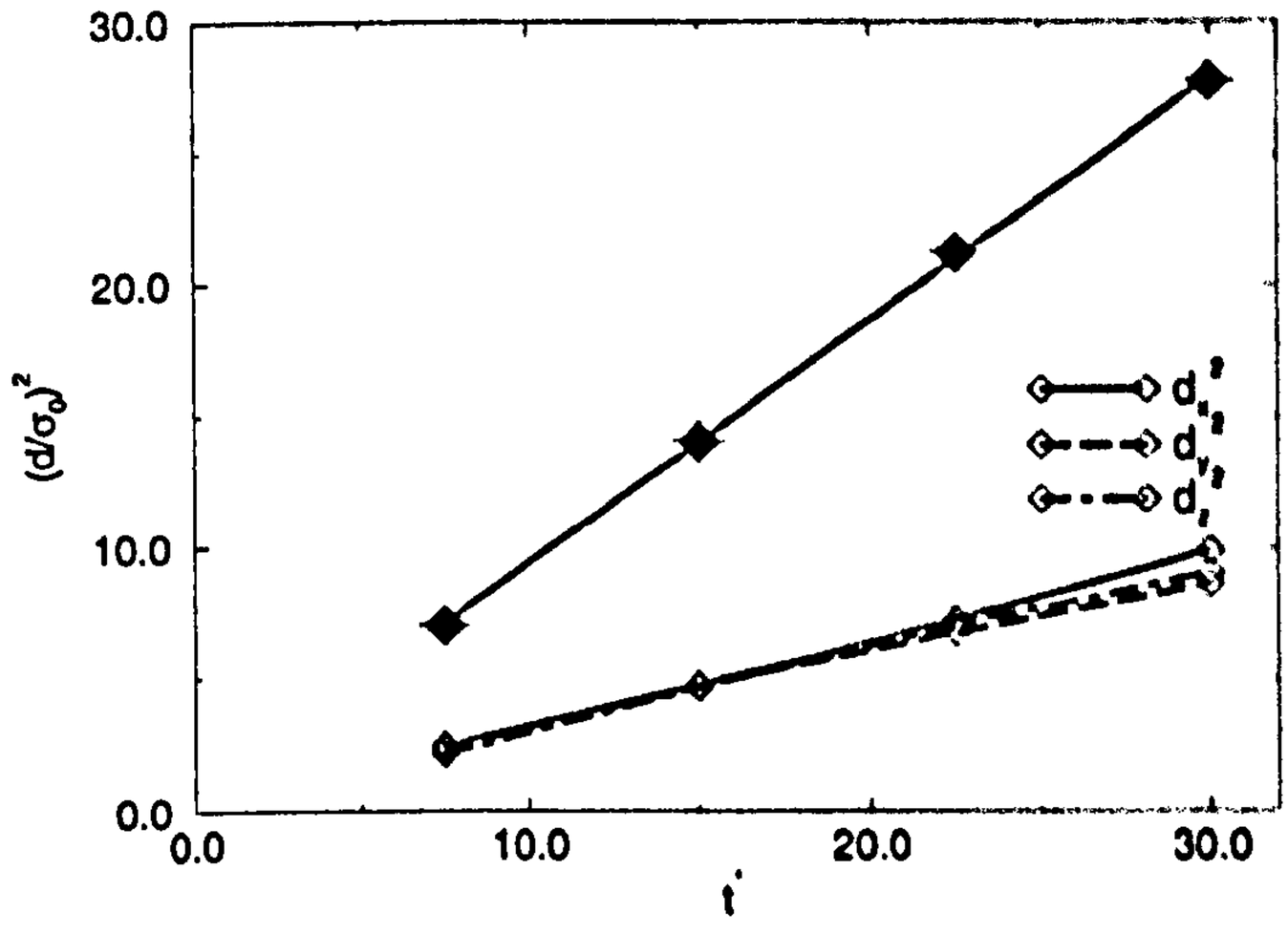

Figure 5.20: Mean-squared displacement with time for the $\kappa = 6.5$, $N = 1500$, $T = 0.60$ bulk system.

Fig. 5.20 and from the gradient the diffusion coefficient is $D_E = 0.1543 \pm 0.0022$, far more typical for the isotropic phase. Searching the final configuration with $r_{nc} \leq 0.35$ indicated no networks and a greatest node size of 4.

5.3 Discussion

In this chapter we have reported investigations of two model systems in which the strength parameter has no anisotropy. Using a 12–4 Kihara model with a spherocylinder core, liquid-vapour properties have been studied for elongations $L/D = 5.0, 5.5$ and 6.0 using Gibbs-Ensemble Monte Carlo and Gibbs-Duhem integration. The critical point is found to fall with increasing elongation, but rather slowly. The details of the model have a measurable effect in line with expectations: use of a 'bare' cut-off gives a coexistence envelope shifted down in temperature from that found when including long-range corrections. In all cases the fluctuations in pressure, measured using the virial, are found to be large in the dense phase, as previous workers have noted [96]. Initial investigations using a fitted cubic tail, taking the potential and its derivative smoothly to zero, indicate fluctuations of

a similar order. Despite choosing potential exponents that enhance the range of attractive interactions, no ordered phases were observed. This is in contrast to the GB fluid, in which the critical point disappears at significantly lower temperatures, (Chapter 3).

The liquid-vapour properties of the GBCE system have also been studied. These prove harder to measure, with GEMC becoming inefficient at the lower temperatures required to obtain liquid-vapour coexistence at $\kappa > 4$. Direct simulation of the two phases using an inhomogeneous system indicate a very low density vapour and an isotropic fluid. Increasing elongation beyond 5 at reasonable temperature resulted in the spontaneous formation of rosettes of particles, giving a state with very low diffusion coefficients. Analysis of this glass-like phase, seen in the slabs and in bulk simulations, indicates no strongly preferred coordination number for these clusters. The competition between binding energy and number of neighbours is rather complicated; simulated annealing for a range of coordinations indicates no energetically favourable size [97], unlike the Lennard-Jones system which is known to favour icosahedral packing. This is an interesting addition to the phase behaviour of this class of attractive, (roughly) ellipsoidal model potentials, warranting further investigation. We have not studied the glass transition temperature in any detail, nor firmly established a threshold elongation, although indications of clustering were found for $\kappa = 5$ upwards. These structures are reminiscent of aggregation patterns formed by ellipsoidal latex particles, used as a rigid-rod model polymer systems [98, 99]. An example is shown in Fig. 5.21; although it is possible to prepare samples with very low polydispersity, relatively small quantities are available. The system shown is at therefore at rather lower density, but the resemblance is clear. Once more, this significant change in phase behaviour indicates that a wide range of behaviour is accessible to this family of model potentials, and that seemingly minor modifications can have dramatic effects.

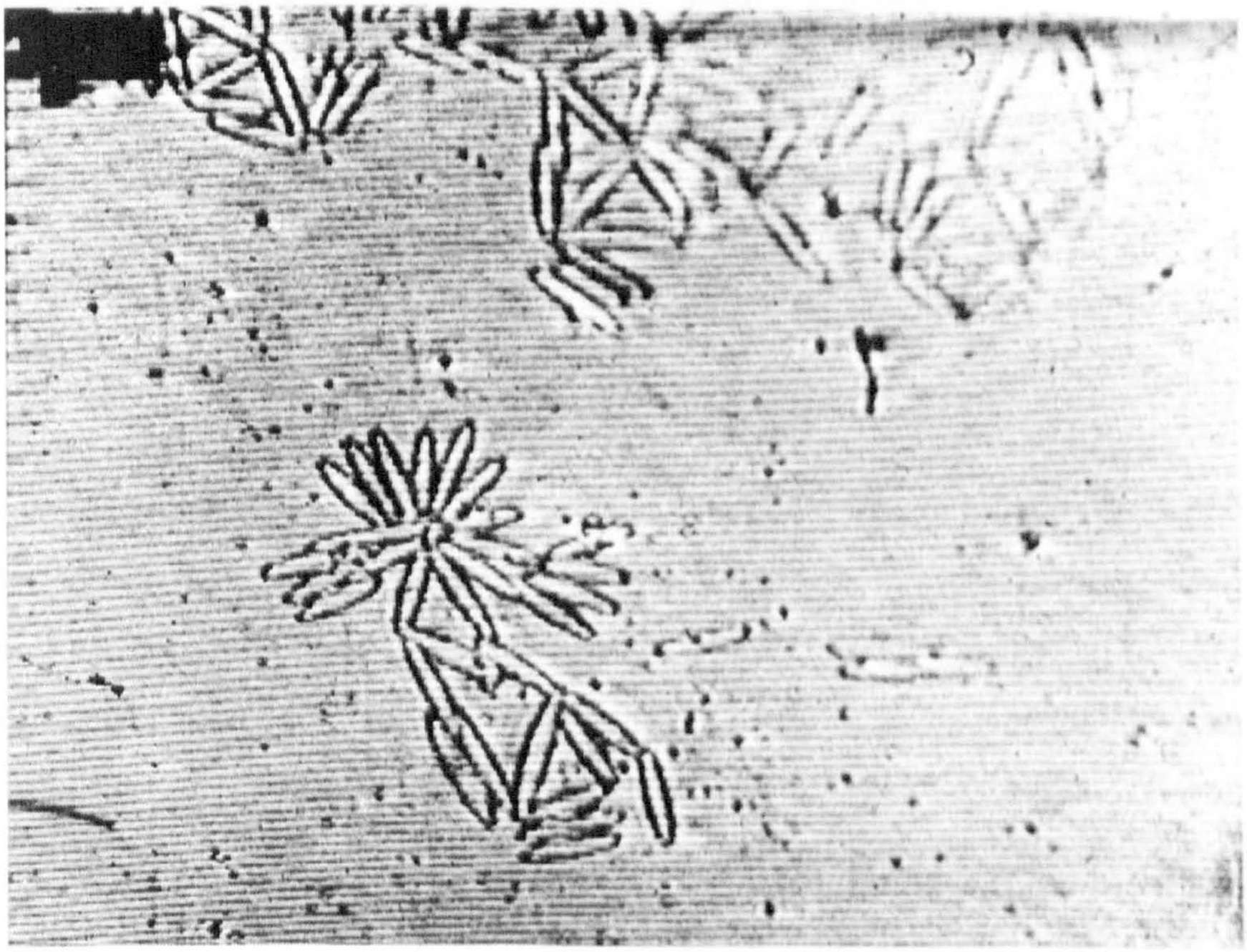

Figure 5.21: Transmission electron micrograph showing aggregation patterns for latex particles of axial ratio 3.3 : 1; reproduced by kind permission of Dr. J. A. Odell.

Chapter 6

Elastic Properties of the Gay-Berne fluid

6.1 Free energy of distortions in a nematic

In a bulk nematic phase, spatial variations in the order tensor, $\mathbf{Q}$, occur over distances large compared with the dimensions of the molecules, and continuum theory, in which structural details on a molecular scale are neglected, provides a good description of the system. On this basis and given the appropriate symmetry conditions [85], the free energy, $\Delta\mathcal{F}$, associated with distortions in the director field, $\mathbf{n}(\mathbf{r})$, may be written [100, 101]

$$\Delta\mathcal{F} = \int \mathrm{d}^3\mathbf{r} \left\{ K_1(\nabla \cdot \mathbf{n})^2 + K_2(\mathbf{n} \cdot \nabla \times \mathbf{n})^2 + K_3(\mathbf{n} \times \nabla \times \mathbf{n})^2 \right\} \tag{6.1}$$

to quadratic order in the director derivatives. The constants in this expression are associated with the three basic types of deformation, namely splay (K_1), twist (K_2) and bend (K_3), as illustrated in Fig. 6.1. Each of these deformations can be generated in a pure form, so each elastic constant must be positive to leave the undistorted nematic as the minimum of free energy. Two other quadratic order terms are possible, giving rise to 'surface' elastic constants for splay-bend, (K_{13}), and saddle-splay, (K_{24}), deformations; we restrict our attention to the three 'bulk' terms.

Experimental measurement of the Frank elastic constants is well established. A standard technique studies the Freedericksz transition, in which the deformation due to an external field is examined in a geometry such that the alignment imposed by the field is in

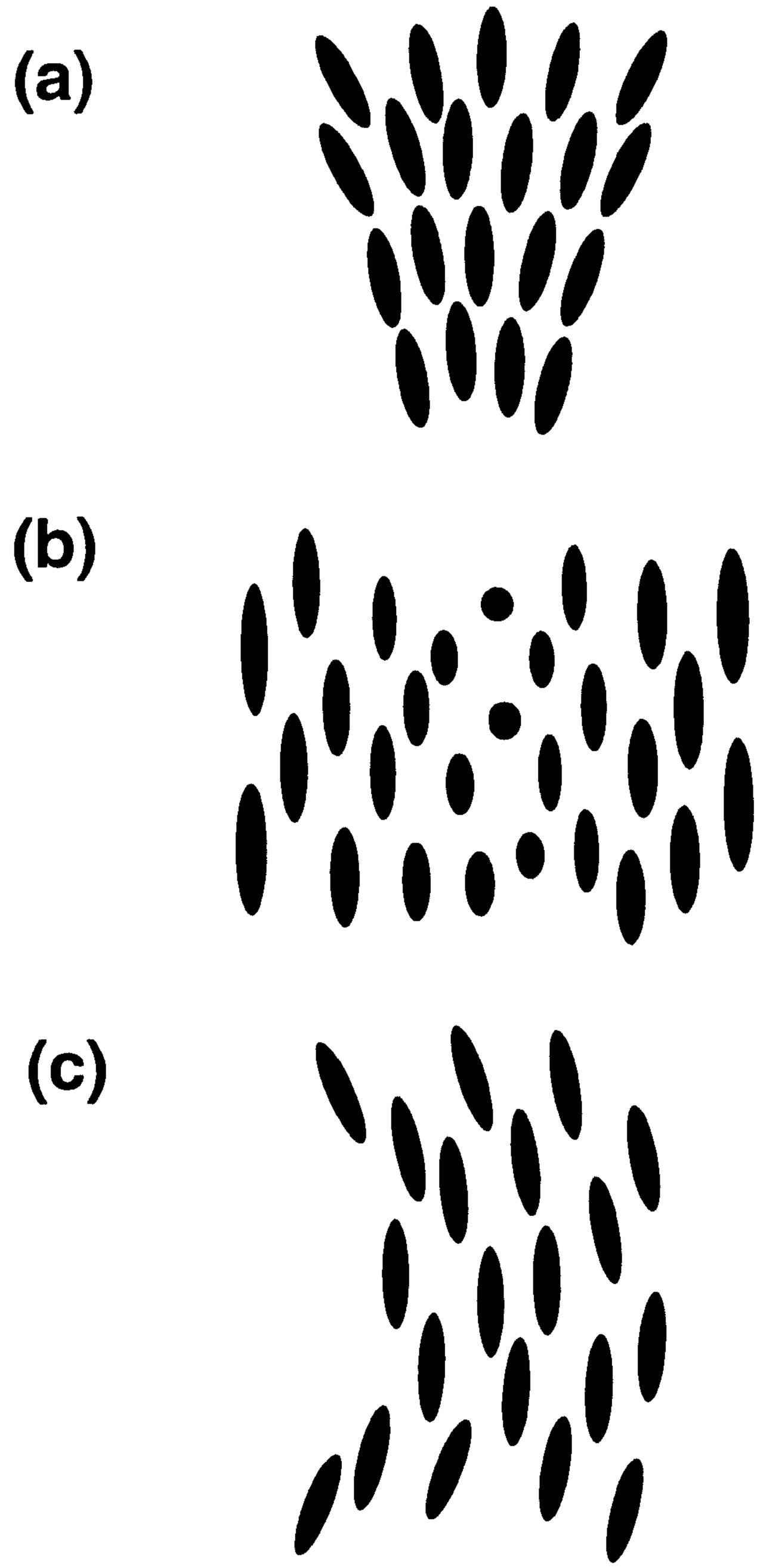

Figure 6.1: The three Frank modes of elastic deformation: (a) splay, (b) twist and (c) bend.

conflict with that favoured by the confining surfaces. Departure from the latter will occur only when the field exceeds some critical value, directly related to the bulk elastic constant appropriate to the experimental geometry. An alternative route to the elastic constants is measurement of fluctuations in the director field at equilibrium using light scattering. The twist elastic constant is also accessible to direct torque measurements [102], since, unlike conventional fluids, a nematic can support a static torque.

The elastic behaviour results directly from the anisotropy leading to formation of liquid crystal phases, and so is of interest on many levels. Its influence on the response to external fields and the transmission of torques provokes significant industrial interest since such properties are exploited in display technologies and switching devices. Development of microscopic theories of the bulk elastic constants has received considerable attention. Including terms up to pair correlations, density functional theory provides expressions for the bulk, (and surface), elastic constants in terms of the single-particle distribution function and direct correlation function of the fluid. Recent results of Stelzer *et al.* [104] use this route to calculate elastic constants for the GB fluid.

6.2 Measurements of Frank elastic constants by simulation

The Frank elastic constants of model systems can often be measured in simulation using techniques directly analogous to those employed for physical systems. The Lebwohl-Lasher model, described below, has already been examined in some detail [103]. This is a lattice model, allowing use of large systems, (up to 32000 spins), and comparison was made of three techniques: the Freedericksz transition, fluctuation expressions for the equilibrium director field and the response to an applied field. These yielded consistent results, but the fluctuation method was found to be most efficient. In other studies this has been applied to systems of hard ellipsoids and spherocylinders [104, 105, 106], but the additional degrees of freedom forced the system size down dramatically. Recently, the technique has also been applied to the Gay-Berne model [3]. This provided elastic constants for two parameter sets over a range of nematic state points for systems of several thousand particles. The elastic constants were found to increase with density for roughly constant order parameter, with $K_1 \sim K_2 < K_3$.

Two techniques are used here as independent investigations of the Gay-Berne fluid. Following [103], a perturbing field is applied to a nematic phase, the elastic response is measured and direct comparison is made with the data used in [3]. Secondly, the torque density resulting from an imposed twist on a nematic is used as a probe of the twist elastic constant, using a method originally applied to hard ellipsoids [107]. Comparison is made with previous results. The director fluctuation technique is outlined below for reference, along with the techniques used here.

6.2.1 Measuring Frank elastic constants using director fluctuations

The thermally-induced, equilibrium fluctuations of the director field in a nematic phase can be related to components of the Fourier transformed order tensor, $\hat{\mathbf{Q}}(\mathbf{k})$, where

$$\hat{Q}_{\alpha\beta}(\mathbf{k}) = \frac{V}{N}\sum_{i=1}^{N}\tfrac{3}{2}\left(e_{i\alpha}e_{i\beta} - \tfrac{1}{3}\delta_{\alpha\beta}\right)\exp\left(-i\mathbf{k}.\mathbf{r}_i\right) \tag{6.2}$$

The coordinate system is chosen such that the director lies along the 3-direction of a Cartesian system, $\mathbf{n} = (0,0,1)$. Since this alone does not fix the 1 and 2 directions, the system can be rotated for each $\mathbf{k}$ to make the perpendicular component lie along the 1 direction. This allows the explicit fluctuation expressions for a generalized wave-vector $\mathbf{k} = (k_1, 0, k_3)$ to be written as [108]

$$\left\langle \hat{Q}_{13}(\mathbf{k})\hat{Q}_{13}(-\mathbf{k})\right\rangle \equiv \left\langle |\hat{Q}_{13}(\mathbf{k})|^2\right\rangle = \frac{\frac{2}{9}S^2 V k_B T}{K_1 k_1^2 + K_3 k_3^2} \tag{6.3a}$$

$$\left\langle \hat{Q}_{23}(\mathbf{k})\hat{Q}_{23}(-\mathbf{k})\right\rangle \equiv \left\langle |\hat{Q}_{23}(\mathbf{k})|^2\right\rangle = \frac{\frac{2}{9}S^2 V k_B T}{K_2 k_1^2 + K_3 k_3^2} \tag{6.3b}$$

valid in the limit of low k. Use of these equations requires measurement of $\left\langle |\hat{Q}_{\alpha 3}(\mathbf{k})|^2\right\rangle$ and extrapolation to $k = 0$, which in turn uses a double-polynomial fit in k_1^2 and k_3^2. Large systems are demanded by the assumption of quadratic behaviour in $\mathbf{k}$ for fitting, and, since the correlation times associated with long-wavelength fluctuations are large, long simulations are also required. Obtaining high quality statistics is therefore expensive, (simulations reported in [3] run to 10^6 MD timesteps), although many wave-vectors can be examined in a single simulation. It is convenient, although not necessary, to employ a fixed set of wave-vectors. During the course of these long simulations thermal processes would cause slow variations in the director frame which must be eliminated if the $\mathbf{k}$ points are

fixed. Application of Lagrangian constraints to conserve the director orientation facilitates this without significantly perturbing the system [3, 39].

6.2.2 Measuring Frank elastic constants using a perturbing field

The only previous use of this method to our knowledge is for the Lebwohl-Lasher lattice model, as indicated above. Linear response theory indicates the average of property A subject to a perturbed Hamiltonian, $\mathcal{H} = \mathcal{H}_0 + \Delta\mathcal{H}$, to be

$$\langle A \rangle = \frac{1}{k_B T} \langle A \Delta\mathcal{H} \rangle_0 \tag{6.4}$$

provided that $\langle A \rangle_0 = 0$, where $\langle \cdots \rangle_0$ indicates an average in the unperturbed system. A possible choice is $\Delta\mathcal{H} = f\hat{Q}_{\alpha 3}(\mathrm{k})$, i.e. a field of strength f coupling to a component of the reciprocal-space ordering tensor. Using (6.4), and making use of translational invariance, the response would be

$$\left\langle \hat{Q}_{\alpha 3}(-\mathrm{k}) \right\rangle = \frac{f}{k_B T} \left\langle \hat{Q}_{\alpha 3}(\mathrm{k}) \hat{Q}_{\alpha 3}(-\mathrm{k}) \right\rangle_0 \tag{6.5}$$

which is related to the elastic constants via (6.3). A more convenient proposition is the real-valued perturbation

$$\begin{aligned} \Delta\mathcal{H} &= f\tfrac{1}{2}\left(\hat{Q}_{\alpha 3}(\mathrm{k}) + \hat{Q}_{\alpha 3}(-\mathrm{k})\right) \\ &= f\left(\frac{V}{N}\sum_{i=1}^{N} \tfrac{3}{2} e_{i\alpha} e_{i3} \cos(\mathrm{k}.\mathbf{r}_i)\right) \end{aligned} \tag{6.6}$$

where α can be either 1 or 2. The response can be measured in reciprocal space,

$$\left\langle \hat{Q}_{\alpha 3}(\mathrm{k}) \right\rangle = \left\langle \hat{Q}_{\alpha 3}(-\mathrm{k}) \right\rangle = \frac{f}{2k_B T} \langle \hat{Q}_{\alpha 3}(\mathrm{k}) \hat{Q}_{\alpha 3}(-\mathrm{k}) \rangle_0 \,, \tag{6.7}$$

or in real space as an oscillatory profile,

$$\langle \hat{Q}_{\alpha 3}(\mathbf{r}) \rangle = \frac{\langle \hat{Q}_{\alpha 3}(\mathrm{k}) \hat{Q}_{\alpha 3}(-\mathrm{k}) \rangle_0}{V k_B T} f \cos(\mathrm{k}.\mathbf{r}_i) \,. \tag{6.8}$$

The imaginary component of the response in reciprocal space will vanish on averaging.

A number of practical points arise. The field strength determines the signal to noise ratio of the measured average, but if made too large, linear response will be violated. If a reasonably large value of f is permitted, statistics of quality comparable with the director

fluctuation method could be obtained with shorter runs. Here, though, only one value of k can be probed in any one simulation. The relative efficiency of this technique will be balanced by the number of simulations required for a reliable extrapolation to $\mathbf{k} = 0$. Finally, as before, it is convenient to fix the director frame during simulation.

6.2.3 Measuring K_2 using twisted periodic boundary conditions

When twisted, a nematic phase allows a continuous response in the bulk, giving a cholesteric. Following Allen and Masters, [107], let the director field $\mathbf{n}(\mathbf{r})$ form a helix about the z-axis:

$$\mathbf{n}(\mathbf{r}) = (\cos\phi(z), \sin\phi(z), 0). \tag{6.9}$$

For a uniformly twisted state,

$$d\phi/dz = k = \text{constant}, \tag{6.10}$$

which corresponds to a distortional free energy

$$\Delta\mathcal{F} = \frac{1}{2}\int \mathrm{d}^3\mathbf{r}\, K_2\, k^2 = \frac{1}{2} K_2\, k^2\, V \tag{6.11}$$

in a volume V. This is a local free energy minimum; the global minimum corresponds to the uniform state, $\mathbf{n}(\mathbf{r}) = (0, 0, 1)$, say, when $\Delta\mathcal{F} = 0$. The twisted state is metastable since, in general, a tendency to move to the untwisted state would be resisted by bend terms in $\Delta\mathcal{F}$. The technique developed by Allen and Masters to obtain K_2 from simulation uses twisted boundary conditions to allow application of a helical distortion whose pitch is greater than the box length. The convention adopted is that the centre-of-mass x and y coordinates of image particles in the neighbouring box in the $+z$ direction are rotated by $\pi/2$ with respect to those in the central box, and in the $-z$ direction by $-\pi/2$. Normal periodic boundaries apply in the x and y directions. The same convention is applied to the orientation vectors, but since these particles are axially symmetric, only the x and y components of each $\mathbf{e}_i$ are involved. When a particle leaves the box through the $+z$ or $-z$ face it is replaced by an image particle at the opposite face which has x and y coordinates rotated by $-\pi/2$ or $+\pi/2$ respectively. Clearly, it is also necessary to rotate the linear and angular velocity vectors consistently with the position and orientation. With this convention the simulation incorporates a helix whose pitch is four times the box length,

the maximum value for a cuboidal simulation box, since the rotated image boxes must match the original box at the boundary faces so as to fill space. We have also employed a hexagonal prism as the basic simulation box, allowing a twist per box of integer multiples of $\pi/3$. The total linear momentum is conserved in the extended set of boxes, and not in the individual box. This has no significant consequences, though, in the same way that the lack of conservation of total angular momentum is not a stumbling block to the use of normal pbc's. Results obtained with twisted pbc's will differ from those obtained with conventional boundaries whenever correlations of the order of a box length are considered; however, such correlations are meaningless in any finite-sized system, so in practice this is not an issue.

If the system under study exhibited long-range translational ordering, these twisted boundaries would impose enormous stresses and would be highly inappropriate. Isotropic and nematic fluids, however, lack translational order and are stress-free. In fact, it is the elastic response to this perturbation in the nematic phase that is to be measured as a route to K_2. Consider the change in potential for a selected pair of molecules resulting from this twist deformation, noting that the potential is pairwise-additive. In general, the centre-centre vector will change, as will the position vectors of the two particles with respect to the centre of the simulation box. This term gives an off-diagonal component of the stress-tensor, and so will vanish on performing an ensemble average. The rotation of the orientation vectors gives a change in potential energy of

$$\delta u_{ij} = -\tau_{ij}^z \phi(z_i) - \tau_{ji}^z \phi(z_j) \tag{6.12}$$

where τ_{ij}^z is the z component of the torque exerted on i by j and τ_{ji}^z is the corresponding torque exerted on j by i. Defining

$$\mathbf{r}_{ij} = \mathbf{r}_i - \mathbf{r}_j \tag{6.13a}$$

$$\mathbf{r}_{mid} = \frac{1}{2}(\mathbf{r}_i + \mathbf{r}_j) \tag{6.13b}$$

$$\phi(z_i) = \phi(z_{mid}) + \frac{1}{2} k z_{ij} \tag{6.13c}$$

$$\phi(z_j) = \phi(z_{mid}) - \frac{1}{2} k z_{ij}\,, \tag{6.13d}$$

this can be written as

$$\delta u_{ij} = -(\tau_{ij}^z + \tau_{ji}^z)\phi(z_{mid}) - \frac{1}{2}(\tau_{ij}^z - \tau_{ji}^z) k z_{ij}. \tag{6.14}$$

From local angular momentum conservation, $(\tau^z_{ij} + \tau^z_{ji}) = -\mathbf{r}_{ij} \times \mathbf{f}_{ij}$, which, being the vector dual of the antisymmetric stress tensor in the neighbourhood of $\mathbf{r}_{mid}$, should vanish. Summing over distinct pairs and averaging gives

$$\langle \delta U \rangle = -\frac{1}{2} k \left\langle \sum_i \sum_{j>i} (\tau^z_{ij} - \tau^z_{ji}) z_{ij} \right\rangle \tag{6.15}$$

Provided the system is in the linear response regime, this gives

$$\left\langle \frac{\partial U}{\partial k} \right\rangle = -\frac{1}{2} \left\langle \sum_i \sum_{j>i} (\tau^z_{ij} - \tau^z_{ji}) z_{ij} \right\rangle . \tag{6.16}$$

Since k will enter the free energy only though the twist deformation contribution, differentiation of the configurational Helmholtz free energy, F_N, and use of (6.11) and (6.16) gives the final result,

$$\frac{\partial F_N}{\partial k} = \left\langle \frac{\partial U}{\partial k} \right\rangle = V K_2 k = -\frac{1}{2} \left\langle \sum_i \sum_{j>i} (\tau^z_{ij} - \tau^z_{ji}) z_{ij} \right\rangle , \tag{6.17}$$

enabling a calculation of K_2 in MD simulation.

6.3 Results and discussion

6.3.1 Perturbed system

Using (6.6) and constraining the director to lie along z, (the 3 direction), MD simulations were performed on a system of $N = 512$ GB particles. The potential parameters were set to $\mu = 2, \nu = 1, \kappa = 3, \kappa' = 5$ [1] and conventional reduced units were used. The potential was cut-and-shifted at $r_c = 4$ and the equations of motion were integrated with a timestep of $\delta t = 0.015$. The components $\hat{Q}_{13}(\mathbf{k})$ and $\hat{Q}_{23}(\mathbf{k})$ were separately measured in simulations at $T = 3.0$, $\rho = 0.38$ for three wave-vectors, $\mathbf{k}_a = (0, 0, 0.569)$, $\mathbf{k}_b = (0, 0, 1.138)$ and $\mathbf{k}_c = (1.138, 0, 1.138)$, affording comparison with [3]. Simulations were carried out for several field strengths at each $\mathbf{k}$, in each case starting with the largest f from an equilibrated, unperturbed nematic state. After initial equilibration for 2×10^4 timesteps, the reciprocal-space response of (6.7) was measured over 5×10^4 timesteps at the higher field strengths and 7.5×10^4 timesteps at $f = 0.25$. Direct comparison with the $\left\langle \hat{Q}_{\alpha 3}(\mathbf{k}) \hat{Q}_{\alpha 3}(-\mathbf{k}) \right\rangle_0$ data used in [3] is then possible [109], and the results are compared in

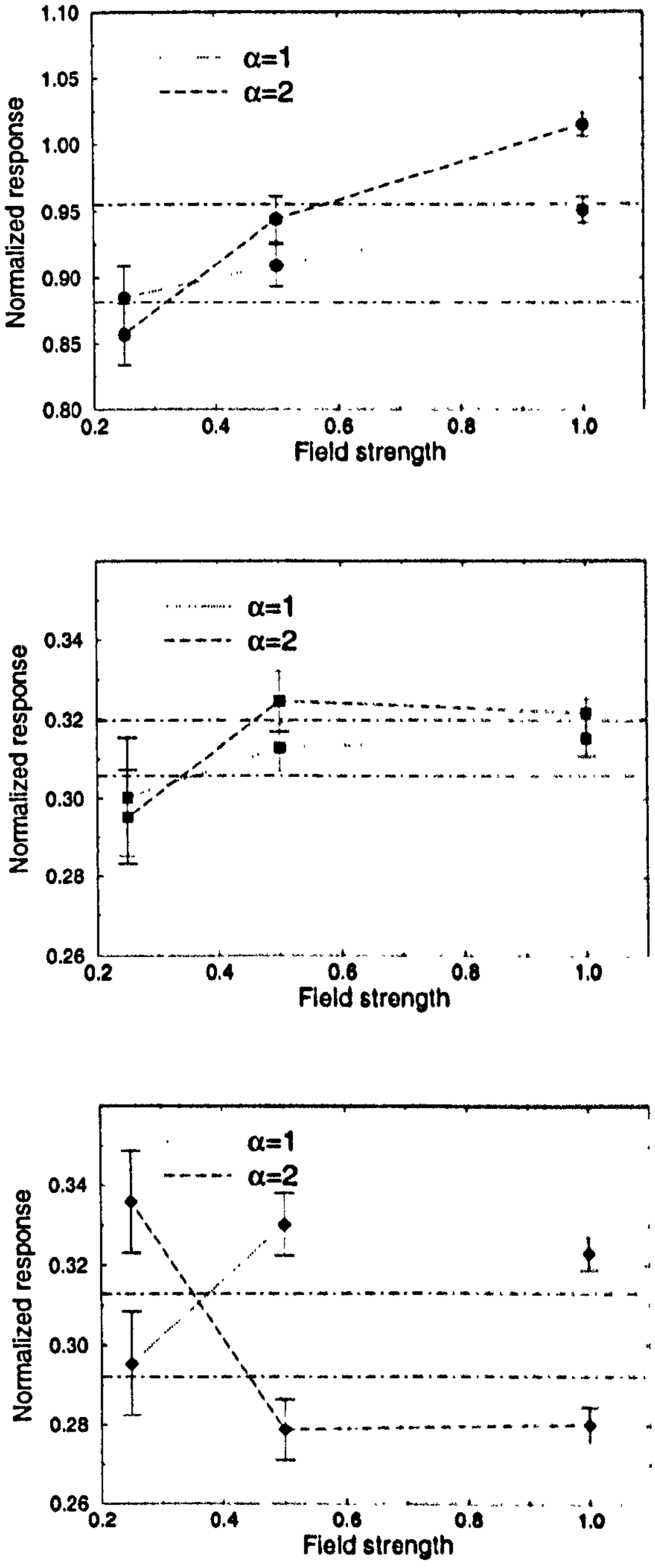

Figure 6.2: Normalized averages of reciprocal order tensor components per unit volume, $(2k_BT/Vf)\left\langle \hat{Q}_{\alpha 3}(\mathrm{k})\right\rangle$, $\alpha = 1, 2$. The corresponding wave-vectors are, from the top, $\mathrm{k}_a = (0, 0, 0.569)$, $\mathrm{k}_b = (0, 0, 1.138)$ and $\mathrm{k}_c = (1.138, 0, 1.138)$. Horizontal lines indicate the maximum range of values for $\left\langle \hat{Q}_{\alpha 3}(\mathrm{k})\hat{Q}_{\alpha 3}(-\mathrm{k})\right\rangle_0 /V$, $\alpha = 1, 2$ taken from [3].

f	S		$(2k_BT/Vf)\left\langle\hat{Q}_{\alpha 3}(\mathbf{k})\right\rangle$		K_3 by
	$\alpha=1$	$\alpha=2$	$\alpha=1$	$\alpha=2$	amplitude
$\mathbf{k}_a$:					
1.00	0.673(2)	0.631(2)	0.95(1)	1.015(9)	9.06
0.50	0.725(2)	0.726(2)	0.91(2)	0.94(2)	11.87
0.25	0.740(1)	0.738(1)	0.89(2)	0.86(2)	13.07
0.00	-	-	0.92(4)	0.91(2)	-
$\mathbf{k}_b$:					
1.00	0.734(1)	0.739(1)	0.315(5)	0.322(4)	8.95
0.50	0.755(1)	0.735(2)	0.313(6)	0.325(8)	8.88
0.25	0.724(2)	0.747(1)	0.30(2)	0.30(1)	9.48
0.00	-	-	0.312(6)	0.313(7)	-
$\mathbf{k}_c$:					
1.00	0.747(1)	0.718(1)	0.323(4)	0.280(4)	-
0.50	0.726(1)	0.754(2)	0.330(8)	0.279(8)	-
0.25	0.731(1)	0.748(1)	0.30(1)	0.34(1)	-
0.00	-	-	0.308(6)	0.298(5)	-

Table 6.1: Perturbed field results for the GB system. Results quoted at $f=0$ are values of $(1/V)\left\langle\hat{Q}_{\alpha 3}(\mathbf{k})\hat{Q}_{\alpha 3}(-\mathbf{k})\right\rangle_0$ taken from [3].

Fig. 6.2. For each of these data points the sine component of $\left\langle\hat{Q}_{\alpha 3}(\mathbf{k})\right\rangle_0$ was zero, within estimated errors.

For $\mathbf{k}_a$ and $\mathbf{k}_b$ the real-space response was also measured as a profile along z using a histogram of 100 bins. Fitting to a functional form $A\cos(kz)$ is an alternative route to K_3 since, from (6.3) and (6.8),

$$A=\frac{\left\langle\hat{Q}_{\alpha 3}(\mathbf{k})\hat{Q}_{\alpha 3}(-\mathbf{k})\right\rangle_0}{Vk_BT}f=\frac{9}{4}f\frac{S^2}{K_3k_3^2}. \tag{6.18}$$

The resulting values are included in Table 6.1, which summarizes the results of these investigations. For each field strength, the function above was was fitted to the mean of the $\alpha=1$ and $\alpha=2$ profiles.

In the asymptotic linear regime the plotted values will not vary with field strength at a given k. Although there are too few points to draw definite conclusions, it would seem that results at $\mathbf{k}_a$ are outside this regime, with the normalized response decreasing as the field is reduced. The values of K_3 inferred from the real-space profile for $\mathbf{k}_a$ are consistent

with a non-linear response. At the other wave-vectors the normalized response shows no clear trend. Results at k_b are steady, as are the K_3 values, although they remain below the $k = 0$ results of [3], where $K_3 = 13.5 \pm 0.1$ and 13.0 ± 0.5 for $\alpha = 1$ and 2 respectively. The threshold for linear response is expected to move to higher fields as k increases, given the predicted k^{-2} dependence of the response amplitude. Results at the largest wave-vector show the greatest scatter, however, with a marked but apparently non-systematic splitting between the $\alpha = 1$ and $\alpha = 2$ cases. Although it is clearly desirable to examine lower fields, the response became difficult to measure with the signal to noise ratio decreasing significantly for fields $f < 0.25$.

With $N = 512$, this system is relatively small. This affects the smallest accessible wave-vector and, more significantly, the signal-to-noise ratio of the response; (note that the results are expressed per unit volume). Reasonably long simulations were performed at these field strengths, although far shorter than those of [3]. The expense of moving to a larger system would be offset to some degree by the improved statistics, but a larger system is unavoidable at low field strengths. Although the results here show moderate agreement with averages in the unperturbed system they are too few to draw any firm conclusions. It may still be possible that with bigger systems this approach will be valid and more efficient than use of director fluctuations.

6.3.2 Reference model for twisted boundaries

The Lebwohl-Lasher model [110, 111] was used as a reference system for these measurements. This takes a lattice of particles with centres of mass held fixed at the vertices of a simple cubic lattice. The resulting spins are allowed to rotate with continuous orientational freedom subject to anisotropic interactions:

$$\mathcal{H} = -\varepsilon \sum_{\langle i,j \rangle} P_2(\mathbf{e}_i \cdot \mathbf{e}_j) \tag{6.19}$$

where the sum runs over distinct pairs of nearest neighbours only, and ε is a positive coupling constant. The symmetry of this Hamiltonian means that the usual three elastic constants are equivalent, destroying the metastability of the uniformly twisted state: applying twisted boundary conditions to a system initially obeying (6.9), gives rapid conversion to the uniform state corresponding to the global free-energy minimum, i.e. aligned

along the twist axis.

The invariance of the Hamiltonian under a global rotation of the spins was exploited to preserve the twisted configuration. At regular intervals, the entire system was rotated to keep the director in the 1–2 plane; this was performed after every MC sweep, each of which comprised N attempted spin moves. The maximum rotation for individual spin moves was adjusted to give $\sim 50\%$ acceptance. Given the smaller scale of these simulations, the results for K show good agreement with those of [103], where the lattice comprised 32^3 spins. Table 6.2 indicates results for a twist per box of $\pi/2$, where estimated uncertainties in the final digit are given in parentheses. Since this is a lattice model it is possible to apply a non-integer multiple of this basic twist to the system. Results obtained using $\pi/3$ per box are in complete agreement with those presented.

Lattice size	Twist/box	T	Run Length (MC sweeps)	S	K/S^2	K/S^2 from [103]
5×5×20	$\pi/2$	0.10	400k	0.97(3)	3.06(21)	3.026(7)
5×5×20	$\pi/2$	0.40	400k	0.89(3)	3.17(24)	3.177(3)
5×5×20	$\pi/2$	0.75	400k	0.75(2)	3.47(21)	3.355(3)

Table 6.2: Simulation Measurements of K for the Lebwohl-Lasher system

6.3.3 The Gay-Berne model : twisted boundaries

MD simulations were performed at a number of state points, all lying in the nematic region, using the simulation parameters described in §6.3.1. Initial configurations were generated according to (6.9), giving an 'ideal' twist. A cuboidal box of aspect ratio $1:1:4$ was simulated with $N = 2048$ particles. State points were chosen to match those of [3], in which density increases are accompanied by temperature increases to preserve the nematic phase. Starting at the lowest temperature/density, NVT MD runs were performed with temperature maintained by velocity rescaling. No external constraint was placed on the director; the magnitude of n_z for the system director was observed as an indicator of the twist stability, and the local director was accumulated in profile bins

ρ	T	$\lvert n_z \rvert$	S	K_2
0.32	0.90	0.010(1)	0.647(1)	0.853(20)
			0.674(2)	0.676(55)
0.33	1.00	0.118(2)	0.654(1)	1.152(24)
			0.708(13)	0.718(42)
0.35	2.00	0.048(2)	0.546(1)	1.774(47)
			0.663(3)	1.099(98)
0.38	3.00	0.156(9)	0.626(3)	3.750(65)
			0.730(5)	2.53(12)

Table 6.3: K_2 for the Gay-Berne system. At each state point the second line indicates the $k = 0$ values of [3].

along the twist axis. Between state-points, the density was changed by isotropic volume scaling over 5000 timesteps. Typically, a further 1.5×10^5 timesteps were performed with production averages taken over the final 1×10^5. These run lengths were required to obtain reasonable statistics on the torque density in which considerable fluctuations were observed. The results obtained are shown in Table 6.3, where for each point the second line gives the data of [3]. The order parameter is obtained by instantaneously 'untwisting' the system, taking $d\phi/dz$ as constant. The profiles of this indicate high stability and reasonable uniformity along the box; examples are shown in Fig. 6.3 for the state points of Table 6.3. Representing the local director by polar angles $\theta(z), \phi(z)$, comparison is made with the ideal values of $\theta_0 = \pi/2$ and $\phi_0 = kz$; values are included in Fig. 6.3. The profiles remained stable within each simulation, fluctuations about the ideal configuration increasing with temperature. The width of profile bins varies by only ~3% across these densities and will have little effect on the measured profiles.

An increase in K_2 with density/temperature is seen with both methods but the values of this work are distinctly larger than those from the director fluctuation approach. The discrepancy increases as the temperature and density are increased, differing by ~60% at $T = 3.0$. Table 6.3 also shows that whilst maintaining nematic-phase values, the

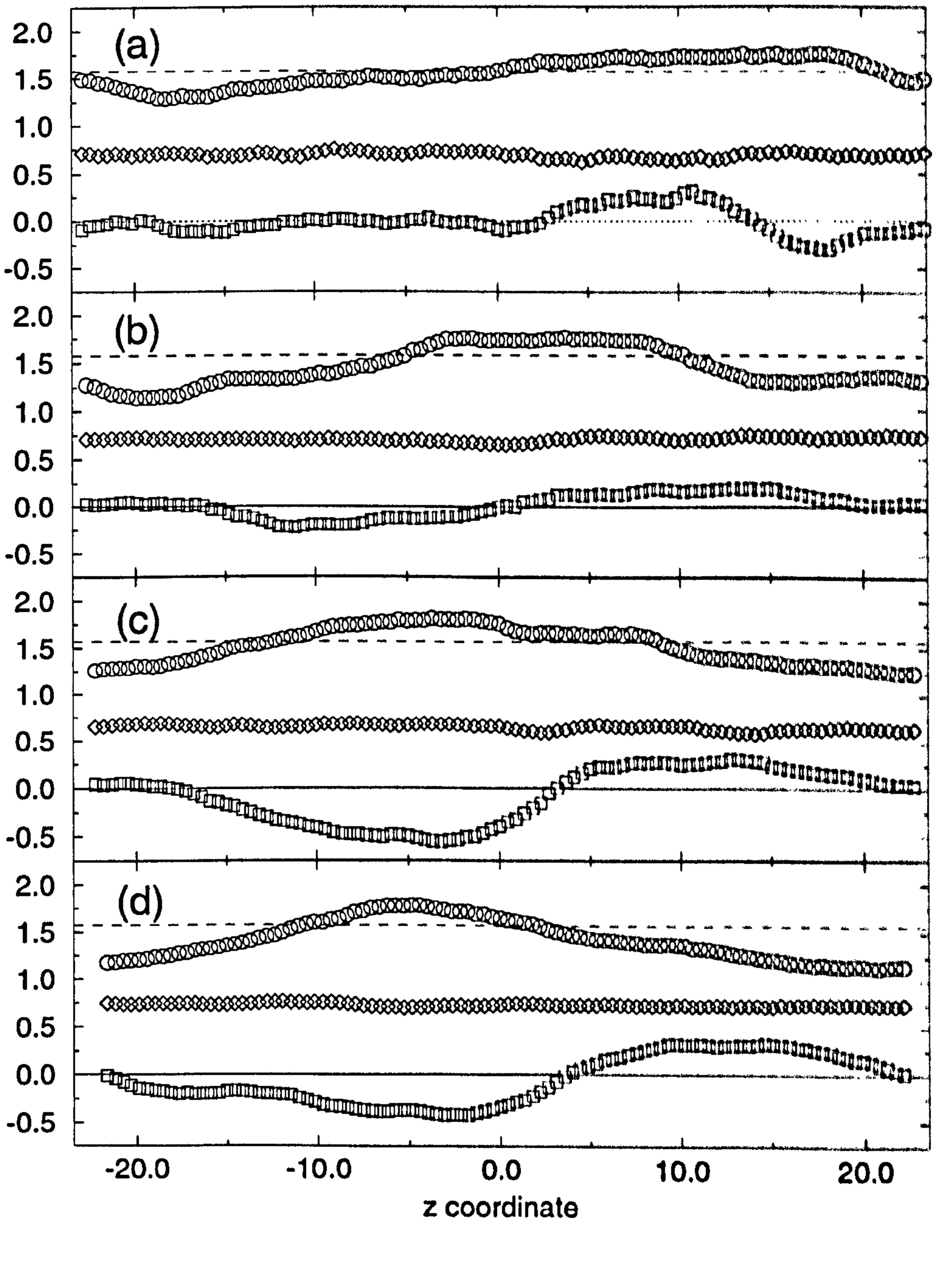

Figure 6.3: Profiles for the GB fluid at $\{\rho, T\}$ values of (a) {0.32,0.9}, (b) {0.33,1.0}, (c) {0.35,2.0} and (d) {0.38,3.0}. Symbols correspond to the order parameter, $S(z)$, (diamonds), and the director angles in radians: $\theta(z)$, (circles) and $\phi(z) - \phi_0(z)$, (squares). The ideal value $\theta(z) = \pi/2$ is indicated by a dashed line.

order parameter is lower in these simulations. Previous implementation of these boundary conditions [107] yielded values for the hard ellipsoid fluid lower than those from director fluctuations. In reporting these results, no attempt has been made to extrapolate to $k = 0$; however, such a procedure is expected to increase the estimates of K_2, based on the low-k curvature of the surfaces in [3]. We note that this system is larger than those used in [3] at all but the highest temperature; the order parameter is consistently lower here, possibly indicating the effects of the boundary condition perturbation, although reasonably large systems and consequentially low values of k have been used. As the temperature increases the stability of the twisted state decreases. This technique relies on maintaining a helical director field, since deviation of $\theta(z)$ from $\pi/2$ allows mixing of the elastic modes. The profiles of $\phi(z)$ at higher temperatures indicate a cross-over around the centre of the box. This may show the system accommodating the elastic deformation in a small region, also affecting the use of (6.17), which assumes a homogeneous stress tensor.

Further simulations were performed to investigate the k-dependence of this method. Maintaining the twist per box, the cuboidal cell was simulated at two other aspect ratios, $1 : 1 : 3\sqrt{3}/2$ and $1 : 1 : \sqrt{2}$, thus varying the pitch of the applied twist. The hexagonal prism cell was also used, simulating $N = 1024$ particles with the ratio of height to (minimum) width fixed to 1.86121 throughout to make a comparison with the cuboidal results. The values of Table 6.4 were obtained using NVE MD with other parameters fixed as above. The variation of K_2 with k is shown in Fig. 6.4. As expected at a fixed density, the estimated elastic constant falls with increasing temperature. Results obtained with a hexagonal prism behave in the manner expected, with the estimate of K_2 rising as $k \to 0$. At the one value of k achieved with both geometries the cuboidal system gives a rather lower result; factors may be the differences in system size and run length, although it is feasible that systematic studies would indicate geometry effects to be significant. The rather high estimate of K_2 for the shortest cuboidal box is likely to result from insufficient sampling.

The use of twisted periodic boundary conditions as a route to K_2 appears to encounter practical difficulties at higher temperatures as thermal energies compete with the metastability of the twisted-director state. Since it is directed at the nematic phase, which in general is unstable at low temperatures for the GB fluid, this appears to be a significant

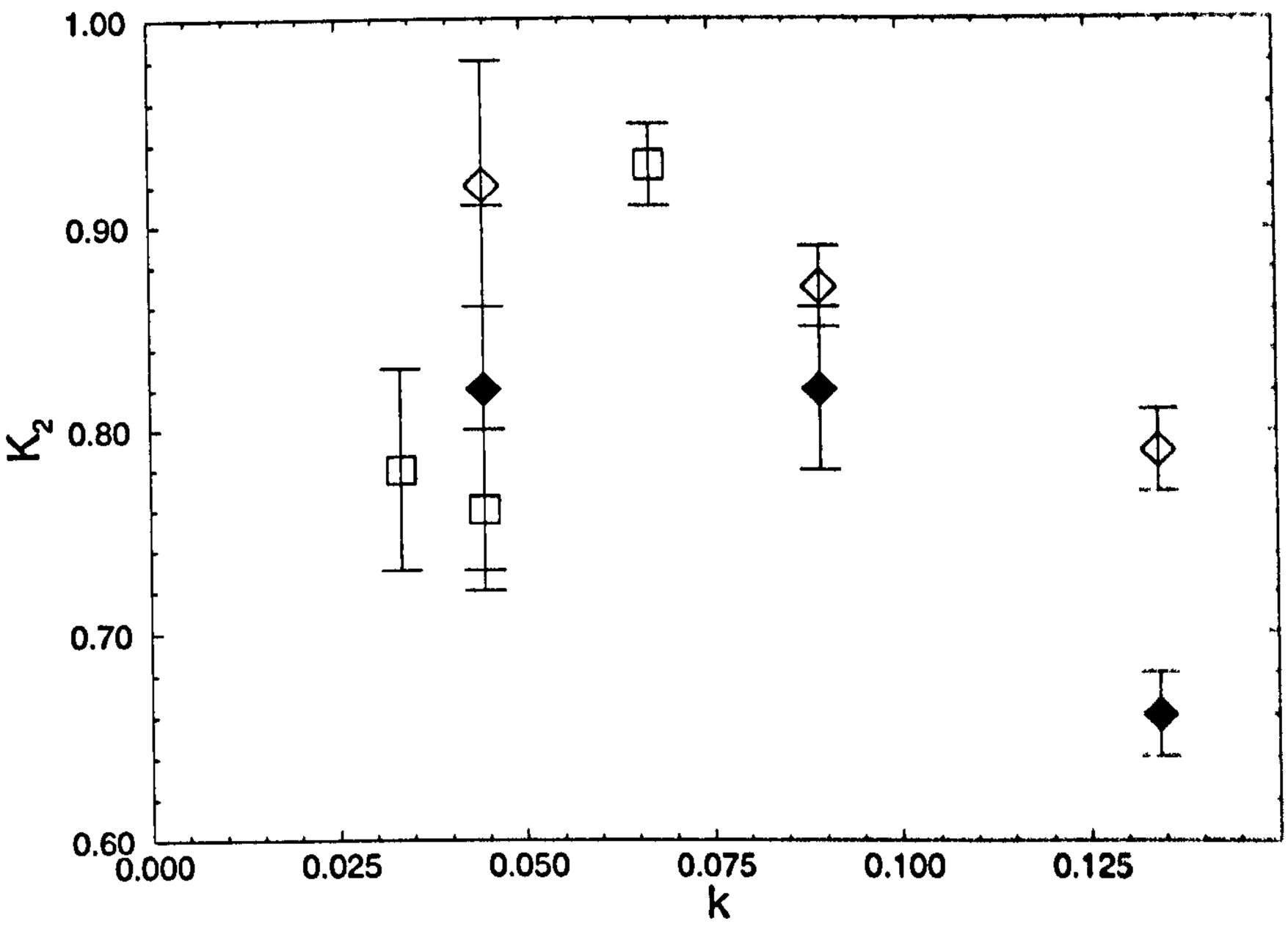

Figure 6.4: Variation of measured K_2 values with pitch wavenumber, k, and boundary conditions. Open symbols : cuboidal box, (squares), and hexagonal prism, (diamonds), at $T = 0.9$. Filled symbols : hexagonal prism at $T = 1.0$.

Simulation	N	Run Length	T	Twist/box	k	K_2
Hex. Prism	1024	200k	0.880(1)	π	0.1343	0.79(2)
Hex. Prism	1024	300k	0.895(2)	$2\pi/3$	0.0895	0.87(2)
Hex. Prism	1024	300k	0.900(2)	$\pi/3$	0.0148	0.92(6)
Cuboid $1:1:\sqrt{2}$	2048	50k	0.894(1)	$\pi/2$	0.0672	0.93(2)
Cuboid $1:1:\frac{3\sqrt{3}}{2}$	2048	100k	0.892(1)	$\pi/2$	0.0148	0.76(4)
Cuboid $1:1:4$	2048	200k	0.900(1)	$\pi/2$	0.0336	0.78(5)
Hex. Prism	1024	200k	0.998(1)	π	0.1343	0.66(2)
Hex. Prism	1024	200k	0.986(2)	$2\pi/3$	0.0895	0.82(4)
Hex. Prism	1024	200k	0.999(2)	$\pi/3$	0.0148	0.82(9)

Table 6.4: Variation of K_2 with helix pitch and boundary conditions

restriction. Twisted periodic boundaries may be usefully applied for other measurements, such as the helical twisting power of dopant molecules [112]. The difficulties encountered here indicate that they should be used with care. We note that previous studies have considered hard particles; it is possible that the method is less suited to this potential, although we have no direct evidence of this.

Chapter 7

Summary

In this thesis we have investigated the behaviour of several model systems for liquid crystals. All have incorporated attractive, anisotropic interactions, and can therefore display much richer phase diagrams than purely repulsive models. The parameters of soft body potentials can be chosen to make contact with real systems. Liquid crystal phase behaviour is known to be highly sensitive to details of molecular structure; we have performed extensive studies to determine the sensitivity of model systems to parameter choice, by mapping out their phase behaviour.

We have examined the effects of independently varying the two main anisotropy parameters of the Gay-Berne fluid: varying the shape anisotropy, κ at fixed well-depth anisotropy, κ', and vice-versa. Dramatic changes in phase behaviour occur with relatively small changes in κ and κ'. We have found that in the range $3 \leq \kappa \leq 4$, a stable S_A region appears. This 'island' in the phase diagram grows both up and down in temperature, and broadens in density as the elongation is increased, remaining bounded in temperature from above by a N–S_A–S_B triple point. The critical temperature for liquid-vapour coexistence is reduced as κ is increased until, at $\kappa \sim 3.4$, it falls below the V–S_B coexistence curve; for higher elongations there is no distinct isotropic liquid phase. At fixed elongation, recent reports have indicated N–V regions for low κ' fluids. We have traced these coexistence curves for systems with $\kappa' \leq 1.25$.

Two other models have been studied, with no anisotropy in the attractive wells. Unlike the Gay-Berne systems, the liquid-vapour region of the Kihara/spherocylinder model

remains firmly established at $L/D = 6$, the highest elongation studied, and the liquid remains isotropic at all temperatures considered. When using Gibbs-ensemble simulations, we noted large fluctuations in the internal pressure of the liquid. By considering several modifications of the potential, we conclude that this is not an artefact of the potential cut-off details. Consideration of the Gay-Berne model with the strength parameter fixed to a constant also indicated isotropic liquid coexisting with a low-density vapour for elongations $\kappa \leq 6.5$. For $\kappa > 5$, a low temperature transition was observed to a glass-like state, with very low diffusion constant. The particles in this state aggregate into 'rosettes', which link into networks traversing the system. With no single pair configuration favoured for isolated molecules, this arrangement is thought to maximize the total binding energy, although no preferred size of rosette was found. Additional studies are required to explore the location of this glass transition and details of the structure for increasing elongations, and to allow closer comparison with experimental systems.

Finally, we have studied the elastic behaviour of the GB fluid. The results of this work serve to highlight the technical demands of such measurements. Large systems and long simulations are required to obtain a reasonable level of statistical confidence. It would appear on this evidence that measuring the response to a perturbing field or a twisted director field does not compete with the director fluctuation technique for efficiency. However, these conclusions can be made only tentatively on the evidence available; further study is required. A number of techniques have now been applied to the GB fluid, with little consensus. Given the wide use of this model system, it would seem appropriate to extend the studies of Chapter 6, although it is apparent that this will require significant computational effort.

We have applied a number of simulation techniques in this work. In Chapter 3, we compared equations of state obtained with NVT MD and NPT MC. The latter is clearly preferable where positional order is present, but broad agreement was obtained. The well-established Gibbs Ensemble method has been applied to liquid-vapour coexistence. The limitations, as well as the benefits, of this technique are becoming widely-known. In a number of cases, we found low temperature regimes of interest, which could not be probed efficiently with standard GEMC due to the expense of particle exchanges. A number of modifications are possible; the pseudo-Gibbs ensemble has recently been

introduced, in which physical particle exchanges can be avoided [113], and the possibility of introducing particles on a continuous scale [62] may allow continuation to lower T. The technique of Gibbs-Duhem integration has been applied in a number of contexts. It has proved possible to integrate reversibly through the I–N transition in one case, although maintaining reversibility is less likely for stronger transitions, such as N–S. The possibility of introducing the GB elongation as the integration variable has been briefly explored, but due to details of the system under study, little progress was made. The technique remains valid, however, and this may prove a useful application in another context. The use of inhomogeneous systems has proved a reliable, if expensive, technique for studying liquid-vapour coexistence, although it becomes more expensive and subject to caveats when one phase displays positional order. When mapping out phase boundaries, the most appropriate use of the method may be to obtain an initial condition for an integration scheme such as GD. However, the technique is particularly well-suited to investigations of interfaces, which we have not undertaken, and should continue to find applications in this field.

Several interesting avenues remain open. The phase diagram studies require free-energy calculations to obtain the exact locations of the phase boundaries. This would be of technical interest in itself, with both S_A and S_B phases to be handled, but would also indicate how the I–N–S triple points are ordered; it is not clear at present whether the N or the S_A wins at lower temperature. The nature of the S_B phase at low temperature has proved to be an interesting question. Although we have found no indication of a phase transition, it would be interesting to investigate finite-size effects by following the phase to low temperature in a larger system. As it is, these results indicate that it is insufficient at low temperatures and high densities to propose phase behaviour using only snapshot configurations.

The discovery of a relatively simple model system displaying nematic-vapour coexistence allows simulation studies of many interesting phenomena. We understand that the group of de Miguel *et al.* are currently studying ordering effects at N–V interfaces in a slab geometry. This is the first simulation study, to our knowledge, of the free nematic surface. No simulations to date have been performed of free nematic droplets; this is also an intrinsically interesting system. Such studies will provide further insight into layering

phenomena already examined by experiment and theory.

Apart from pure academic interest, these results have several potential applications. In seeking to simulate ever-more realistic systems, use of the Gay-Berne model is being extended, with parameters tuned to specific molecules [114]. Since this can result in values far from those previously studied, the process should be informed by an understanding of systematic effects. In a different approach, simple particles are used as building blocks in constructing chain molecules [115, 116]; Gay-Berne mesogens are a suitable choice, but parameter selection will be significant. Furthermore, the GB potential is being generalized to treat biaxial particles [117, 47]; a good understanding of the uniaxial case will provide a solid groundwork for such investigations.

Bibliography

[1] DE MIGUEL, E. , RULL, L. F. , CHALAM, M. K. , and GUBBINS, K. E. , *Molec. Phys.* **74**, 405 (1991).

[2] DE MIGUEL, E. , MARTÍN DEL RÍO, E. , BROWN, J. T. , and ALLEN, M. P. , *J. Chem. Phys.* **105**, 4234 (1996).

[3] ALLEN, M. P. , WARREN, M. A. , WILSON, M. R. , SAURON, A. , and SMITH, W. , *J. Chem. Phys.* **105**, 2850 (1996).

[4] PANAGIOTOPOULOS, A. Z. , QUIRKE, N. , STAPLETON, M. , and TILDESLEY, D. J. , *Molec. Phys.* **63**, 527 (1988).

[5] ZANNONI, C. , in *The Molecular Physics of Liquid Crystals*, edited by LUCKHURST, G. R. and GRAY, G. W. , chapter 3, pp. 191–220, Academic Press, New York, 1979.

[6] EPPENGA, R. and FRENKEL, D. , *Molec. Phys.* **52**, 1303 (1984).

[7] ALLEN, M. P. , EVANS, G. T. , FRENKEL, D. , and MULDER, B. , *Adv. Chem. Phys.* **86**, 1 (1993).

[8] CHANDRASEKHAR, S. , *Liquid Crystals*, Cambridge University Press, Cambridge, second edition, 1992.

[9] ALLEN, M. P. and TILDESLEY, D. J. , *Computer simulation of liquids*, Clarendon Press, Oxford, paperback edition, 1989, ISBN 0-19-855645-4, 385pp.

[10] METROPOLIS, N. , ROSENBLUTH, A. W. , ROSENBLUTH, M. N. , TELLER, A. H. , and TELLER, E. , *J. Chem. Phys.* **21**, 1087 (1953).

[11] LINKE, A. , HEERMANN, D. W. , ALTEVOGT, P. , and SIEGERT, M. , *Physica A* **222**, 205 (1995).

[12] ALDER, B. J. and WAINWRIGHT, T. E. , *Phys. Rev.* **A1**, 18 (1970).

[13] ALLEN, M. P. , MASON, C. P. , DE MIGUEL, E. , and STELZER, J. , *Phys. Rev. E* **52**, R25 (1995).

[14] STELZER, J. , LONGA, L. , and TREBIN, H.-R. , *J. Chem. Phys.* **103**, 3098 (1995).

[15] *Monte Carlo and molecular dynamics of condensed matter systems*, volume 49, Bologna, 1996, Italian Physical Society, Proceedings of Euroconference, Como, Italy, July 3–28, 1995, ISBN 88–7794–078–6.

[16] VIEILLARD-BARON, J. , *J. Chem. Phys.* **56**, 4729 (1972).

[17] VIEILLARD-BARON, J. , *Molec. Phys.* **28**, 809 (1974).

[18] FRENKEL, D. and MULDER, B. M. , *Molec. Phys.* **55**, 1171 (1985).

[19] VEERMAN, J. A. C. and FRENKEL, D. , *Phys. Rev. A* **41**, 3237 (1990).

[20] SADUS, R. J. and PRAUSNITZ, J. M. , *J. Chem. Phys.* **104**, 4784 (1995).

[21] MULLER, E. A. , VEGA, L. F. , GUBBINS, K. E. , and RULL, L. F. , *Molec. Phys.* **85**, 9 (1995).

[22] KIHARA, T. , *J. Phys. Soc. Japan* **6**, 289 (1951).

[23] PAVLICEK, J. and BOUBLIK, T. , *J. Phys. C* **00**, 2298 (1992).

[24] BOUBLIK, T. , *Molec. Phys.* **76**, 327 (1992).

[25] BERNE, B. J. and PECHUKAS, P. , *J. Chem. Phys.* **56**, 4213 (1972).

[26] KUSHICK, J. and BERNE, B. J. , *J. Chem. Phys.* **64**, 1362 (1976).

[27] KABADI, V. N. and STEELE, W. A. , *Ber. Bunsenges. Phys. Chem.* **89**, 2 (1985).

[28] SEDIAWAN, W. , GUPTA, S. , and MCLAUGHLIN, E. , *Molec. Phys.* **63**, 691 (1988).

[29] KABADI, V. N. and STEELE, W. A. , *Ber. Bunsenges. Phys. Chem.* **80**, 9 (1985).

[30] OROZCO, J. and CASTILLO, R. , *J. Chem. Phys.* **00**, 1300 (1993).

[31] GAY, J. G. and BERNE, B. J. , *J. Chem. Phys.* **74**, 3316 (1981).

[32] LUCKHURST, G. R. , STEPHENS, R. A. , and PHIPPEN, R. W. , *Liq. Cryst.* **8**, 451 (1990).

[33] BERARDI, R. , EMERSON, A. P. J. , and ZANNONI, C. , *J. Chem. Soc. Faraday Trans.* **89**, 4069 (1993).

[34] DE MIGUEL, E. , RULL, L. , and GUBBINS, K. , *Phys. Rev. A* **45**, 3813 (1992).

[35] PALKE, W. E. , EMSLEY, J. W. , and TILDESLEY, D. J. , *Molec. Phys.* **82**, 177 (1994).

[36] ALEJANDRE, J. , TILDESLEY, D. J. , and CHAPELA, G. A. , *J. Chem. Phys.* **102**, 4574 (1995).

[37] MARTÍN DEL RÍO, E. , DE MIGUEL, E. , and RULL, L. , *Physica A* **213**, 138 (1995).

[38] SARMAN, S. , *J. Chem. Phys.* **101**, 480 (1994).

[39] SARMAN, S. and EVANS, D. J. , *J. Chem. Phys.* **00**, 620 (1993).

[40] SARMAN, S. and EVANS, D. J. , *J. Chem. Phys.* **00**, 9021 (1993).

[41] SARMAN, S. , *J. Chem. Phys.* **103**, 393 (1995).

[42] SMONDYREV, A. M. , LORIOT, G. B. , and PELCOVITS, R. A. , *Phys. Rev. Lett.* **75**, 2340 (1995).

[43] EMERSON, A. P. J. and ZANNONI, C. , *J. Chem. Soc. Faraday Trans.* **01**, 3141 (1995).

[44] SEDIAWAN, W. , GUPTA, S. , and MCLAUGHLIN, E. , *J. Chem. Phys.* **00**, 1888 (1989).

[45] TJIPTO-MARGO, B. and SULLIVAN, D. , *J. Chem. Phys.* **88**, 6620 (1988).

[46] VELASCO, E. , SOMOZA, A. M. , and MEDEROS, L. , *J. Chem. Phys.* **102**, 8107 (1995).

[47] CLEAVER, D. J. , CARE, C. M. , ALLEN, M. P. , and NEAL, M. P. , *Phys. Rev. E* **54**, 559 (1996).

[48] GOLDSTEIN, H. , *Classical Mechanics*, Addison Wesley, Reading, Massachusetts, second edition, 1980.

[49] HASHIM, R. , LUCKHURST, G. , and ROMANO, S. , *J. Chem. Soc. Faraday Trans.* **91**, 2141 (1995).

[50] PRESS, W. H. , FLANNERY, B. P. , TEUKOLSKY, S. A. , and VETTERLING, W. T. , *Numerical Recipes in Fortran*, Cambridge University Press, Cambridge, 2nd edition, 1992.

[51] JAMES, F. , *Comput. Phys. Commun.* **60**, 329 (1990).

[52] VAN DUIJNEVELDT, J. S. , Private communication.

[53] ALLEN, M. P. , FRENKEL, D. , and TALBOT, J. , *Comput. Phys. Rep.* **9**, 301 (1989).

[54] ALLEN, M. P. , Molecular dynamics for hard particles, in *Monte Carlo and molecular dynamics of condensed matter systems*, edited by BINDER, K. and CICCOTTI, G. , volume 49, pp. 89–106, Italian Physical Society, Bologna, 1996, Proceedings of the Euroconference on 'Monte Carlo and molecular dynamics of condensed matter systems', Como, Italy, July 3–28, 1995, ISBN 88-7794-078-6.

[55] HOCKNEY, R. W. and EASTWOOD, J. W. , *Computer simulations using particles*, Adam Hilger, Bristol, 1988.

[56] SWOPE, W. C. , ANDERSEN, H. C. , BERENS, P. H. , and WILSON, K. R. , *J. Chem. Phys.* **76**, 637 (1982).

[57] FINCHAM, D. , *Molec. Simul.* **11**, 79 (1993).

[58] ADAMS, D. J. , *CCP5 Quarterly* **10**, 30 (1983).

[59] ALLEN, M. P. , BROWN, J. T. , MASON, C. P. , and WARREN, M. A. , *Molec. Phys.* , submitted.

[60] DEITRICK, G. L. , SCRIVEN, L. E. , and DAVIS, H. T. , *J. Chem. Phys.* **90**, 2370 (1989).

[61] MON, K. K. and GRIFFITHS, R. B. , *Phys. Rev. A* **31**, 956 (1985).

[62] NEZBEDA, I. and KOLAFA, J. , *Molec. Simul.* **5**, 391 (1991).

[63] ATTARD, P. , *J. Chem. Phys.* **98**, 2225 (1993).

[64] MASON, C. P. , *The computer simulation of the hard ellipsoid fluid*, PhD thesis, University of Bristol, 1994.

[65] GRAY, C. and GUBBINS, K. E. , *Theory of Molecular Fluids*, Clarendon Press, Oxford, 1984.

[66] FRENKEL, D. and SMIT, B. , *Understanding molecular simulation : from algorithms to applications*, Academic Press, Inc., San Diego, 1996, ISBN 0-12-267370-0.

[67] NIJMEIJER, M. J. P. , BRUIN, C. , VAN WOERKOM, A. B. , BAKKER, A. F. , and VAN LEEUWEN, J. M. M. , *J. Chem. Phys.* **96**, 565 (1992).

[68] ROWLINSON, J. S. , *J. Phys. Cond. Mat.* **6**, A1 (1994).

[69] EGGEBRECHT, J. , THOMPSON, S. M. , and GUBBINS, K. E. , *J. Chem. Phys.* **80**, 2299 (1986).

[70] HOLCOMB, C. D. , CLANCY, P. , and ZOLLWEG, J. A. , *Molec. Phys.* **78**, 437 (1993).

[71] SCHOFIELD, P. and HENDERSON, J. R. , *Proc. Roy. Soc. Lond. A* **379**, 231 (1982).

[72] HARASIMA, A. , *Adv. Chem. Phys.* **1**, 203 (1958).

[73] IRVING, J. H. and KIRKWOOD, J. G. , *J. Chem. Phys.* **18**, 817 (1950).

[74] WALTON, J. P. R. B. , TILDESLEY, D. J. , and ROWLINSON, J. S. , *Molec. Phys.* **48**, 1357 (1983).

[75] PANAGIOTOPOULOS, A. Z. , *Molec. Phys.* **61**, 813 (1987).

[76] SMIT, B. , DE SMEDT, P. , and FRENKEL, D. , *Molec. Phys.* **68**, 931 (1989).

[77] KOFKE, D. A. , *Molec. Phys.* **78**, 1331 (1993).

[78] KOFKE, D. A. , *J. Chem. Phys.* **98**, 4149 (1993).

[79] MEIJER, E. J. and EL AZHAR, F. , preprint.

[80] CAMP, P. J. , MASON, C. P. , ALLEN, M. P. , KHARE, A. A. , and KOFKE, D. A. , *J. Chem. Phys.* **105**, 2837 (1996).

[81] DE MIGUEL, E. , RULL, L. F. , and GUBBINS, K. E. , *Physica A* **177**, 174 (1991).

[82] MCGROTHER, S. C. , WILLIAMSON, D. C. , and JACKSON, G. , *J. Chem. Phys.* **104**, 6755 (1996).

[83] GINZBURG, V. V. , GLASER, M. A. , and CLARK, N. A. , *Liq. Cryst.* **21**, 265 (1996).

[84] DE MIGUEL, E. and ALLEN, M. P. , *Molec. Phys.* **70**, 1275 (1992).

[85] DE GENNES, P. G. and PROST, J. , *The Physics of Liquid Crystals*, Clarendon Press, Oxford, second, paperback edition, 1995.

[86] QUESNEL, D. J. , RIMAI, D. S. , and DE MEJO, L. P. , *Phys. Rev. B* **48**, 6795 (1993).

[87] FRENKEL, D. and LADD, A. J. C. , *J. Chem. Phys.* **81**, 3188 (1984).

[88] VEGA, C. , PARAS, E. P. A. , and MONSON, P. A. , *J. Chem. Phys.* **96**, 9060 (1992).

[89] BOLHUIS, P. , *Liquid-like behaviour in solids; Solid-like behaviour in liquids*, PhD thesis, FOM-Institute for Atomic and Molecular Physics, 1996.

[90] TELO DA GAMA, M. , Liquid Crystal Interfaces, in *Observation, Prediction and Simulation of Phase Transitions in Complex Fluids*, edited by BAUS, M. , RULL,

L. F. , and RYCKAERT, J. P. , volume 460 of NATO *ASI Series C*, pp. 243-292. Kluwer Academic Publishers, Dordrecht, 1995, Proceedings of the NATO Advanced Study Institute and Enrico Fermi Course LXXIX on 'Observation and Prediction of Phase Transitions in Complex Fluids', Varenna, Italy, July 25-August 8, 1991. ISBN 0-7923-3439-6.

[91] DE MIGUEL, E. , RULL, L. F. , CHALAM, M. K. , and GUBBINS, K. E. , *Molec. Phys.* **71**, 1223 (1990).

[92] KIHARA, T. , *Chem. Phys. Lett.* **92**, 175 (1982).

[93] VEGA, C. and FRENKEL, D. , *Molec. Phys.* **67**, 633 (1989).

[94] SMIT, B. , *J. Chem. Phys.* **96**, 8639 (1992).

[95] VEGA, L. , LAGO, S. , DE MIGUEL, E. , and RULL, L. F. , *J. Phys. C* **00**, 7431 (1992).

[96] VEGA, L. , DE MIGUEL, E. , RULL, L. F. , JACKSON, G. , and MCLURE, I. A. , *J. Chem. Phys.* **96**, 2296 (1992).

[97] CAMP, P. J. , Private communication.

[98] NAGY, M. and KELLER, A. , *Polymer Commun.* **30**, 130 (1989).

[99] ODELL, J. A. , KELLER, A. , ATKINS, E. D. T. , NAGY, M. , FEIJOO, J. L. , and UNGAR, G. , in *Rigid Rod Polymer Molecules*, edited by ADAMS, W. , volume 134 of *Mat. Res. Soc. Symp. Proc.*, p. 223, Pittsburgh, 1989, Materials Research Society.

[100] FRANK, F. C. , *Discuss. Faraday Soc.* **25**, 19 (1958).

[101] NEHRING, J. and SAUPE, A. , *J. Chem. Phys.* **54**, 337 (1971).

[102] FAETTI, S. and PALLESCHI, V. , *Liq. Cryst.* **2**, 261 (1987).

[103] CLEAVER, D. J. and ALLEN, M. P. , *Phys. Rev. A* **43**, 1918 (1991).

[104] ALLEN, M. P. and FRENKEL, D. , *Phys. Rev. A* **37**, 1813 (1988).

[105] ALLEN, M. P. and FRENKEL, D. , *Phys. Rev. A* **42**, 3641 (1990), Erratum.

[106] TJIPTO-MARGO, B. , EVANS, G. T. , ALLEN, M. P. , and FRENKEL, D. , *J. Phys. Chem.* **96**, 3942 (1992).

[107] ALLEN, M. P. and MASTERS, A. J. , *Molec. Phys.* **79**, 277 (1993).

[108] FORSTER, D. , *Ann. Phys.* **85**, 505 (1974).

[109] WARREN, M. A. , Private communication.

[110] LEBWOHL, P. A. and LASHER, G. , *Phys. Rev. A* **6**, 426 (1972).

[111] LEBWOHL, P. A. and LASHER, G. , *Phys. Rev. A* **7**, 2222 (1973), Erratum.

[112] ALLEN, M. P. , *Phys. Rev. E* **47**, 4611 (1993).

[113] CAMP, P. J. and ALLEN, M. P. , *Molec. Phys.* **88**, 1459 (1996).

[114] LUCKHURST, G. R. and SIMMONDS, P. S. J. , *Molec. Phys.* **80**, 233 (1993).

[115] WILSON, M. R. , *Molec. Phys.* **81**, 675 (1994).

[116] LEVESQUE, D. , MAZARS, M. , and WEIS, J.-J. , *J. Chem. Phys.* **103**, 3820 (1995).

[117] BERARDI, R. , FAVA, C. , and ZANNONI, C. , *Chem. Phys. Lett.* **236**, 462 (1995).